Uncertainty Analysis in a Shipboard Integrated Power System using Multi-Element Polynomial Chaos

by

Pradya Prempraneerach

Submitted to the Department of Mechanical Engineering
in partial fulfillment of the requirements for the degree of

Doctor of Philosophy in Ocean Engineering

at the

MASSACHUSETTS INSTITUTE OF TECHNOLOGY

June 2007

Author .....
Department of Mechanical Engineering
February 28, 2007

Certified by .....
Michael S. Triantafyllou
Professor of Mechanical and Ocean Engineering
Director, Center for Ocean Engineering
Thesis Supervisor

Accepted by .....
Lallit Anand
Chairman, Department Committee on Graduate Students

Uncertainty Analysis in a Shipboard Integrated Power System using Multi-Element Polynomial Chaos

by

Pradya Prempraneerach

Submitted to the Department of Mechanical Engineering
on February 28, 2007, in partial fulfillment of the
requirements for the degree of
Doctor of Philosophy in Ocean Engineering
ERRATA submitted on October 31, 2007

Abstract

The integrated power system has become increasingly important in electric ships due to the integrated capability of high-power equipment, for example, electromagnetic rail guns, advance radar system, etc. Several parameters of the shipboard power system are uncertain, caused by a measurement difficulty, a temperature dependency, and random fluctuation of its environment. To date, there has been little if any studies which account for these stochastic effects in the large and complex shipboard power system from either an analytical or a numerical perspective. Furthermore, all insensitive parameters must be identified so that the stochastic analysis with the reduced dimensional parameters can accelerate the process. Therefore, this thesis is focused on two main issues - stochastic and sensitivity analysis - on the shipboard power system.

The stochastic analysis of the large and complex nonlinear systems with the non-Gaussian random variables or processes, in their initial states or parameters, are prohibited analytically and very time consuming using the brute force Monte Carlo method. As a result, numerical stochastic solutions of these systems can be efficiently solved by the generalized Polynomial Chaos (gPC) and Probabilistic Collocation Method (PCM). In the case of the long-time integration and discontinuity in the stochastic solutions, the multi-element technique of PCM, which refines the solution in random space, can significantly improve the solutions' accuracy. Furthermore, the hybrid gPC+PCM is developed to extend the gPC ability to handle a system with nonlinear non-polynomial functions. Then, we systematically establish the convergence rate and compare the convergence performance among all numerical stochastic algorithms on various systems with both continuous and discontinuous solutions as a function of random dimension and the algorithms' accuracy governing parameters.

To identify the most significant parameter in the large-scale complex systems, we propose new sensitivity analysis techniques - Monte Carlo Sampling, Collocation, Variance, and Inverse Variance methods - for static functions and show that they agree well with Morris method, which is one of the existing sensitivity analysis techniques

for a function with large input dimensions. In addition, we extend the capability of the Sampling, Collocation, Variance, and the Morris methods to study both the parameters' sensitivity and the interaction of the ordinary differential equations. In each approach, both strength and limitations of the sensitivity ranking accuracy and the convergence performance are emphasized. The convergence rate of the Collocation and Variance methods are more than an order of magnitude faster than that of Morris and Sampling methods for low and medium parameters' dimensions.

At last, we successfully apply both stochastic and sensitivity analysis techniques to the integrated shipboard power system, with both open-and close-loop control of the propulsion system, to study a propagation of uncertainties and rank parameters in the order of their importance, respectively.

Thesis Supervisor: Michael S. Triantafyllou
Title: Professor of Mechanical and Ocean Engineering
Director, Center for Ocean Engineering

ERRATA

In Chapter 5, the convergence formulation in Equation 5.11 and 5.12, defined as a difference between low and high accuracy solutions for each sensitivity analysis method, does not represent true convergence characteristics of each technique. The correct approach to measure and compare the convergence characteristics among these techniques is to compute the absolute difference between estimated and reference solutions that has a higher accuracy and to normalize with the absolute value of the reference solution. Similar to Equation 5.11 and 5.12, the RMS values of the normalized absolute difference must be considered for a function or system with n inputs as shown below (also see two references below)

$$\epsilon^j_{i,mean} = \frac{|E[EE^j_i(t)] - E[EE^j_{i,ref}(t)]|}{|E[EE^j_{i,ref}(t)]|} \quad (1)$$

$$\epsilon^j_{i,var} = \frac{|\sigma[EE^j_i(t)] - \sigma[EE^j_{i,ref}(t)]|}{|\sigma[EE^j_{i,ref}(t)]|} \quad (2)$$

$$RMS(\epsilon^j_{i,mean}) = \sqrt{\frac{1}{n}\sum_{i=1}^{n}(\epsilon^j_{i,mean})^2} \quad (3)$$

$$RMS(\epsilon^j_{i,var}) = \sqrt{\frac{1}{n}\sum_{i=1}^{n}(\epsilon^j_{i,var})^2} \quad (4)$$

These convergence formula can be applied to the variance method by replacing $(E[EE_i^j], \sigma[EE_i^j])$ with (VEE_i^j, IEE_i^j). The Morris method required to use its own solution with highest accuracy as the reference solution because the solution from the finite difference depends on Δ. The other gradient-methods can used the solution from Monte Carlo Sampling and Collocation methods with highest accuracy as the reference solution. The more accurate convergence results of all methods, particularly for the modified Morris's function (in Section 5.2.4) and an open-loop induction machine with an infinite bus (in Section 5.3.3), exhibit faster convergence rates (see two reference below).

In addition, the references below give the quasi-Monte Carlo Sampling method and a combined Variance with quasi-Monte Carlo method that provides the fastest convergence among all sensitivity analysis techniques.

Reference

1) "Stochastic Sensitivity Methods and Application to the Shipboard Power System", Prempraneerach P., Hover F.S., Triantafyllou M.S., McCoy T.J., Chryssostomidis C., and Karniadakis G.E., submitted to IEEE Transaction on Power Systems in April 2007 and resubmitted in October 2007.

2) "Sensitivity Analysis of the Shipboard Integrated Power System", Prempraneerach P., Hover F.S., Triantafyllou M.S., McCoy T.J., Chryssostomidis C., and Karniadakis G.E., Naval Engineering Journal, Vol. 119, No. 2, 2007.

Acknowledgments

First, I would like to thank Professor Triantafyllou, Michael and Dr. Hover, Franz who gave me an opportunity to do research on these exciting fields of the electric machine and stochastic analysis as well as advised me through these four years of my doctoral program. Moreover, thank you for pushing me to improve my writing and analytical skills.

Second, another big thank must be to Professor Karniadakis, George, you always encourage me to get excited about this research, particularly on the very huge system simulation, and about all various great ideas on the stochastic algorithms. However, I will always remember to first start with a small system, before jumping to a bigger system.

Third, I also like to thank Professor McCoy, Timothy for guiding me and giving me an inside in the field of electric machines and power systems. Many thanks for helping me publish some of my results in different Conferences.

I also would like to acknowledge Sea Grant for supporting me on a Research Assistantship and all Conference meetings. And thank to Thai Government for a scholarship during my Bachelor and Master degrees and a support during the first year of this doctoral program.

Without friends here at the towing tank to have fun and to help each other during these past four years, my life would have been so miserable. So many thanks to David Beal, Steve Licht, Victor Polidoro, Jason Dahl, and Karl McLetchie. In addition, I like to thank to several colleages at Brown University, including Didier Lucor, Xiaoliang Wan, and Guang Lin for the discussion on the generalized Polynomial Chaos, Probabilistic Collocation, and multi-element techniques.

Finally, I would like to thank my wife: Pranisa Boonkham for her support in my daily life, I probably would not come this far without her encouragement. Also, thank to my family in Thailand for their support during this long years of studying aboard. Finally, it has come to the end of my student life. And, I am now ready to start the next chapter of my life.

Contents

List of Figures

5-105The $ES_{2,(j,i)}$ plots using the Monte Carlo Sampling method with $NN = 3000$ and $\sigma_{x_i} = 0.3$ for ranking the input sensitivity within $t \in [0, 0.2]$ (Left) and $t \in [0, 1.62]$ (Right). Note that the order of the **power converter's parameters** (x_i) on the x-axis are [L_c, r_{dc}, L_{dc}, C_{dc}, L_{filter}, r_{filter}, C_{filter}] from left to right and the order of y_j outputs on the y-axis are [ψ^e_{qs}, ψ'^e_{kq1}, ψ'^e_{kq2}, ψ^e_{ds}, ψ'^e_{fd}, ψ'^e_{kd}, ψ^e_{0s}, θ, e'_{xfd}, VF, V_{an}, V_{bn}, V_{cn}, i_a, i_b, i_c, V_{c1}, V_{c2}, V_{c3},ψ^e_{qs}, ψ'^e_{qr}, ψ^e_{ds}, ψ'^e_{dr}, ψ^e_{0s}, ω_r] from top to bottom. 288

List of Tables

Chapter 1

Introduction

The advent of modern power electronics and large scale solid-state power converters is ushering in a new age for electric ship propulsion. This is embodied in the All Electric Ship (AES) concept where a single set of prime movers is used to power both propulsion and all other loads aboard the vessel [65]. This system has many advantages over traditional mechanically driven ships, including reduced fuel usage, reduced maintenance and greater design flexibility. Many sectors of the commercial marine industry are adopting this new technology.

Military ships can also benefit from many of the same advantages as their commercial counterparts by adopting an integrated power system (IPS) architecture. A general diagram of the IPS in the electric ship architecture, shown in Figure 1-1, consists of an interdependent connection among: (1) power-generation systems or sets of a prime mover directly coupled with a synchronous machine (SM); (2) propulsion systems or induction machines (IM); and (3) high-power equipment or the electromagnetic (EM) railguns [13] and other auxillary electrical services. However, warships can also benefit from the much larger installed generation capacity for powering advanced electric weapons and sensors. In the future warship, the major requirements of the IPS can be summarized as the following: 1) a capability to maintain continuity of service with sufficient reserve margin in the presence of critical loads, component and cascaded failures, and internal errors; 2) a fault containment ability, which leads to an optimal dynamic reconfiguration of the zonal topology; 3) an advance intelligent

control in both component and central levels.

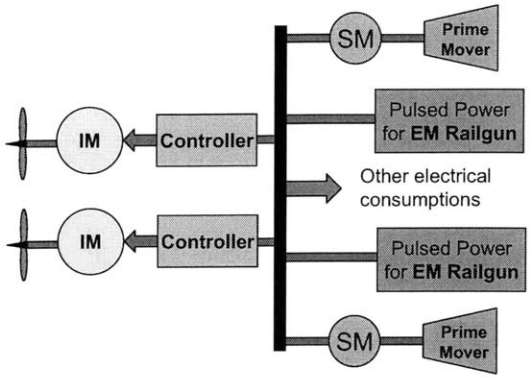

Figure 1-1: A general model configuration of the AES system.

In contrast, the large-grid utility power system consists of many power supplies, branches, and switches. The reconfiguration of the utility network mainly aims to satisfy the following criteria: 1) line loss minimization [42]; 2) load balancing and loadability maximization [59]; and 3) voltage stability margin maximization [5]. Moreover, the transmission, load, and generator dynamics are neglected in most reconfiguration problems, and thus the power flow problem needs to be solved with a system of differential-algebraic equations (DAE). That is a more time-consuming process than solving a system of ordinary differential equation (ODE). However, the shipboard power systems are limited due to small numbers of generators that are closely sized with loads, short tie line with low impedance, and a small group of loads [4], [9]. To enhance redundancy in the AES system, the electrical distribution system uses a zonal configuration [67],[57]. Therefore, the fault propagation can be contained within each electrical zone and the intelligent control unit is able to perform a system reconfiguration and fault containment to further increase survivability.

The power sharing between the propulsion units and the high-power equipment, especially under heavy propulsion demand and casualty conditions, has recently been identified as an another important issue [16], [13], [30], [56], [67]. In a new AES configuration, there is an increasing demand for electric power for ship system automation, electrical weaponry, electric propulsion, and ship service distribution. About 70% to

90% of power from the generator units in the fully IPS is consumed in the propulsion systems [16]. Thus, when a sudden and large power demand for periodically charging and discharging the pulse forming network of electric guns is imposed on an electrical bus during a mission or life critical situation, the power distribution must be optimally modified to yield the most efficient power usage and to maintain a continuity of service [66], [67]. Recently, a work by [30], [56] with single-generator distributed electric power to single propulsion and pulsed power loads showed that the bus voltage drops significantly during a charging sequence of the pulse forming network and a heavy propulsion load. Thus, a coordinate of distributed power between the pulsed power and propulsion load is necessary to maintain the system stability and to improve the continuity and quality of electrical service.

The Office of Naval Research (ONR) developed a prototype IPS testbed, including simulated and experimental systems. The ONR-IPS model and simulation separate the AC power generation and propulsion systems into port and starboard subsystems, and divide the DC zonal electric distribution into three main zones along the ship hull, as shown in Figure 1-2. Each AC subsystem is composed of a 59-kW synchronous generator, a close-loop drive of a propulsion system, and a power supply for providing DC power to either the port or starboard bus. In DC zonal electric distribution, there are a port bus, a starboard bus, six Ship Service Converter Modules (SSCM's), a Ship Service Inverter Module (SSIM), a motor controller (MC), and a constant power load (CPL) [28]. A mathematical model of the AC subsystem is described in more detail later in Chapter 2 of this thesis. The experimental Naval Combat Survivability testbed [56], constructed at Purdue University, has all components and a similar structure as that in Figure 1-2.

1.1 Problem Statement

Because of the complexity and large scale of the shipboard integrated power system, a simulation of the AES model must be able to capture various situations for investigating the transient stability and system interaction accurately. Thus, the model

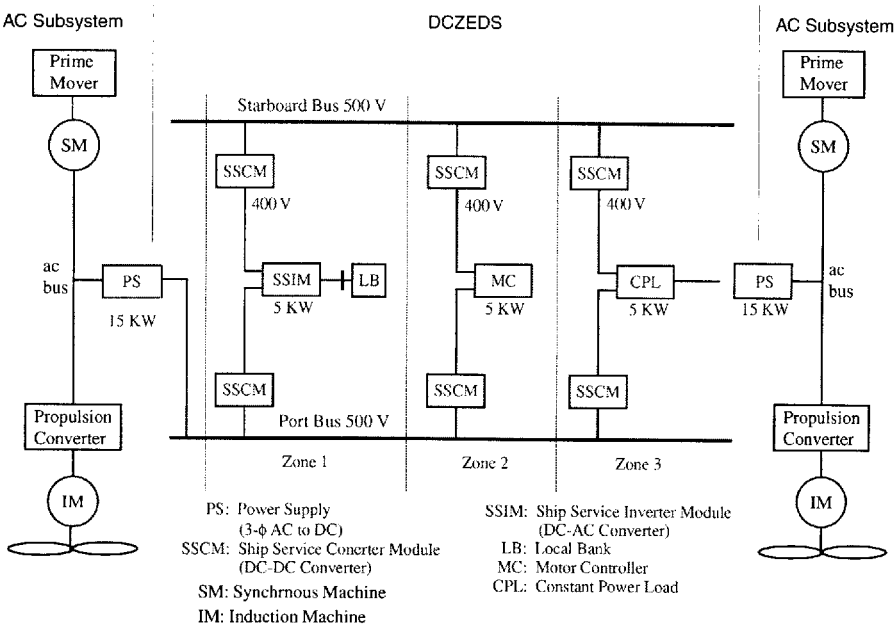

Figure 1-2: A one-line diagram of the ONR integrated power system consisting of port and starboard AC and DC zones [28].

of the AC power distributions with propulsion and DC power network is sufficient for our study purpose. For example, the model developed for the ONR challenge problem [27] has a total number of 133 state equations and 231 associated parameters. Only the AC power distribution and the propulsion system, one of the most important sections of the ONR challenge problem, are the main focus in this study.

Other significant goals of future AES are to minimize the number of crew and to increase system monitoring and control automation [67] for reduction of operational costs and increased reliability. However, to maintain the situation awareness and fault tolerance, a fusion of redundant sensor measurement is required to accurately estimate the current environment and conditions. This leads to another important issue of estimation and prediction in the uncertain situation; therefore, the dynamic performance of single machines as well as machine interaction must be tested for efficiency and dependability under stochastic variations.

Many research projects have been conducted on the AES system under conditions of deterministic propulsion-load and electrical-load deviations [16], [56], [58]. However, a stochastic analysis of the AES system with the presence of load uncer-

tainties has not been addressed, except in utility power systems [41]. The Monte Carlo (MC) method and traditional stochastic processes, characterized by a joint probability density function and analytically based on the power spectral density of auto-correlation and cross-correlation [33], are often used in the stochastic analysis of both discrete- and continuous-time systems. Although the Monte Carlo simulation is easy to apply for both linear and nonlinear systems, it requires extensive computation, due to its low convergence of statistical solutions, and provides no bounds for probability estimation - two major disadvantages. To accelerate the convergence of the Monte Carlo method, the Quasi-Monte Carlo (QMC) method [40],[46] has been introduced; nevetheless, the QMC still suffers the same limitations. For the traditional stochastic processes, the difficulty in analysis limits the computation only to the Gaussian random process of linear time-invariant [33] and simple-nonlinear [26] systems. Thus, a stochastic process using the Galerkin and Collocation techniques of the polynomial chaos, which are applicable to various classes of random process, are better alternatives for examining uncertainty propagation of high-order parametric and load variations in the large-scale AES system.

The generalized Polynomial Chaos (gPC), based on the Galerkin projection and Wiener-Askey polynomial chaos, [19], [35], [60], [62], has been successfully applied for the stochastic analysis in various applications, such as a finite element in solid mechanics [19], fluid dynamics [64], and electrical circuits [54]. Major advantages of the gPC technique are that a probability density function, as well as statistical moments of system variables, can be obtained explicitly after solving nodal system equations and the accuracy of the gPC statistical solution converges faster than that of the Collocation method. However, an additional computational cost is required for the Galerkin projection. The limitations associated with the gPC are the expansion complexity of nonlinear non-polynomial terms onto the orthogonal polynomial-chaos basis and its trade-off between computational cost and accuracy for a large system with many random inputs.

Uncertainty analysis using the Probabilistic Collocation Method (PCM), based on the Collocation approach of polynomial chaos, has been used for examining the tran-

sient behavior of utility power systems [21], [22] and ocean circulation [61]. The theory underlying the PCM, called the full-grid PCM, is the numerical Gauss-quadrature, which is an efficient numerical integration technique [46] for a low-dimensional problem. However, when the dimension of stochastic inputs increases as in the system with many well-correlated inputs and in the large-scale system, the computational cost of the full-grid PCM becomes prohibitive. Therefore, another collocation technique of numerical integration, known as the Smolyak quadrature [63], [45], has been shown to provide a smaller computational cost for similar accuracy. We call this technique the sparse-grid PCM. Major advantages of full- and sparse-grid PCM are that the modal equations of the ODE are decoupled and all statistical solutions, as well as the probability density function, can be directly obtained from the modal solutions. Due to the discrete nature or modal characteristics of the PCM, the accuracy of stochastic solutions deteriorates quickly, when the integration time is prolonged or there exists a discontinuity in statistical solutions. Moreover, sufficient collocation points must be available to fully cover the stochastic characteristics of the system.

The sensitivity analysis is an important tool for identifying how the system responds to the input variation, such that a full understanding of the model development and validation can be achieved and unimportant variables can be eliminated from the parametric space or experimental tests [51], [52]. Since the inputs and model structure are subjected to many uncertainties from sensor measurement, poor understanding of system characteristics, and stochastic disturbance, the sensitivity analysis must provide the model developer the key factors to fully comprehend the system mechanism.

Sensitivity analysis techniques can be classified into two main categories - local, and global methods [51] - according to the range of the parameter variation. The local method [21], [48], [51], based on the computation of the partial derivative of output with respect to input around the nominal operating point, cannot correctly predict the sensitivity of nonlinear systems within the entire range of input uncertainty. In the global approach, a priori knowledge or special structure of the system model are required for each of the following three techniques:

- The regression analysis or correlation measurement combining with the Monte Carlo method [51], [20];
- partitioning uncertainty with Latin Hypercube Sampling [36]; and
- ANOVA-Decomposition [53].

On the contrary, the Morris method [39], which is the most efficient factor screening technique for system with a large number of inputs, qualitatively ranks the importance and interaction of input parameters in systems without any assumption about the system. Nevertheless, the Morris method requires intensive computation to guarantee the convergence of the sensitivity index. The model independence, simplicity of implementation, and accuracy in identifying the important parameters, especially in large-scale systems, are the key factors in developing our sensitivity analysis method.

1.2 Scope and Contributions of the Thesis

Multi-discipline areas - power systems in the AES application, numerical stochastic analysis using both Galerkin and Collocation approaches of the polynomial chaos, and sensitivity analysis - must be combined within this research project. For the preliminary stochastic and sensitivity analyses of large-scale AES systems, parametric and load uncertainties are assumed to be associated only with the uniform distribution because of its symmetrical and bounded range. We summarize the key contributions of this thesis in the following list below.

1) It conducts stochastic analyses of a single electric machine and of large-scale AC power distribution and propulsion systems in a shipboard integrated power system with high-order parametric and load uncertainties to examine the propagation of uncertainties.

2) It develops and implements the hybrid gPC+PCM technique to extend the capability of the gPC to handle nonlinear non-polynomial functions, for example, the ODE with a trigonometric or step discontinuity term.

3) It develops and implements the Multi-Element (ME) technique for both full- and sparse-grid PCM to improve accuracy of stochastic solutions, especially in lengthy integration problems. Generally, the MEPCM yields about an order of magnitude faster computational time than the MEgPC [60] for the same accuracy of stochastic solutions.

4) It examines thoroughly and systematically the convergence characteristics of different numerical stochastic techniques - MC, QMC, gPC, MEgPC, full- and sparse-grid PCM, full- and sparse-grid MEPCM - on various systems with both continuous and discontinuous stochastic solutions. The convergence rate is expressed in terms of their governing variables and the random dimension.

5) It invents four new sensitivity analysis techniques, based on the numerical stochastic techniques, for identifying ranking and interaction of parameters. These four techniques are applicable to static functions. We then compare the sensitivity indices from these four methods with the existing Morris method, which reveals a good agreement in both parameter ranking and interaction. Three of the techniques can be successfully extended to deal with the sensitivity analysis of the ODE. Lastly, the sensitivity analysis of the AC power distribution with open- and close-loop propulsion drive systems, which is one of the important sections in large-scale AES systems, is investigated.

1.3 Organization of the Thesis

This thesis is composed of five chapters and two appendices. The system modeling of individual electric machines and propulsion drive with power converter as well as two different interconnections of subsystems are presented in Chapter 2. All of these component mathematical models are building blocks for the AC power distribution and propulsion systems in the ONR challenge problem [27]. In Chapter 3 we explain the theory of numerical stochastic techniques, based on the Galerkin (gPC) and Collocation (PCM) approaches of the polynomial chaos, the concept of the multi-element technique, which is applicable to both gPC and PCM, and the represen-

tation of stochastic inputs as the Random Variables (RV) or the Random Processes (RP). Chapter 4 thoroughly examines the convergence characteristics of all stochastic analysis techniques for solving the Stochastic Differential Equation (SDE) with both continuous and discontinuous statistical solutions. Moreover, the stochastic analysis of the AC power distribution with the close-loop propulsion drive is examined when all 31 parameters become random variables. Table 1.1 summarizes various numerical stochastic algorithms that apply on different SDEs in Chapter 4. In Table 1.1, FPCM and SPCM stand for full- and sparse-grid PCM. In Chapter 5, new sensitivity analysis techniques - the Sampling, Collocation, Variance, and Inverse Variance methods - are first introduced for ranking inputs in their significant order as well as identifying inputs interaction for various static functions. These results are then confirmed with that from the Morris method. Second, the capability of these sensitivity analysis techniques are extended to handle the ODE system, such as Duffing's oscillator, the single induction machine, and the AC power distribution and propulsion system. Chapter 6 then concludes the thesis and mentions future research directions. Lastly, Appendix A and B summarize the Legendre, Jacobi, and Chebyshev polynomial chaos properties and all machine parameters of all AES systems studied in this thesis, respectively.

Table 1.1: Summary of application using different stochastic algorithms on various nonlinear (NL) SDEs with both Continuous (Cont.) and Discontinuous (Discont.) stochastic solutions in Chapter 4. Note: the gPC is applied only to the linear and quadratic 1st-order SDEs.

System	MC	QMC	ME gPC	Hybrid gPC +PCM	FPCM	ME FPCM	Adap ME FPCM	SPCM	ME SPCM
Linear 1st SDE			x		x	x			
Quadratic NL 1st SDE			x		x	x			
Cubic NL 1st SDE						x			
Quartic NL 1st SDE						x			
Trigonometric NL 1st SDE				x	x	x			
1D RV Cont. KO system	x	x			x	x			
2D RV Cont. KO system	x	x	x		x	x			
3D RV Cont. KO system	x	x			x	x		x	x
Step Discont. 1st SDE				x	x	x			
1D RV Discont. KO sys.	x	x			x	x	x		
2D RV Discont. KO sys.	x	x	x		x	x			
3D RV Discont. KO sys.	x	x			x	x		x	x
1D RV IM with Inf. Bus	x	x	x		x	x	x		
2D RV IM with Inf. Bus	x	x			x	x			
3D RP IM with Inf. Bus	x	x	x		x	x	x		
6D RV AC power sys.		x			x			x	x
31D RV AC power sys.		x						x	

Table 1.2: Summary of various nonlinear (NL) SDEs with both Continuous (Cont.) and Discontinuous (Discont.) stochastic solutions in Chapter 4.

System	Equation Number	Section
Linear 1st SDE	4.3	4.1.1
Quadratic NL 1st SDE	4.6	4.1.2
Cubic NL 1st SDE	4.9	4.1.3
Quartic NL 1st SDE	4.13	4.1.4
Trigonometric NL 1st SDE	4.16	4.1.5
1D RV Cont. KO System	4.17 – 4.19	4.1.6
2D RV Cont. KO System	4.17 – 4.19	4.1.7
3D RV Cont. KO System	4.17 – 4.19	4.1.8
Step Discont 1st SDE	4.20	4.2.1
1D RV Discont. KO System	4.17 – 4.19	4.2.2
2D RV Discont. KO System	4.17 – 4.19	4.2.3
3D RV Discont. KO System	4.17 – 4.19	4.2.4
1D RV IM with Inf. Bus	4.23 – 4.29	4.3.1
2D RV IM with Inf. Bus	4.23 – 4.29	4.3.2
3D RP IM with Inf. Bus	4.23 – 4.29	4.3.3
6D RV AC power sys.	in Ch.2 see Figure 4-96	4.4.1
31D RV AC power sys.	in Ch.2 see Figure 4-97	4.4.2

Chapter 2

System Modeling

Many types of power system modeling have been introduced in the literature [3], [25], [30], [42]. Because of the different time scales associated with each sub-component in each electric machine (electrical and mechanical time constants), we must appropriately select the model according to the study objective to accelerate the simulation process. For example, to reduce a high-harmonic frequency to improve a power-converter's quality and efficiency, all fast transient dynamics of electrical components must be carefully modeled and included in the systems' mathematical model, while only slow dynamics of electric circuits of machines are needed along with the mechanical transients in the stability and load shedding of an inter-area terrestrial power system.

Another important issue is how to connect all these electric machines, generator and motor, together to form a power grid network and loads. In the past, most modeling approaches of simulated power systems formed the Differential-Algebraic Equations (DAEs) after connecting electric machines together [2], [31] and the simulation of these DAEs was time consuming. To avoid solving DAEs, two types of machine connections or three-phase buses, which form the Ordinary Differential Equations (ODEs), are considered in this study. In this chapter, a typical configuration of the AC power distribution and propulsion systems that is one of the subsystems in Figure 1-2 is first introduced and then the mathematical model of each component is presented in more detail.

2.1 Components of Naval Shipboard Power System

A typical arrangement of the AC power distribution and propulsion systems in the shipboard integrated power system [47], [55], shown in Figure 2-1, consists of a power generation unit (prime mover, synchronous generator, and their controller), a AC bus (tie line connecting to power supply), and a propulsion unit (propulsion drive and induction motor). However, an actual configuration of this electrical network must take into account an optimization for power flow and load shedding, a reconfiguration of the DC zonal areas for survivability, and an efficient management of the storage energy. Moreover, all these machines must be optimized for an installation space, a transmission loss, and a signature noise reduction. In the following sections, the mathematical models of each machine and a simplified power converter are introduced along with their interconnection such that the transient dynamics of the AC power distribution and propulsion systems can be further examined from both deterministic and stochastic perspectives.

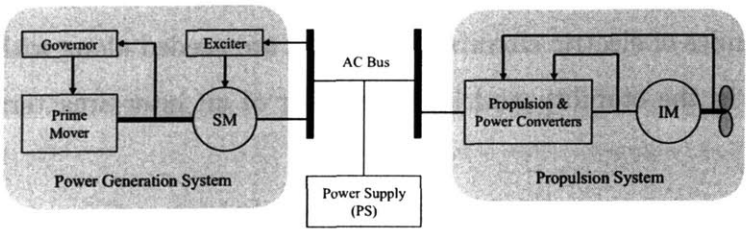

Figure 2-1: An one-line diagram for the typical configuration of the AC power generation and propulsion systems.

We consider three different reference frames: the *abc* reference frame, the *qd*0 rotor reference frame, and the *qd*0 synchronous reference frame, where the q- and d-axes of the *qd*0 reference frame consequently lead and lag the a-axis frame by a constant angle of θ_e. All the transformations between these reference frames will be introduced in later sections. Note, $d\theta_e/dt = \omega_e$. And the synchronous speed, ω_e, is fixed at 60 Hz.

2.1.1 Tie line connection and bus

To connect electric machines together, a three-phase transmission line can be modeled as a symmetrical, three-phase, series RLC circuit. This series RLC circuit includes resistor ($\mathbf{r}_t$), self inductance ($\mathbf{L}_t$) from line leakage and magnetizing inductance, mutual inductance ($\mathbf{M}_t$) from coupling of each line, and capacitance ($\mathbf{C}_t$) for line compensation. Furthermore, the line capacitance also acts as a filter between generator and propulsion drive.

The symmetrical, three-phase resistive element, which represents the transmission loss in the tie line, can be simply expressed in the abc or qd0 synchronous reference frame as the following:

$$\mathbf{v}_{abc} = \mathbf{r}_t \mathbf{i}_{abc} \tag{2.1}$$

or

$$\mathbf{v}^e_{qd0} = \mathbf{r}_t \mathbf{i}^e_{qd0}, \tag{2.2}$$

where $\mathbf{r}_t$ is diag$[r_t\ r_t\ r_t]$.

For a magnetically linear circuit, the symmetrical, three-phase self and mutual inductance can be represented by the following matrix in the abc reference frame:

$$\mathbf{L}_{abct} = \begin{bmatrix} L_t & M_t & M_t \\ M_t & L_t & M_t \\ M_t & M_t & L_t \end{bmatrix} \tag{2.3}$$

or in the qd0 synchronous reference frame

$$\mathbf{L}_{qd0t} = \begin{bmatrix} L_s - M_t & 0 & 0 \\ 0 & L_t - M_t & 0 \\ 0 & 0 & L_t + 2M_t \end{bmatrix}. \tag{2.4}$$

The relation between voltage and current is expressed in the following form:

$$\mathbf{v}_{abc} = \mathbf{L}_{abct} p\, \mathbf{i}_{abc} \tag{2.5}$$

or

$$\mathbf{v}^{e}_{qd0t} = \omega_e \mathbf{T}_1 \mathbf{L}_{qd0t} \mathbf{i}^{e}_{qd0t} + \mathbf{L}_{qd0t} p\, \mathbf{i}^{e}_{qd0t}, \tag{2.6}$$

where the $\mathbf{T}_1$ matrix represents speed-voltage terms, with $\mathbf{T}_1(1,2) = 1$ and $\mathbf{T}_1(2,1) = -1$, and the p symbol denotes the derivative operation.

Similarly, the voltage-current relationship of the symmetrical, three-phase capacitive element can be written in the abc or qd0 synchronous reference frame as the following:

$$\mathbf{i}_{abct} = \mathbf{C}_t p\, \mathbf{v}_{abct} \tag{2.7}$$

or

$$\mathbf{i}^{e}_{qd0t} = \omega_e \mathbf{T}_1 \mathbf{C}_t \mathbf{v}^{e}_{qd0t} + \mathbf{C}_t p\, \mathbf{v}^{e}_{qd0t}, \tag{2.8}$$

where $\mathbf{T}_1$ matrix, which is exactly identical to that in the inductance element, represents speed-current terms.

Two types of the tie line considered later on are series RL and RC circuits. The equation for the three-phase RL tie line is:

$$p\, \mathbf{i}^{e}_{qd0t} = \mathbf{L}^{-1}_{qd0t} \left(\mathbf{v}_{qd0t} - \mathbf{r}_t \mathbf{i}^{e}_{qd0t} - \omega_e \mathbf{L}_{qd0t} \mathbf{T}_1 \mathbf{i}^{e}_{qd0t} \right), \tag{2.9}$$

where $\mathbf{v}_{qd0t}$ represents the voltage difference between two different buses or machines.

The equation for the three-phase RC tie line is:

$$p\, \mathbf{v}^{e}_{qd0t} = \mathbf{C}^{-1}_{t} \left(\mathbf{i}_{qd0t} - \mathbf{r}^{-1}_{t} \mathbf{v}^{e}_{qd0t} - \omega_e \mathbf{C}_t \mathbf{T}_1 \mathbf{v}^{e}_{qd0t} \right) \tag{2.10}$$

where $\mathbf{i}_{qd0l}$ represents the current difference between two different buses or machines. Next, we describe several kinds of electric machines used in the propulsion and power generation units.

2.1.2 Propulsion system

For more than a century, DC motors have been used in propulsion drives due to the simplicity of its precise speed control and low noise generation compared to the direct drive of combustion engines. Due to the high maintenance, low power density of DC machines and fast advancement in power electronic technology, the AC motors, especially the synchronous/induction machines, become a more attractive alternative for the propulsion in electric ships. With a new development of podded propulsion for improving maneuverability of the ship, the induction machine is an appropriate choice because of its high power density and low maintenance. In the rest of this section, the construction and mathematical representation of the induction machine is introduced.

Generally, the induction machine can be considered as a system of coupled electric and magnetic circuits and the mechanical system, the rotor inertia. Its assembly consists of resistances, self inductances, and mutual inductances between stator and rotor windings. The three-phase induction machines are asynchronous-type machines, that operate below and above a synchronous speed in the motoring and generating operations, respectively. They are less expensive compared to the synchronous or DC machines of the equivalent size because of its simple structure. Typically, they are rugged and reliable; thus, they become an important machine in present industry. The main characteristics of this machine are that it requires large starting current and yields poor lagging power factor when a light load is applied. For variable speed drive, they are fed from a power electronic converter at variable voltage amplitudes and frequencies.

We briefly describe the formulation of a general mathematical model for the symmetrical three-phase squirrel-cage induction machines with four poles and three-phase windings in both the stator and rotor connected in a wye configuration. The governing

equations are written in the $qd0$ synchronous reference frame (denoted by superscript e). The voltage equations of the stator and rotor windings can be written as

$$\mathbf{v}^e_{qd0s} = -\mathbf{r}_s\mathbf{i}^e_{qd0s} + \frac{\omega_e}{\omega_b}\mathbf{T}_1\psi^e_{qd0s} + \frac{p}{\omega_b}\psi^e_{qd0s} \tag{2.11}$$

$$\mathbf{v}'^e_{qd0r} = \mathbf{r}'_r\mathbf{i}'^e_{qd0r} + \frac{\omega_e - \omega_r}{\omega_b}\mathbf{T}_1\psi'^e_{qd0r} + \frac{p}{\omega_b}\psi'^e_{qd0r}. \tag{2.12}$$

where $\mathbf{v}^e_{qd0s}$, $\mathbf{i}^e_{qd0s}$, ψ^e_{qd0s} and $\mathbf{v}'^e_{qd0r}$, $\mathbf{i}'^e_{qd0r}$, ψ'^e_{qd0r} are the stator and rotor variables of voltage, current, and flux, expressed in a vector form as $\mathbf{f}^e_{qd0s} = [f^e_{qs}, f^e_{ds}, f^e_{0s}]^T$ and $\mathbf{f}'^e_{qd0r} = [f'^e_{qr}, f'^e_{dr}, f'^e_{0r}]^T$, respectively. The resistance matrices $\mathbf{r}_s$ and $\mathbf{r}'_r$ are diag$[r_s, r_s, r_s]$ and diag$[r'_r, r'_r, r'_r]$. ω_r and ω_b are the rotor angular and base velocities; the synchronous speed ω_e is the same as ω_b in the absence of a controller. The positive direction of stator current is assumed to be outward from the stator winding. The prime symbol denotes that the rotor variables are scaled by a stator to rotor turn ratio.

The equations of flux linkage per second are

$$\psi^e_{qd0s} = -\mathbf{X}_{ls}\mathbf{i}^e_{qd0s} + \psi^e_{mqd} \tag{2.13}$$

$$\psi^e_{qd0r} = \mathbf{X}'_{lr}\mathbf{i}'^e_{qd0r} + \psi^e_{mqd}. \tag{2.14}$$

where the flux leakage matrices $\mathbf{X}_{ls}$ and $\mathbf{X}'_{lr}$ are diag$[x_{ls}, x_{ls}, x_{ls}]$ and diag$[x'_{lr}, x'_{lr}, x'_{lr}]$. We write $\psi^e_{mqd} = -\mathbf{X}_b\mathbf{i}^e_{qd0s} + \mathbf{A}_r\psi^e_{qd0r}$, where $\mathbf{X}_b = \text{diag}[x_b, x_b, 0]$ with $x_b = (x_m x'_{lr})/(x_m + x'_{lr})$, and $\mathbf{A}_r = \text{diag}[x_b/x'_{lr}, x_b/x'_{lr}, 0]$. x_m is the mutual inductance of the stator and rotor.

The dynamics of the mechanical subsystem can be written as

$$p\,\omega_r = \frac{\omega_b}{2H}(T_e - T_L). \tag{2.15}$$

where $T_e = \psi^e_{qs}i^e_{ds} - \psi^e_{ds}i^e_{qs}$ and T_L are the electromagnetic and load torques, respectively. The rotor inertia (in seconds) is H.

Let us consider a 4-pole, 200-hp induction machine connected with an infinite bus or a constant voltage source through an RL tie line. All machine parameters can be found in Appendix B [38]. Although the absence of a controller makes this an idealized case (see Figure 2-2) this system shows the response of a start-up transient, which consists of fast and slow dynamics of electrical and mechanical components, respectively. Then, the machine is subjected to a step change in torque load from 0 to 1 p.u. after 1.5 seconds.

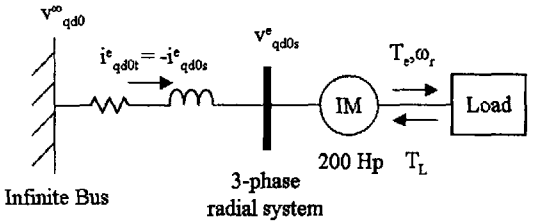

Figure 2-2: A single induction machine connected with an infinite bus.

Assume that all state and output variables are described in the per unit system of the base impedance and in the qd0 synchronous reference frame. The 0-axis variables remain constant at zero due to a balance operation of machine and a perfect cancellation from the reference frame transformation.

From Figure 2-3, we can see a large start-up current in both q- and d-axes during the free acceleration. After the first 0.5 second, the fast transient of the electrical component dies out, only the slow transient of the mechanical component is dominant up to 1 second before reaching the steady state. As the torque load changes from 0 to 1 p.u. at 1.5 seconds, both q- and d-axes tie line currents and the electromagnetic torque increases to handle the increasing torque load, as shown in Figure 2-4.

2.1.3 Power generation system

The synchronous machines are the largest and most common electric machines that convert energy from mechanical to electrical energy. Even though the three-phase synchronous machines are relatively more expensive than the induction machines, the synchronous machines provide higher efficiency at a higher power rating, which

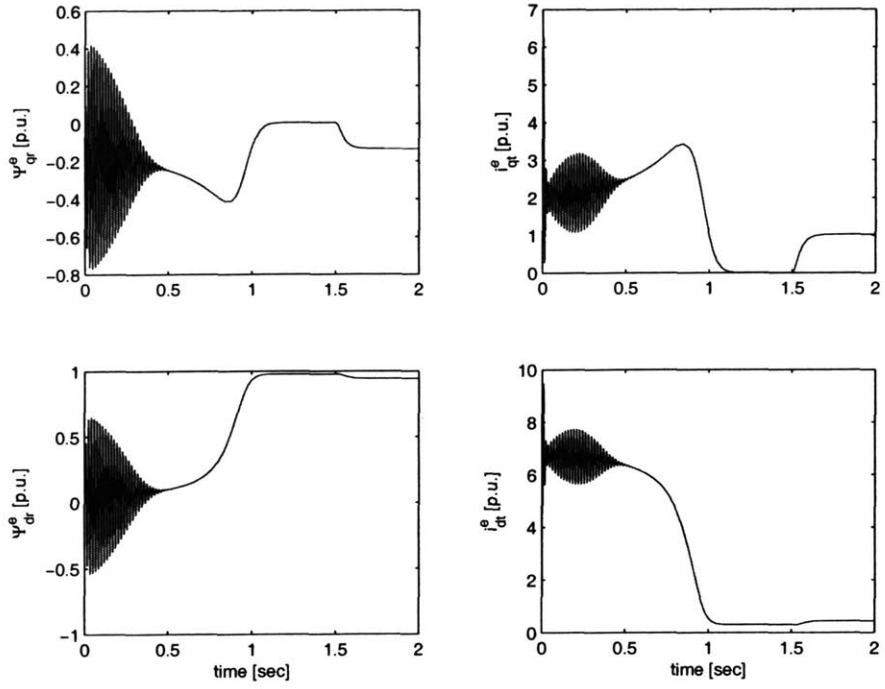

Figure 2-3: The flux linkages per second, ψ^e_{qdr}, of induction machine (right column) and tie line's current, i^e_{qdt}, (left column) during the start-up transient and after a step change in the mechanical torque load at 1.5 seconds.

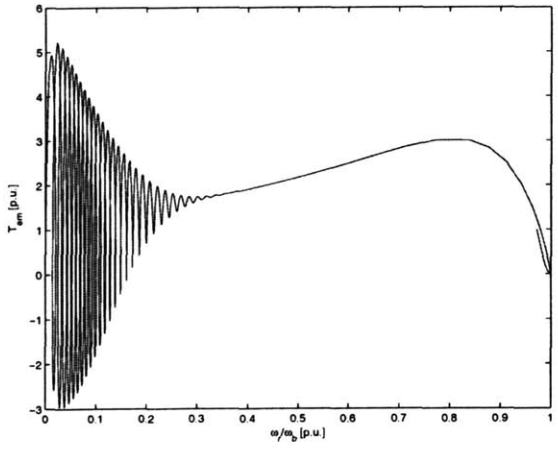

Figure 2-4: The torque-speed curve during the start-up transient and after a step change in the mechanical torque load at 1.5 seconds.

makes this machine suitable for generating electrical power. Generally, the rotor of the synchronous machine is composed of a field and damper windings that have different or unsymmetrical electrical characteristics. Therefore the generated voltage can be compensated by an exciter/voltage regulator, if there is an increasing of the electrical load. Unlike the rotor winding, the stator windings of this machine are mostly identical so that the symmetrical or balance three-phase voltage is produced.

The mathematical model described here is based on the concept of a three-phase salient-pole synchronous machine, consisting of linear magnetic circuits without any saturation. The fields produced by the winding currents are assumed to be sinusoidally distributed around the airgap, which ignores the space harmonics. The rotor windings consist of the field winding (fd) and damper windings (kq and kd), and the stator windings (qs,ds,0s) are symmetrical. The voltage equations of the stator and rotor windings expressed in the rotor reference frame can be written as the following:

$$\mathbf{v}^r_{qd0s} = -\mathbf{r}_s\mathbf{i}^r_{qd0s} + \frac{\omega_r}{\omega_b}\mathbf{T}_1\psi^r_{qd0s} + \frac{p}{\omega_b}\psi^r_{qd0s} \tag{2.16}$$

$$\mathbf{v}'^r_{qdr} = \mathbf{r}'_r\mathbf{i}'^r_{qdr} + \frac{p}{\omega_b}\psi'^r_{qdr}. \tag{2.17}$$

where $(\mathbf{v}^r_{qd0s},\ \mathbf{i}^r_{qd0s},\ \psi^r_{qd0s})$ and $(\mathbf{v}'^r_{qdr},\ \mathbf{i}'^r_{qdr},\ \psi'^r_{qdr})$ are the stator and rotor variables of voltage, current, and flux, expressed in a vector form as $\mathbf{f}^r_{qd0s} = [f^r_{qs}, f^r_{ds}, f^r_{0s}]^T$ and $\mathbf{f}'^r_{qdr} = [f'^r_{kq}, f'^{fd}_{dr}, f'^r_{kd}]^T$, respectively. The resistance matrices $\mathbf{r}_s$ and $\mathbf{r}'_r$ are diag$[r_s, r_s, r_s]$ and diag$[r'_{kq}, r'_{fd}, r'_{kd}]$. Again, the $\mathbf{T}_1$ matrix is used with voltage terms, induced by the speed due to a reference frame transformation. The negative sign in the stator voltage and flux linkage equations represent an assumption that the positive direction of stator current is outward from the stator winding.

The equations of flux linkage per second are given below:

$$\psi^r_{qd0s} = -\mathbf{X}_{ls}\mathbf{i}^r_{qd0s} + \psi^r_{mqd} \tag{2.18}$$

$$\psi^r_{qd0r} = \mathbf{X}'_{lr}\mathbf{i}'^r_{qd0r} + \mathbf{T}_2\psi^r_{mqd}. \tag{2.19}$$

where the flux leakage matrices $\mathbf{X}_{ls}$ and $\mathbf{X}'_{lr}$ consequently are diag$[x_{ls}, x_{ls}, x_{ls}]$ and diag$[x'_{lkq}, x'_{lfd}, x'_{lkd}]$. $\mathbf{T}_2$ is simply the selection matrix:

$$\mathbf{T}_2 = \begin{bmatrix} 1 & 0 & 0 \\ 0 & 1 & 0 \\ 0 & 1 & 0 \end{bmatrix} \tag{2.20}$$

The expression of ψ^r_{mqd} can be written as the following: $\psi^r_{mqd} = -\mathbf{X}_b \mathbf{i}^r_{qd0s} + \mathbf{A}_r \psi^r_{qdr}$, where $\mathbf{X}_b = \text{diag}[x_{bq}, x_{bd}, 0]$ with $X_{bq} = (1/X_{mq} + 1/X'_{lkq})^{-1}$ and $X_{bd} = (1/X_{md} + 1/X'_{lfd} + 1/X'_{lkd})^{-1}$.

$$\mathbf{A}_r = \begin{bmatrix} X_{bq}/X'_{lkq} & 0 & 0 \\ 0 & X_{bd}/X'_{lfd} & X_{bd}/X'_{lkd} \\ 0 & 0 & 0 \end{bmatrix} \tag{2.21}$$

The dynamics of the mechanical subsystem can be written as

$$p\,\omega_r = \frac{\omega_b}{2H}(T_{pm} - T_e). \tag{2.22}$$

$$p\,\delta = \omega_r - \omega_e. \tag{2.23}$$

where $T_e = \psi^r_{ds} i^r_{qs} - \psi^r_{qs} i^r_{ds}$ and T_{pm} are the opposing electromagnetic torque and driven torque from the prime mover, respectively. Again, H denotes the rotor inertia (in seconds). The angle difference between the the synchronous reference frame and the rotor rotating frame is represented by δ. To transform the state variables from the rotor to synchronous reference frame, the transformation matrix ($^r\mathbf{K}^e$) can be applied to $\mathbf{f}^r_{qd0s}$. Due to the Hermitian property of this transformation matrix, the inverse transformation from the synchronous to rotor reference frame is just the transpose of $^r\mathbf{K}^e$.

$$^r\mathbf{K}^e = \begin{bmatrix} cos\delta & sin\delta & 0 \\ -sin\delta & cos\delta & 0 \\ 0 & 0 & 1 \end{bmatrix} \tag{2.24}$$

A combustion engine, either a diesel engine or gas turbine depending on the size of the vessel, supplies the mechanical energy to the generator. The size of this combustion engine in the electric-driven ship is usually smaller than that in the direct mechanic-driven ship. For the purpose of examining the transient stability of the power generation unit in the large-scale vessel, a simplified model of a heavy-duty gas turbine is sufficient for this study. Based on the mathematical model of the single-shaft gas turbine in [49], the more simplified model, found in [38], is mainly composed of the speed governor (SG), valve positioner (VP), fuel system (FS), and turbine (T_{pm}). The state equation can be expressed as the following:

$$p\,SG = \frac{K_c}{T_c}\left(1 - \frac{\omega_r}{\omega_b}\right) - \frac{K_c}{\omega_b} p\,\omega_r \tag{2.25}$$

$$p\,VP = -\frac{1}{T_{FV}} VP + \frac{1}{T_{FV}}\left(SG + W_{F10s}\right) \tag{2.26}$$

$$p\,FS = -\frac{1}{T_{FT}} FS + \frac{1}{T_{FT}} VP \tag{2.27}$$

$$\tag{2.28}$$

where the torque supplied by the turbine shaft is given by the following relation: $T_{pm} = C_{1GT}(FS - C_{2GT}) + C_{GNGT}\left(1 - \frac{\omega_r}{\omega_b}\right)$. All parameters of this model, given in Appendix B, are obtained from [38] to approximate the Allison 501 gas turbine.

Furthermore, the exciter/voltage regulator, controlling the field winding of the synchronous generator, is modeled according to a simplified model of the IEEE type 2 [23] or the IEEE type DC1A representation [24]. This type of exciter is typically accepted in the industry due to the model's simplicity. Three main components of this exciter are an independent power supply, a self-excited shunt field, and a stabilization feedback associated with gains and time constants. However, we neglect the nonlinear saturation in the shunt field. The state equations for this type of exciter

can be described as the following:

$$
\begin{aligned}
p\,V_R &= -\frac{1}{T_A}V_R + \frac{K_A}{T_A}\Big(V_{ref} - V_t - V_{stab}\Big) && (2.29)\\
p\,E_{fd} &= -\frac{K_E}{T_E}E_{fd} + \frac{1}{T_E}V_R && (2.30)\\
p\,V_f &= \frac{K_F}{T_{F1}}V_R - \frac{1}{T_{F1}}V_f && (2.31)\\
p\,V_{stab} &= -\frac{1}{T_{F2}}V_{stab} + \frac{1}{T_{F2}}\Big(\frac{K_F}{T_{F1}}V_R - V_f\Big). && (2.32)\\
& && (2.33)
\end{aligned}
$$

All parameters of this exciter model, called the Type 1 exciter, are given in the per unit system in Appendix B. In this case, V_{ref} is fixed at a constant voltage of 1 p.u. and V_t is a magnitude of the generator's stator voltage. K_i and T_i respectively represent the gain and time constant corresponding to each subcomponent.

To simplify the model of the DC1A exciter even more, we can neglect the voltage stabilizer component such that the exciter model is left with only two states, V_R and E_{fd}, where the state equations of these two variables are given below. We call this exciter model the Type 2 exciter.

$$
\begin{aligned}
p\,V_R &= -\frac{1}{T_A}V_R + \frac{K_A}{T_A}\Big(V_{ref} - V_t\Big) && (2.34)\\
p\,E_{fd} &= -\frac{K_E}{T_E}E_{fd} + \frac{1}{T_E}V_R && (2.35)\\
& && (2.36)
\end{aligned}
$$

In the ideal case, the 3.125 MW synchronous generator, driven by the Allison 501 gas turbine and controlled by the type DC1A exciter, supplies the electric energy to an infinite bus as shown in Figure 2-5. In this example, we assume that the generator initially operates close to its steady-state conditions.

From Figure 2-6 to 2-8, we can see that state variables of the synchronous machine, exciter, and gas turbine are closely coupled and they approach steady-state values within the first 10 seconds. Notice from the responses that the time constant associated with the exciter is the slowest one. In this case, the bus voltage is maintained

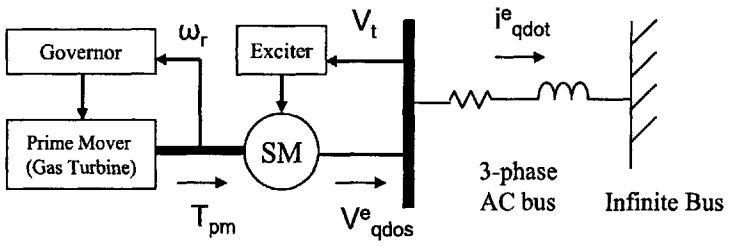

Figure 2-5: A synchronous machine supplies the electrical power to an infinite bus.

close to 1 p.u. with a feedback correction from the exciter. In later sections, this power generation and the propulsion units will be connected together to form the AC power distribution and propulsion systems, which is more realistic than connecting them to the ideal infinite bus.

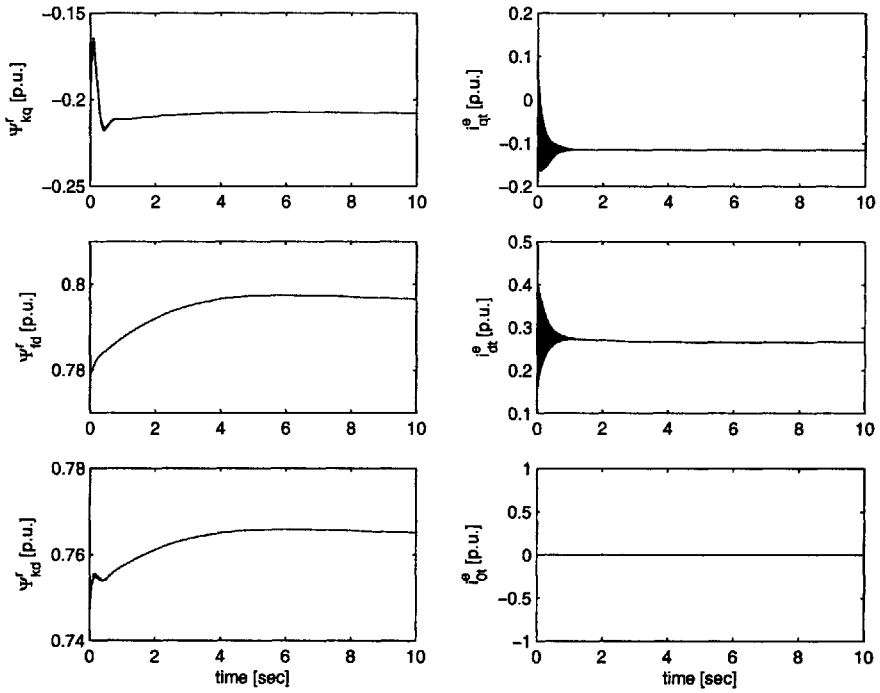

Figure 2-6: The flux linkages per second, ψ^e_{qdr}, of synchronous machine (right column) and tie line's current, i^e_{qd0t}, (left column) when the machine initially operates close to its steady-state conditions.

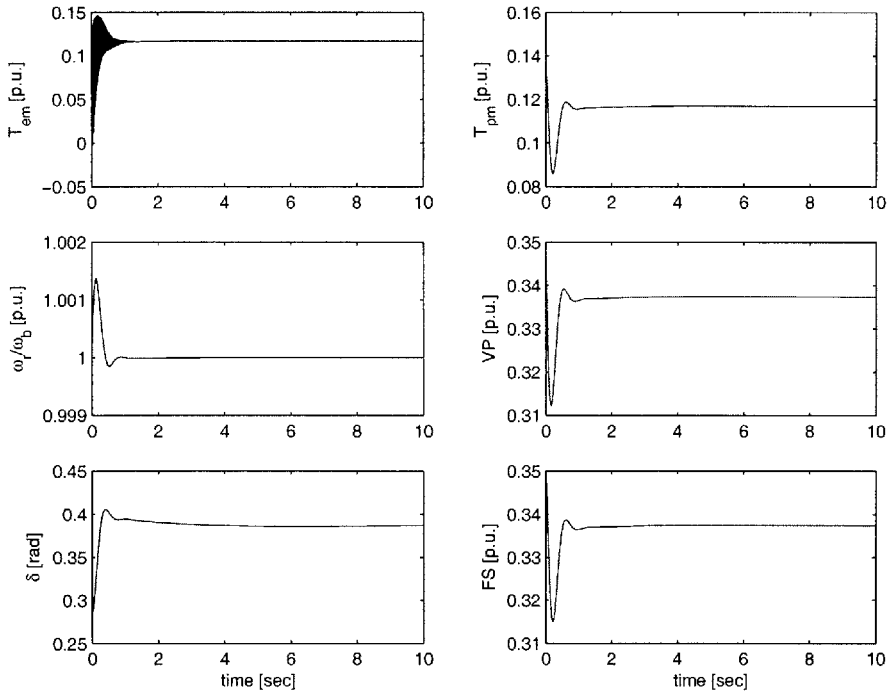

Figure 2-7: The electromagnetic torque (T_{em}), normalized speed (ω_r/ω_b), and power angle (δ) of the synchronous machine (left column) and the generated torque (T_{pm}) and other two variables of the gas turbine (right column).

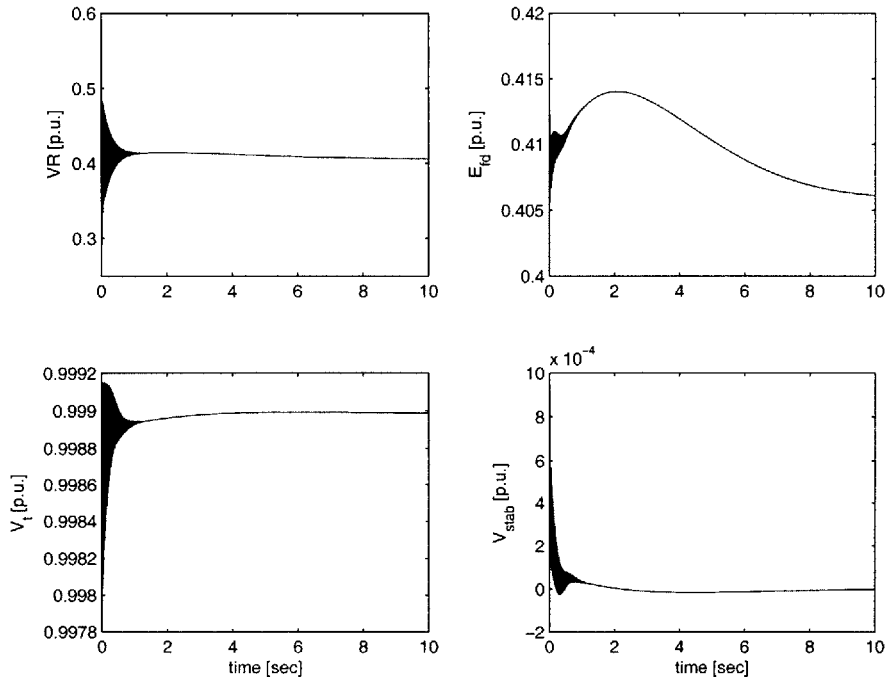

Figure 2-8: All three variables of the exciter and the magnitude of bus voltage (V_t).

2.1.4 Pulsed-power load

Recently, increasing demand on electric power in the Navy electric ships requires a large supply of electricity for the high-power radar and electric weapon systems, for example, the Free Electron Laser and the Electromagnetic Railgun system. Reduction of cost per round, of on-board storage, and of time-to-impact are some major advantages of Railguns. However, the Pulse Forming Network (PFN), which draws a pulsed power load from the ship integrated power distribution, is needed for operating the Railgun system. At the present, two existing pulsed power supplies are the capacitor-base and rotating machine systems [13],[37]. According to [56], the 37 kW propulsion and PFN systems consume around 63% and 22% of the generated power at their peak load from the 59 kW synchronous generator with $V_{base} = 457V$; therefore, power management is required in the actual integrated power system.

The pulsed power load can be modeled as a large pulsed current, supplied from the electrical bus to the capacitor charging circuit [30],[56],[16]. This pulsed current represents a periodically charging and discharging cycle of the capacitor-based PFN. Figure 2-9 [56] shows the first two cycles of charging and discharging current. In the first charging cycle, the PFN must store 200 kJ peak power and each discharging cycle consumes about 128 kJ from the capacitor network. Due to our time constraint, we will investigate a stochastic analysis of the pulsed power load in the AES system in the future.

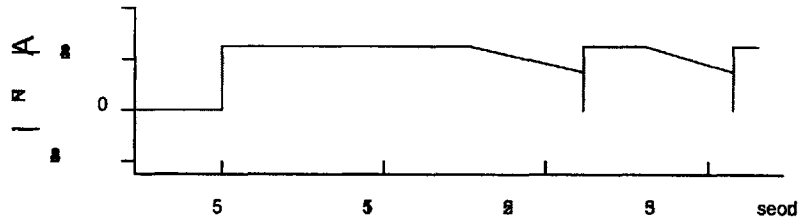

Figure 2-9: A current waveform during the first and second charging and discharging cycle of the Pulse Forming Network, which is drawn from the AC power distribution bus.

2.2 Electric Machine Drive with Power Converter

Many control strategies have been examined and implemented for the electric machine due to the recent advancement of the power electronic technology. Typically, the converter, consisting of a rectifier, inverter, and DC-link filter, converts the control command into voltage supplied to the machine. In this study, a dynamic average-value model of the 6-pulse, full-wave rectifier with the Y-connected voltage source is examined and constructed from the equivalent circuit in Figure 2-10, similar to those found in [29]. This rectifier is directly connected to the DC-link filter, which supplies a DC voltage to the three-phase inverter using the hysteresis modulation technique. To derive the equation for the rectifier average-value model, we need to assume the following - 1) the AC source voltage has a constant rms magnitude, 2) the DC current (I_{dc}) is constant during each commuting cycle, and 3) each leg of the three-phase diode bridge commutes one at a time.

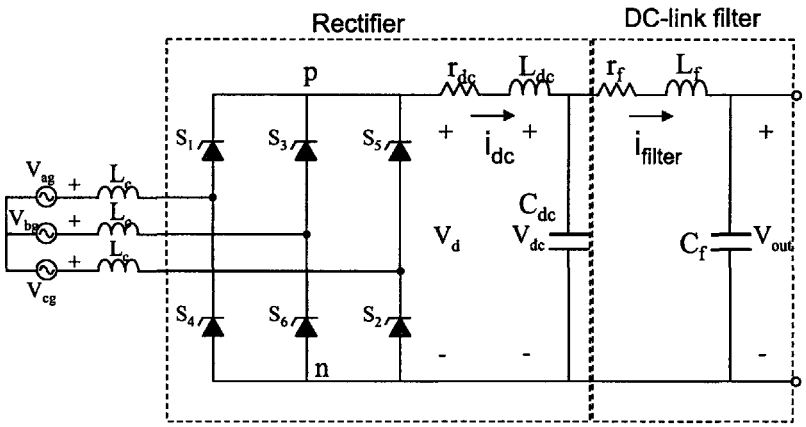

Figure 2-10: An equivalent circuit of the three-phase rectifier.

The $\mathbf{v}_{abcg}$ and L_c denote the Y-connected AC voltage source, operating with the based frequency (ω_b), and the inductance associated with the source. First, we transform the voltage in the *abc* frame to the *qd*0 synchronous reference frame and then to a *qd*0 arbitrary frame, called g frame, where the rms magnitude of d- and 0-axis is

zero using K^e and ${}^eK^g$ transformations respectively.

$$\mathbf{K^e} = \frac{2}{3}\begin{bmatrix} cos\theta_e & cos(\theta_e - \frac{2\pi}{3}) & cos(\theta_e + \frac{2\pi}{3}) \\ sin\theta_e & sin(\theta_e - \frac{2\pi}{3}) & sin(\theta_e + \frac{2\pi}{3}) \\ \frac{1}{2} & \frac{1}{2} & \frac{1}{2} \end{bmatrix}, \tag{2.37}$$

$$^{\mathbf{a}}\mathbf{K^g} = \begin{bmatrix} cos\phi_g & sin\phi_g \\ -sin\phi_g & cos\phi_g \end{bmatrix}, \tag{2.38}$$

where

$$\phi_g = tan^{-1}(v_q^e/v_d^e) \tag{2.39}$$

and $\mathbf{v}_{abcg}$ is transformed to $[v_q^g, 0, 0]$. Furthermore, the average DC current over one switching or $\pi/3$ cycle of ω_b, denoted by $\bar{i}_{dc}$, can be computed from the DC RL circuit equation, given below [29], by assuming that the variation in one switching cycle is small compared to next cycles.

$$p\,\bar{i}_{dc} = \frac{\frac{3\sqrt{3}}{\pi}v_q^g cos\alpha - (r_{dc} + \frac{3}{\pi}L_c\omega_b)\bar{i}_{dc} - v_{dc}}{L_{dc} + 2L_c} \tag{2.40}$$

where v_{dc} is the voltage across the C_{dc} capacitor and α is the firing angle of each diode. We assign $\alpha = 0$ such that this full-wave rectifier is ideally operated in an uncontrolled mode. The commutation angle (u), given in the equation below [29], represents an angle between the turn-off and turn-on times of [S_1,S_3] or [S_3,S_5] diodes.

$$u = -\alpha + \arccos\left[cos\alpha - \frac{L_c\omega_b\bar{i}_{dc}}{v_q^g/\sqrt{2}}\right] \tag{2.41}$$

Next, the average qd0 current in each leg of the full-bridge rectifier can be calculated by integrating over $[\alpha,\frac{\pi}{3}+\alpha]$, $[\frac{\pi}{3}+\alpha,\frac{2\pi}{3}+\alpha]$, or $[\frac{2\pi}{3}+\alpha,\pi+\alpha]$ interval of ω_b. The average current during the conducting interval is composed of the source current and the average DC current. During the short commutating interval, the average current

in each rectifier phase leg only equals the average DC current, $\bar{i}_{dc}$. Thus, in each interval, $\mathbf{i}^g_{qd}$ is a sum of the conducting current ($\bar{\mathbf{i}}^g_{q,cond}$) and commutating current ($\bar{\mathbf{i}}^g_{q,com}$) [29], expressed below:

$$\bar{i}^g_q = \bar{i}^g_{q,cond} + \bar{i}^g_{q,com} \tag{2.42}$$

$$\bar{i}^g_d = \bar{i}^g_{d,cond} + \bar{i}^g_{d,com} \tag{2.43}$$

where

$$\bar{i}^g_{q,cond} = \frac{2\sqrt{3}}{\pi}\bar{i}_{dc}\Big[sin\Big(\alpha+\frac{7\pi}{6}\Big) - sin\Big(\alpha+u+\frac{5\pi}{6}\Big)\Big] \tag{2.44}$$

$$\bar{i}^g_{d,cond} = \frac{2\sqrt{3}}{\pi}\bar{i}_{dc}\Big[-cos\Big(\alpha+\frac{7\pi}{6}\Big) + cos\Big(\alpha+u+\frac{5\pi}{6}\Big)\Big] \tag{2.45}$$

$$\begin{aligned}\bar{i}^g_{q,com} = {} & \frac{6\sqrt{3}\bar{i}_{dc}v^g_q}{\pi^2 L_c\omega_b}\Big[sin\Big(u+\alpha-\frac{5\pi}{6}\Big) - sin\Big(\alpha-\frac{5\pi}{6}\Big)\Big] \\ & \times cos\alpha[cos(u+\alpha) - cos\alpha] + \frac{3v^g_q}{4\pi L_c\omega_b}[cos(2u) - cos(2\alpha+2u)]\end{aligned} \tag{2.46}$$

$$\begin{aligned}\bar{i}^g_{d,com} = {} & \frac{6\sqrt{3}\bar{i}_{dc}v^g_q}{\pi^2 L_c\omega_b}\Big[-cos\Big(u+\alpha-\frac{5\pi}{6}\Big) + cos\Big(\alpha-\frac{5\pi}{6}\Big)\Big] \\ & \times cos\alpha[sin(u+\alpha) - sin\alpha] + \frac{3v^g_q}{4\pi L_c\omega_b}[sin(2u) - sin(2\alpha+2u)] - \frac{3v^g_q u}{2\pi L_c\omega_b}\end{aligned} \tag{2.47}$$

Lastly, v_{dc} and i_{LC} can be found from the state equations of the C_{dc} capacitor and the DC-link filter, given below.

$$p\,v_{dc} = \frac{1}{C_{dc}}(i_{dc} - i_{LC}) \tag{2.48}$$

$$p\,i_{LC} = \frac{1}{L_f}(v_{dc} - v_{out} - r_f L_f i_{LC}) \tag{2.49}$$

where v_{out} is the voltage supplied to the inverter.

To summarize the derivation of the rectifier average model, the block diagram in Figure 2-11 represents the interconnection of Equation 2.37 until 2.49. The input and output of this block diagram are consequently $(\mathbf{v}_{abcg}, \alpha, i_{LC})$ and $(\mathbf{i}_{abcg}, v_{dc})$.

To adjust the voltage magnitude and frequency to control the induction machine,

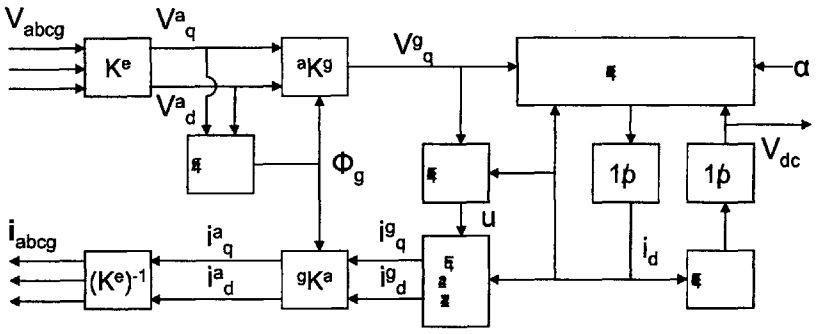

Figure 2-11: An block diagram of the three-phase, full-wave rectifier.

the hysteresis modulation type of the three-phase inverter provides a current regulator when it is combined with a motor-control technique. This modulation approach is effective in regulating the current within the hysteresis band (h) according to the difference between the machine current and current command from the motor controller. The hysteresis function, shown in Figure 2-12, in each phase can be approximated by the following equation [27]:

$$S_a = \frac{1}{2.0078}\arctan\left[\arctan\left[2.1003\left(\frac{I_a^* - I_a}{h}\right)^5 + 1.16\left(\frac{I_a^* - I_a}{h}\right)\right]\right] + \frac{1}{2} \qquad (2.50)$$

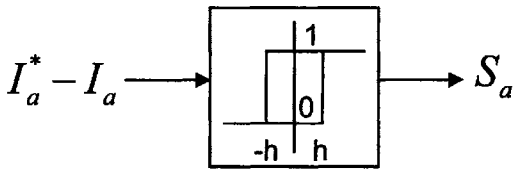

Figure 2-12: An hysteresis function for the a-phase hysteresis current-regulation technique.

where S_a is the switching command for the a-phase leg of the inverter, I_a^* and I_a are the a-phase current command from the controller and the a-phase stator current of the induction machine, respectively. Using the ideal three-phase, full-bridge inverter,

the supplied voltage to the induction machine can be obtained as the following:

$$[v_a, v_b, v_c] = [S_a, S_b, S_c]v_{dc} \tag{2.51}$$

2.2.1 Control of induction machine

Many control strategies for the induction machine have been introduced in the literature, but only four techniques are briefly mentioned here. The volts-per-hertz [29],[6], constant-slip current [29], field-oriented [29], and passive-based [32],[43] control of the induction machine have been extensively studied and implemented. The volts-per-hertz control algorithm adjusts the magnitude and frequency of the applied voltage such that the speed of the induction machine can be controlled according to the machine torque-speed curve without any speed feedback. The constant-slip current control, which is our main focus, can directly control the machine torque and it is robust against the parameter variation; nevertheless, an additional feedback loop is required for a variable speed control. Similarly, the field-oriented control directly manipulates the machine torque, but it is sensitive to the parameter fluctuation. For the passivity-based control of the induction machine, an accurate machine model as well as parameters are required to rewrite the system equations into the electrical and mechanical components; thus, this control strategy is not robust against the variation in load or parameters.

Combined with the hysteresis modulation, the constant-slip current control method can maximize the machine torque for a given input current by exploiting the steady-state electromagnetic torque relation [29] as a function of the slip frequency (ω_s), expressed below:

$$T_e = \frac{2(\frac{P}{2})\omega_s L_M^2 I_s^2 r_r'}{(r_r')^2 + (\omega_s L_{rr}')^2} \tag{2.52}$$

where ω_s denotes a fixed slip frequency ($\omega_s = \omega_e - \omega_r$). I_s and (r_r', L_{rr}', and L_M) are the magnitude of the stator current and parameters of the induction machine, respectively. To solve for the stator-current magnitude for a given torque command,

the following relation in Equation 2.53, expressed in terms of the estimated machine parameters ($r'_{r,est}$ and $L'_{r,est}$), is used.

$$I_s = \sqrt{\frac{2|T_e^*|(r'_{r,est})^2 + (\omega_s L'_{rr,est})^2}{3P|\omega_s|L^2_{M,est}r'_{r,est}}} \tag{2.53}$$

To maximize the torque per stator current, ω_s can be calculated by taking the derivative of $\frac{T_e}{I_s^2}$ in Equation 2.52 with respect to ω_s and setting it equal to zero. Thus, we obtain ω_s^*, given below, resulting in the maximum torque per stator current.

$$\omega_s^* = \frac{r'_{r,est}}{L'_{rr,est}} \tag{2.54}$$

To avoid operating in a machine saturated regime, the torque command must be limited within a certain threshold that can be found in [29] for more detailed calculation of $T_{e,threshold}$. Therefore, we can summarize this control strategy in the block diagram form, shown in Figure 2-13. The magnitude of the stator current (I_s) is arbitrarily assigned to the q-axis current (i_{qs}^{*e}), while i_{ds}^{*e} and i_{0s}^{*e} are set to zero to simplify the calculation. The $\sqrt{2}$ takes into account converting the magnitude of I_s into the *rms* value.

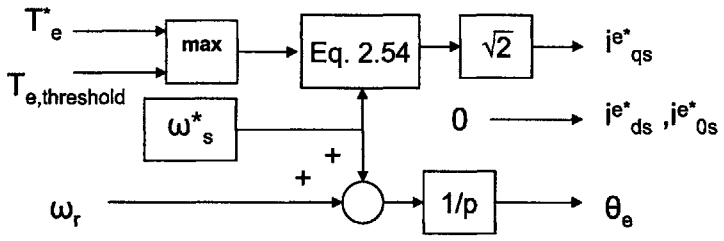

Figure 2-13: A block diagram of the constant-slip current control of the induction machine.

2.3 Difference in Interconnection of Subsystems

Two types of interconnections that can connect electric machines together without forming the differential-algebraic equations are 1) static electrical bus [38], and 2) dynamic electrical bus [27]. Each approach is associated with benefits and limitations. To couple electric machines on the same electrical bus in the first approach, the causality of the voltage equations must be resolved into the root and non-root machine models. The root machine imposes the voltage on the static bus, while the non-root machine provides the current to the bus, which is the same as those equations described in Section 2.1.2 and 2.1.3. Using the static bus, some of the root machine's state equations are combined with that of the tie line; as a result, the total numbers of state equations are reduced. However, the machine drive technique can be applied only to the non-root machine. In the second approach, the dynamic equations of the three-phase RC circuit must be included along with the machine equations; however, no transformation of the machine equations is required and the controller can be directly coupled with the machine model.

Let us consider the first method using the static bus. The derivation of both root and non-root models of synchronous and induction machines is given in the following section. The state and output equations of the root induction machine are:

$$p\,\psi^e_{qd0r} = \omega_b \mathbf{r}'_r(\mathbf{X}'_{lr})^{-1}(\psi^e_{mqd} - \psi^e_{qd0r}) + (\omega_r - \omega_e)\mathbf{T}_1\psi'^e_{qd0r} \tag{2.55}$$

$$\mathbf{v}^e_{qd0s} = -\mathbf{r}_s\mathbf{i}^e_{qd0s} + \frac{\omega_e}{\omega_b}\mathbf{T}_1\psi^e_{qd0s} - \frac{1}{\omega_b}\mathbf{X}_s p\,\mathbf{i}^e_{qd0s} + \frac{1}{\omega_b}\mathbf{A}_r p\,\psi'^e_{qd0r} \tag{2.56}$$

The equations for the non-root induction machine are:

$$p\,\psi^e_{qd0r} = \omega_b \mathbf{r}'_r(\mathbf{X}'_{lr})^{-1}(\psi^e_{mqd} - \psi^e_{qd0r}) + (\omega_r - \omega_e)\mathbf{T}_1\psi'^e_{qd0r} \tag{2.57}$$

$$p\,\mathbf{i}^e_{qd0s} = \omega_b\mathbf{B}_s\mathbf{v}^e_{qd0s} - \omega_b\Big[\mathbf{B}_s(\mathbf{r}_s\mathbf{i}^e_{qd0s} + \frac{\omega_e}{\omega_b}\mathbf{T}_1\psi^e_{qd0s}) + \frac{1}{\omega_b}\mathbf{B}_r p\,\psi'^e_{qd0r}\Big] \tag{2.58}$$

where $\psi^e_{qd0s} = -\mathbf{X}_{ls}\mathbf{i}^e_{qd0s} + \psi^e_{mqd}$ and $\mathbf{B}_s = (\mathbf{X}_{ls} + \mathbf{X}_b)^{-1}$ and $\mathbf{B}_r = (\mathbf{X}_{ls})^{-1}\mathbf{A}_r$, using our previous definitions in Section 2.1.2.

Similarly, the synchronous machine can be modified to be either root or non-

root machines such that they can be coupled together using the static bus. The mathematical model of the root machine, which controls the voltage the machine supplies to the bus, can be expressed in the following form:

$$p\,\psi'^{r}_{qdr} = \omega_b \mathbf{r}'_r (\mathbf{X}'_{lr})^{-1}(\mathbf{T}_2\psi^r_{mqd} - \psi'^{r}_{qdr}) + \omega_b \mathbf{v}^r_{qdr} \tag{2.59}$$

$$\mathbf{v}^e_{qd0s} = -\mathbf{r}_s \mathbf{i}^e_{qd0s} + ({}^r\mathbf{K}^e)\Big[\frac{\omega_r}{\omega_b}\mathbf{T}_1\psi^r_{qd0s} + \frac{\omega_r - \omega_e}{\omega_b}\mathbf{X}_s\mathbf{T}_1\mathbf{i}^r_{qd0s} - \frac{1}{\omega_b}\mathbf{A}_r p\,\psi^r_{qdr}\Big] \tag{2.60}$$
$$-\frac{1}{\omega_b}({}^r\mathbf{K}^e)\mathbf{X}_s({}^e\mathbf{K}^r)p\,\mathbf{i}^e_{qd0s}.$$

where $\mathbf{X}_s = \mathbf{X}_{ls} + \mathbf{X}_b$.

The equations for the non-root synchronous machine can be written as follows:

$$p\,\psi'^{r}_{qdr} = \omega_b \mathbf{r}'_r (\mathbf{X}'_{lr})^{-1}(\mathbf{T}_2\psi^r_{mqd} - \psi'^{r}_{qdr}) + \omega_b \mathbf{v}^r_{qdr} \tag{2.61}$$

$$p\,\mathbf{i}^e_{qd0s} = ({}^r\mathbf{K}^e)\Big[-\omega_b\mathbf{B}_s(\mathbf{v}^r_{qd0s} + \mathbf{r}_s\mathbf{i}^r_{qd0s} - \frac{\omega_r}{\omega_b}\mathbf{T}_1\psi^r_{qd0s}) \tag{2.62}$$
$$+\mathbf{B}_r p\,\psi'^{r}_{qdr} + (\omega_r - \omega_e)\mathbf{i}^r_{qd0s}\Big]$$

When M+1 machines and N loads connect together to the same static bus, Kirchoff's current law can be expressed to sum all currents from the root machine, the M non-root machines, and the N RL tie lines, written below.

$$^{root}\mathbf{i}^e_{qd0s} = -\Sigma_{i=1}^{M}\,{}^{nonroot}\mathbf{i}^e_{qd0s,i} - \Sigma_{j=1}^{N}\mathbf{i}^e_{qd0t,j} \tag{2.63}$$

Next, we differentiate both sides of the above equation. Then, we substitute the derivative currents of the non-root machines and RL tie lines from their state equations such that the derivative current of the root machine can be found and substituted into its state equations. As a result, the voltage or output equations of the root machine are combined with the current summation of the static bus. Therefore, all casualities of all machines and tie lines are resolved.

In the second type of system interconnection, when M machines and N loads connect on the same dynamic bus, again all currents supplied to or drawn from the AC bus must be summed using Kirchoff's current law to obtain the bus current (i_t).

Then, $\mathbf{i}_{qd0t}$ can be directly substituted in the RC tie line equation, Equation 2.10, and we integrate the RC line voltage equation such that the bus voltage can be found and substituted back into the machine and load equations. However, when the propulsion drive is connected onto the AC bus, the fast dynamics from the high-harmonic current can reflect back onto the AC bus, which leads to instability of the entire interconnected system. Therefore, the harmonic filter, represented by the low-pass filter RLC circuit, is required to reduce the high-harmonic waveform. A simplified one-line diagram of this three-phase AC bus connecting with 2 machines - synchronous generator and induction motor -, harmonic filter, and power supply is illustrated in Figure 2-14.

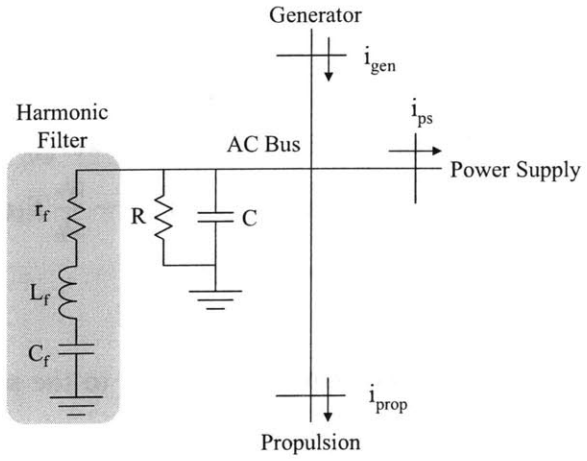

Figure 2-14: A one-line diagram of the three-phase AC Bus [27] in the second type of system interconnection.

2.4 Source of Uncertainties

Due to the complexity of the AES, several components and loads can contribute to the uncertainties in the entire system. The list below includes some major sources of uncertainties in the AES integrated power system.

1) Time-varying parameters of the electric machines [43], [6], [29] - 1.1) temperature dependent resistances and capacitances, 1.2) bearing friction, 1.3) nonlinearities and saturations of magnetic material, inducing heat from the hysteresis loss and skin effect.

2) Fault or failure of components in electric machines and thermal management systems [34] (e.g., machine's bearing, stator, rotor, and insulation failure or piping damage).

3) Unknown load disturbances - 3.1) fluctuation of the propeller loads due to the unpredictable sea state, caused by wind and underwater current, 3.2) magnitude and frequency of charging and discharging cycles of the PFN [13], [16], consisting of many energy-storage capacitors.

4) Unreliable sensor measurement (e.g., bias or drift) or even a sensor failure [34], which triggers an unnecessary maintenance or action of the intelligent control.

Chapter 3

Numerical Stochastic Techniques

As mentioned previously, the stochastic analysis of nonlinear systems, particularly a network of electric machines, is too complicated to perform analytically. In the previous chapter, we have derived the deterministic model for a shipboard power system, which consists of tens states. To predict a probabilistic outcome of system response subject to random excitation, numerical stochastic algorithms are needed. In this chapter, five different stochastic techniques - 1) Monte Carlo (MC), 2) generalized Polynomial Chaos (gPC) or Galerkin approach, 3) Probabilistic Collocation Method (PCM), 4) hybrid gPC with PCM, and 5) Multi-Element (ME) technique of the gPC, PCM and hybrid are described from both theoretical and implementation points of view. Even though all of these algorithms can provide the statistical moments as well as the probability density function, the complexity of calculating statistics is different among these methods. Note that the first and second moments are mean and variance, respectively. In a realistic situation, uncertainty of system parameters and load tends to vary within a specified range, and therefore the uniform and exponential distributions are more suitable to represent these uncertainties than the Gaussian distribution. Only the uniform distribution, where the sample space (Ω) is within [-1,1], will be the main focus in this study, because both parametric and external disturbances are often described within a known bound, which can be scaled accordingly using the uniform distribution.

In this chapter, we describe an underlying theorem of these stochastic algorithms.

Then, we briefly discuss the implementation techniques, which provide an insight on algorithms' structure, as well as their advantages and disadvantages for a practical purpose.

3.1 Representing Stochastic Input

In an uncertainty analysis, the first step is to realize what type of probability distribution best describes the uncertainty, associated with the random input. In this work, the stochastic response of nonlinear systems subjected to both stationary and non-stationary stochastic inputs, which exist in external input or system parameters, will be studied. Moreover, an uncertainty in initial condition or boundary condition is also considered as a random parameter in the system. When the stochastic input is fully correlated in time, known as a random variable case, this type of random input is fixed with time or has an infinite correlation length. The magnitude of random input is unknown and prescribed within a specified bound. On the other hand, when the stochastic input becomes a time-dependent variable, the random input becomes a partially correlated random process. We describe both of these random inputs mathematically as well as their numerical implementation.

3.1.1 Random Variable

A characteristic of most parametric and load excitations of any system is often unknown precisely. Therefore, a preliminary study of stochastic analysis can be modeled by a stationary random variable. A random variable is a linear mapping function from a random number (ξ), associated with a specific probability distribution, to outcome ($x(\xi)$), which lies within the range space of a random experiment. The random variable can be expressed in terms of mean (x_0) and standard deviation (σ_x) from a nominal value, as shown below.

$$\mathbf{x}(\zeta) = \mathbf{x}_0 + \sigma_{\mathbf{x}}\zeta \tag{3.1}$$

where $\mathbf{x}(\xi)$ represents a vector of all possible random variables in the system. Note that in this chapter, the random input (ξ) denotes a random number with zero mean and variance of one. Only a continuous random variable [33] will be considered in this study. For example, the range of uniform random variables is specified between a and b, so a corresponding probability density function is given by $1/(b-a)$.

3.1.2 Random Process with Karhunen-Loeve Expansion

For a non-stationary random process, random input is fluctuating with time and can be either partially correlated or uncorrelated in time, which is represented by a slow-varying variable or random white noise, respectively. The Karhunen-Loeve (K-L) Expansion is one of the approaches to model the random process with a spectral expansion of a specified covariance function. The K-L expansion decomposes the random processes ($X(t)$) into a time-dependent orthogonal basis function ($\phi_k(t)$) with orthogonal random variable ($X_k(\omega)$) as coefficients. Similar to the Fourier Series, the K-L expansion can provide various good properties, especially for a random input that is non-periodic. For example, if $X(t)$ is the Gaussian process, the coefficients, ξ_k are independent Gaussian random variables with magnitude corresponding to the eigenvalue, λ_k. The K-L expansion can be expressed as the following:

$$\mathbf{x}(t,\omega) = \bar{\mathbf{x}}(t) + \sigma_{\mathbf{x}} \sum_{k=1}^{\infty} \sqrt{\lambda_k}\phi_k(t)\xi_k(\omega), \tag{3.2}$$

where $\bar{\mathbf{x}}(t)$ and $\sigma_{\mathbf{x}}$ consequently stand for mean and standard deviation of the random process. And λ_k and $\phi_k(t)$ are the real-value eigenvalues and complex-value eigenfunctions of the covariance function, $R_{xx}(\mathbf{t_1}, \mathbf{t_2})$. The $\xi_k(\omega)$ are orthogonal independent random variables. As shown later on, this modal representation of the K-L expansion, with $\xi_k(\omega)$, is very well suited for stochastic input of the Galerkin approach. Both eigenvalues and eigenfunctions are the solution of the following integral equation:

$$\int R_{xx}(\mathbf{t_1}, \mathbf{t_2})\phi_k(\mathbf{t_2})d\mathbf{t_2} = \lambda_k\phi_k(\mathbf{t_1}) \tag{3.3}$$

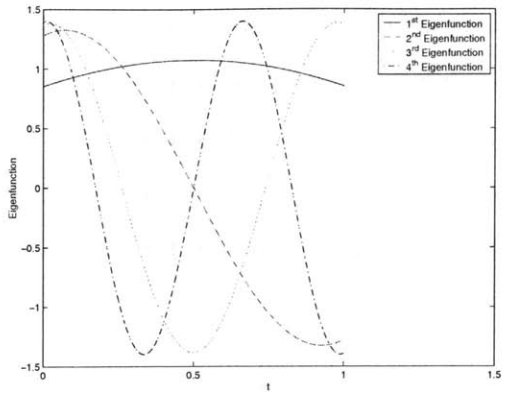

Figure 3-1: Eigenfunctions $f_n(t)$ with $0 \leq t \leq 1$ and $n = 1, 2, 3, 4$ and $cl = 1$ from the Exponential Covariance kernel.

Again an assumption on the covariance structure of random input must be specified in advance. In this work, a time-dependent exponential function will be used as the covariance function over a time interval $[0, T]$, expressed in the following form:

$$R_{xx}(\mathbf{t_1}, \mathbf{t_2}) = \sigma_{\mathbf{x}}^2 e^{-|t_2 - t_1|/cl} \tag{3.4}$$

where cl denotes a correlation length between t_1 and t_2. From a numerical implementation aspect, the summation in equation 3.1.2 must be truncated up to an N term such that the accuracy of the covariance characteristic is maintained. We will show that it is possible to reconstruct this covariance kernel with this N-term decomposition and estimate an associated error. The mean-square error of the process, obtaining from the K-L expansion, is minimal with a finite-term expansion. We will show how well the reconstruction of the approximated covariance kernel with N-terms truncation becomes, as we increase the number of N. Figure 3-1 shows the first four eigenfunctions, obtained from the exponential covariance function with $cl = 1$. Figures 3-2 to 3-6 consequently show the exact exponential covariance kernel, the approximated kernel with $N = 4$ and $N = 10$, and their corresponding associated errors. Furthermore, the convergence of eigenvalue can indicate how many term are needed in the expansion to closely approximate the exact covariance kernel, as shown in Figure 3-7

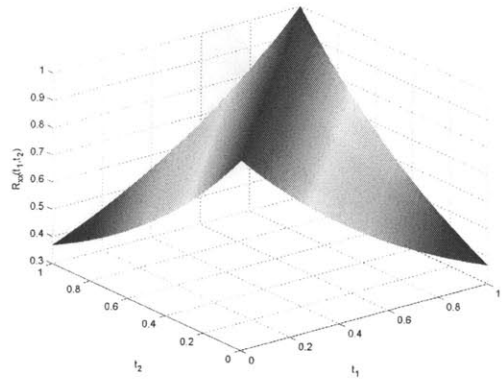

Figure 3-2: Exact Covariance Surface versus t_1 and t_2 with $cl = 1$.

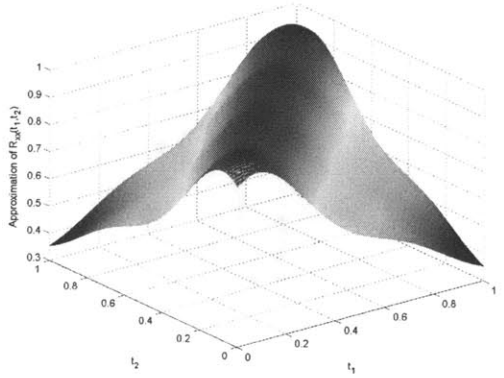

Figure 3-3: 4-term approximation of Covariance Surface versus t_1 and t_2 with $cl = 1$.

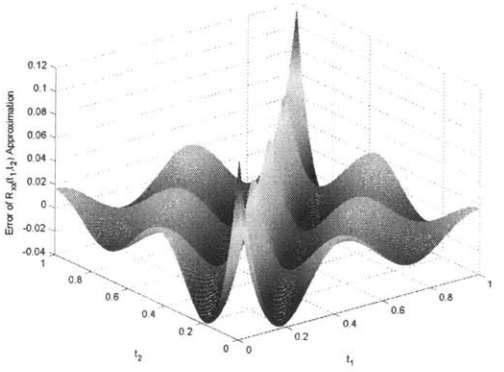

Figure 3-4: 4-term relative error surface of Covariance Approximation versus t_1 and t_2 with $cl = 1(MaxError = 0.1126)$.

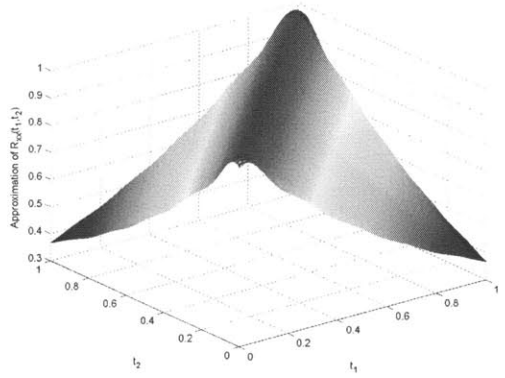

Figure 3-5: 10-term approximation of Covariance Surface versus t_1 and t_2 with $cl = 1$.

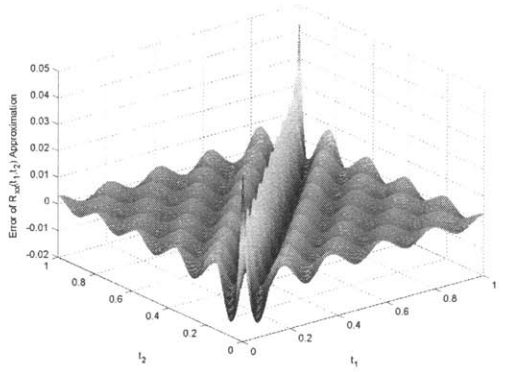

Figure 3-6: 10-term relative error surface of Covariance Approximation versus t_1 and t_2 with $cl = 1(MaxError = 0.0425)$.

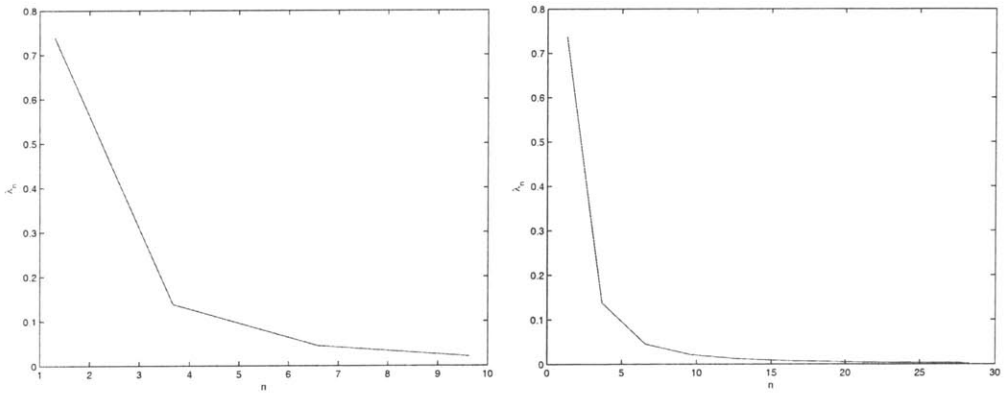

Figure 3-7: For cl=1, the eigenvalue of the exponential covariance kernel as a function of the approximation terms (4-term : left) and (10-term : right) indicates how many terms are required in the approximation to obtain a convergence.

3.2 Monte Carlo method

3.2.1 Algorithmic Framework

According to the probability theory, an event is related to a set of outcomes in the sample space and a probability of the event is associated with a ratio of a subspace or volume and the entire sample space in d dimension (Ω^d). Instead of calculating the event probability as in the probability theory, the Monte Carlo (MC) method uses a concept of sampling randomly and independently from a specific volume to obtain the probability of the outcome. Let us consider X_i to be the independent random variable of i event in the sampling of ω^d and let S denote a set of the outcomes from NN events or realizations, $S_{NN} = X_1, X_2, \cdots, X_{NN}$. Thus, an estimated mean value ($\hat{\mu}$) can be computed as the following: $\mu = \sum(X_1 + X_2 + \cdots + X_{NN})$. The strong law of large numbers guarantees that the estimated mean, $\hat{\mu}$, converges to an exact mean, μ, with the probability of 1 as NN approaches infinity. To calculate the variation of $\hat{\mu}$ from μ or to estimate the error associated with each specific outcome, a variance can be computed according to the central limit theorem. Several approaches have been proposed to reduce the variation in estimating statistics, which include the stratified sampling, the important sampling, and the latin hypercube sampling.

For the continuous random variable, the expectation, μ, and variance, σ_f^2, of system output can be computed from a volume integral as the following.

$$\mu = \int_{\Omega} f(x)\, dx, \tag{3.5}$$

$$\sigma_f^2 = \int_{\Omega} (f(x) - \mu)^2\, dx. \tag{3.6}$$

The sample space Ω of the uniform distribution is in [-1,1]. While, in the Monte Carlo method, the discrete random variable is employed in the uniform sampling, so the estimated expectation, $\hat{\mu}$ and variance, $\hat{\sigma_f^2}$ can be computed from an averaging

summation as the following.

$$\hat{\mu} = \frac{1}{NN}\sum_{i=1}^{NN} f(x_i), \tag{3.7}$$

$$\hat{\sigma_f^2} = (\frac{1}{NN}\sum_{i=1}^{NN}(f(x_i) - \hat{\mu})^2). \tag{3.8}$$

Note that the above volume integral and averaging summation can be extended to the sample space in higher dimension, Ω^d.

How accurate the statistical results are depends on several factors, i.e., the number of samplings or realizations and a randomization of a random generator. When the pseudo-random number generator [46] is employed in the MC to generate the uniformly independent identical random number, the accuracy of statistics improves proportional to $1/\sqrt{NN}$. Thus, a large number of realizations is required in the MC to yield the accurate statistics as well as to capture the probability density function accurately. To overcome this limitation, the quasi-Monte Carlo (QMC) [46] can further enhance the statistical accuracy such that its accuracy increases proportional to $1/NN$. The QMC method requires the quasi-random number generator, which samples the sample space more evenly than those of the pseudo-random number generator. We show the characteristic of both pseudo-random and quasi-random numbers for a two random dimensions in Figure 3-8. The major advantage of both MC and QMC is their insensitivity of the statistical accuracy to the random dimension.

3.3 Galerkin Approach of Polynomial Chaos

According to the Cameron-Martin theorem [10], the so-called Wiener-Askey polynomial chaos expansion can approximate and describe all stochastic processes with finite second-order moment; this is satisfied for most physical systems. The Askey scheme of polynomials contains various classes of orthogonal polynomials and their associated weighting functions are identical to the probability density function of different distributions. As shown by [62], these orthogonal polynomials yield an optimal

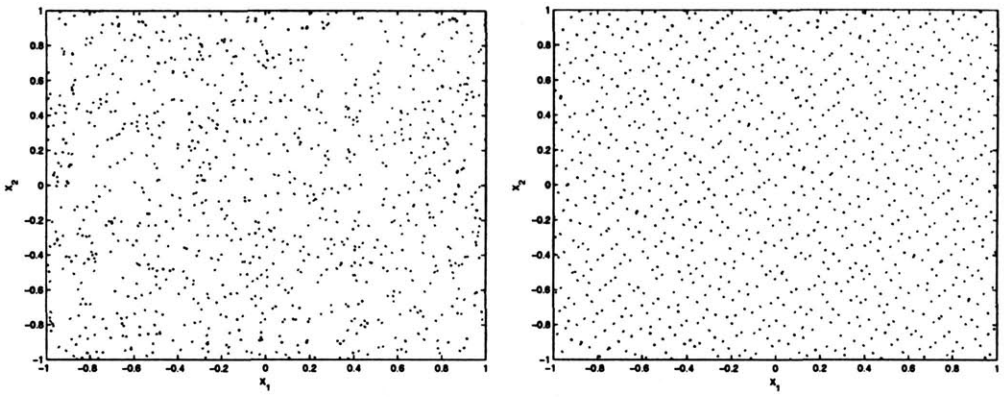

Figure 3-8: 1000 realizations of the pseudo-random (left) and quasi-random (right) variable for two random dimensions.

(exponential) convergence of stochastic solutions for their corresponding probability distribution, as shown in Table 3.1 below.

Table 3.1: Orthogonal polynomials and their associated probability distribution.

Orthogonal polynomial	Probability Distribution
Hermite	Gaussian
Legendre	Uniform
Laguerre	Gamma
Jacobi	Beta
Charlier	Poisson
Meixner	Negative Binomial
Krawtchouk	Binomial
Hahn	Hypergeometric

3.3.1 Algorithmic framework for generalized Polynomial Chaos method

The main concept of the generalized Polynomial Chaos (gPC) is that all state variables of a random process are expanded in terms of the weighted sum of orthogonal polynomial bases of standard random variables. A general second-order random pro-

cess can be concisely expressed in the following form:

$$\mathbf{X}(\omega) = \sum_{i=0}^{\infty} \mathbf{c}_i(t)\phi_i(\xi(\omega)), \tag{3.9}$$

where ϕ_i denotes the polynomial basis from the Wiener-Askey polynomial chaos, expressed as a function of a d-dimension random variable $\xi = (\xi_1, ..., \xi_d)$. This form of expansion optimally converges to L_2 random process in L_2 sense. ω represents a random event confined within the sample space of the particular distribution. $\mathbf{c}_i(t)$ is the i'th modal coefficient, from which statistics can be directly calculated. In numerical implementation, the expansion onto the orthogonal polynomial basis is truncated at P terms. We have $P = (d+p)!/d!p!$, where d and p are the dimension of random variable ξ and the highest order of the polynomial chaos, respectively. The accuracy of stochastic solution can be improved by increasing the polynomial order, known as the p-type refinement. The convergence rate of p-refinement is an exponential for a smooth and continuous solutions.

An important property of the Wiener-Askey polynomial chaos is orthogonality:

$$\langle \phi_\mathrm{i}, \phi_\mathrm{j} \rangle = \langle \phi_\mathrm{i}^2 \rangle \delta_{ij}, \tag{3.10}$$

where δ_{ij} is the Kronecker delta and $\langle \cdot, \cdot \rangle$ represents the inner product on the support of random variable ξ. In the continuous case, the inner product is defined as:

$$\langle f(\xi), g(\xi) \rangle = \int f(\xi) \cdot g(\xi) \cdot W(\xi) d\xi, \tag{3.11}$$

where $W(\xi)$ is the weighting function corresponding to the Wiener-Askey polynomial chaos. In our case, we assume all the uncertainties to have uniform distribution, and thus the Legendre polynomial chaos, which is the same as Jacobi polynomial with $\alpha = 0$ and $\beta = 0$, is the most efficient basis. The formulas and properties for the Legendre polynomials are shown in Appendix A.

3.3.2 Numerical Implementation

The major advantage of applying the gPC is that an SDE can be transformed into a system of deterministic equations. To solve a particular SDE, all state variables $(x(t,\omega))$ and random inputs $(u(t,\omega))$ must be expanded by the polynomial chaos and by corresponding modal coefficients with the the following result:

$$x(t,\omega) = \sum_{i=0}^{P} x_i(t)\phi_i(\xi(\omega)) \quad \text{and} \quad u(t,\omega) = \sum_{i=0}^{P} u_i(t)\phi_i(\xi(\omega)) \tag{3.12}$$

A Galerkin projection is applied to this SDE for each $(\phi_i(\omega))$ such that the SDE can be simplified to one of many P+1 coupled ordinary differential equations (ODE's) for each mode, using the orthogonality property of polynomial chaos. Then, these deterministic modal ODE's can be solved with any numerical method dealing with initial-value problems, e.g., the Ruge-Kutta method. Consider now the ODE of the induction machine mechanical subsystem. After expanding all the state variables onto the orthogonal polynomial basis that includes the uncertainty in torque load, the stochastic differential equation becomes

$$\begin{aligned} \sum_{i=0}^{P} \frac{d\omega_{ri}}{dt}\phi_i \;=\; & \frac{\omega_b x_b}{2Hx'_{lr}} \left(\sum_{i=0}^{P} \psi'^{e}_{qri}\phi_i \sum_{j=0}^{P} i^{e}_{dsj}\phi_j \right) - \qquad (3.13) \\ & \frac{\omega_b x_b}{2Hx'_{lr}} \left(\sum_{i=0}^{P} \psi'^{e}_{dri}\phi_i \sum_{j=0}^{P} i^{e}_{qsj}\phi_j \right) - \\ & \frac{\omega_b}{2H} \sum_{i=0}^{P} T_{Li}\phi_i. \qquad (3.14) \end{aligned}$$

Projecting the above equation onto each of the $P+1$ modes of the polynomial chaos, using the Galerkin method, results in $P+1$ deterministic ODE's for each mode in

the expansion:

$$\frac{d\omega_{rk}}{dt}\langle\phi_k^2\rangle = \frac{\omega_b x_b}{2Hx'_{lr}}\sum_{i=0}^{N_P}\sum_{j=0}^{N_P}\psi'^e_{qri}i^e_{dsj}e_{ijk} - \tag{3.15}$$

$$\frac{\omega_b x_b}{2Hx'_{lr}}\sum_{i=0}^{N_P}\sum_{j=0}^{N_P}\psi'^e_{dri}i^e_{qsj}e_{ijk} - \frac{\omega_b}{2H}T_{Lk}\langle\phi_k^2\rangle \quad . \tag{3.16}$$

where e_{ijk} denotes the triple product $\langle\phi_i,\phi_j,\phi_k\rangle$. This e_{ijk} should be calculated in advance for the system with the random dimension less than three; otherwise on-line computing of the tensor product of one-dimensional polynomial basis results in faster computational time for the systems with high-dimension random inputs. The rest of the SDE's of the system are similarly transformed into deterministic ODE's. Once the time integration of the modes is complete, first and second moments of each state can be directly obtained from the zero modes and from a summation of the squared modal amplitudes, each multiplied by $\langle\phi_k^2\rangle$, as shown below.

$$\mu_1(f(t,\xi)) = x_0(t), \tag{3.17}$$

$$\mu_2(f(t,\xi)) = \sum_{i=1}^{P} x_i^2(t)\langle\phi_i^2\rangle. \tag{3.18}$$

To construct a probability density function (PDF) of state or output from modal solutions, n realizations associated with the random distribution must be generated for P+1 polynomial bases. The range of realizations of state or output can be used to form its PDF with a histogram function, h_j for $j = 1,\cdots,n$.

$$PDF(x(t,\xi)) = h_j\Big(\sum_{i=0}^{P} x_i(t)\phi_i(\xi(\omega))\Big). \tag{3.19}$$

3.3.3 Algorithmic framework for Multi-Element gPC

According to Wan and Karniadakis [60], if the domain of random inputs (ω) is subdivided into multiple elements, the accuracy of stochastic solutions can be improved,

especially for cases of discontinuity in stochastic solutions or for problems of long-time integration. As a result of the h-refinement, a local integration error at each time step can be reduced and the domain of solutions' discontinuity can be approximated more accurately within a smaller decomposed domain. We will briefly explain the basic concept of the Multi-Element gPC (MEgPC) [60] for a d-dimension random input.

First, let $\xi(\omega) = [\xi_1(\omega), \xi_2(\omega), \ldots, \xi_d(\omega)]$, which denotes a vector random input in d dimension. Each ξ_i is an identical independent distributed (IID) uniform random variable, $U[-1, 1]$. Second, we decompose the d-dimension domain of the random input into N non-intersecting intervals or elements (E_k). The domain of each element is contained within a hypercube, $[a_1^k, b_1^k) \times [a_2^k, b_2^k) \times \cdots \times [a_d^k, b_d^k)$, where a and b denote a lower and upper bound of that element, respectively. We must scale the random variable of each element ($\zeta^{\mathbf{k}} = [\zeta_1^k(\omega), \zeta_2^k(\omega), \ldots, \zeta_d^k(\omega)]$) accordingly with its conditional probability density function, $p_{\zeta^k} = \frac{1}{(b_i^k - a_i^k)}$, where $i = 1, \cdots, d$ and $k = 1, \cdots, N$. The mapping of random variables from global to local or element domain is governed by the following relationship.

$$\zeta_i^k = \frac{b_i^k - a_i^k}{2}\xi_i^k + \frac{b_i^k + a_i^k}{2}, \tag{3.20}$$

where the global random variable, ξ_i^k, is ranged between $[a_i^k, b_i^k)$. The local random variable, ζ_i^k, is a uniform random variable, $U[-1, 1]$; therefore we can apply the gPC with the Legendre polynomial chaos basis to solve SDE, $\frac{dx(t,\xi)}{dt} = f(x(t, \xi))$, in each local element for N times. Using Bayes' Rule and the total probability theorem, the global statistical moments ($\mu_m(f(\xi))$ can be calculated from the local statistics ($\mu_m(f(\zeta))$) as shown below.

$$\mu_m(f(\xi)) = \int_{[-1,1]^d} f^m(\xi)\left(\frac{1}{2}\right)^d d\xi = \sum_{k=1}^{N} p_{\zeta^k} \int_{[-1,1]^d} f^m(\zeta^k)\left(\frac{1}{2}\right)^d d\zeta^k, \tag{3.21}$$

where μ_1 and μ_2 denote mean and variance solutions. One of the numerical implementations is assigning the initial condition after splitting the random dimension into multiple elements, which has been done by solving the inverse of a linear system [60]. Let

us denote the expansion of state variables at the upper level, $\hat{x}^k(\xi^k) = \sum_{i=0}^{P} \hat{x}_i^k \phi_k(\xi^k)$ for $k = 1, \cdots, N$, for N elements. If we split each element into two sub-elements at the refined level, the state-variable expansion can be expressed as $\tilde{x}^k(\zeta^k) = \sum_{i=0}^{P} \tilde{x}_i^k \phi_k(\zeta^k)$ for $k = 1, \cdots, 2N$. To assign the initial condition for $\tilde{x}_i^k$, we must solve the following linear system:

$$\begin{pmatrix} \phi_{00} & \phi_{10} & \cdots & \phi_{P0} \\ \phi_{01} & \phi_{11} & \cdots & \phi_{P1} \\ \vdots & \vdots & \ddots & \vdots \\ \phi_{0P} & \phi_{1P} & \cdots & \phi_{PP} \end{pmatrix} \begin{pmatrix} \tilde{x}_0 \\ \tilde{x}_1 \\ \vdots \\ \tilde{x}_P \end{pmatrix} = \begin{pmatrix} \sum_{i=0}^{P} \hat{x}_i \phi_i(\zeta^0) \\ \sum_{i=0}^{P} \hat{x}_i \phi_i(\zeta^1) \\ \vdots \\ \sum_{i=0}^{P} \hat{x}_i \phi_i(\zeta^P) \end{pmatrix} \tag{3.22}$$

where $\phi_{ij} = \phi_i(\zeta^j)$.

3.4 Collocation Approach of Polynomial Chaos

The collocation method is an alternative approach to solve stochastic random processes with the Polynomial Chaos. Instead of projecting each state variable onto the polynomial chaos basis, the collocation approach evaluates the function at roots of the basis polynomials. Therefore, if the governing equations become more complex, the simplicity of collocation framework, which is only repetition runs of deterministic solvers, results in a faster algorithm than the gPC, particularly in high dimension problems. In this section, two collocation techniques, full- and sparse-grid collocation methods, are explained in detail along with a framework for the multi-element technique and an adaptive criteria.

3.4.1 Probabilistic Collocation Method (PCM)

Two underlined concepts for the PCM are the orthogonal polynomial and their associated quadrature rule. As mentioned earlier, each class of the orthogonal polynomial chaos has a different associated weighting function, which is identical to a different probability distribution. Since only uniform random distribution, $U[-1, 1]$, is consid-

ered here, the full-grid collocation method specifies its collocation points according to roots of the Legendre polynomials ($L(\xi)$) or the Jacobi polynomials ($J^{\alpha,\beta}(\xi)$) with $\alpha = \beta = 0$. Similar to the gPC approach, $L(\xi)$ yields the fastest or exponential convergent rate for the uniform process. For the sparse-grid collocation method, the collocation points are determined from zeros of the Chebyshev polynomials of the first kind ($T(\xi)$) or $J^{\alpha,\beta}(\xi)$ with $\alpha = \beta = -1/2$. The domain of all these polynomials are on [-1,1]. The main difference between $L(\xi)$ and $T(\xi)$ are 1) roots of $L(\xi)$ do not include the end support and vice versa for $T(\xi)$, and 2) roots of $L(\xi)$ fully cover the entire domain, while roots of $T(\xi)$ form a sparse structure. All properties of $L(\xi)$, $J^{\alpha,\beta}(\xi)$ and $T(\xi)$ polynomials are given in Appendix A. The highest order of polynomials or roots of polynomials determines a number of collocation points (Nc).

Full-grid PCM

For the uniform random process, the full-grid PCM relies on the non-equidistant abscissas of the Legendre polynomials for specifying the collocation points and the Gauss-Legendre quadrature rule for computing statistics. Similar to the p-refinement, the more the number of collocation points, Nc, increases, the better the accuracy of stochastic solutions is. We call this improvement an Nc-refinement. Figure 3-9 displays an example of the non-nested collocation points' location for $Nc = 10$ and $Nc = 11$ in a two random dimension.

The Gauss quadrature formula, which is a well-known numerical integration technique, yields an exact integration value for any function in a polynomial form ($f(\xi)$) of order less than or equal to $2Nc - 1$. An approximation of the integration by the Gauss quadrature rule is shown in the equation below.

$$\int_R f(\xi)W(\xi)dx = \sum_{i=1}^{Nc} f_i(\xi_i)w_i, \tag{3.23}$$

where ξ_i, a collocation point, is determined from the abscissas of the orthogonal polynomials of Nc order over a domain, R, which can be found numerically using Newton's method [46]. f_i denotes a value of the function evaluated at this collocation

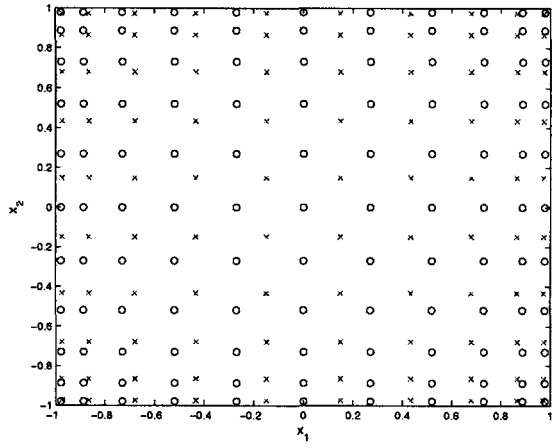

Figure 3-9: The non-equidistant and non-nested abscissas or collocation points for Nc=10 (x) and Nc=11 (o) of the full-grid PCM in two random dimensions.

point and w_i is the weight of the Gauss-Legendre formula. The analytical formula for w_i in one dimension is given below:

$$w_i = \frac{2(1-\xi_i^2)}{(Nc+1)^2[L_{Nc+1}(\xi_i)]^2}. \tag{3.24}$$

For a higher dimension random process, Nc equals the number of collocation points in one dimension raised to d power. From now on, Nc represents the total number of collocation points in d dimensions. The probabilistic collocation method is simply performed by solving the deterministic solution Nc times with random parameters specified at these collocation or nodal points. Using either the Gauss-Legendre or Gauss-Lobatto-Jacobi (with $\alpha = \beta = 0$) quadrature, the statistical moments of stochastic solution, $u(t,\xi)$, in d dimension can be computed accurately and efficiently after solving for Nc deterministic state solutions at these abscissas.

$$\mu_1 = \frac{1}{2^d}\sum_{i=1}^{Nc} u(t,\xi_i)w_i^d, \tag{3.25}$$

$$\mu_2 = (\frac{1}{2^d}\sum_{i=1}^{Nc} u^2(t,\xi_i)w_i^d) - \mu_1^2. \tag{3.26}$$

μ_1 and μ_2 are the mean and variance solutions, respectively. The factor $\frac{1}{2}$ is required owing to normalization of the one-dimensional Gauss-Legendre weight ($\sum_{i=1}^{Nc} w_i = 2$).

To construct the PDF from the nodal points of the PCM, we need to project these nodal points onto the Lagrange interpolant basis ($H_j(\xi)$). The Lagrange interpolant polynomials are generated based on Nc collocation points at any arbitrary value, ξ, where $-1 < \xi < 1$.

$$H_j(\xi) = \begin{cases} \dfrac{(1-\xi^2)J_{Nc-2}^{\alpha+1,\beta+1}(\xi)}{\Big((1-\xi_j^2)[J_{Nc-2}^{\alpha+1,\beta+1}(\xi_j)]' - 2\xi_j J_{Nc-2}^{\alpha+1,\beta+1}(\xi_j)\Big)(\xi-\xi_j)} & \text{if } \xi \neq \xi_j \\ 1 & \text{otherwise} \end{cases} \tag{3.27}$$

where $J_i^{\alpha,\beta}(\xi)$ is the i order Jacobi polynomial. If $\alpha = \beta = 0$, the Jacobi polynomial becomes the Legendre polynomial. Then, the PDF can be constructed with the following relation: $PDF(x(t,\xi)) = h_j\Big(\sum_{j=1}^{Nc} f(\xi_j,t)H_j(\xi)\Big)$, where $f(\xi_j,t)$ is the evaluation of system equations at a specific nodal point and time and h_j again denotes a histogram function with $j = 1, \cdots, Nc$.

Sparse-grid PCM

The zeros of $T(x)$ are sparsely distributed in the random domain and nested as the number of collocations, known as level (l) [63], increases. With these two advantages, the sparse-grid PCM can significantly reduce the computational cost and still maintain the accuracy of quadrature integration, especially in a high random dimension. In one dimension, non-equidistant abscissas of $T(x)$ that include the end points can be written in an analytical form as a cosine function [63]:

$$\xi_{li} = -\cos\frac{\pi(i-1)}{n_l^1 - 1} \quad \text{for} \quad i = 1, \cdots, l, \tag{3.28}$$

where n_l^1 denotes the number of collocation points in a single dimension. $n_l^1 = 2^{l-1}+1$, for $l \geq 2$. To approximate the integral of statistical moment, the sparse-grid PCM employs the weight (w_i) from the Clenshaw-Curtis formulas. The w_{li} is given by

$$w_{li} = \frac{2}{n_l^1 - 1}\Big(1 + 2 \cdot \sum_{j=1}^{(n_l^1-1)/2}{}' \frac{1}{1-4j^2} \cdot cos\frac{2\pi(i-1)j}{n_l^1 - 1}\Big) \quad \text{for} \quad 2 \leq i \leq n_l^1 - 1 \tag{3.29}$$

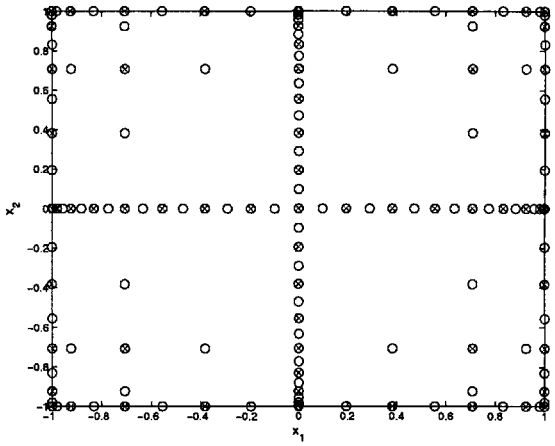

Figure 3-10: The non-equidistant and nested abscissas or collocation points for level=5 (x) and level=6 (o) of the sparse-grid PCM in two random dimensions.

$$\text{and} \quad w_{l1} = w_{ln_l^1} = \frac{1}{n_l^1(n_l^1-2)}. \tag{3.30}$$

A $\sum'$ notation denotes that the last term of the summation is divided by a factor of two. Instead of using the Gauss quadrature, Smolyak's quadrature, requiring the nested collocation points, is used for calculating all statistics. We show the characteristic of the nested collocation points of the sparse-grid PCM in two random dimensions as shown in Figure 3-10.

Let us define a notation of the one-dimensional quadrature formula for the l level as the following: $U_l^1 f = \sum_{i=1}^{n_l} f(\xi_{li}) w_{li}$. Then, the difference quadrature formula $(\Delta_l^1 f)$ is defined as the difference of one-dimensional quadrature formula between the current level and one lower level: $\Delta_k^1 f = (U_k^1 - U_{k-1}^1) f$. The d-dimension Smolyak quadrature formula [18] can be constructed as a function of either $\Delta_l^1 f$ or $U_l^1 f$:

$$U_l^d f = \sum_{|li| \le l+d+1} (\Delta_{l1}^1 \otimes \cdots \otimes \Delta_{ld}^1) f, \quad \text{or} \tag{3.31}$$

$$U_l^d f = \sum_{l \le |li| \le l+d+1} (-1)^{l+d-|li|-1} \cdot \binom{d-1}{|li|-l} \cdot (U_{l1}^1 \otimes \cdots \otimes U_{ld}^1) f \tag{3.32}$$

The symbol, $\otimes$, represents the tensor product. From a numerical implementation

aspect [18], expression 3.4.1 can be written explicitly in terms of nested grid points and weights as:

$$U_l^d f = \sum_{|li| \leq l+d+1} \sum_{j_1=1}^{n_l^1} \cdots \sum_{j_d=1}^{n_l^d} w_{\mathbf{lj}} f(\xi_{\mathbf{lj}}). \tag{3.33}$$

$\xi_{\mathbf{lj}}$ denotes the d-dimension vector of $(x_{l_1 j_1}, \cdots, x_{l_d j_d})$. And the nested weight can be written as

$$w_{\mathbf{lj}} = \sum_{|l+k| \leq l+2d-1} z_{(l1+k1)j_1} \cdot \cdots \cdot z_{(ld+kd)j_d}, \tag{3.34}$$

where

$$z_{(l+k)j_1} = \begin{cases} w_{lj} & \text{if } k = 1 \\ w_{(l+k-1)m} - w_{(l+k-2)n} & \text{if } k > 1, \xi_{lj} = \xi_{(l+k-1)m} = \xi_{(l+k-2)n} \end{cases} \tag{3.35}$$

Compared to the full-grid PCM, the computing cost grows with Nc raised to a d power of random dimension and it can approximate precisely the integration of any polynomial function of order $\leq 2Nc - 1$. The sparse-grid PCM using the Clenshaw-Curtis formulas can provide an accurate result for integrating polynomial functions of order up to $n_l^1 - 1$. According to Table 3.2, 3.3, and 3.4, the computational cost of the sparse-grid PCM is far less than those of the full-grid PCM for the same level when the random dimension is greater than 5. In case of smooth and continuous solutions, the level represents the accuracy for both the full- and sparse-grid PCM.

3.4.2 Algorithmic framework for Multi-Element PCM

Parallel to the MEgPC, a basic concept of Multi-Element PCM (MEPCM) is to divide the random variable into multiple elements such that the degree of randomness in the original space is reduced proportional to the number of elements. Let us consider the orthogonal polynomial as a function of the random variable in a d-dimensional hypercube, $\xi = [\xi_1, \xi_2, \cdots, \xi_d]$, where $\xi_i \in U[-1, 1]$ with a constant PDF of $1/2$. By

Table 3.2: Comparison of the number of collocation points (Nc), corresponding to the computing cost, between the full-grid PCM and the sparse-grid PCM for small random dimensions $d \leq 4$ and levels.

Random dimension	Level	Nc(Full-grid PCM)	Nc(Sparse-grid PCM)
2	2	4	5
	3	9	13
	4	16	29
	5	25	65
	6	36	145
	7	49	321
	8	64	705
	9	81	1,537
	10	100	
3	2	8	7
	3	27	25
	4	64	**69**
	5	125	177
	6	215	441
	7	343	1,073
	8	512	2,561
	9	729	6,017
	10	1,000	13,953
4	2	16	9
	3	81	41
	4	256	137
	5	625	401
	6	1,296	1,105
	7	2,401	**2,929**
	8	4,096	7,537
	9	6,561	18,945
	10	10,000	46,721

Table 3.3: Comparison of the number of collocation points (Nc), corresponding to the computing cost, between the full-grid PCM and the sparse-grid PCM for medium random dimensions $5 \leq d \leq 9$ and levels.

Random dimension	Level	Nc(Full-grid PCM)	Nc(Sparse-grid PCM)
5	2	32	11
	3	243	61
	4	1,024	241
	5	3,125	801
	6	7,776	2,433
	7	16,807	6,993
	8	32,768	19,313
	9	59,049	51,713
	10	100,000	**135,073**
7	2	128	113
	3	2,187	589
	4	16,384	2,465
	5	78,125	9,017
	6	279,936	30,241
	7	823,543	95,441
	8	2,097,152	287,745
	9	4,782,969	836,769
	10	10,000,000	2,362,881
9	2	512	181
	3	19,683	1,177
	4	262,144	6,001
	5	1,953,125	26,017
	6	10,077,696	100,897
	7	40,353,607	361,249

Table 3.4: Comparison of the number of collocation points (Nc), corresponding to the computing cost, between the full-grid PCM and the sparse-grid PCM for large random dimensions $d \geq 10$ and levels.

Random dimension	Level	Nc(Full-grid PCM)	Nc(Sparse-grid PCM)
10	2	1,024	21
	3	59,049	221
	4	1,048,576	1,581
	5	9,765,625	8,801
	6	60,466,176	41,265
20	2	1,048,576	41
	3	3,486,784,401	841
	4	1,099,511,627,776	11,561
	5	95,367,431,640,625	120,401

separating the random variable (ξ) in the global level into N non-overlapping elements (E^k), the local element in a d-dimensional hypercube can expressed as the following:

$$E^k = [a_1^k, b_1^k) \times [a_2^k, b_2^k) \times \cdots \times [a_d^k, b_d^k) \quad \text{for } i = 1, \cdots, N. \tag{3.36}$$

where a_i and b_i are respectively lower and upper bounds in the i random dimension and $E^i \cap E^j = \emptyset$. As a result, the local random variable (ζ^k) in each element can be computed by the following mapping relationship.

$$\zeta_i^k = \frac{b_i^k - a_i^k}{2} \xi_i^k + \frac{b_i^k + a_i^k}{2}. \tag{3.37}$$

And an associated conditional probability is given by $p_{\zeta^k} = \frac{1}{(b_i^k - a_i^k)}$, for $i = 1, \cdots, d$ and $k = 1, \cdots, N$. The main difference between the MEgPC and MEPCM is the method of mapping the initial condition from current-level meshes to those in a refined level. At each time step, system solutions, $f(\xi_i)$, are evaluated only at the nodal points in the current-level meshes. If one of the elements in the current mesh is split into two new elements at the next time step, initial conditions of new elements

can be either assigned directly from the original element in the case of $\xi^k = \zeta^k$ or derived numerically in the case of $\xi^k \neq \zeta^k$. To numerically compute the initial condition for system function at these new collocation points, we must solve the system at these new nodal points from an initial time. As a result, the original PCM, associated with the global random space, is decomposed into N sub-problems of the PCM, corresponding to N local random spaces.

Then, local statistical solutions ($\mu_m(f(\zeta))$) in each element are computed by the Gauss quadrature formula for the full-grid PCM and the Smolyak quadrature formula for the sparse-grid PCM. To calculate global m-th moments ($\mu_m(f(\xi))$), Bayes' Rule and the law of total probability can be applied as the following:

$$\mu_m(f(\xi)) = \int_{[-1,1]^d} f^m(\xi) W(\xi) \left(\frac{1}{2}\right)^d d\xi = \sum_{k=1}^{N} p_{\zeta^k} \int_{[-1,1]^d} f^m(\zeta^k) W(\zeta^k) \left(\frac{1}{2}\right)^d d\zeta^k. \quad (3.38)$$

3.4.3 Adaptive Multi-Element technique

There are two approaches to determine the number of element, N, in the h-type refinement: 1) uniform decomposition of the global random space into N equal elements, and 2) adaptively splitting the global domain according to a local variance error. For the uniform multi-element case, using a fixed number of elements can directly reduce the local error at the initial time step, which leads to a smaller global error for the long-time integration. The benefit of this approach is more pronounced when a randomness is in the initial conditions or a discontinuity in stochastic solutions occurs at the initial time step. However, an accumulative error from time integration as well as errors from discontinuity that happens at a later time will dominate the error reduction using the fixed number of elements. Thus, adaptively decomposing the random space into multiple elements can identify a time step where the global error becomes larger than a specified threshold or the discontinuity exists and further reduces these errors. A local error of the k-element (η_k) is defined as a normalized difference of the local variance between using Nc+2 and using Nc collocation points, which is defined as $\eta_k = \frac{\sigma^2_{k,Nc+2} - \sigma^2_{k,Nc}}{\sigma^2_{k,Nc+2}}$. An adaptive criterion for splitting into two

equal elements is $\eta_k > \left(\frac{\theta_1}{p_{\zeta^k}}\right)^2$, where θ_1 is a threshold of the specified accuracy and p_{ζ^k} is the conditional probability of that element. A power factor is set to be a square such that the range of the threshold value (θ_1) can be adjusted in a wider accuracy range. This adaptive multi-element technique for handling the discontinuous solutions of the Kraichnan-Orszag system as well as for improving the error convergence in a high random-dimension stochastic process will be shown in the next chapter.

3.5 Hybrid gPC + PCM approach

Because the Galerkin projection is used in the gPC for transforming the SDE to deterministic coupled equations, the system nonlinearity is limited only to a polynomial form, i.e., quadratic, cubic, quartic, etc. To be able to handle the nonlinearity in a more general form including trigonometric and signum functions, we need to perform additional mapping so that any function can be expanded onto the polynomial chaos basis, associated with the specified distribution. Moreover, this approach still maintains the advantages of the gPC-exponential convergence and separation of randomness from variables.

3.5.1 Algorithmic framework

A general procedure for this technique can be applied to any SDE, $\frac{dx(t,\xi)}{dt} = f(x)$, as the following. First, we expand all state variables, $x(t,\xi)$, onto the orthogonal basis of the polynomial chaos, $\phi(\xi)$. However, when the function, $f(x)$, is not in a polynomial form, consisting of state and random input, we cannot directly apply the Galerkin projection to the SDE. Therefore, the modal coefficients of the function, $f_i(x)$, must be calculated separately before substituting into the chaos expansion. In the second step, we assume the function, $f(x)$, can be expressed in the following form: $f(x,\xi) = \sum_{i=0}^{P} f_i(x)\phi_i(\xi)$. Next, we project and compute the inner product for each mode of the polynomial chaos as shown below:

$$f_j(x)\langle\phi_j^2\rangle = \int_\Omega f(x,\xi)\phi_j(\xi)W(\xi)d\xi, \tag{3.39}$$

where $W(\xi)$ is the weighting function associated with the polynomial chaos. In this study, only random variables with the uniform distribution are considered, so $\phi_i(\xi)$ is the Legendre polynomial and $D \subset U[-1,1]$. Instead of computing the inner product analytically, we use the Gauss-Legendre quadrature to evaluate the inner-product integral as:

$$f_j(x) = \frac{1}{\langle \phi_j^2 \rangle} \sum_{j=1}^{Nc} f_j(x, \xi_j) \phi_j(\xi_j) w_j. \tag{3.40}$$

The larger the Nc is, the more accurate an approximation of the Gauss quadrature becomes. An appropriate value of Nc must be chosen to trade off between accuracy and computational efficiency. Generally, the value of Nc between 10 and 20 provides a good accuracy for a small computational cost. Lastly, the SDE can be solved with the normal gPC using the modal coefficients, f_j. Both p- and h-type refinements can enhance the accuracy of stochastic solutions.

Chapter 4

Convergence Study of Various Stochastic Algorithms

Generally, the accuracy of solution, the efficiency of computation, and the simplicity of implementation must be considered to compare a performance of the stochastic algorithms, outlined in Chapter 3. First, a convergence study shows how accurate the statistical solutions become as a governing parameter of that algorithm increases. The governing parameters of MC, QMC, gPC, full-grid PCM, sparse-grid PCM and Multi-Element techniques consequently are a number of realizations (NN), a polynomial order (p), The number of collocation points (Nc) for the full-grid PCM, a level ($level$) for the sparse-grid PCM, and a number of elements (N). A number of operations performed at each time step or computational time can indicate the algorithm's efficiency. An algorithm's structure is related to its implementation complexity, which closely connects to the computational speed. All numerical computations in this chapter are performed with the Microsoft C++ compiler on an Intel Pentium 4 3.0GHz Processor.

To study the rate of convergence, a statistical error that will be used regularly is defined as a L_2 norm difference between estimated and analytical solutions of mean and variance, normalized by the L_2 norm of the analytical or reference solution. This normalized L_2 norm difference is similar to that defined by Xiu and Karniadakis [62]. The absolute and L_∞ differences are employed in their convergence calculation

of gPC. Since we need to include the accumulating error, especially in a long-time integration problem, the L_2 differences is more suitable for our convergence study. When the system is large and more complex, the analytical or exact statistical solution becomes more involved and difficult to derive. Thus, the exact solution can be replaced by a reference solution with higher accuracy than estimated solutions. The error measurements of mean $\bar{y}$ and variance σ_y^2 solutions can be expressed as the following:

$$\varepsilon_{mean} = \frac{\|\bar{y}(t) - \bar{y}_{exact}(t)\|_2}{\|\bar{y}_{exact}(t)\|_2}, \tag{4.1}$$

$$\varepsilon_{var} = \frac{\|\sigma_y^2(t) - \sigma_{y,exact}^2(t)\|_2}{\|\sigma_{y,exact}^2(t)\|_2}, \tag{4.2}$$

According to Xiu and Karniadakis [62], the gPC with an appropriate Wiener-Askey polynomial chaos has been shown to yield an exponential rate of convergence as a function of polynomial order (p) for the corresponding type of random inputs. Moreover, the empirical convergence rate of the uniform MEgPC has been estimated to be in the order of $O(N^{-2(p+1)})$ by Wan and Karniadakis [60]. However, the convergence rates of the PCM as well as MEPCM have not been systematically examined for either full- or sparse-grid collocation method in terms of a stochastic analysis aspect.

This chapter considers the convergence property of these stochastic algorithms on four different SDEs: 1) 1st-order SDEs; 2) the Kraichnan-Orszag three-mode system with quadratic-nonlinearities, which has either continuous or discontinuous solutions depending on the random initial condition; 3) a single induction machine; and 4) a shipboard AC power distribution with propulsion system. And, we establish an empirical formula for the convergence rate of these algorithms for both continuous and discontinuous solutions. Furthermore, a relationship between gPC and PCM as well as between MEgPC and MEPCM show how closely these algorithms are related. Lastly, this chapter compares the algorithms' efficiency, influence of sparse structure of the collocation method, and effect of the random dimension on the convergence of estimated statistics.

4.1 Continuous Stochastic Solutions

This section investigates the L_2 convergence rate of different algorithms for both linear vs. nonlinear systems with continuity in their stochastic solutions. First, we study the convergence characteristic of simple SDEs, since exact statistical solutions of these systems can be derived. Second, a more complicated SDE, the Kraichnan-Orszag system with random initial conditions, further confirms the convergence rate of these stochastic algorithms as a function of the random dimension. Moreover, the multi-element technique helps improve the statistical accuracy in case of a long-time integration, particularly for the sparse-grid PCM. This section considers five types of SDEs. Note that in this section, the PCM approach is referred to the full-grid PCM, described in the last chapter, and the multi-element technique of the gPC and PCM is employed only a uniform decomposition of the random dimension.

4.1.1 Linear first-order SDE

Let us first consider the simplest SDE system, the first-order linear ODE, described by the following equation:

$$\frac{dy}{dt} = -ky, \qquad \text{with } y\,(t=0) = y_0 = 1 \text{ and } t \in [0,T] \tag{4.3}$$

where the decay rate coefficient k is considered to be a random variable, $k = \bar{k} + \sigma_k \xi$, with constant mean $(\bar{k})$ and standard deviation (σ_k) in the fully correlated case. We assume that the k random variable is associated with the uniform distribution, $U[-1,1]$. The deterministic solution of the first-order ODE is $y(t) = y_0 e^{-\bar{k}t}$. The mean and variance of the stochastic solutions are given by the following:

$$\bar{y}_{exact}(t) = y_0 \int_{-1}^{1} e^{-kt} f(k) dk = y_0 \frac{e^{(\bar{k}+\sigma_k)t}(e^{2\sigma_k t} - 1)}{2\sigma_k t}, \tag{4.4}$$

$$\sigma^2_{exact}(t) = y_0^2 \frac{e^{-2\bar{k}t}}{2} \left(\frac{(e^{-2\sigma_k t} - e^{2\sigma_k t})}{2\sigma_k t} + \frac{(e^{\sigma_k t} - e^{-\sigma_k t})^2}{2\sigma_k^2 t^2} \right). \tag{4.5}$$

Considering the case where $\bar{k} = 2$ and $\sigma_k = 1$, we display the exact mean and variance solutions in Figure 4-1, which are bounded and approach steady-state values with an exponential decay.

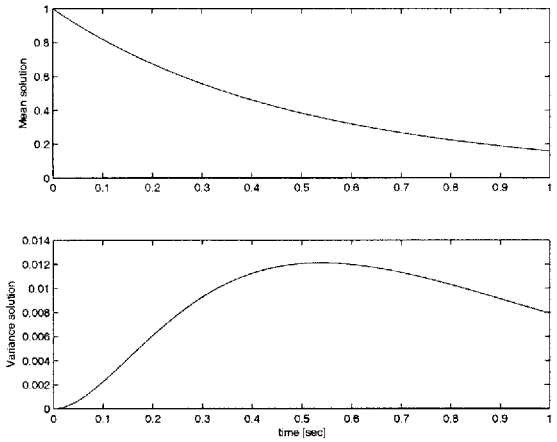

Figure 4-1: The exact mean (top) and variance (bottom) solutions for $\dot{y} = -ky$.

We can compare the convergence characteristic between the gPC with $p = [1, 2, 3, 4]$ and the PCM with $Nc = [2, 3, 4, 5]$ for $t \in [0, 1]$. From Figure 4-2, the gPC and the PCM exhibit exponential convergence rates of $O(e^{-5p})$ and $O(e^{-5(Nc-1)})$, respectively. Both methods exhibit the same L_2 convergence error, so this suggests a relationship of $p = Nc - 1$ between gPC and PCM. An equal number of system equations in the gPC with p polynomial order, requiring p+1 terms in the polynomial expansion, and in the PCM with Nc collocation points or roots of Nc polynomial order, requiring Nc terms in the Gauss quadrature, uses the same highest-order Legendre chaos.

Instead of the exponential p- and Nc-convergence of the single-element gPC and PCM, the multi-element technique provides an algebriac convergence relation. For $t \in [0, 1]$, the statistics are calculated numerically from the MEPCM with $Nc = [2, 3, 4]$ and the MEgPC with $p = [1, 2, 3]$. Both MEPCM and MEgPC methods with uniformly distributed elements yield a linear L_2 convergence rate, as the number of elements (N) increases. Figure 4-3 shows the convergence rates of $O(N^{-2(Nc)})$ and $O(N^{-2(p+1)})$, using MEPCM and MEgPC, respectively.

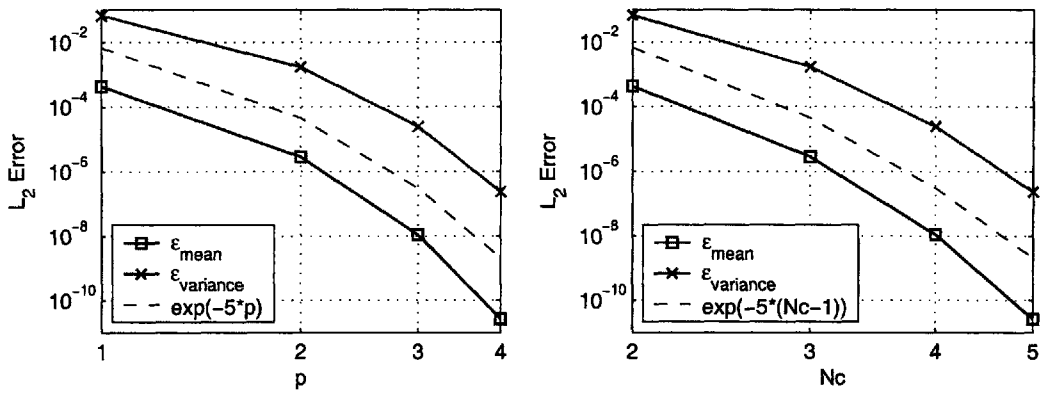

Figure 4-2: The L_2 error convergence of mean and variance solutions as a function p for the gPC(left) and Nc for the PCM (right) for $\dot{y} = -ky$.

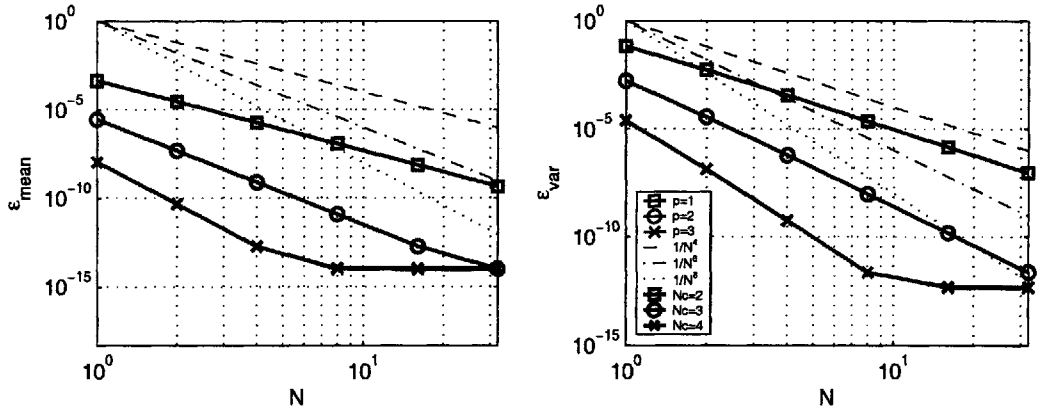

Figure 4-3: The convergence rates of mean (left) and variance (right) errors as a function of number of elements, using MEPCM (thick line) and MEgPC (thin line), for $\dot{y} = -ky$.

4.1.2 Quadratic nonlinear first-order SDE

Next, the first-order SDE with a similar decay factor as in the previous system is modified to be a quadratic nonlinear function instead of the linear function

$$\frac{dy}{dt} = -ky^2, \qquad \text{with } y\,(t=0) = y_0 \text{ and } t \in [0,T] \tag{4.6}$$

and a random variable decay rate $k = \bar{k} + \sigma_k \xi$, where ξ is a uniform distribution within U[-1,1]. The deterministic solution is $y(t) = \frac{y_0}{y_0 kt+1}$ with $y_0 = 1$. Exact solutions of mean and variance are:

$$\bar{y}_{exact}(t) = \frac{1}{2t\sigma_k} ln \left| \frac{y_0 t(\bar{k}+\sigma_k)+1}{y_0 t(\bar{k}-\sigma_k)+1} \right| \tag{4.7}$$

$$\sigma^2_{exact}(t) = \frac{y_0^2}{(1+y_0\bar{k}t)^2 + (y_0\sigma_k t)^2} - \frac{1}{4t^2\sigma_k^2} \left(ln \left| \frac{y_0 t(\bar{k}+\sigma_k)+1}{y_0 t(\bar{k}-\sigma_k)+1} \right| \right)^2. \tag{4.8}$$

Consider the case where $\bar{k} = 2$, $\sigma_k = 2$ and $t \in [0,5]$. Figure 4-4 displays the first and second moments, which still approach their steady-state values with an exponential decay.

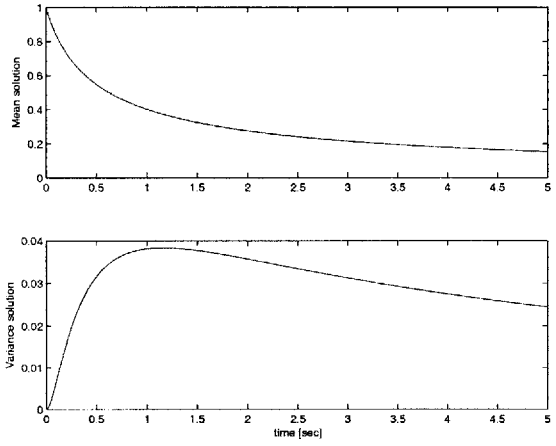

Figure 4-4: The exact mean (top) and variance (bottom) solutions of $\dot{y} = -ky^2$.

Similarly, we examine the p- and Nc-convergence of the gPC with $p = [1,2,3,4,5]$ and the PCM with $Nc = [2,3,4,5,6]$ respectively, as shown in Figure 4-5. The con-

vergence rates are still exponential in the order of $O(e^{-p})$ for the gPC and $O(e^{-(Nc-1)})$ for the PCM, but they decrease by a factor of 5 comparing to those of the linear system. Again, the $Nc = p + 1$ relationship between gPC and PCM in terms of the convergence accuracy still holds for this case.

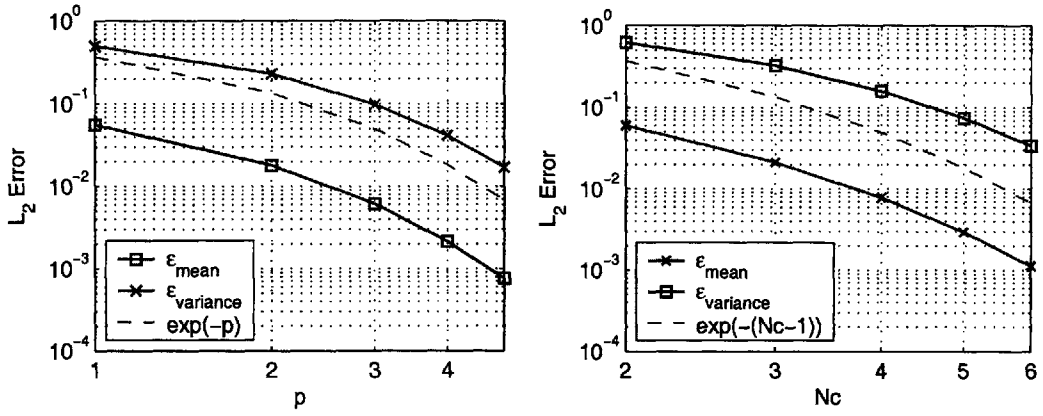

Figure 4-5: The L_2 error convergence of mean and variance solutions as a function p for the gPC(left) and Nc for the PCM (right) for $\dot{y} = -ky^2$.

For the N-convergence, the statistics are calculated numerically from MEgPC with $p = [1, 2, 3]$ and MEPCM with $Nc = [2, 3, 4]$. Notice that the L_2 norm error of mean and variance does not linearly decrease as in the previous case. The error convergence can be characterized into two regimes: the non-asymptotic and asymptotic ranges. In the asymptotic or linear range, the convergence rates of MEgPC and MEPCM are still approximated by $O(N^{-2(p+1)})$ and $O(N^{-2(Nc)})$, respectively, as shown in Figure 4-6. Again, for the same level of accuracy, Figure 4-6 also confirms that the $Nc = p + 1$ relation holds.

4.1.3 Cubic nonlinear first-order SDE

To confirm a generality of the convergence characteristics of this multi-element technique for the nonlinear system, shown in the previous example, we consider another first-order SDE with a cubic nonlinearity:

$$\frac{dy}{dt} = -ky^3 \qquad \text{with } y\,(t=0) = y_0 \text{ and } t \in [0, T] \tag{4.9}$$

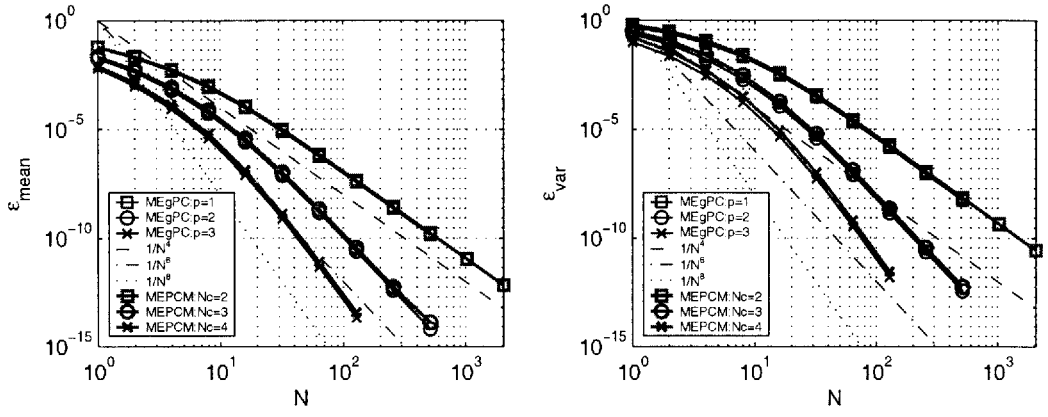

Figure 4-6: The convergence rate of mean (left) and variance (right) errors as a function of number of elements, using MEPCM (thick line) and MEgPC (thin line), for $\dot{y} = -ky^2$.

Likewise, the coefficient, k, of SDE is assumed to be a random variable, corresponding to the uniform distribution $U[-1, 1]$. The deterministic solution is given by $y = \frac{y_0}{(2y_0^2kt+1)^{1/2}}$. Furthermore, exact mean and variance solutions can be derived as the following:

$$\bar{y}_{exact}(t) = \frac{1}{2y_0\sigma_k t}\left(\left(2y_0^2t(\bar{k}+\sigma_k)+1\right)^{1/2} - \left(2y_0^2t(\bar{k}-\sigma_k)+1\right)^{1/2}\right), \quad (4.10)$$

$$(4.11)$$

$$\sigma^2_{exact}(t) = \frac{1}{4\sigma_k t} ln\left|\frac{2y_0^2t(\bar{k}+\sigma_k)+1}{2y_0^2t(\bar{k}-\sigma_k)+1}\right| - \frac{1}{4y_0^2t^2\sigma_k^2}\left(\left(2y_0^2t(\bar{k}+\sigma_k)+1\right)^{1/2} - \left(2y_0^2t(\bar{k}-\sigma_k)+1\right)^{1/2}\right). \quad (4.12)$$

The convergence of the L_2 norm error is considered for a case with $\bar{k} = 2$ and $\sigma_k = 2$ within a time interval [0,5]. Using only MEPCM with $Nc = [2, 3, 4]$, Figure 4-7 shows the same convergence characteristic with a convergence rate of $O(N^{-2Nc})$ in the asymptotic range.

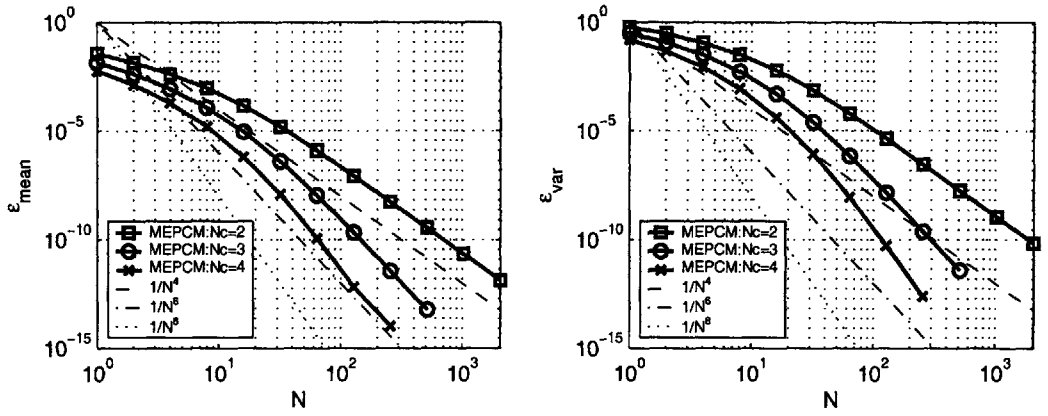

Figure 4-7: The convergence rates of mean (left) and variance (right) errors as a function of number of elements, using MEPCM, for $\dot{y} = -ky^3$.

4.1.4 Quartic nonlinear first-order SDE

If we increase a nonlinearity to the fourth-order polynomial, the convergence characteristic and rate of the multi-element technique must be shown not to depend on the order of the nonlinearity. Thus, let us consider the fourth-order polynomial nonlinearity, expressed in the equation below, with a random variable coefficient, k.

$$\frac{dy}{dt} = -ky^4, \qquad \text{with } y\,(t=0) = y_0 \text{ and } t \in [0,T]\,. \tag{4.13}$$

The deterministic solution is $y = \frac{y_0}{(3y_0^3kt+1)^{1/3}}$. Then, analytical mean and variance solutions can be derived as the following:

$$\bar{y}_{exact}(t) = \frac{1}{4y_0^2\sigma_k t}\left(\left(3y_0^3t(\bar{k}+\sigma_k)+1\right)^{2/3} - \left(3y_0^3t(\bar{k}-\sigma_k)+1\right)^{2/3}\right), \tag{4.14}$$

$$\begin{aligned}\sigma^2_{exact}(t) = {} & \frac{1}{2y_0\sigma_k t}\left(\left(3y_0^3t(\bar{k}+\sigma_k)+1\right)^{1/3} - \left(3y_0^3t(\bar{k}-\sigma_k)+1\right)^{1/3}\right) \\ & - \frac{1}{16y_0^4t^2\sigma_k^2}\left(\left(3y_0^3t(\bar{k}+\sigma_k)+1\right)^{2/3} - \left(3y_0^3t(\bar{k}-\sigma_k)+1\right)^{2/3}\right).\end{aligned} \tag{4.15}$$

Assigning $\bar{k} = 2$ and $\sigma_k = 2$ with $t \in [0,5]$, the MEPCM with $Nc = [2,3,4]$ yields a similar convergence characteristic, which has both non-asymptotic and asymptotic convergence ranges, as in the previous two cases. In the asymptotic range, the convergence rate of MEPCM is approximated in the order of $O(N^{-2Nc})$, as shown in

Figure 4-8. Therefore when the stochastic solution is smooth and continuous, we can expect a similar characteristic and rate of the statistical L_2 error convergence for any higher nonlinear SDE.

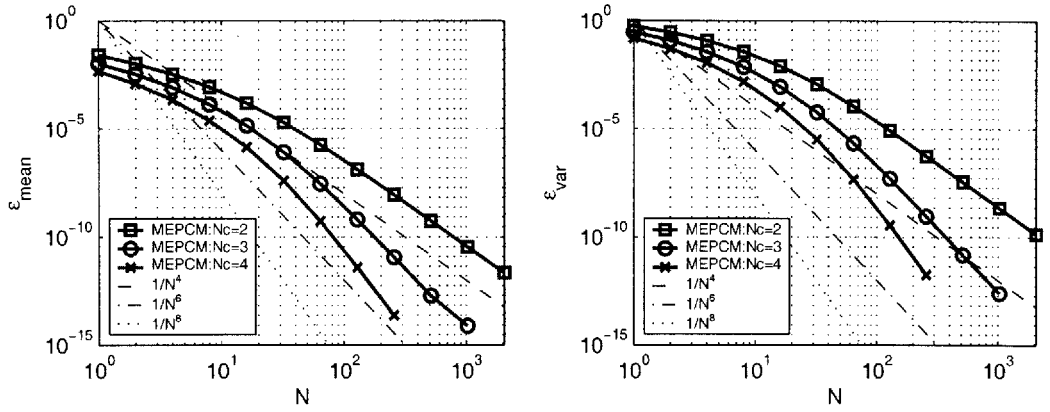

Figure 4-8: The convergence rate of mean (left) and variance (right) errors as a function of number of elements, using MEPCM, for $\dot{y} = -ky^4$.

4.1.5 Trigonometric nonlinear first-order SDE

To demonstrate the effectiveness of the Hybrid gPC+PCM method as well as its combination with the multi-element technique, we examine the SDE with a sine function, given by an equation below:

$$\frac{dy}{dt} = -k \cdot sin(3y), \qquad \text{with } y(t=0) = y_0 \text{ and } t \in [0,T]. \tag{4.16}$$

The decay coefficient, k, again is assumed to be a random variable, associated with the uniform distribution U[-1,1]. $\bar{k} = 2$ and $\sigma_k^2 = 1$. Instead of deriving an exact statistical solutions, we compute the L_2 error convergence using the reference solution, obtained from the PCM with $Nc = 100$. The reference mean and variance solutions are shown in Figure 4-9 below for $t \in [0, 1]$ second.

As shown in Figure 4-10, the Hybrid gPC+PCM exhibits a similar convergence characteristic as that of the PCM. Despite of the trigonometric function, the convergence rates of Hybrid gPC+PCM, extending the gPC capability to handle more general nonlinearity, and PCM are still in the order of $O(e^{-2p})$ and $O(e^{-2(Nc-1)})$,

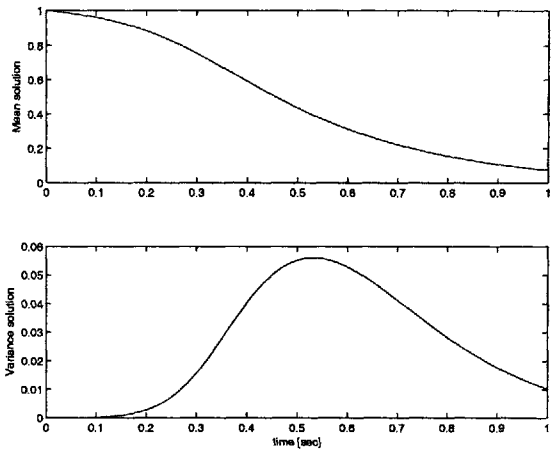

Figure 4-9: The exact mean (top) and variance (bottom) solutions for $\dot{y} = -k \cdot sin(3y)$.

respectively. Again, the suggested relationship of $p = Nc - 1$ between gPC and PCM is shown here to be applicable to the other classes of nonlinearity.

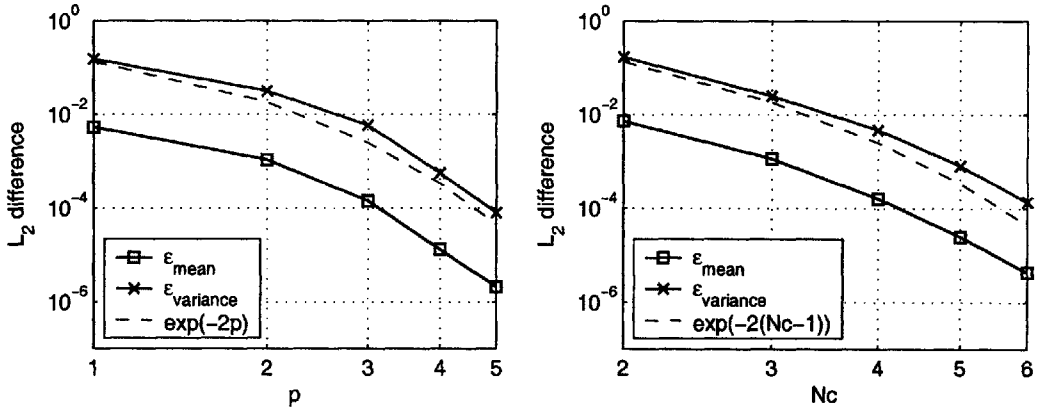

Figure 4-10: The L_2 error convergence of mean and variance solutions as a function p using the Hybrid gPC+PCM (left) and Nc using the PCM (right) for $\dot{y} = -k \cdot sin(3y)$.

Also, the multi-element technique using uniform elements provides an algebraic convergence rate of $O(N^{-2(p+1)})$ for the Hybrid gPC+PCM with $p = [1, 2, 3], Nc = 10$ and of $O(N^{-2Nc})$ for the PCM with $Nc = [2, 3, 4]$, which are the same as the previous four cases. According to Figure 4-11, the asymptotic range is dominate the entire range of the L_2 error convergence in this case.

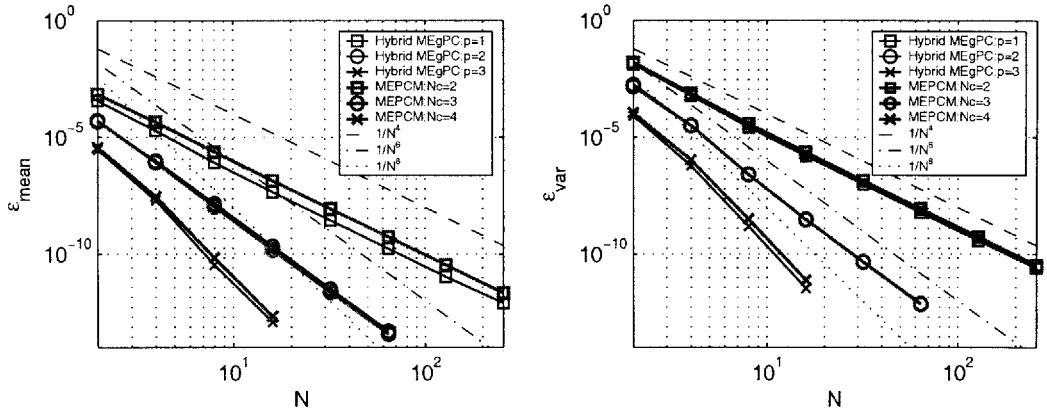

Figure 4-11: The convergence rate of mean (left) and variance (right) errors as a function of number of elements, using Hybrid MEgPC+PCM and MEPCM, for $\dot{y} = -k \cdot sin(3y)$.

4.1.6 Kraichnan-Orszag system in one random dimension

Originally, Orszag and Bissonnette [44] employed the Wiener-Hermite expansion, which is the same as gPC, to study the dynamics of turbulent flow. They considered Burgers' equation, which is a simplification of a one-dimensional Navier-Stokes equation for incompressible flow. To further simplify the problem, they neglect the viscosity term, and thus Burgers' equation is modified to be a three-mode dynamic system, known as the Kraichnan-Orszag three-mode system. Moreover, Orszag and Bissonnette discovered that there exists an instability associated with this three-mode system using Wiener-Hermite expansion, when time approaches infinity. Recently, Wan and Karniadakis [60] have reinvestigated and solved the instability problem corresponding to insufficient numerical accuracy using the gPC alone. Therefore, only instability induced by the system dynamics can be revealed. Also, the analytical solutions of this three-mode problem have been derived for only the case of smooth and continuous stochastic solutions. However, Wan and Karniadakis considered only the case with discontinuous solutions in one, two, and three dimensions due to random initial conditions.

In this section, we introduce the Kraichnan-Orszag three-mode equations, given below, and their dynamical characteristic. The initial conditions can lead to either continuity or discontinuity in stochastic solutions. In the rest of this chapter, we spec-

ify initial conditions for continuous cases in one, two, and three random dimensions, but the initial conditions that lead to discontinuous solutions are obtained from Wan and Karniadakis. Also, we formulate the convergence rate, corresponding to the characteristic of solutions–continuous vs. discontinuous–as well as the random dimension. The integration time step of the 4-order Runge-Kutta method, associated with the Kraichnan-Orszag system, is set to be 10^{-3}.

$$\frac{dy_1}{dt} = y_1 y_3 \tag{4.17}$$

$$\frac{dy_2}{dt} = -y_2 y_3 \tag{4.18}$$

$$\frac{dy_3}{dt} = -y_1^2 + y_2^2, \tag{4.19}$$

where y_i represents an i mode. This has been shown to have a discontinuity in the solution on the $y_1 = 0$ and $y_2 = 0$ planes by [60]. Depending on the initial condition, the deterministic solutions can be separated into eight different groups (g1 to g8) as seen in Figure 4-12. When the initial condition becomes random, the stochastic solution can be either continuous or discontinuous.

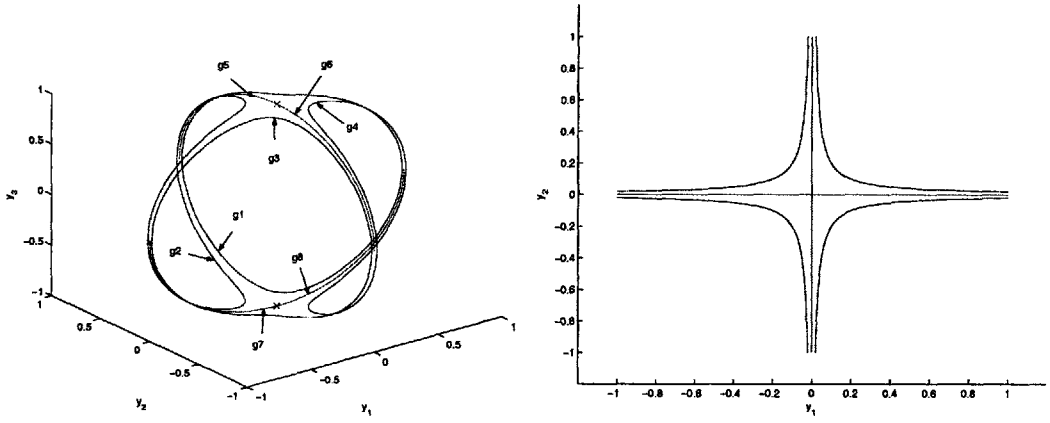

Figure 4-12: The phase portrait of eight group deterministic solutions of the Kraichnan-Orszag system, obtained from different initial conditions, in three dimension (left) and two dimension (right) on the y1-y2 plane.

Let us consider the case where the deterministic solution is sensitive to a small change in the initial condition of y_2 around zero, when $[y_1, y_3]$ are kept fixed at $[1, 0]$.

Figure 4-13 shows how the discontinuity exists in the solution for $y_2(0) > 0$, $y_2(0) = 0$, and $y_2(0) < 0$. Moreover, the oscillating frequency of the deterministic solution varies with random y_2 initial condition that has the same sign. As a result, the variance solution of this case grows with time, as shown in Section 4.2.2.

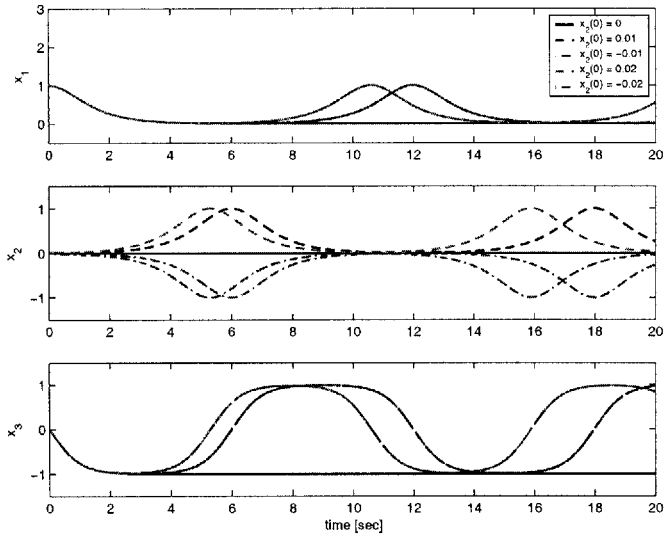

Figure 4-13: Various deterministic solutions of the Kraichnan-Orszag three modes for small change in the y_2 initial condition around zero.

First, let us consider the case where the statistical solution is continuous and subjected to one random initial condition. The random initial condition, $[y_1(0,\xi), y_2(0,\xi), y_3(0,\xi)]$, is set as $[\sqrt{2}/4, \sqrt{2}/4, \xi(\omega)]$, where $\xi \in U[-1,1]$. The stochastic mean and variance solutions, shown in Figure 4-14, are underdamped with a time constant of 2.5 seconds and approach the steady-state within about 40 seconds.

For $t \in [0,30]$, we compare the convergence rate among 1) MC and QMC with $NN = [1,000, \cdot, 100,000]$, 2) the single element PCM with $Nc = [2, \cdot, 400]$, and 3) the uniformly fixed elements of MEPCM with $Nc = 5$ and $N = [2, \cdot, 256]$. Instead of formulating the analytical solution to compute the L_2 norm error, the reference solution is numerically calculated from the MEPCM with $Nc = 5$ and $N = 2048$. The computational time of reference solution is 383.687 seconds. As mentioned previously, the convergence rates of MC and QMC are in the order of $O(NN^{-1/2})$ and $O(NN^{-1})$, respectively, as shown in Figure 4-15. Even though, for the NN-convergence, the random number of MC and QMC in a coarse level with low value of NN are reused in

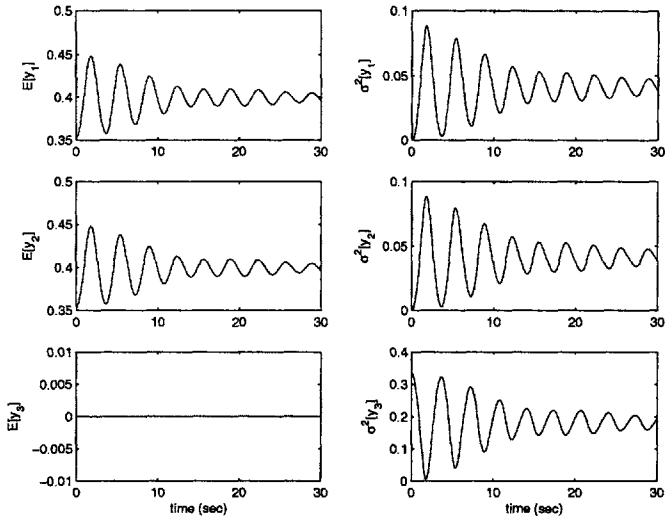

Figure 4-14: The stochastic mean and variance solutions of three mode from the reference solution when $[y_1(0,\xi), y_2(0,\xi), y_3(0,\xi)] = [\sqrt{2}/4, \sqrt{2}/4, \xi(\omega)]$.

a more refined level with a larger value of NN, the statistical error does not converge smoothly.

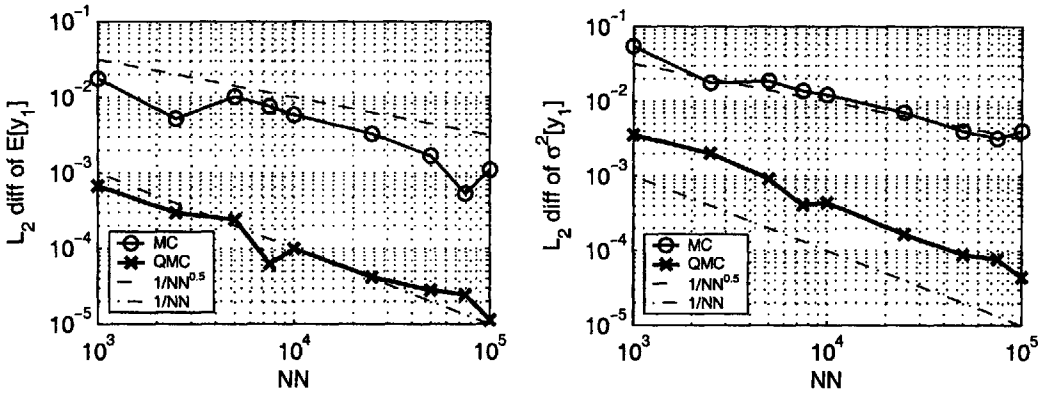

Figure 4-15: The L_2 norm error of mean (left) and variance (right) solutions as a function of NN exhibit the algebraic convergence rate of $O(NN^{-1/2})$ using MC and of $O(NN^{-1})$ using QMC.

Figure 4-16 shows that a convergence rate of PCM, as a function of Nc, decreases exponentially, which can be approximated by $O(e^{-0.3*Nc})$ and a comparison on the computational cost for a given accuracy. The computational efficiency of the single-element PCM surpasses those of the other algorithms when the solutions are smooth and continuous. Especially, the computational time of PCM is three orders of mag-

nitude smaller than that of MC at low accuracy range.

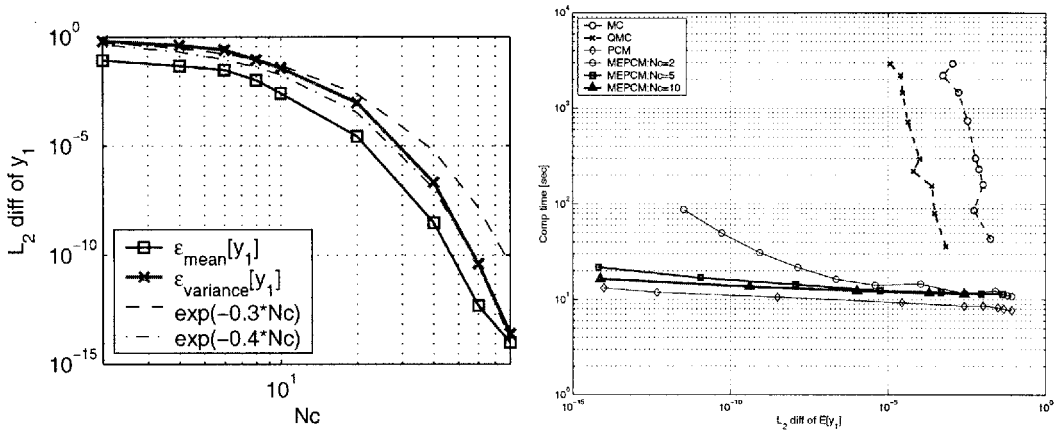

Figure 4-16: The Nc-convergence of mean and variance solutions using PCM (left) and the computational time of MC, QMC, PCM, MEPCM with fixed element (right).

The convergence rate of MEPCM as a function of N again contains both non-asymptotic (nonlinear) and asymptotic (linear) ranges. In the linear range, MEPCM provides the convergence rate of $O(N^{-2Nc})$, as seen in Figure 4-17. The cost to perform MEPCM is not much different when Nc is above 5. Due to the high accuracy of the Nc-convergence of PCM, increasing Nc can further improve the solutions' accuracy more than increasing N in this case.

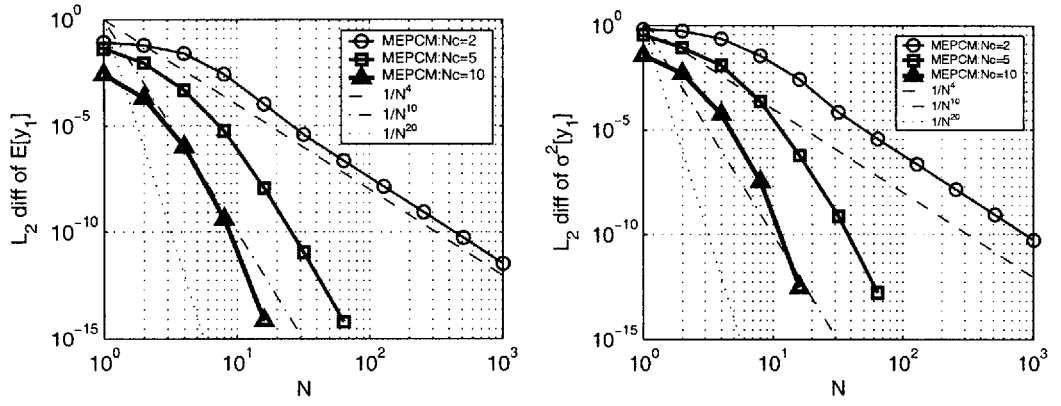

Figure 4-17: The L_2 norm error of mean (left) and variance (right) solutions as a function of N exhibit the algebraic convergence rate of $O(N^{-4})$ using MEPCM with $Nc = 2$, $O(N^{-10})$ using MEPCM with $Nc = 5$, and $O(NN^{-20})$ using MEPCM with $Nc = 10$.

4.1.7 Kraichnan-Orszag system in two random dimensions

When the random dimension in the initial condition increases to two, we will show an effect of increasing random dimension on the convergence rate of these stochastic algorithms. To guarantee smooth statistical solutions, the two-dimensional random initial condition is assigned as $[\sqrt{2}/4, \sqrt{2}/4 + 0.1\xi_1(\omega), \xi_2(\omega)]$ such that the deterministic solution is always contained within the g1 group. Therefore, we obtain smooth stochastic solutions without any discontinuity, as shown in Figure 4-18.

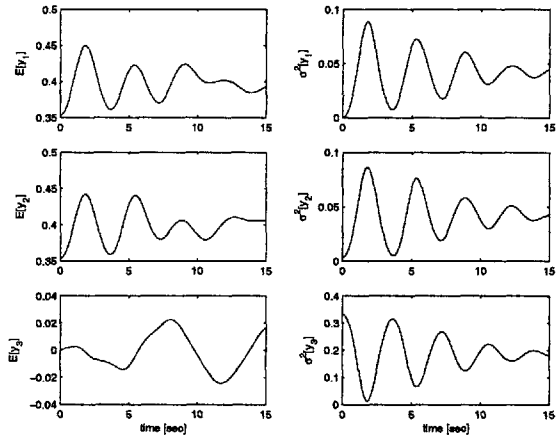

Figure 4-18: The stochastic mean and variance solutions of three modes from the reference solution when $[y_1(0,\xi), y_2(0,\xi), y_3(0,\xi)] = [\sqrt{2}/4, \sqrt{2}/4 + 0.1\xi_1(\omega), \xi_2(\omega)]$.

Again, the accuracy and computational time are compared among four algorithms: 1) MC and QMC, 2) PCM, 3) MEPCM with $Nc = [2, 5, 10]$, and 4) MEgPC with $p = [1, 4]$. The result from MEPCM with Nc=10 and N=900 is used for a reference solution. We can see from Figure 4-19 that the convergence rate of the Monte Carlo method, which is still slow in the order of $O(NN^{-1/2})$ for MC and $O(NN^{-1})$ for QMC, is not affected by increasing random dimension because an implementation of computing statistics in the Monte Carlo method, which acts like a low-pass filter, does not depend on the random dimension.

On the other hand, the computation of statistics in PCM and MEPCM requires an additional summation for each random dimension, resulting in higher computational cost for a larger random dimension. Despite the additional cost, the Gauss-quadrature provides fast convergence of an approximation of solution as we increase Nc. As shown

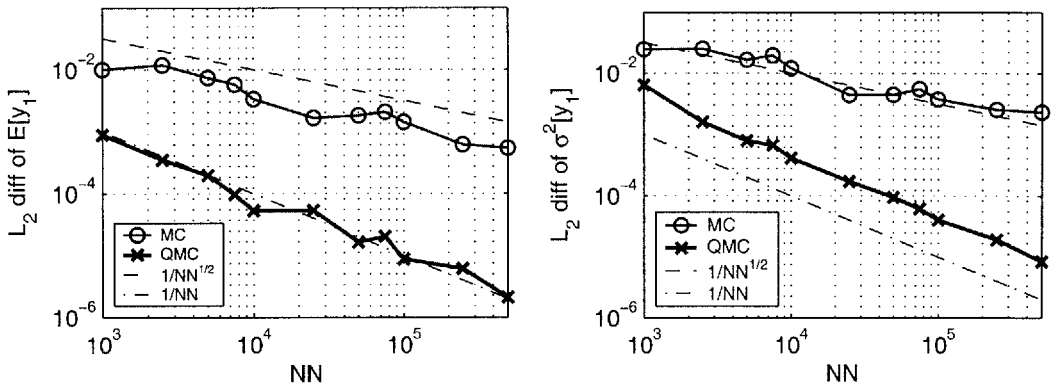

Figure 4-19: The L_2 norm error of mean (left) and variance (right) solutions as a function of NN exhibit the algebraic convergence rate of $O(NN^{-1/2})$ using MC and of $O(NN^{-1})$ using QMC.

in Figure 4-20, the PCM yields the exponential convergence rate of $O(e^{-0.3(Nc/d)})$, where Nc/d denotes the number of collocation points per random dimension. This convergence rate of PCM is the same order as in the one-dimensional case, when Nc is normalized by d random dimension.

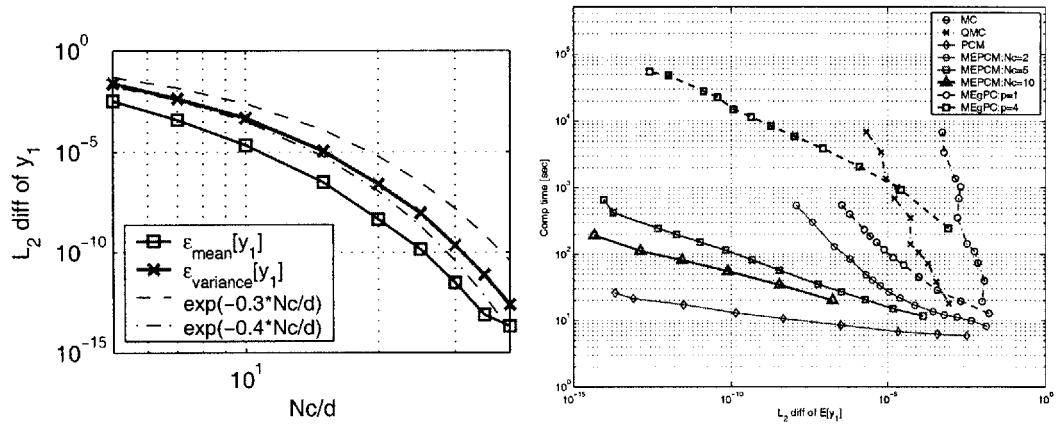

Figure 4-20: The Nc-convergence of mean and variance solutions using PCM (left) and the computational time of MC, QMC, PCM, MEPCM with fixed element (right).

Likewise, the convergence rate of MEPCM can be classified into non-asymptotic and asymptotic regimes. Here, we focus on formulating an empirical convergence relation for the linear range, since the convergence rate of the nonlinear range is much slower. Using the MEPCM with $Nc = [2, 5, 10]$, the convergence rate can be expressed in terms of either total Nc in two dimension (in Figure 4-23) or Nc/d (in

Figure 4-21 and 4-22). The convergence rate of MEPCM can be approximated by $(N/d)^{-2Nc}$. When we use the total Nc and the Nc/d, the convergence rates are in the order of $O(N^{-Nc})$ and $O((N/d)^{-2Nc})$, respectively. The accuracy of y_1 statistics using MEPCM with $Nc = [5, 10]$ approaches the machine precision too fast before reaching the asymptotic range. Hence, the statistical results for the third mode (y_3), shown in Figure 4-22, confirmed the convergence relation as in y_1 results.

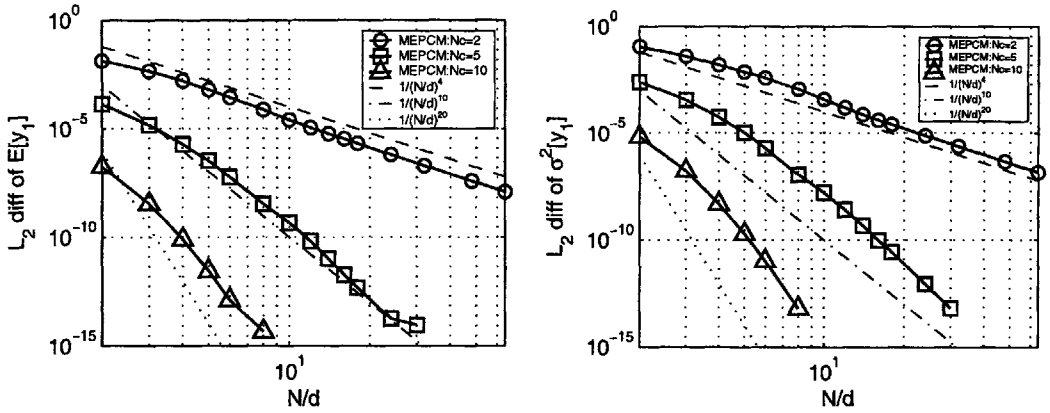

Figure 4-21: The L_2 norm error of y_1 mean (left) and variance (right) solutions as a function of total N exhibit the algebraic convergence rate of $O(N^{-4})$ for $Nc = 2$, $O(N^{-10})$ for $Nc = 5$, and $O(N^{-20})$ for $Nc = 10$, using MEPCM.

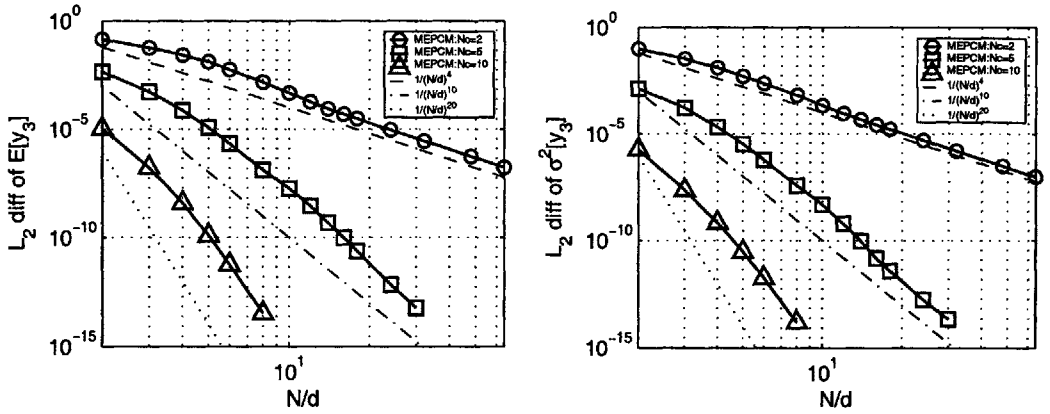

Figure 4-22: The L_2 norm error of y_3 mean (left) and variance (right) solutions as a function of total N exhibit the algebraic convergence rate of $O(N^{-4})$ for $Nc = 2$, $O(N^{-10})$ for $Nc = 5$, and $O(N^{-20})$ for $Nc = 10$, using MEPCM.

Similarly, this per dimension convergence rate is also applicable to the MEgPC. Figure 4-24 displays how the mean and variance errors converge as a function of

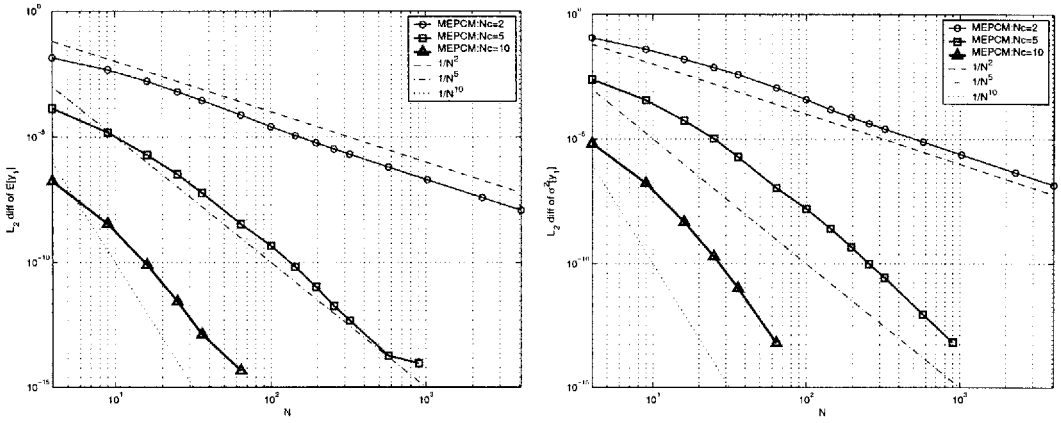

Figure 4-23: The L_2 norm error of y_1 mean (left) and variance (right) solutions as a function of total N exhibit the algebraic convergence rate of $O(N^{-2})$ for $Nc = 2$, $O(N^{-5})$ for $Nc = 5$, and $O(N^{-10})$ for $Nc = 10$ using MEPCM.

N/d. The empirical convergence rate of MEgPC can be expressed as $O((N/d)^{-2(p+1)})$. Even though the accuracy of MEgPC is a bit lower than that of MEPCM, the error convergence of MEgPC approaches the aymptotic range within a few N/d. In a later section, only the N/d convergence results are considered in the discussion. In terms of the computational efficiency, the PCM and MC are consequently the best and worst approaches for the problem with continuous solutions in two random dimensions. The slope of the computational cost vs. ϵ_{mean} of PCM and MEPCM in two dimensions is larger than those in one dimension, shown in Section 4.1.6. Nevertheless, the MEPCM with higher Nc and using only few elements can further decrease the computation-time slope. This shows the advantage of Nc- and N- convergences of MEPCM.

4.1.8 Kraichnan-Orszag system in three random dimensions

Let us look at how the convergence relation and efficiency of each algorithm scale up with the random dimension in the case when the random initial conditions of the Kraichnan-Orszag system become three dimensions. We consider the case with smooth and continuous solutions by assigning the following random initial condition: $[y_1(0,\xi),y_2(0,\xi),y_3(0,\xi)] = [\sqrt{2}/4 + 0.1\xi_1(\omega),\sqrt{2}/4 + 0.1\xi_2(\omega),\xi_3(\omega)]$. Similar to Section 4.1.7, the deterministic solution is in the g1 group. The stochastic responses of all three modes, shown in Figure 4-25, are underdamped. All statistics approach

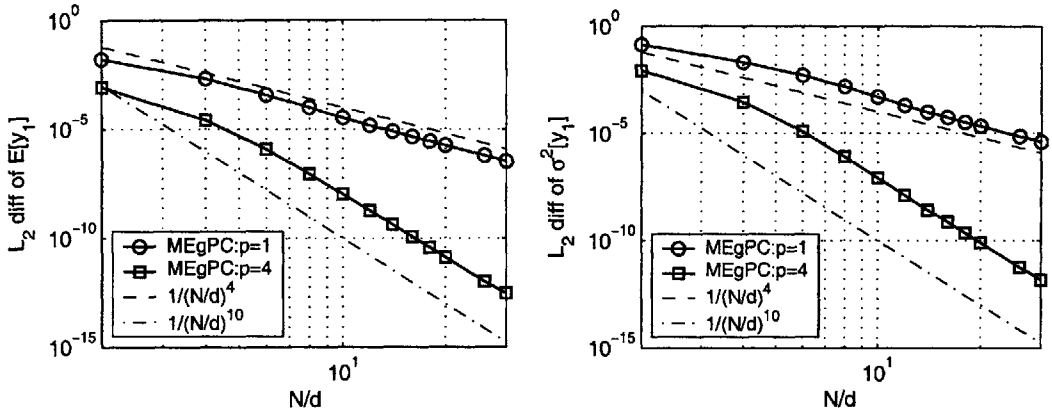

Figure 4-24: The L_2 norm error of y_1 mean (left) and variance (right) solutions as a function of total N exhibit the algebraic convergence rate of $O(N^{-2})$ for $p = 1$ and $O(N^{-10})$ for $p = 4$, using MEgPC.

their steady-state values in about 20 seconds. The range of integral time is between 0 and 15 seconds.

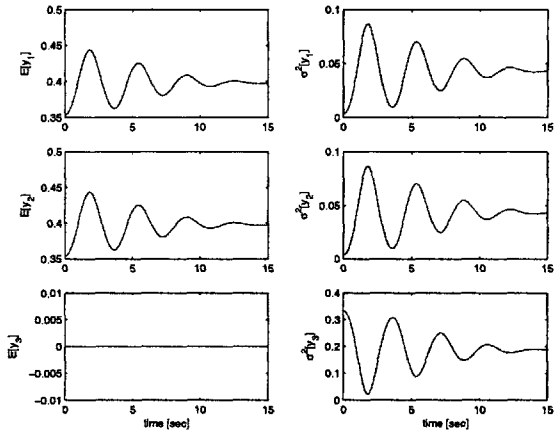

Figure 4-25: The stochastic mean and variance solutions of three modes from the reference solution when $[y_1(0,\xi), y_2(0,\xi), y_3(0,\xi)] = [\sqrt{2}/4 + 0.1\xi_1(\omega), \sqrt{2}/4 + 0.1\xi_2(\omega), \xi_3(\omega)]$.

We investigate the relationship of the convergence rate and computational cost as a function of the random dimension among five stochastic algorithms: 1) MC and QMC, 2) full-grid PCM, 3) full-grid MEPCM with $Nc = [2, 5, 10]$, 4) sparse-grid PCM, and 5) sparse-grid MEPCM with $Nc = 5$. Owing to the inefficiency of MEgPC, it is not included in this section. We address both issues of the sparseness of nodal points and multi-element technique, particularly for the long-time integration. A

reference solution is numerically computed from PCM with $Nc/d = 80$. As shown in Figure 4-26, the MC and QMC convergence rates are still in the order of $O(NN^{-1/2})$ and $O(NN^{-1})$, respectively, and the accuracy of both methods is closely matched with that in Section 4.1.6 and 4.1.7. Hence, we can conclude that the convergence rate of the Monte Carlo method does not depend on the random dimension.

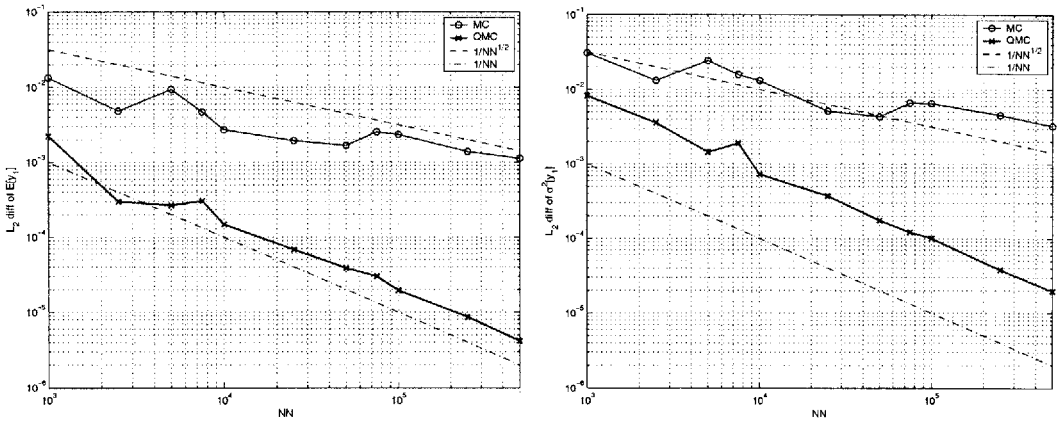

Figure 4-26: The L_2 norm error of mean (left) and variance (right) solutions as a function of NN exhibits the algebraic convergence rate of $O(NN^{-1/2})$ using MC and of $O(NN^{-1})$ using QMC.

The Nc-convergence of the full-grid PCM, described as a function number of Nc/d, is also insensitive to an increase of random dimension, as shown in Figure 4-27. Moreover, the L_2 error convergence per dimension of the sparse-grid PCM, shown in Figure 4-27, exhibits an exponential rate as well. Both full- and sparse-grid PCMs yield exponential convergence rates, which are faster than $O(e^{-0.4*(Nc/d)})$. The sparse-grid PCM has not been considered until now because its computing cost is larger than that of the full-grid PCM in a low-dimension problem.

Likewise, the convergence rate of uniform MEPCM can be classified into non-asymptotic and asymptotic regimes. Again, an empirical convergence relation for the linear range is our main interest. Using the full-grid MEPCM with $Nc = [2, 5, 10]$, the convergence rate can be expressed in terms of Nc/d in Figure 4-28. The convergence rate of MEPCM is in the order of $O(N^{-2*(Nc/d)})$. The accuracy of y_1 statistics using the full-grid MEPCM with $Nc = 10$ approaches the machine precision very quickly before reaching the asymptotic range. The $E[y_1]$ error convergence of the sparse-grid

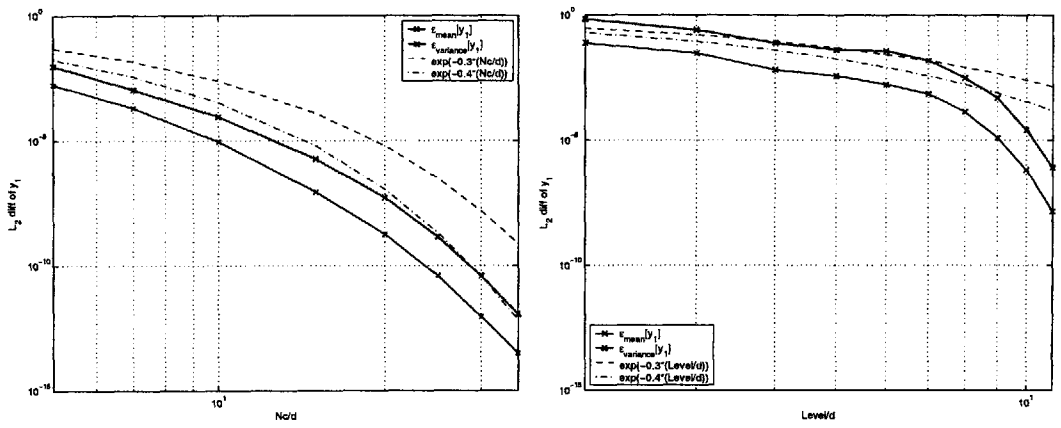

Figure 4-27: The Nc-convergence of mean and variance solutions using Full-grid PCM (left) and using Sparse-grid PCM (right).

MEPCM with $Level = 5$ as a function of N/d decreases faster than that of the full-grid MEPCM with $Nc = 5$ because of two reasons: there are more collocation points in the sparse-grid PCM than in the full-grid PCM for $Level = Nc$ in three-dimensional random dimensions and there are multiple elements of sparse structure.

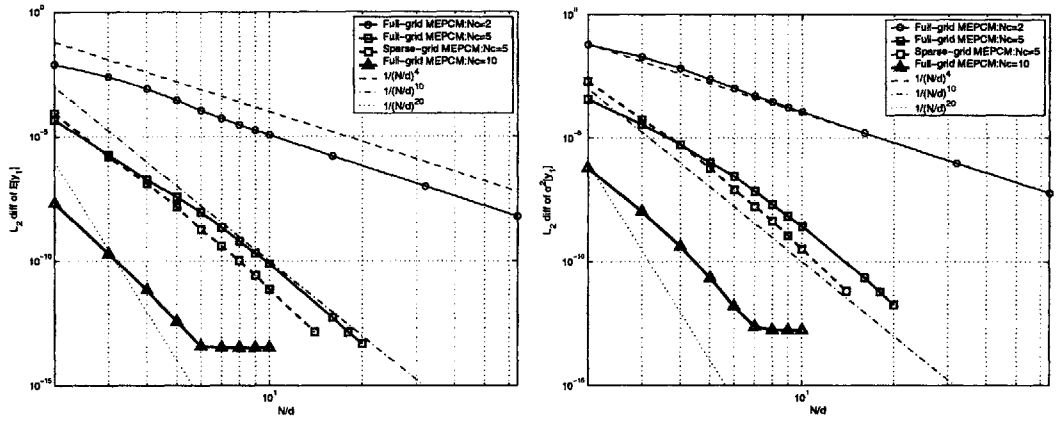

Figure 4-28: The L_2 error convergence of y_1 mean (left) and variance (right) solutions as a function of total N exhibit the algebraic convergence rate of $O(N^{-4})$ for $Nc = 2$, $O(N^{-10})$ for $Nc = 5$ and $O(N^{-20})$ for $Nc = 10$, using full- and sparse-grid MEPCM.

Even though the convergence rate per dimension of the full-grid PCM stays constant, its computation time grows with a cubic power of Nc in three random dimensions. For the full-grid MEPCM with uniform distributed elements, the cost per accuracy is always greater than that of the full-grid PCM, as shown in Figure 4-29. As we mentioned in the previous chapter, the computing cost of the sparse-grid PCM

increases even faster than Nc^d in the small random dimension as we increase the level, and therefore a slope of the cost per accuracy curve is much larger. Notice that the multi-element technique can improve the accuracy of the sparse-grid PCM with cost significantly less than the level refinement alone. Again, the full-grid PCM provides us the most effective algorithm in terms of the cost per accuracy, when the stochastic solutions are continuous and smooth.

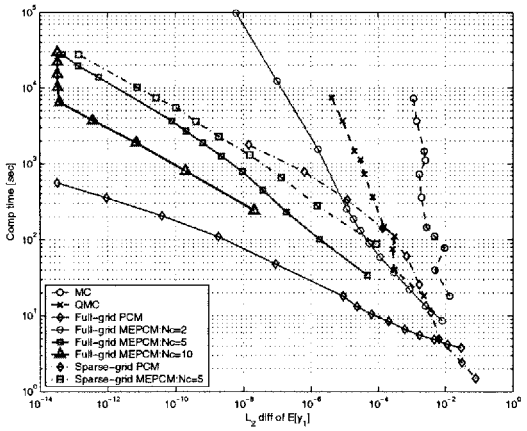

Figure 4-29: The computational time vs. $E[y_1]$ accuracy of MC, QMC, Full-grid PCM, Full-grid uniform-MEPCM, Sparse-grid PCM, and Sparse-grid uniform-MEPCM.

Results for a long-time integration

When the integral time, $t \in [0, T_f]$, is extended to $T_f = 50$ and $T_f = 100$ seconds, we would like to examine an effect of the long-time integration on the performance of these stochastic algorithms. Furthermore, we want to examine how both the multi-element technique and sparse structure of collocation points influence on the solution accuracy and computational efficiency. For the same random initial conditions as in Section 4.1.8, the mean and variance solutions of the reference solution, PCM with $Nc/d = 80$, are displayed in Figure 4-30.

The performance of quasi-Monte Carlo deteriorates for a long-time integration as shown in Figure 4-32. The error convergence curves shift upward for $T_f = 50$ and $T_f = 100$ seconds due to a propagation of numerical-integration error at an initial time step, which leads to a large accumulating error at a later time, as shown in

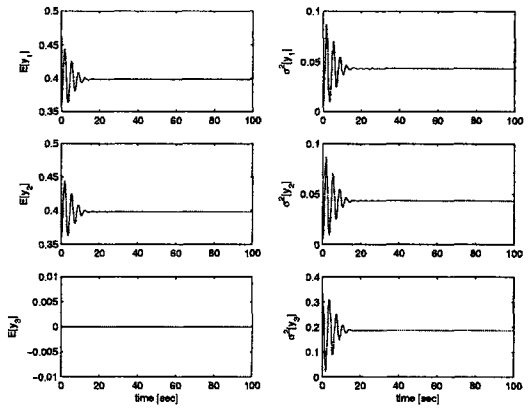

Figure 4-30: The stochastic mean and variance solutions of three modes from the reference solution when $[y_1(0,\xi),y_2(0,\xi),y_3(0,\xi)] = [\sqrt{2}/4+0.1\xi_1(\omega),\sqrt{2}/4+0.1\xi_2(\omega),\xi_3(\omega)]$.

Figure 4-31. After 50 seconds, the statistical responses already reach their steady-state values,; therefore, an effect of accumulating error in each algorithm can be easily distinguished. According to Figure 4-31, this error can be reduced by increasing the number of realizations; however the Monte Carlo method converges linearly with the rate of $O(NN^{-1})$. Thus, a large value of NN is required to obtain accurate stochastic solutions.

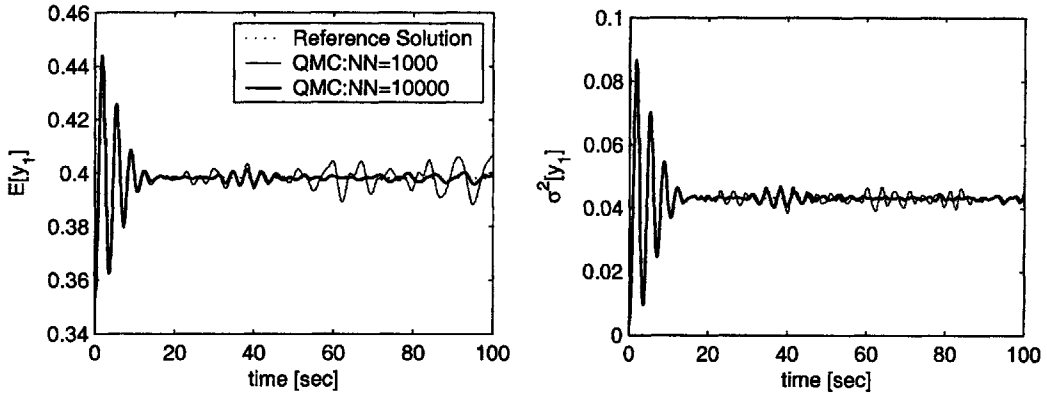

Figure 4-31: The stochastic mean (left) and variance (right) solutions of three modes from the reference solution, QMC with $NN = 1000$, and QMC with $NN = 1000$.

For both full- and sparse-grid PCMs, the statistical accuracy, particularly in the high-accuracy region, get worse very quickly as the final integration increases. The convergence results of the full-grid PCM, shown in Figure 4-33, and of the sparse-grid PCM, shown in Figure 4-34, respectively lose about 6 and 5 orders of magnitude in

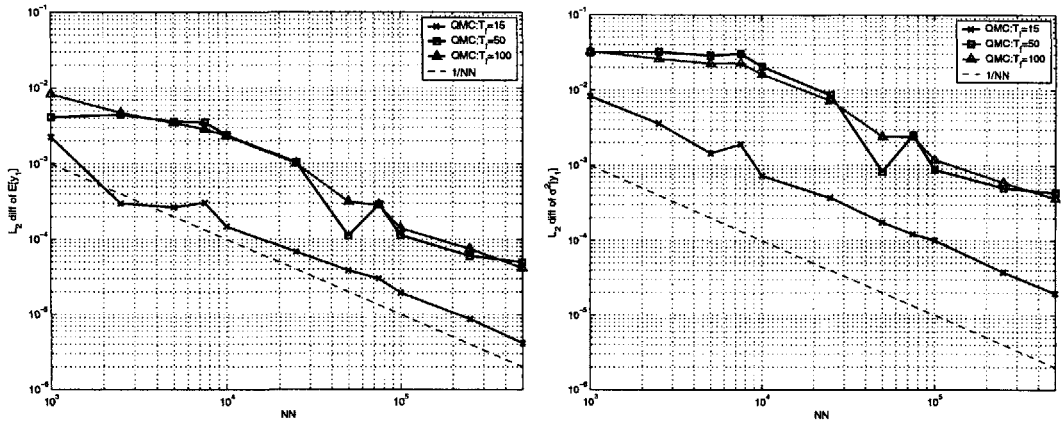

Figure 4-32: The L_2 error convergence of mean (left) and variance (right) solutions as a function of NN and T_f using QMC.

the mean accuracy when T_f increases from 15 to 100 seconds. The full-grid PCM again yields a faster error convergence than the sparse-grid PCM. Both collocation methods are not robust against a problem of the long-time integration because the accumulating error, contributed by each Nc deterministic run, propagates very quickly in time.

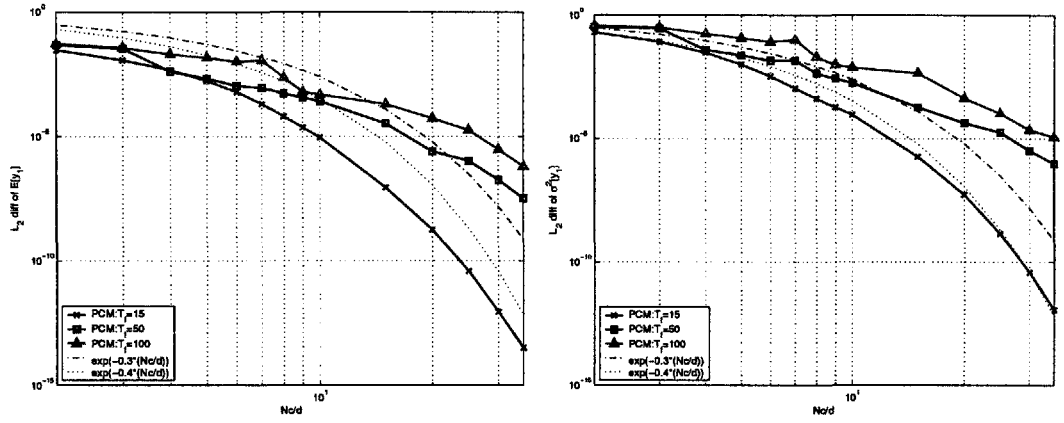

Figure 4-33: The Nc-convergence of mean (left) and variance (right) solutions using Full-grid PCM as T_f increases.

To lessen the effect of accumulating error especially for the sparse-grid PCM, the multi-element technique can be combined with both collocation methods. According to Figure 4-36, the full-grid MEPCM with $Nc/d = 2$ exhibits an insensitivity to increasing T_f, while the others with larger Nc/d get worse as T_f increases. With

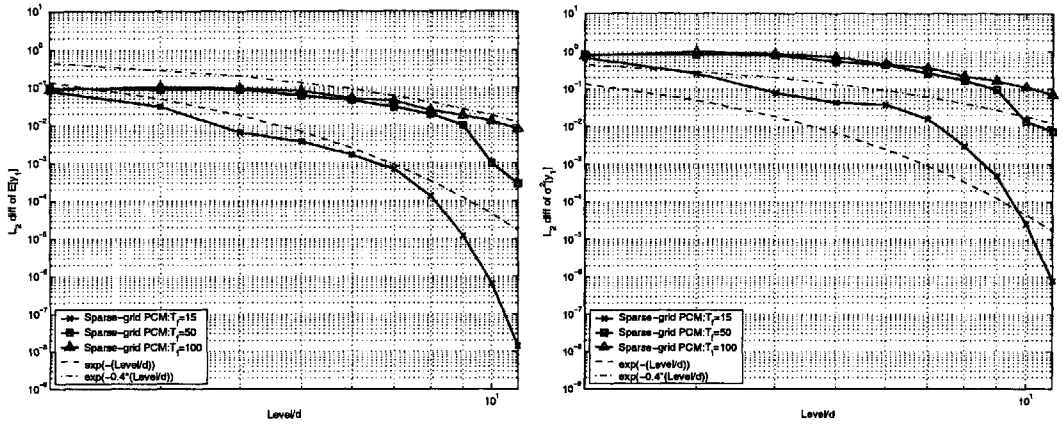

Figure 4-34: The Level-convergence of mean (left) and variance (right) solutions using Sparse-grid PCM as T_f increases.

the smallest $Nc/d = 2$, the Nc-convergence of the full-grid PCM does not contribute a lot of error in the long-time integration when it combines with the multi-element technique; therefore, the error convergence of the full-grid uniform MEPCM with $Nc/d = 2$ does not change much for $T_f = 15$ or 50 seconds. When T_f is prolonged, the former empirical formula for the convergence rate of the full-grid uniform MEPCM is no long satisfied. The convergence rate of the full-grid uniform MEPCM becomes more flatter as the accumulating error dominates in the steady-state regime.

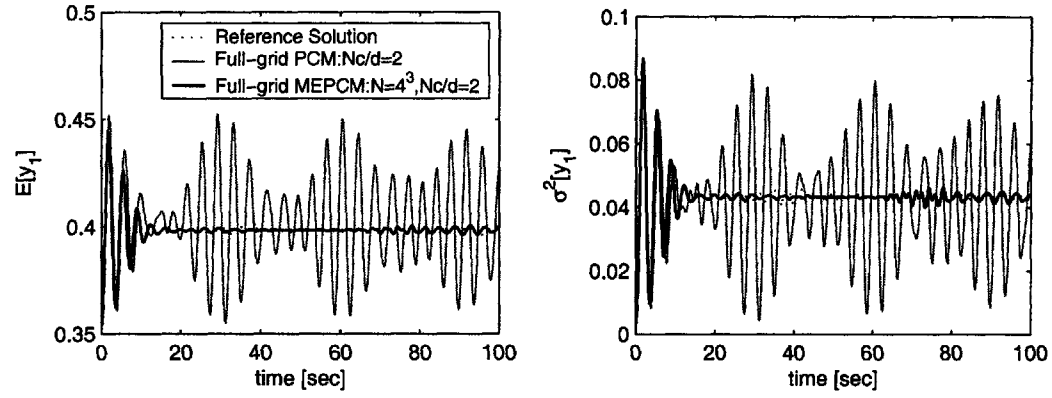

Figure 4-35: The stochastic mean (left) and variance (right) solutions of three modes from the reference solution, full-grid PCM with $Nc/d = 2$, and full-grid uniform MEPCM with $N = 4^3, Nc/d = 2$.

Similarly, the multi-element technique can help improve the accuracy of the sparse-grid PCM. Figure 4-37 shows that even though the multi-element technique can reduce

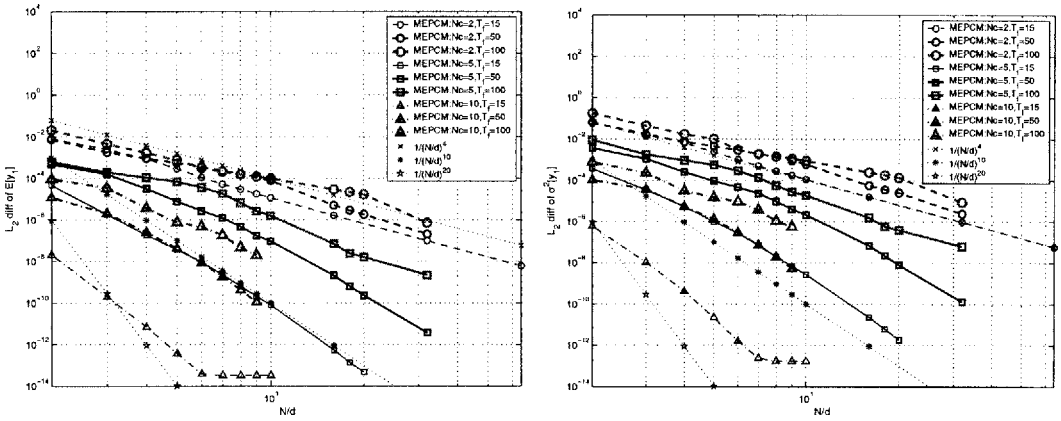

Figure 4-36: The L_2 error convergence of y_1 mean (left) and variance (right) solutions as a function of total N exhibits the algebraic convergence rates of $O(N^{-4})$ for $Nc/d = 2$, $O(N^{-10})$ for $Nc/d = 5$ and $O(N^{-20})$ for $Nc/d = 10$, using full-grid uniform MEPCM.

the L_2 norm statistical error of the sparse-grid uniform MEPCM with $Level/d = 5$, the full-grid uniform MEPCM with $Nc/d = 5$ can better maintain the solution accuracy better than the sparse-grid uniform MEPCM with $Level/d = 5$ in the case of continuous solutions, as T_f increases.

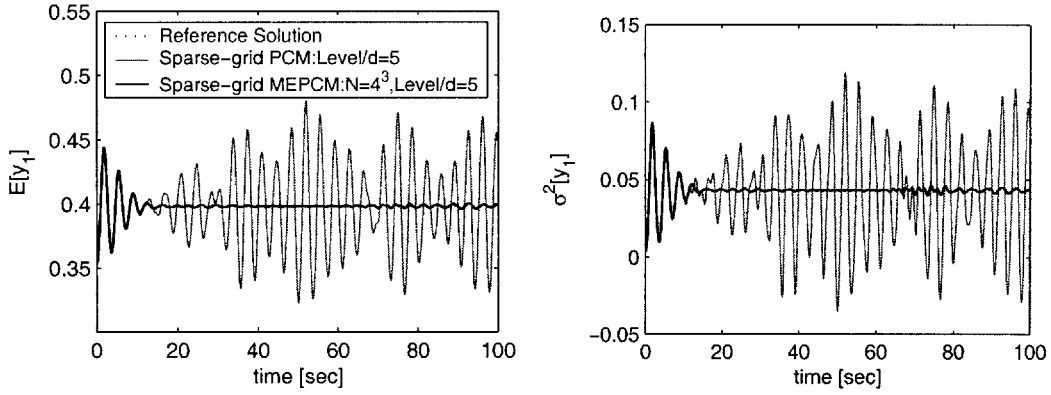

Figure 4-37: The stochastic mean (left) and variance (right) solutions of three modes from the reference solution, sparse-grid PCM with $Level/d = 5$, and sparse-grid MEPCM with $N = 4^3, Level/d = 5$.

In terms of the computing cost per accuracy, the full-grid PCM is still the best algorithm, as shown in Figure 4-39. Notice that the curves of the full-grid uniform MEPCM collapse into the same curve for $T_f = 100$ seconds, since the computational cost increases faster than the solution accuracy decreases. As a result, the h-type

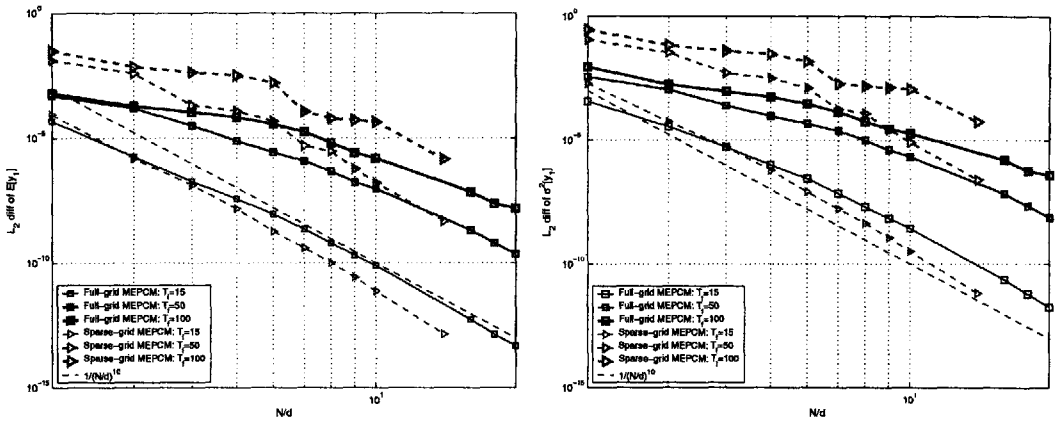

Figure 4-38: Comparison between the full-grid MEPCM with $Nc/d = 5$ and the sparse-grid MEPCM with $Level/d = 5$ on the L_2 error convergence of y_1 mean (left) and variance (right) solutions as a function of total N exhibits the algebraic convergence rate.

refinement totally dominates the Nc-type refinement of the full-grid PCM. According to Figure 4-39, the cost per accuracy of the sparse-grid PCM is larger than that of QMC; nevertheless, the multi-element technique can significantly improve the sparse-grid PCM, as seen from the much smaller slope of the sparse-grid uniform MEPCM. In Section 4.4, when the random dimension and system equations are very large, the computing cost per accuracy of the sparse-grid PCM will be much cheaper than those of QMC and the full-grid PCM.

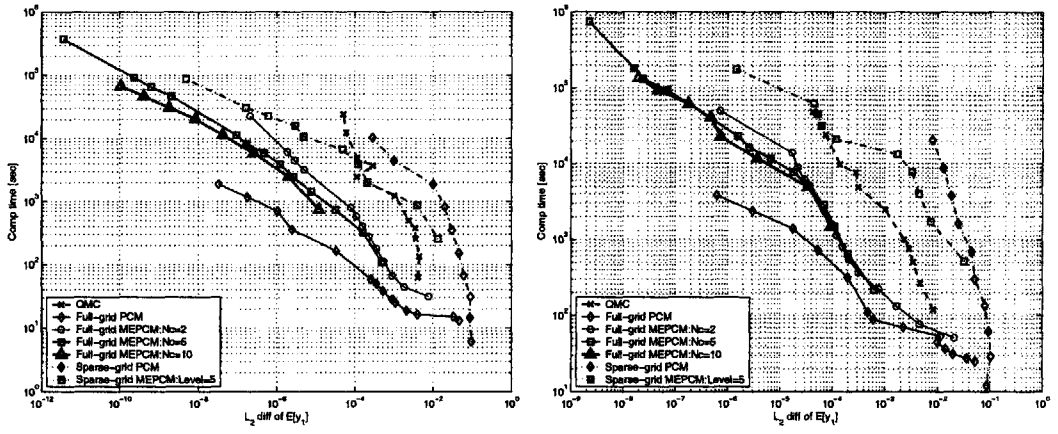

Figure 4-39: The cost per $E[y_1]$ accuracy of QMC, Full-grid PCM, Full-grid uniform-MEPCM, Sparse-grid PCM, and Sparse-grid uniform-MEPCM for $T_f = 50$ sec (left) and $T_f = 100$ sec (right).

Table 4.1: Summary of the convergence rates for various stochastic algorithms in the case of continuous stochastic solutions

Stochastic Algorithms	Rate of convergence
MC	$O(NN^{-1/2})$
QMC	$O(NN^{-1})$
gPC	$O(e^{-p/d})$
full- and sparse-grid PCM	$O(e^{-(Nc-1)/d})$
MEgPC	$O((N/d)^{-2(p+1)})$
full- and sparse-grid MEPCM	$O((N/d)^{-2Nc})$

The convergence rate of all stochastic algorithms, considered in this section, can be summarized in Table 4.1 below. Both gPC and PCM yield the rates of convergence that depend on the ratio of their governing parameters (p or Nc) and the random dimension. Likewise, the convergence rate of the multi-element technique must be normalized by the random dimension as well. Although the Monte Carlo method exhibits the convergence rate that is independent of the random dimension, it is not competitive against the full-grid PCM in small and medium random dimensions and the sparse-grid PCM in large random dimensions because of its slow rate of convergence. Even for the long-time integration problem, the computational efficiency of the full-grid PCM is still the best among these stochastic algorithms.

4.2 Discontinuous Stochastic Solutions

When a system has a discontinuity either in its stochastic solutions or in its derivative due to random initial conditions, parameters, or equations themselves, this discontinuity can reduce the statistical accuracy obtained from all stochastic algorithms. Also, this discontinuity has a direct impact on the convergence rate of both Galerkin and Collocation approaches. However, the uniform and adaptive multi-element technique can significantly improve the L_2 error convergence of statistical solutions. Similar to the last section, the h-type refinement helps maintain the solution accuracy in a long-time integration. This section considers two types of SDEs, step discontinuity

and the Kraichnan-Orszag systems. Again, the PCM denotes the full-grid PCM, if we do not specify whether it is a full- or sparse-grid PCM.

4.2.1 Step-discontinuity first-order SDE

Let us examine a system with a discontinuity in its derivative. The first-order ODE with a signum function is expressed as the following:

$$\frac{dy}{dt} = -\text{sign}(y), \qquad \text{with } y\,(t=0) = y_0 \text{ and } t \in [0,T] \tag{4.20}$$

where $t \in [0,1]$ and y_0 is considered to be a zero-mean and one-variance random variable, associated with the uniform distribution $U[-1,1]$. Exact solutions of mean and variance can be derived analytically as the following:

$$\bar{y}_{exact}(t) = 0, \tag{4.21}$$

$$\sigma^2_{exact}(t) = \frac{1}{3}(1 - 3t - 3t^2 - t^3). \tag{4.22}$$

First, the convergence characteristic and rate of PCM and Hybrid gPC+PCM with $Nc = 20$ appears in Figure 4-40, when a discontinuity occurs on the zero axis. The convergence rate of PCM becomes algebraic in the order of $O((Nc-1)^{-2})$; however, the error convergence of Hybrid gPC+PCM, which is linearly approximated by $O(p^{-2})$, fluctuates around that of PCM. An explanation of this phenomenon is that the even-order modes of the polynomial chaos basis do not capture the dynamic of discontinuity at zero because they cross the zero axis at the origin. Therefore, the L_2 variance difference improves only when an additional odd mode of polynomial chaos is added. Nevertheless, the relation $Nc = p + 1$ is still valid between the PCM and Hybrid gPC+PCM.

We compare the results between MEPCM with $Nc = [2,3]$ and hybrid MEgPC+PCM with $p = [1,2]$. The convergence rates for both MEPCM and hybrid MEgPC+PCM do not depend on the Nc and p and they stay fixed at $O(NN^{-3})$. Figure 4-41 shows

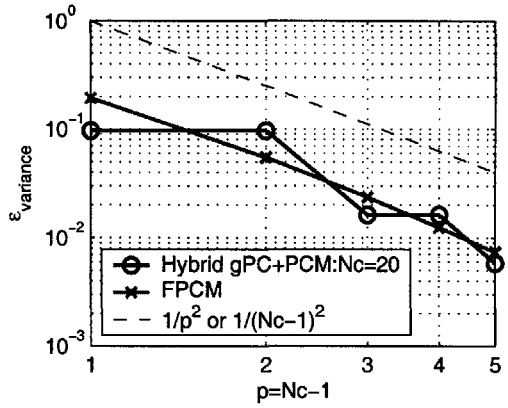

Figure 4-40: The L_2 error convergence of variance solutions as a function of Nc or $p+1$ using the PCM or Hybrid gPC+PCM, respectively, for $\dot{y} = -sign(y)$.

that hybrid MEgPC+PCM has lower accuracy than that of MEPCM, which is consistent with the accuracy of the Hybrid gPC+PCM, which is less than that of the PCM.

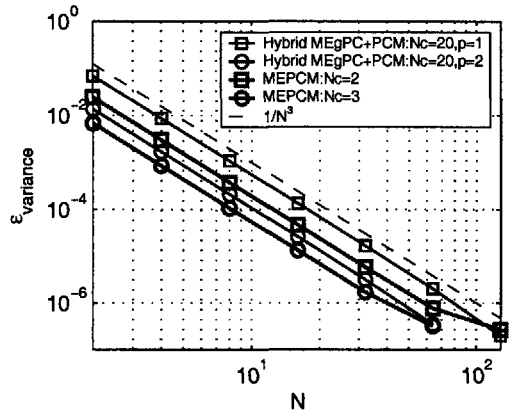

Figure 4-41: The L_2 error convergence of variance solutions as a function of Nc for the PCM for $\dot{y} = -sign(y)$.

4.2.2 Kraichnan-Orszag system in one random dimension

An initial condition of the Kraichnan-Orszag system is set as the following $[y_1(0,\xi), y_2(0,\xi), y_3(0,\xi)] = [1, 0.1\xi, 0]$. This random initial condition leads to the discontinuity in stochastic solution on the y_2 plane. For $t \in [0, 30]$, the convergence rate as well as computational efficiency are compared among these four stochastic algorithms: 1) MC and QMC, 2)

PCM, 3) uniformly MEPCM with $Nc = 5$, and 4) Adaptive MEPCM with $Nc = 5$ and $\theta_1 = [0.1, 0.05, 0.01, 0.005]$. Using the adaptive criterion described in Section 3.4.3, the evolution of the element mesh of random space as a function of time can reveal how this adaptive algorithm specifies the location of discontinuity. The reference solution is numerically computed by the quasi-Monte Carlo method with a million realizations, which consumes 19.63 hours of the computational time. As seen in Figure 4-42, the variance solutions of three modes grow with time as T_f approaches 30 seconds due to a change in frequency of oscillation and the discontinuity on the zero axis of the y_2 initial condition. As a result, the statistical solutions from both gPC and PCM will fail to converge, particularly for the long-time integration. Figure 4-43 shows an effect of increasing p in gPC and increasing Nc in PCM to delay a divergence of the statistics. With small p and Nc, the estimated variance solutions start to diverge after a few seconds.

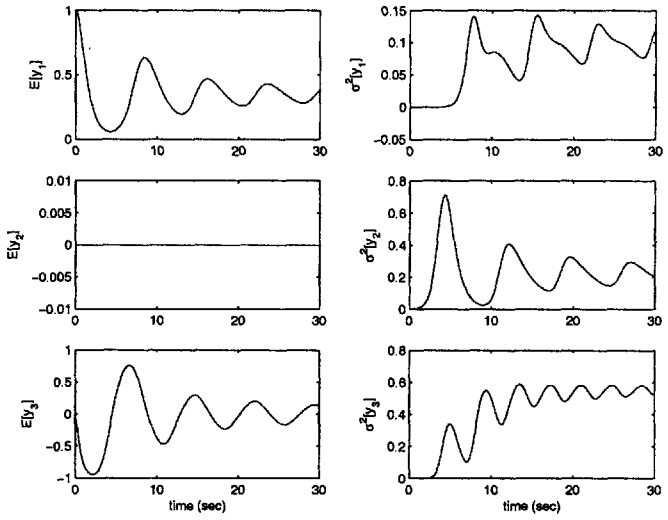

Figure 4-42: The stochastic mean and variance solutions of three modes from the reference solution when $[y_1(0,\xi), y_2(0,\xi), y_3(0,\xi)] = [1, 0.1\xi(\omega), 0]$.

To improve the accuracy of estimated statistics, we can increase either Nc or N by a significant amount. Figures 4-45 and 4-46 show that the convergence rate of both PCM and MEPCM with uniformly fixed elements are on the order of $O(N^{-1})$; however, the computational time of uniform MEPCM is more than two times faster than that of PCM for the same accuracy, especially in a high-accuracy region. Also,

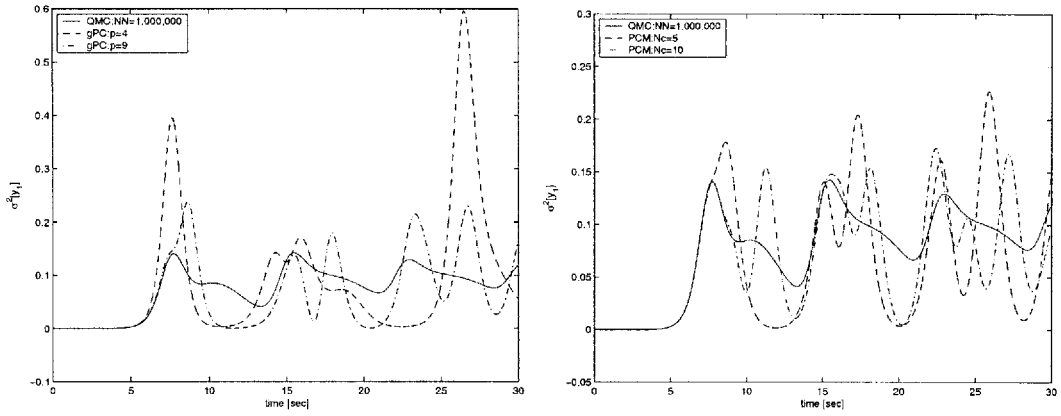

Figure 4-43: The divergence of y_1 variance solution using gPC (left) and using PCM (right).

notice that the convergence rate of uniform MEPCM does not depend on Nc, when the solutions have a discontinuity. On the contrary, the convergence rate of both MC and QMC are not sensitive to the discontinuity in the solution. We can see in Figure 4-44 that the convergence rates of $O(NN^{-1/2})$ using MC and $O(NN^{-1})$ using QMC are very similar to those in the previous continuous cases. However, the computational cost per accuracy in low dimensions of QMC is still 5 and 10 times larger than that of PCM and MEPCM with $Nc = 10$, respectively.

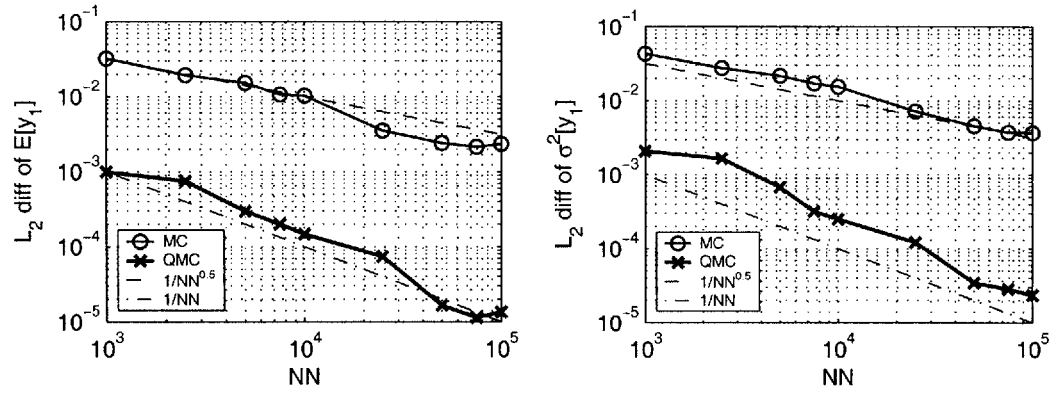

Figure 4-44: The L_2 norm error of mean (left) and variance (right) solutions as a function of NN exhibit the algebraic convergence rate of $O(NN^{-1/2})$ using MC and of $O(NN^{-1})$ using QMC.

The convergence rate can be further decreased to $O(N^{-3})$ or greater with the adaptive MEPCM, as Figure 4-47 shows. For the same accuracy of mean solutions at

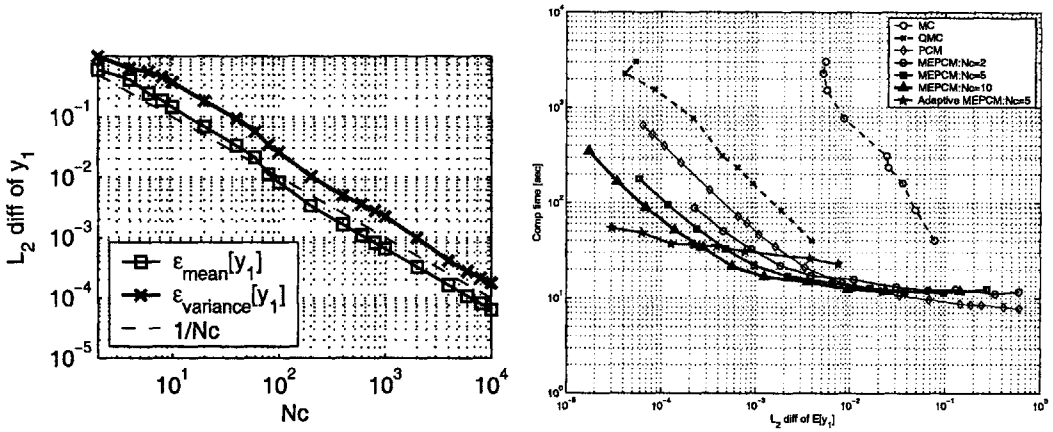

Figure 4-45: The Nc-convergence of mean and variance solutions using PCM (left) and the computational time of MC, QMC, PCM, and uniform MEPCM (right).

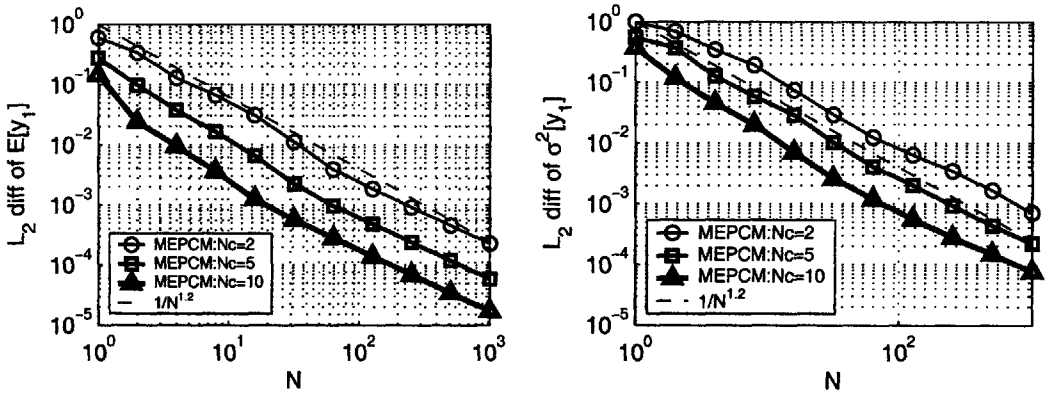

Figure 4-46: The L_2 norm error of mean (left) and variance (right) solutions as a function of N exhibit the algebraic convergence rate of $O(N^{-1})$ using MEPCM with $Nc = 2$, $Nc = 5$, and $Nc = 10$.

10^{-4}, the computational efficiency of the adaptive MEPCM is about 10 and 5 times higher than that of the normal PCM, and of the MEPCM with uniform elements, respectively. With the threshold, θ_1 = [0.1, 0.05, 0.01, 0.005, 0.004, 0.003, 0.002, 0.001, 0.0005], the corresponding numbers of the element are [10, 14, 22, 26, 30, 32, 34, 63, 78]. The progression of new elements generated in time, shown in Figure 4-48, reveals how the adaptive criterion decomposes the random space to capture the location where discontinuity occurs. For $\theta_1 = 0.1$, the random space is gradually divided in time to decrease the error from the discontinuity at zero. With $\theta_1 = 0.01$, the decomposition occurs very fast within the first 10 seconds near the zero to reduce the error from the discontinuity. After 10 seconds, the h-type refinement also captures the error due to a long-time integration.

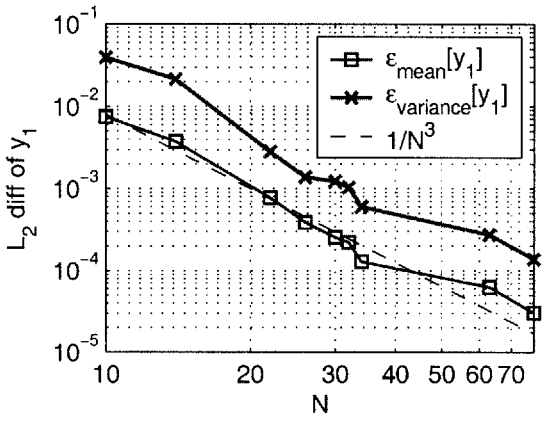

Figure 4-47: Using the adaptive MEPCM, the error convergence of mean and variance solutions are shown as a function of N.

4.2.3 Kraichnan-Orszag system in two random dimensions

When a discontinuity of stochastic solutions occurs in two random dimensions, the accuracy and efficiency again are compared among these stochastic algorithms: MC, QMC, PCM, uniform MEPCM, and uniform MEgPC. For these initial conditions, $[1, 0.1\xi_1(\omega), \xi_2(\omega)]$, the Kraichnan-Orszag system exhibits a discontinuity on the y_2 plane such that the stochastic solutions in three dimensions can fall into g1, g4, or g8 groups. The reference mean and variance solutions, obtained from the QMC with

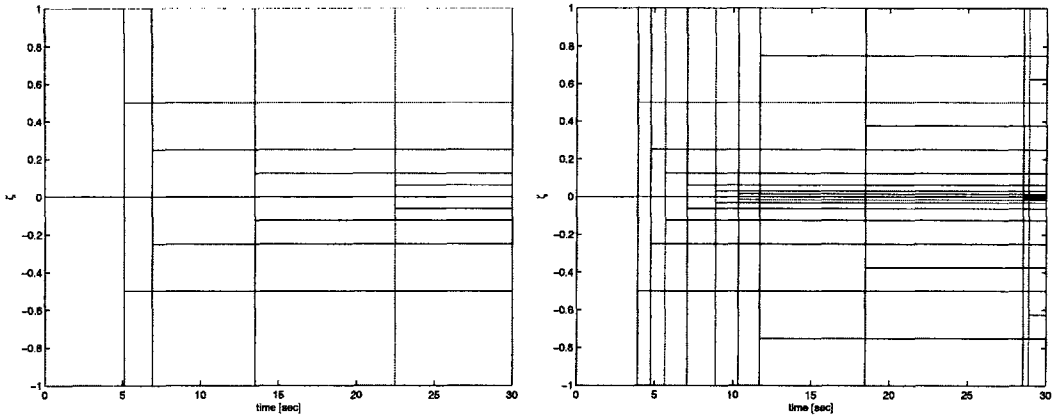

Figure 4-48: Adaptive meshes of the random space for $\theta_1 = 0.1$ (left) and $\theta_1 = 0.01$ (right) splitting into multiple elements as time evolves.

$NN = 1,000,000$ for $t \in [0, 15]$, are shown in Figure 4-49.

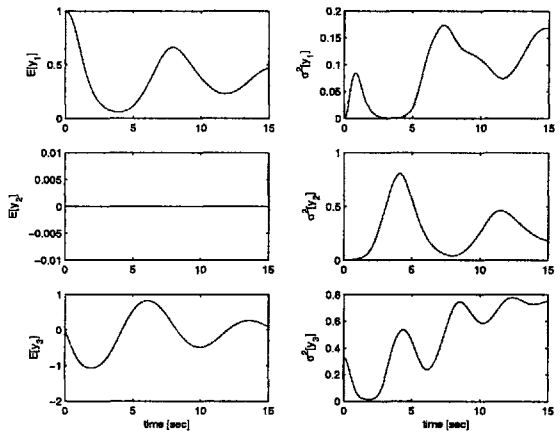

Figure 4-49: The stochastic mean and variance solutions of three modes from the reference solution when $[y_1(0,\xi), y_2(0,\xi), y_3(0,\xi)] = [1, 0.1\xi_1(\omega), \xi_2(\omega)]$.

The performance and rate of convergence are compared among four stochastic algorithms: 1) MC and QMC, 2) PCM , 3) MEPCM with $Nc = [2, 5, 10]$, and 4) MEgPC with $p = [1, 4]$. As shown in Figure 4-50 below, the L_2 error convergence of MC and QMC are consequently on the order of $O(NN^{-1/2})$ and $O(NN^{-1})$. Insensitivity of the convergence rate to both random dimension and discontinuity in stochastic solutions makes the Monte Carlo method more competitive against PCM and gPC in large dimensions of random inputs.

Similar to the discontinuity of solutions in one random dimension of the Kraichnan-

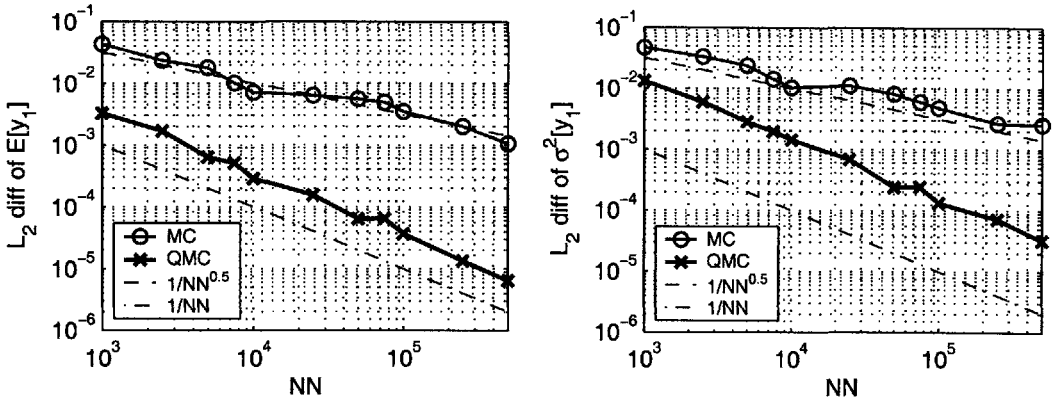

Figure 4-50: The L_2 norm error of mean (left) and variance (right) solutions as a function of NN exhibits the algebraic convergence rate of $O(NN^{-1/2})$ using MC and that of $O(NN^{-1})$ using QMC.

Orszag system, the error convergence rates of PCM and MEPCM are in the order of $O((Nc/d)^{2/3})$ and $O((N/d)^{1.4})$, respectively. The computing cost per accuracy in Figure 4-51 reveals that the single-element PCM cannot handle the discontinuity in stochastic solutions as efficiently as the uniform MEPCM with large Nc. On the other hand, the cost per accuracy of MEgPC increases as the polynomial order, p, increases. Without the p-type refinement, MEgPC with $p = 1$ can also yield a good computing efficiency, which is more than an order of magnitude better than that of MC for the same accuracy.

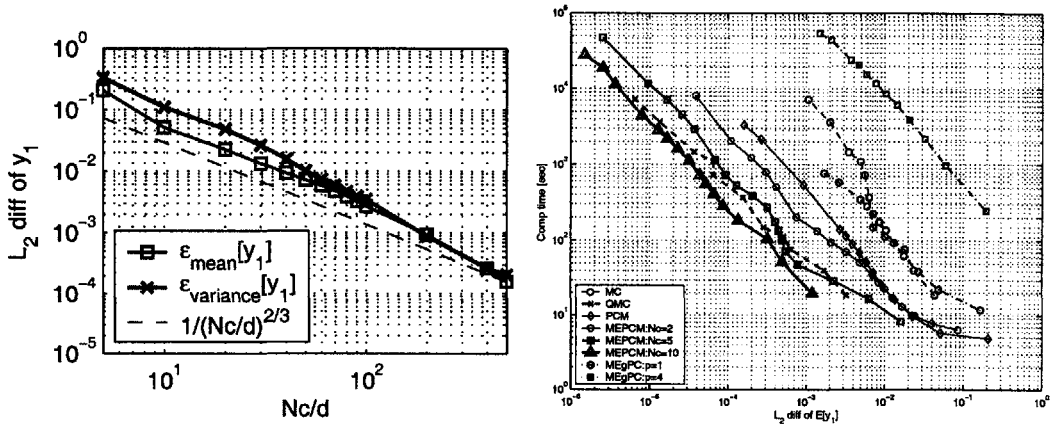

Figure 4-51: The Nc-convergence of mean and variance solutions using PCM (left) and the computational time of MC, QMC, PCM, and MEPCM with uniform element (right).

Even though the convergence rate of uniform MEPCM is independent of Nc, a linear improvement in both Nc- and h-type refinements can be seen in Figure 4-52. The convergence rate of the statistical moments, particularly of y_1, is not smooth; therefore, we also show the statistical convergence of y_3, which is much smoother, to confirm the convergence rate of $O((N/d)^{1.2})$, as shown in Figure 4-53. The error of state y_3 converges much more smoothly because the discontinuity occurs directly on the y_1 plane and the statistical response of y_3 just oscillates around zero.

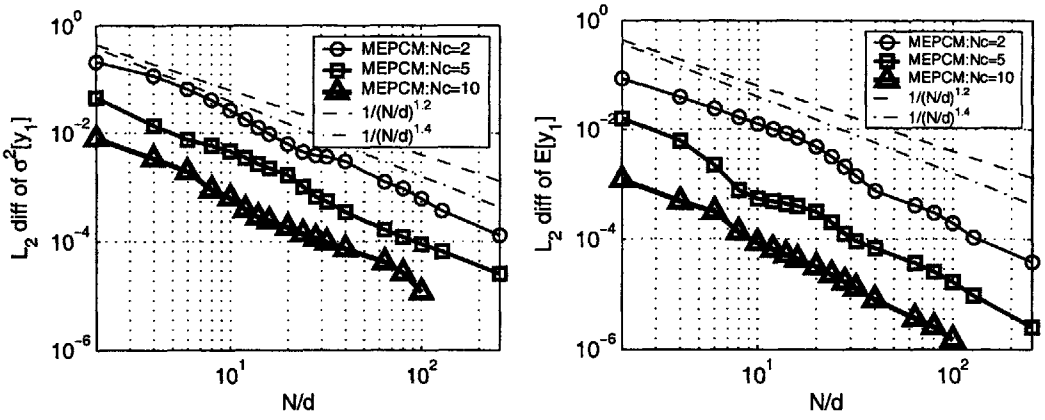

Figure 4-52: The L_2 norm error of mean (left) and variance (right) solutions as a function of N/d exhibits the algebraic convergence rate of $O(N^{-1.4})$ using the uniform MEPCM with $Nc = [2, 5, 10]$.

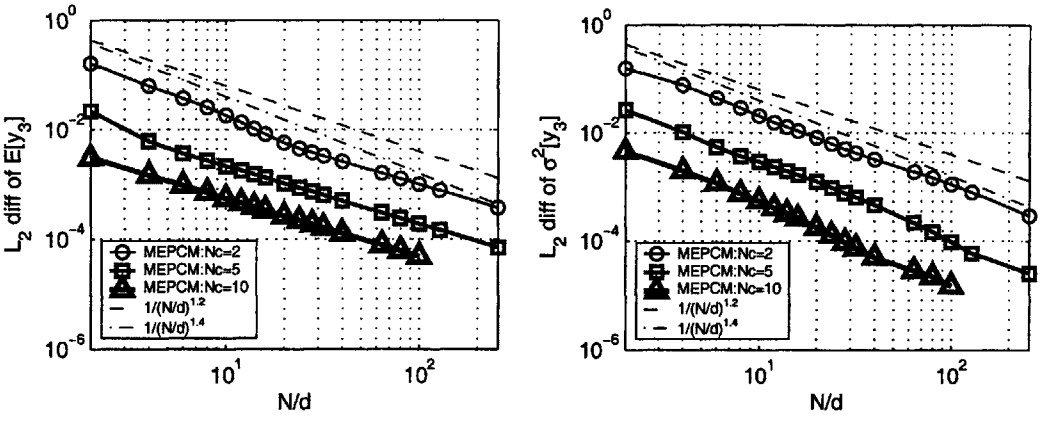

Figure 4-53: The L_2 norm error of mean (left) and variance (right) solutions as a function of N/d exhibits the algebraic convergence rate of $O(N^{-1.2})$ using the uniform MEPCM with $Nc = [2, 5, 10]$.

In spite of the large computational cost per accuracy of uniform MEgPC, the

uniform MEgPC exhibits an algebraic error convergence rate of $O((N/d)^2)$, which is about an order faster that of the uniform MEPCM. As shown in Figure 4-54, the p-type convergence of uniform MEgPC exhibits smaller improvement than the Nc-type convergence of uniform MEPCM in the presence of the discontinuous solutions.

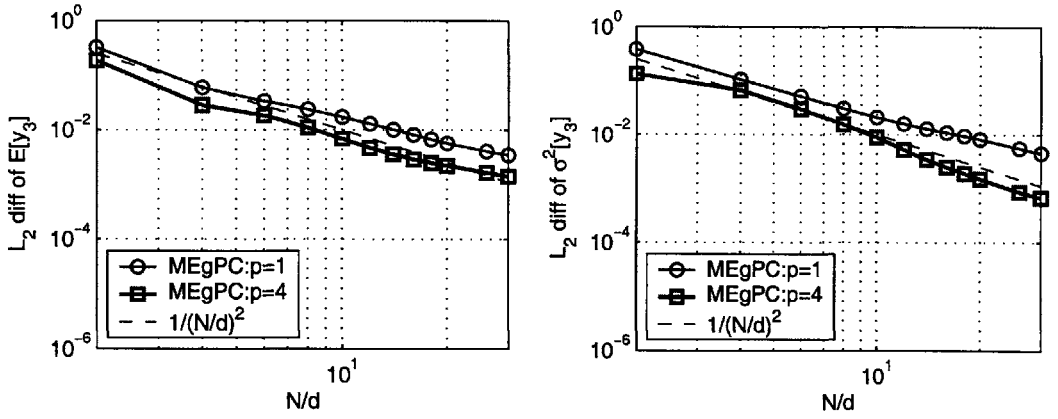

Figure 4-54: The L_2 norm error of mean (left) and variance (right) solutions as a function of N/d exhibits the algebraic convergence rate of $O(N^{-2})$ using the uniform MEgPC with $p = 1$ and $p = 4$.

4.2.4 Kraichnan-Orszag system in three random dimensions

With three random initial conditions of $[\xi_1(\omega),0.1\xi_2(\omega),\xi_3(\omega)]$ for the Kraichnan-Orszag system, the discontinuity occurs on both the y_1 and y_2 planes; thus the stochastic solutions can occur in any one of the eight groups. As a result, the time constants of mean and variance are longer than in previous discontinuous cases. The statistical results from the QMC with $NN = 1,000,000$, shown in Figure 4-55 for $t \in [0, 15]$, are used as a reference solution to compute the error convergence.

We compare the performance among these five stochastic algorithms: 1) MC and QMC, 2) full-grid PCM , 3) full-grid MEPCM with $Nc = [2, 5, 10]$, 4) sparse-grid PCM, and 5) sparse-grid MEPCM with $Level = 5$. Hence, both effects of the sparseness of collocation points and uniform decomposition of random space are our main focuses in this section. As illustrated in Figure 4-56, the MC and QMC again yield the convergence rate of $O(NN^{-1/2})$ and $O(NN^{-1})$, respectively.

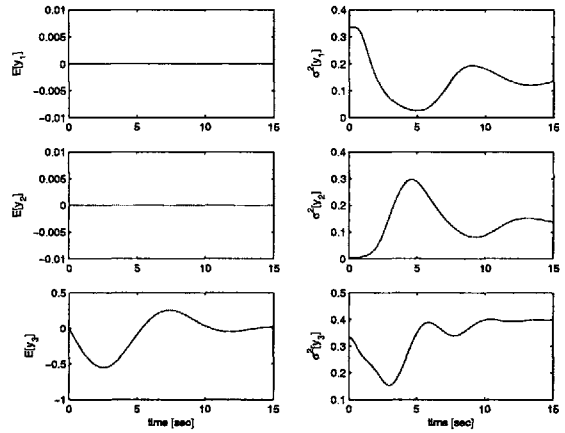

Figure 4-55: The stochastic mean and variance solutions of three modes from the reference solution when $[y_1(0,\xi),y_2(0,\xi),y_3(0,\xi)] = [\xi_1(\omega),0.1\xi_2(\omega),\xi_3(\omega)]$.

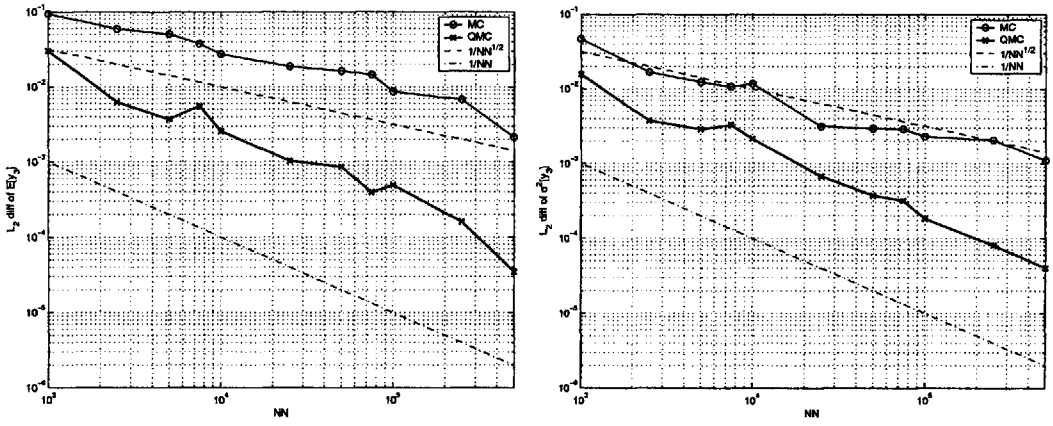

Figure 4-56: The L_2 norm error of mean (left) and variance (right) solutions as a function of NN exhibits the algebraic convergence rate of $O(NN^{-1/2})$ using MC and of $O(NN^{-1})$ using QMC.

According to Figure 4-57, the algebraic convergence rate of full-grid PCM is still in the order of $O((Nc/d)^{1.2})$; however, the sparse-grid PCM yields an exponential convergence rate faster than $O(e^{-0.3(Level/d)})$, which results in a more efficient algorithm for discontinuous stochastic solutions. The results using the sparse-grid collocation method have not been considered in one- and two-dimensional cases because its computing cost per accuracy is not competitive against the full-grid PCM. In Section 4.4, the advantage of the sparse-grid PCM will be more pronouced for a large integrated power system with high random dimensions.

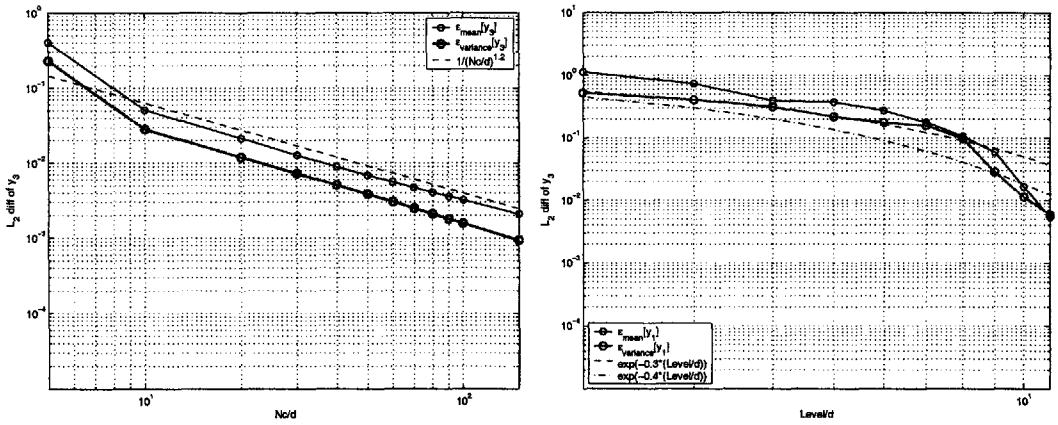

Figure 4-57: The Nc-convergence of mean and variance solutions using full-grid PCM (left) and using sparse-grid PCM (right).

Both Nc- and N-type refinements of full- and sparse-grid uniform MEPCM are shown in Figure 4-58. The full-grid MEPCM exhibits an algebraic convergence as a function of both N/d and Nc, and the multi-element technique alone yields the convergence rate per random dimension of $O((N/d)^{-1})$. In this case, the sparse-grid uniform MEPCM provides more than three orders of magnitude in algebraic convergence faster than the full-grid uniform MEPCM. One explanation of this faster convergence characteristic is that the sparse collocation points as a function of either level or element number are distributed close to the boundary and the zero-axis of the hypercube, where the planes of discontinuity occur.

In terms of the cost per accuracy, even though the QMC seems to be the most efficient, the sparse-grid uniform MEPCM with a larger level can easily provide better accuracy than the QMC with a smaller computing cost. As shown in Figure 4-59, the

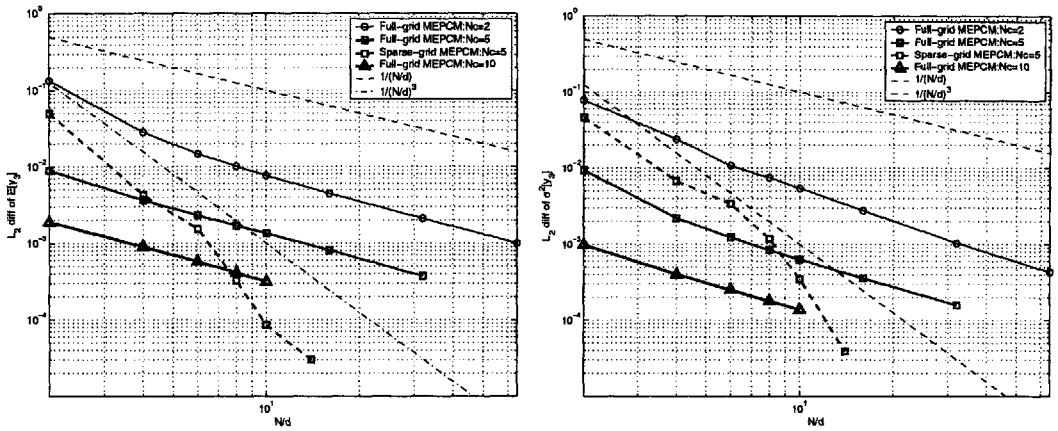

Figure 4-58: The L_2 norm error of y_1 mean (left) and variance (right) solutions as a function of total N exhibit the algebraic convergence rate of $O(N^{-1})$ for $Nc = 2$ and $Nc = 5$, using MEPCM.

cost per accuracy of full-grid uniform MEPCM, which is lower than that of the single-element full-grid PCM, tends to improve slower than those of QMC and sparse-grid uniform MEPCM for the short-time integration problem. If the random dimension increases further, the computational efficiency of the sparse-grid MEPCM will become more distinguished in the system with discontinuity in stochastic solutions.

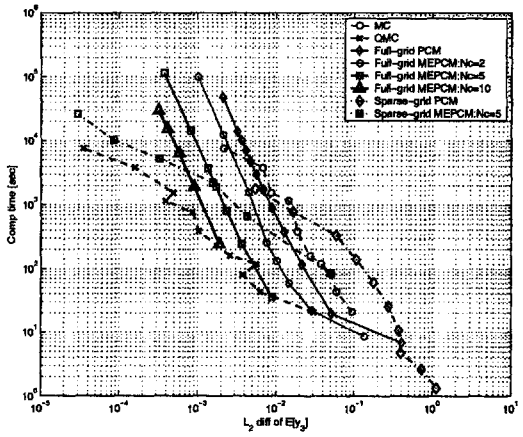

Figure 4-59: The computational time of MC, QMC, full- and sparse-grid PCM, full- and sparse-grid MEPCM with uniform element.

Results for a long-time integration

This section discusses and compares the performance of stochastic algorithms when the final time of integration (T_f) increases to 50 and 100 seconds. Figure 4-60 shows mean and variance solutions of the reference solutions, obtained from QMC with a million realizations, similar to Section 4.2.4. These reference solutions approach their steady-state values within the first 30 seconds. Thus, using $T_f = 100$ seconds emphasizes the propagation of accumulating error in the long-time integration problem. Therefore, we can see the effectiveness of the multi-element technique to decrease the global integration error, specifically with a discontinuity in stochastic solutions.

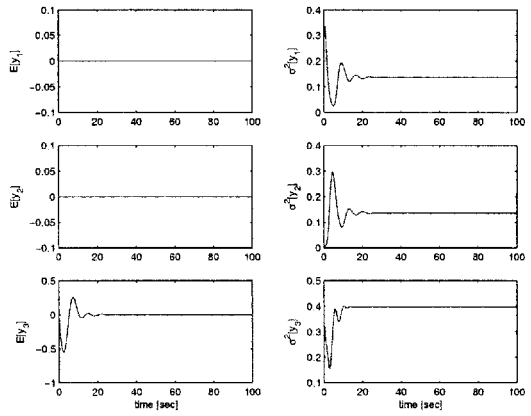

Figure 4-60: The stochastic mean and variance solutions of three modes from the reference solution when $[y_1(0,\xi),y_2(0,\xi),y_3(0,\xi)] = [\xi_1(\omega),0.1\xi_2(\omega),\xi_3(\omega)]$.

The averaging characteristic of the Monte Carlo technique requires a large number of NN to approximate the statistical moment accurately in the presence of the accumulating error in each realization, as shown in Figure 4-61. The accuracy of error convergence using QMC becomes worse as the integration time lengthen; nonetheless, the rate of convergence is still in the order of $O(NN^{-1})$. As a result, the L_2 error convergence of moments is shifted upward for $T_f = 50$ and 100 seconds, shown in Figure 4-62.

Similarly, the error convergence of the single-element full-grid PCM and sparse-grid PCM becomes worse as we increase the final integration time. Figure 4-63 shows that the error convergence of full-grid PCM still has the algebraic rate of $O((Nc/d)^{1.2})$

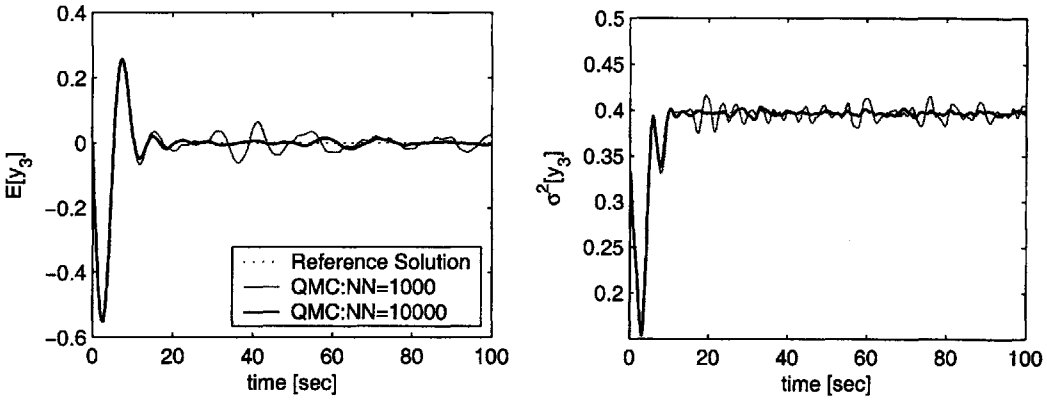

Figure 4-61: The stochastic mean (left) and variance (right) solutions of three modes from the reference solution, QMC with $NN = 1,000$, and QMC with $NN = 10,000$.

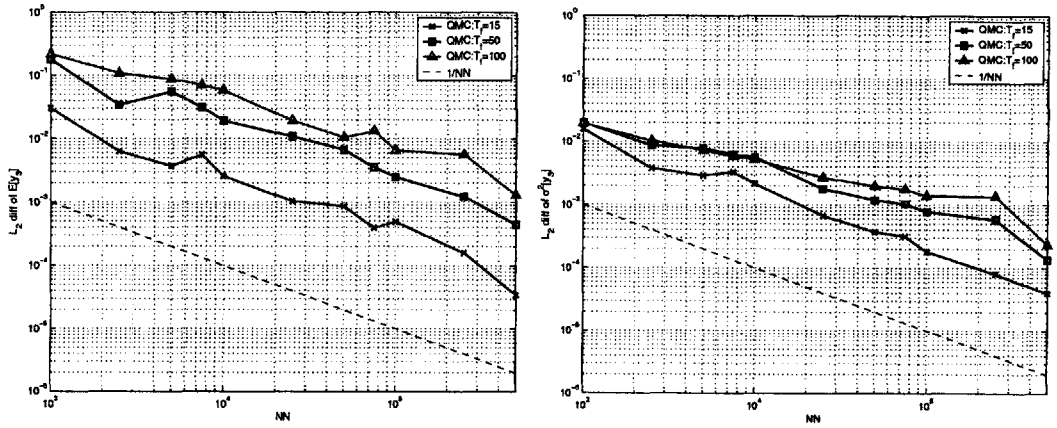

Figure 4-62: The L_2 error convergence of mean (left) and variance (right) solutions as a function of NN and T_f using the QMC.

for $T_f = [15, 50, 100]$. For the sparse-grid PCM, the L_2 exponential convergence of error becomes much worse when T_f increases, as seen in Figure 4-64. Closely related to Section 4.1.8, both of these collocation techniques are sensitive to the final integration time because of a fast propagation of accumulating error, associated with each run of the deterministic solver.

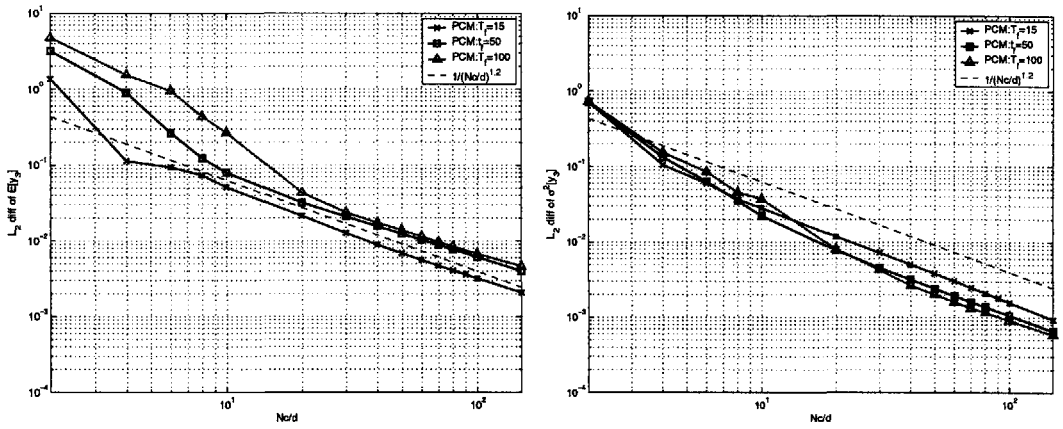

Figure 4-63: The Nc-convergence of mean (left) and variance (right) solutions using the full-grid PCM as T_f increases.

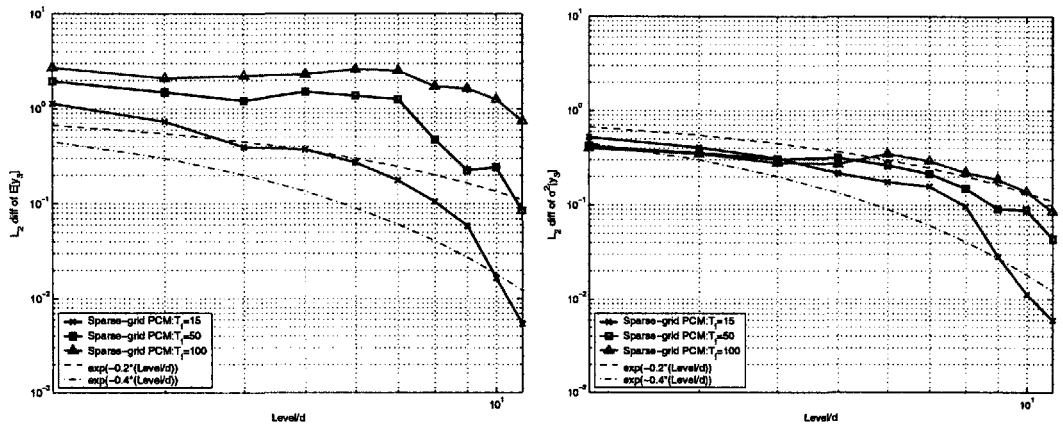

Figure 4-64: The Level-convergence of mean (left) and variance (right) solutions using the sparse-grid PCM as T_f increases.

When the multi-element technique is combined with the full-grid PCM, the global accumulating error can be decreased significantly because of the reduction of accumulating error in each local element. As shown in Figure 4-65, with only a few elements in the h-type refinement, the full-grid MEPCM significantly delays the divergence of

statistical solutions. The full-grid PCM with only two collocation points per random dimension cannot handle the discontinuity around the zero axis, which leads to oscillatory responses of the first and second moments. Figure 4-66 shows the linear convergence using the full-grid uniform MEPCM as a function of both N/d and Nc. The linear-convergence characteristic of full-grid uniform MEPCM does not change as T_f increases.

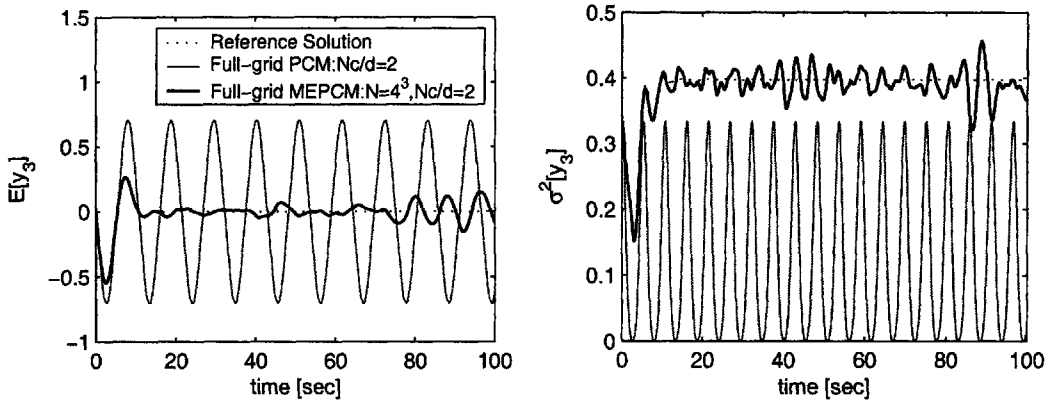

Figure 4-65: The stochastic mean (left) and variance (right) solutions of three modes from the reference solution, full-grid PCM with $Nc/d = 2$, and full-grid uniform MEPCM with $N = 4^3, Nc/d = 2$.

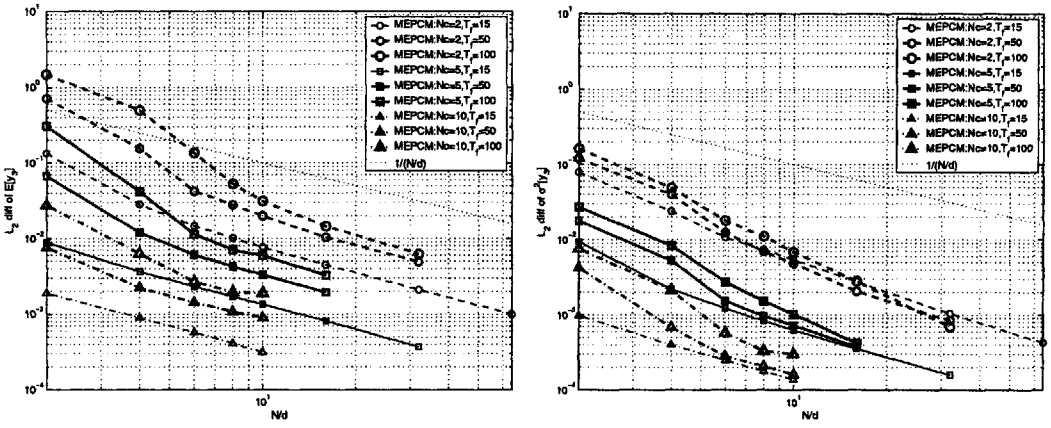

Figure 4-66: The L_2 error convergence of y_3 mean (left) and variance (right) solutions as a function of total N exhibits the algebraic convergence rate of $O(N^{-4})$ for $Nc = 2$, $O(N^{-10})$ for $Nc = 5$ and $O(N^{-20})$ for $Nc = 10$, using the full-grid uniform MEPCM.

Similar to the full-grid uniform MEPCM, the sparse-grid uniform MEPCM could also delay the divergence, resulting from the accumulating error of integration, as

shown in Figure 4-67. Although the sparse-grid uniform MEPCM provides a better convergence rate than the full-grid uniform MEPCM for a short-time integration ($T_f = 15$), the sparse-grid uniform MEPCM loses its accuracy quickly due to the deterioration of the performance of the sparse-grid PCM, as shown in Figure 4-68. However, the multi-element technique helps maintain the linear convergence rate in the long-time integration.

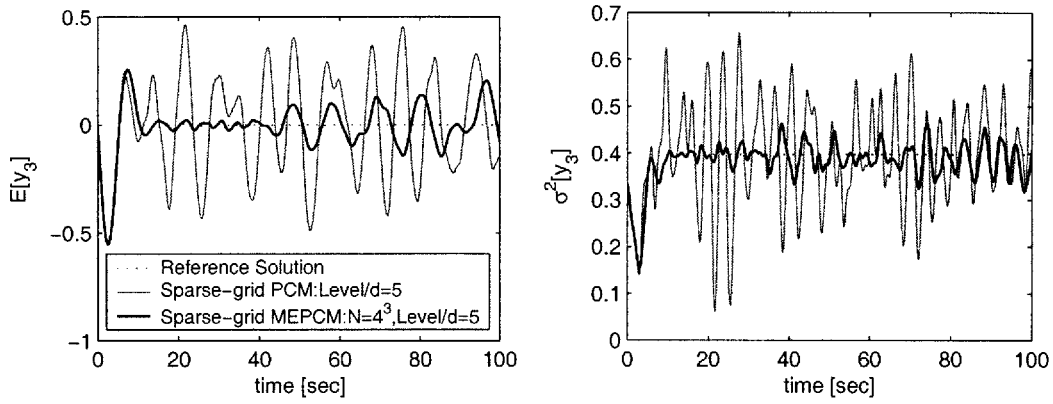

Figure 4-67: The stochastic mean (left) and variance (right) solutions of three modes from the reference solution, sparse-grid PCM with $Level/d = 5$, and sparse-grid uniform MEPCM with $N = 4^3, Level/d = 5$.

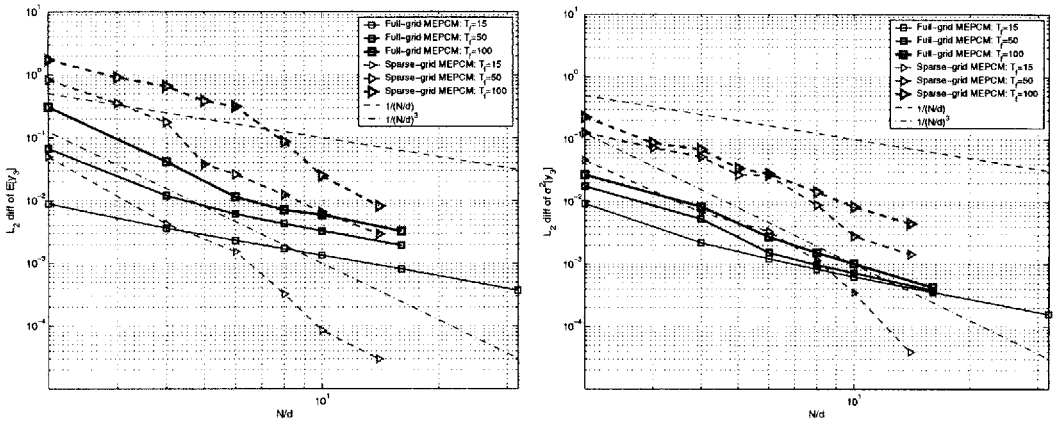

Figure 4-68: Comparison between the full-grid uniform MEPCM with $Nc = 5$ and the sparse-grid uniform MEPCM with $Level = 5$ on the L_2 error convergence of y_1 mean (left) and variance (right) solutions as a function of N/d exhibits the algebraic convergence rate.

To compare the computational performance of these stochastic algorithms, the computing cost per mean accuracy in Figure 4-69 shows that the full-grid uniform

MEPCM becomes more effective over the QMC, while the performance of the sparse-grid uniform MEPCM degrades. Similar to Section 4.1.8, in the long-time integration, all the cost-per-accuracy curves of the full-grid uniform MEPCM with any Nc merge into a single curve, aligning with that of QMC. One explanation for this characteristic is that once the statistical solutions approach their steady-state values after a few oscillations, the accumulating error becomes a random fluctuation in the case of evenly sampling the random space using the QMC or full-grid uniform MEPCM. With unevenly distributed collocation points of the sparse-grid PCM, the accumulating error grows much quicker. In summary, the full-grid PCM maintains its accuracy better than the sparse-grid PCM, and the multi-element technique can delay the divergence for a long-time integration, when there is a discontinuity in stochastic solutions. Next, we will consider a small system of a single induction machine, which has more oscillatory stochastic responses.

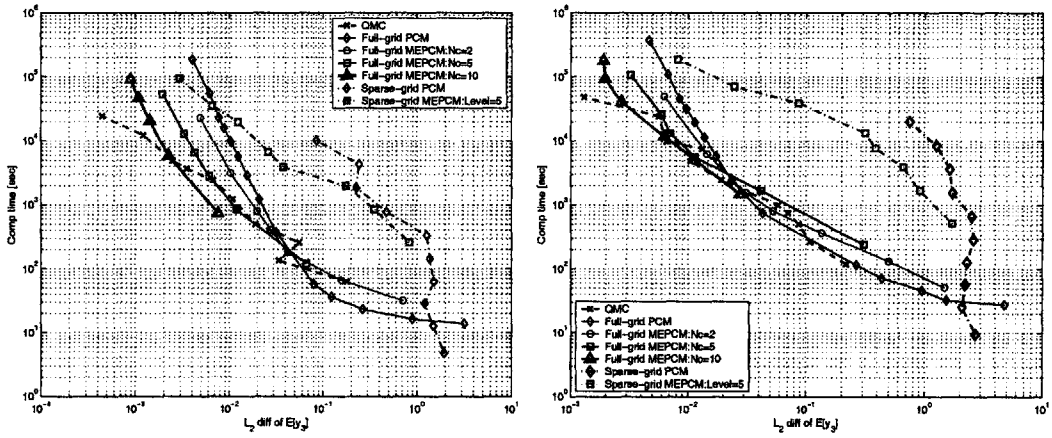

Figure 4-69: The cost per $E[y_3]$ accuracy of QMC, full-grid PCM, full-grid uniform MEPCM, sparse-grid PCM, and sparse-grid uniform MEPCM for $T_f = 50$ sec (left) and $T_f = 100$ sec (right).

Table 4.2 summarizes all convergence rates of various stochastic algorithms, when the stochastic solutions contain a discontinuity either in derivative or solutions themselves. We describe the convergence rates of all algorithms, except that of the Monte Carlo method, with an arbitrary constant (c), because the c value can vary depending on the severity of solutions' discontinuity. Similar to the continuous case, the rate of convergence of Galerkin, Collocation, and multi-element techniques must be nor-

Table 4.2: Summary of the convergence rates for various stochastic algorithms in the case of discontinuous stochastic solutions, where c is a arbitrary constant

Stochastic Algorithms	Rate of convergence
MC	$O(NN^{-1/2})$
QMC	$O(NN^{-1})$
gPC	$O((p/d)^{-c})$
full- PCM	$O(((Nc-1)/d)^{-c})$
sparse-grid PCM	$O(e^{-c*(level)/d})$
MEgPC	$O((N/d)^{-c})$
full- and sparse-grid MEPCM	$O((N/d)^{-c})$

malized by the random dimension, while the convergence rate of the Monte Carlo is independent of the random dimension. As shown in this section, the cost per accuracy of the Monte Carlo method is still large compared to either full- or sparse-grid MEPCM even in the long-time integration problem, even though the slow convergence rate of the Monte Carlo method is independent of the random dimension.

4.3 An open-loop induction machine with the infinite bus

The parametric uncertainty in a single induction machine directly connected to an infinite bus is considered in this section from both error convergence and uncertainty propagation aspects. The configuration of this system is shown in Figure 4-70. The machine equations are expressed in a qd0-synchronous reference frame. These equations of this three-phase system with quadratic nonlinearities consist of seven state variables: three rotor reactances $[\psi'^e_{qr}, \psi'^e_{dr}, \psi'^e_{0r}]$, the rotor's angular velocity $[\omega_r]$, and three stator or tie-line currents $[i^e_{qt}, i^e_{dt}, i^e_{0t}]$ (see Equation 4-23 to 4-29). Two states, ψ'^e_{0r} and i^e_{0t}, are uncoupled from the others. All parameters, given in Table 4.3, are lumped into α_i variables for a simplification of state equations. The detailed derivation of system modeling can be found in Section ??. The start-up dynamics of a 200-hp induction machine in an open-loop configuration, considered here for $t \in [0, 3]$

seconds, includes fast transient dynamics from electrical components, stator and rotor windings, and slow dynamics of a mechanical subsystem, a rotor inertia.

The uncertainty in a rotor resistance ($r_r^{'}$) can be modeled with two types of stochastic inputs - random variable in Section 4.3.1 and random process in Section 4.3.3. In the random variable case, the value of the rotor resistance ,$r_r^{'}(\omega) = \bar{r_r^{'}} + \sigma_r\xi(\omega)$, is assumed to be unknown, but it is described by the mean value ($\bar{r_r^{'}}$) and bounded within the specified range (σ_r). In a more realistic situation, the rotor resistance, which normally fluctuates with an operating temperature, is modeled by a time-varying parameter. Thus, in the random process case, this time-dependent parameter (R'r) can be represented by the Karhunen-Loeve (K-L) expansion [33], described in the following form: $r_r^{'}(t,\omega) = \bar{r_r^{'}} + \sigma_r \sum_{i=1}^{KL} \sqrt{\lambda_i}\psi_i(t)\xi_i(\omega)$, where $\bar{r_r^{'}}$ and σ_r are consequently the mean and standard deviation of rotor resistance. λ_i and ψ_i are an eigenvalue and an eigenfunction associated with i term from the expansion, truncated at KL random dimensions. The $\xi(\omega)$ is the random variable as a function of random space, ω. For this process, the ϕ_i and λ_i are determined from an exponential covariance function: $K(t_1,t_2) = \sigma_r^2 e^{\frac{-|t_2-t_1|}{CL}}$, governed by the correlation length (CL) of a time difference. In both cases, the values of $\bar{r_r^{'}}$ and σ_r are 0.0261 p.u. and 0.01. Three realizations from the K-L expansion of $r_r^{'}$ are shown in Figure 4-70.

$$\frac{d\psi_{qr}^{'e}}{dt} = \alpha_1\psi_{qr}^{'e} - \alpha_2\psi_{dr}^{'e} + \omega_r\psi_{dr}^{'e} + \alpha_3 i_{qt}^{e}, \tag{4.23}$$

$$\frac{d\psi_{dr}^{'e}}{dt} = \alpha_2\psi_{qr}^{'e} + \alpha_1\psi_{dr}^{'e} - \omega_r\psi_{qr}^{'e} + \alpha_3 i_{dt}^{e}, \tag{4.24}$$

$$\frac{d\psi_{0r}^{'e}}{dt} = -\alpha_4\psi_{0r}^{'e}, \tag{4.25}$$

$$\frac{d\omega_r}{dt} = -\alpha_5\psi_{qr}^{'e}i_{dt}^{e} + \alpha_5\psi_{dr}^{'e}i_{qt}^{e} - \alpha_6, \tag{4.26}$$

$$\frac{di_{qt}^{e}}{dt} = \alpha_7\psi_{qr}^{'e} - \alpha_8\omega_r\psi_{dr}^{'e} - \alpha_9 i_{qt}^{e} - \alpha_{10}i_{dt}^{e} + \alpha_{11}, \tag{4.27}$$

$$\frac{di_{dt}^{e}}{dt} = \alpha_8\omega_r\psi_{qr}^{'e} + \alpha_7\psi_{dr}^{'e} + \alpha_{10}i_{qt}^{e} - \alpha_9 i_{dt}^{e}, \tag{4.28}$$

$$\frac{di_{0t}^{e}}{dt} = -\alpha_{12}i_{0t}^{e}. \tag{4.29}$$

Table 4.3: Parameters of a 200-hp induction machine

Parameters	r_s	X_{ls}	X_m	X'_{lr}	r'_r	H
in [p.u.]	0.01	0.0655	3.225	0.0655	0.0261	0.922

where

$$\alpha_1 = -\omega_b \frac{r_r^{'}}{x_{lr}^{'2}}(x_{lr}^{'} - x_b), \alpha_2 = \omega_e, \tag{4.30}$$

$$\alpha_3 = \omega_b r_r^{'} \frac{x_b}{x_{lr}^{'}}, \alpha_4 = \omega_b \frac{r_r^{'}}{x_{lr}^{'}}, \tag{4.31}$$

$$\alpha_5 = \frac{\omega_b}{2H}\frac{x_b}{x_{lr}^{'}}, \alpha_6 = \frac{\omega_b}{2H} T_{load}, \tag{4.32}$$

$$\alpha_7 = \frac{1}{aa}\left(\frac{r_r^{'} x_b}{x_{lr}^{'3}}\right)\left(\frac{x_{lr}^{'} - x_b}{L_t - M_t}\right), \alpha_8 = \frac{1}{aa}\left(\frac{x_b}{\omega_b x_{lr}^{'}}\right)\left(\frac{1}{L_t - M_t}\right), \tag{4.33}$$

$$\alpha_9 = \frac{1}{aa}\frac{r_s + r_t + r_r^{'}\left(\frac{x_b}{x_{lr}^{'}}\right)^2}{L_t - M_t}, \alpha_{10} = \frac{\omega_e}{aa}\left(\frac{x_{ls} + x_b}{\omega_b(L_t - M_t)} + \omega_b\right), \tag{4.34}$$

$$\alpha_{11} = \frac{1}{aa}\frac{1}{L_t - M_t}, \alpha_{12} = \frac{1}{bb}\frac{r_s + r_t}{L_t - M_t}, \tag{4.35}$$

$$aa = 1 + \frac{x_{ls} + x_b}{\omega_b(L_t - M_t)}, bb = 1 + \frac{x_{ls}}{\omega_b(L_t + 2M_t)}. \tag{4.36}$$

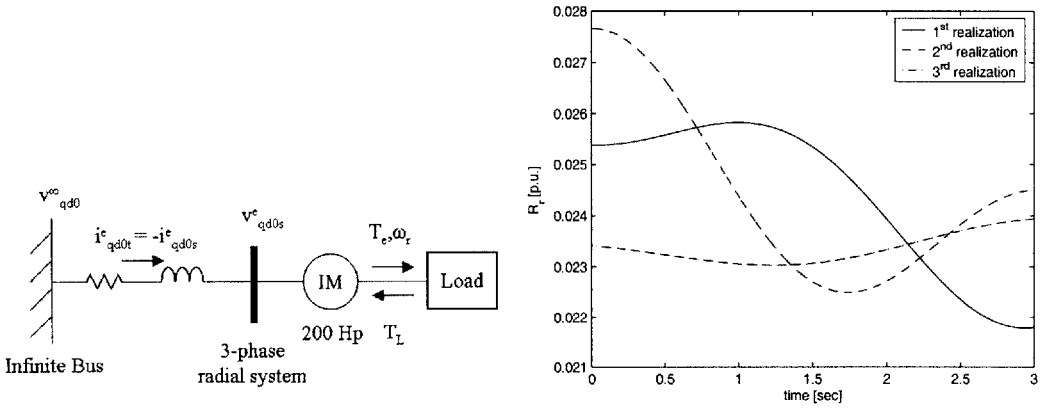

Figure 4-70: A one-line diagram of the induction machine connected to the infinite bus through a RL tie line (Left). Three realizations of the rotor resistance modeled by the three-term K-L expansion with CL = 10 second (Right).

4.3.1 One-dimensional random variable as the stochastic input

An evolution of the probability density function caused by a propagation of r_r' uncertainty can be constructed as described in Section 3.4.1 using the solutions at the nodal points of the PCM with $Nc = 100$. As shown in Figure 4-71, the peak of the q-axis rotor reactance, $\psi_{qr}'^{e}$, and the d-axis stator or tie-line current, i_{dt}^{e}, shift rapidly between top and bottom of the sinusoidal transient dynamics during the first second, when the rotor resistance is a uniform stochastic input. For $t \in [1, 2]$ seconds, the PDFs of both states spread out over a wide range before reaching steady state conditions. In the steady state, all states' PDFs form a prominent peak around their steady state deterministic solutions.

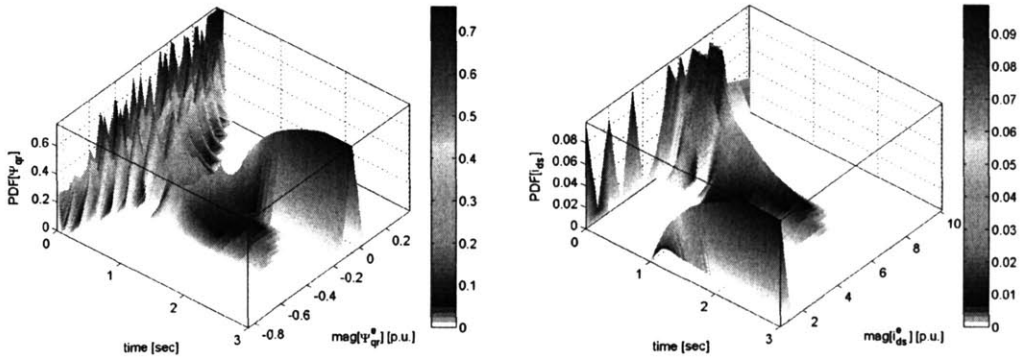

Figure 4-71: The PDFs of the q-axis rotor reactance, $\psi'^{(e)}{}_{qr}$, (left) and the d-axis stator or tie-line current, i_{dt}^{e}, (right) evolve with time due to the propagation of the rotor resistance uncertainty.

When the rotor resistance is modeled by the one dimensional random variable with $t \in [0, 3]$ seconds, the convergence rate of statistical errors can be compared among five different stochastic algorithms: MC, QMC, MEgPC, uniform MEPCM, and adaptive MEPCM. Due to the complexity of the machine's analytical solution, the reference solution from the PCM with $Nc = 2000$ is used in the L_2 error convergence computation. In this section, PCM refers to only the full-grid collocation technique. According to Figure 4-73, the MC and QMC methods respectively yield algebraic convergence rates of $O(NN^{-1/2})$ and $O(NN^{-1})$ as a function of the number

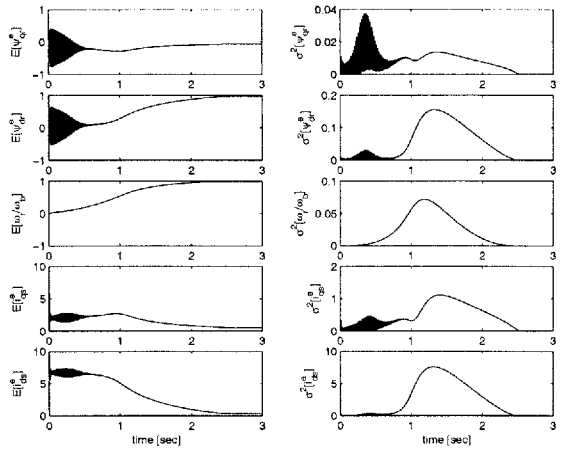

Figure 4-72: The reference stochastic mean (left column) and variance (right column) solutions of five state variables in per unit of the 200-hp induction machine, obtained from PCM with $Nc = 2000$.

of realizations, NN, similar to those obtained in Section 4.1. With NN = [10^3,10^5], the accuracy stays within a $[10^{-2}, 10^{-5}]$ range. The L_2 norm difference of statistics needs a substantially large NN to further increase the accuracy. Compared to the MEPCM and MEgPC results shown in Figure 4-74 and 4-75, a characteristic of the convergence rate again can be classified into two ranges: non-asymptotic (nonlinear) range with small N, and asymptotic (linear) range with large N. The larger the value of Nc in MEPCM and p in MEgPC is, the wider the nonlinear range becomes. This trend occurs when all solutions of coupled nonlinear equations are smooth and continuous, like those of the Kraichnan-Orszag system with the continuous solutions. The convergence rates as a function of N in the linear range are in the order of $O(N^{-4})$, $O(N^{-10})$, $O(N^{-20})$ for [$Nc = 2$ or $p = 1$], [$Nc = 5$ or $p = 4$], and [$Nc = 10$ or $p = 9$], consequently. These convergence rates also follow the approximation of the convergence relation of $O(N^{-2(p+1)})$ for MEgPC and $O(N^{-2Nc})$ for MEPCM, mentioned in Section 4.1.

Furthermore, the adaptive MEPCM with $Nc = 5$ and θ_1=[0.1, 0.01, 0.005, 0.001, 0.0005, 0.0001] yields a minor improvement in the error convergence over the MEPCM with uniformly distributed elements, as shown in Figure 4-76, since the solutions of this system are smooth and continuous. In the low accuracy region, adaptively dividing the random space into multiple elements can reduce the error much faster

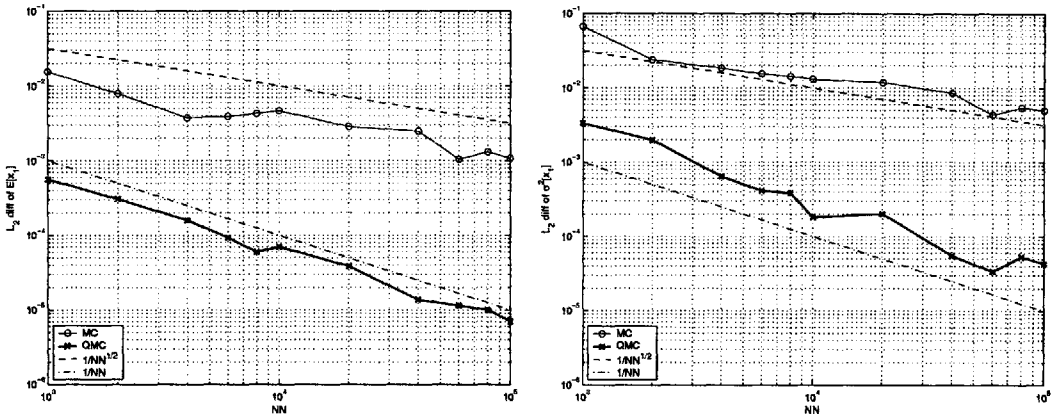

Figure 4-73: The L_2 norm error of mean (left) and variance (right) solutions as a function of realization (NN) exhibit the algebraic convergence rate of $O(NN^{-1/2})$ using pseudo-Monte Carlo and of $O(NN^{-1})$ using quasi-Monte Carlo.

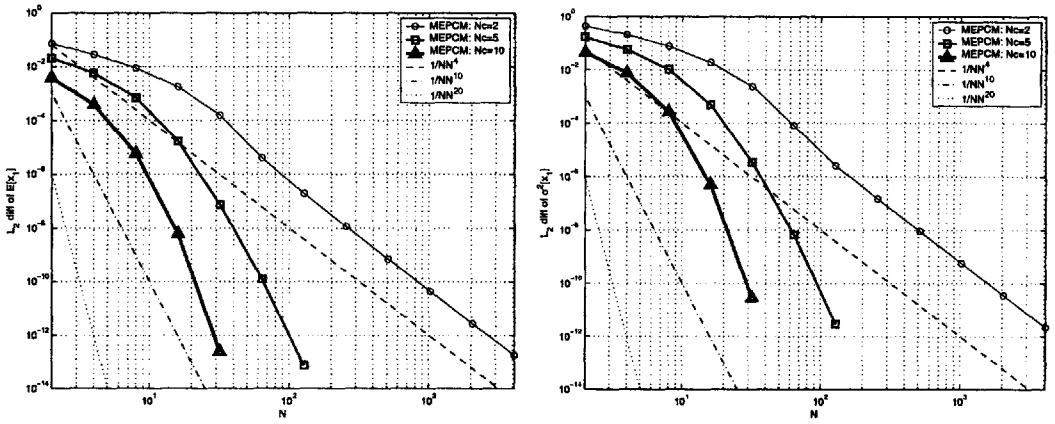

Figure 4-74: The L_2 norm error of mean (left) and variance (right) solutions as a function of N, using the MEPCM, exhibit the algebraic convergence rate of $O(N^{-4})$ for $Nc = 2$, $O(N^{-10})$ for $Nc = 5$, and $O(N^{-20})$ for $Nc = 10$.

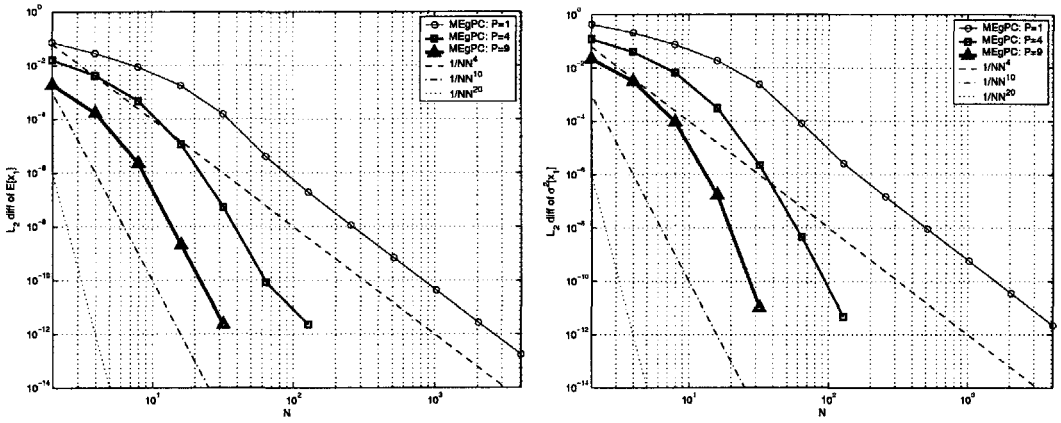

Figure 4-75: The L_2 norm error of mean (left) and variance (right) solutions as a function of N, using the MEgPC, exhibit the algebraic convergence rate of $O(N^{-4})$ for $p = 1$, $O(N^{-10})$ for $p = 4$, and $O(N^{-20})$ for $p = 9$.

than employing equally distributed elements. However, in the high accuracy region, uniformly decomposing the random space into large numbers can eliminate the error in an initial time step very quickly such that its performance is as good as that of adaptively decomposing the random space as time progresses.

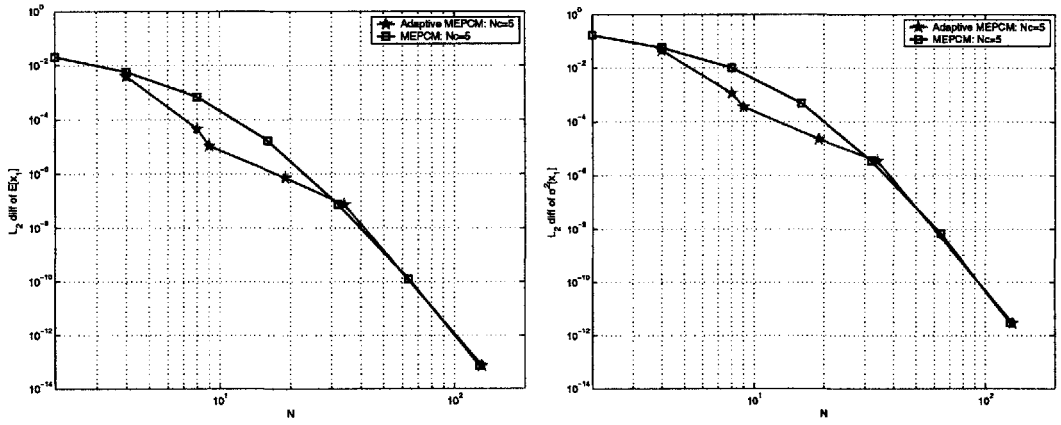

Figure 4-76: The comparison of the convergence rate of the mean (left) and variance (right) solutions between MEPCM with fixed and uniformly distributed elements and adaptive MEPCM.

In terms of the computational efficiency, we compare the computational time vs. accuracy among these four algorithms, as shown in Figure 4-77. To obtain a solution with high accuracy, the MC and QMC require a huge computational effort, and thus these two algorithms are not competitive against MEPCM and MEgPC in the one

random dimension. Also, Figure 4-77 shows a tremendous advantage of MEPCM over MEgPC for the entire range of accuracy, especially in the high accuracy region near a machine precision of 10^{-14}. The computational time of uniform MEPCM with $Nc = 5$ and 10 is about two orders of magnitude less than that of uniform MEgPC with $p = 4$ and 9. For MEPCM with $Nc = 2$ and MEgPC with $p = 1$, there is only linear improvement in accuracy as a function of the computational time because only linear polynomial chaos is used in the projection in the MEgPC, and linear approximation of uniform distribution by two collocation points is used in the MEPCM. The computational time per accuracy of the adaptive MEPCM with $Nc = 5$ is equivalent to that of the non-adaptive MEPCM with $Nc = 5$, shown in Figure 4-77.

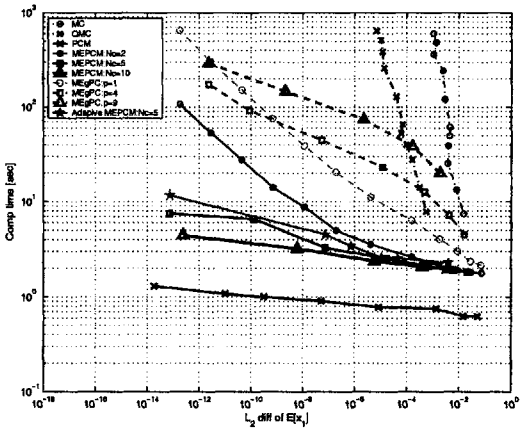

Figure 4-77: The computational time as a function of the mean error accuracy using MC, QMC, MEPCM and MEgPC with fixed element, and Adaptive MEPCM.

4.3.2 Two-dimensional random variables as stochastic inputs

Both the rotor resistance (r_r') and load torque (T_{load}) become a random variable, described by $r_r'(\omega) = \bar{r_r'} + \sigma_r \xi(\omega)$ and $T_{load}(\omega) = \bar{T}_{load} + \sigma_T \xi(\omega)$. The r_r''s mean and variance are assumed to have the same values as in the previous case. The $\bar{T}_{load}$ is set at 50 percent of the machine base torque ($\bar{T}_{load} = 0.5$) with 30 percent variation ($\sigma_T = 0.3$). Applying both parametric and load uncertainties to this induction machine during its start-up transient dynamics, statistical responses take a longer time to reach their final values, as shown in Figure 4-78. The transient responses of electrical

components, which causes fast oscillatory behavior in the first second, quickly die out, and after that the mechanical transient governs a slow response of all states.

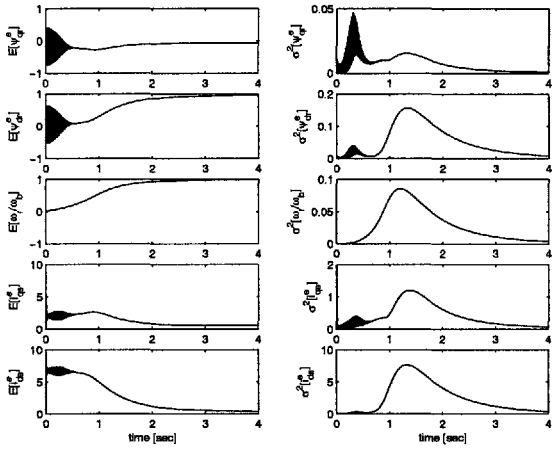

Figure 4-78: The stochastic mean (left column) and variance (right column) solutions of five state variables in per unit of the 200-hp induction machine, obtained from the reference solution using uniform MEPCM with $Nc = 10$ and $N = 90^2$.

Again, we compare the performance among MC, QMC, PCM, and uniform MEPCM techniques for these two random dimensions. The MC and QMC again converge linearly with a rate of $O(NN^{-1/2})$ and $O(NN^{-1})$, respectively. As seen in Figure 4-79, the accuracy of error convergence is contained within a range of magnitude, $[10^{-2}, 10^{-5}]$, similar to the previous section with the one random variable.

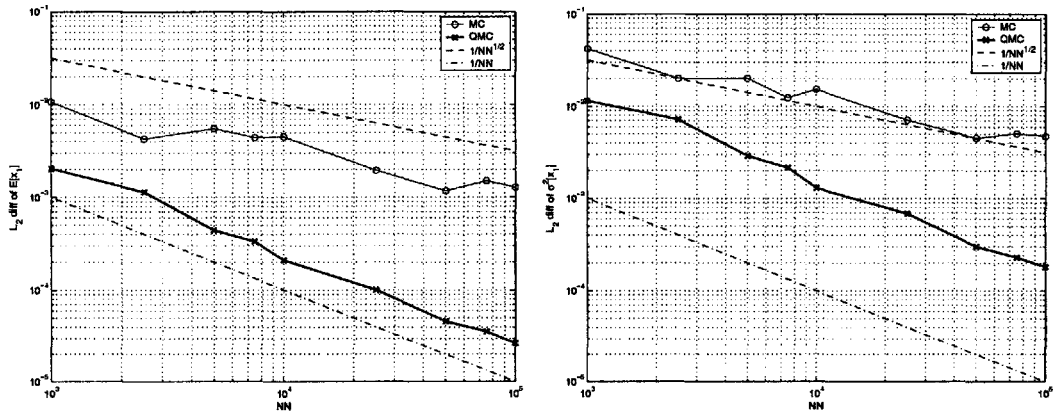

Figure 4-79: The L_2 error convergence of mean (left) and variance (right) solutions as a function of realization (NN) exhibit the algebraic convergence rate of $O(NN^{-1/2})$ using pseudo-Monte Carlo method and of $O(NN^{-1})$ using quasi-Monte Carlo method.

For the uniform MEPCM, the convergence relation of $O((N/d)^{-2(Nc)})$ is still ap-

plied to this system, similar to that of Section 4.1.7. For the fixed elements, we obtained the convergence rates of the uniform MEPCM with $Nc = [2, 5, 10]$ on the order of $O((N/d)^{-4})$, $O((N/d)^{-10})$, and $O((N/d)^{-20})$, consequently. However, the non-asymptotic convergence range is extended longer, as shown in Figure 4-80, due to a combined effect from the large variation of two random variables and the fast transient in the first second.

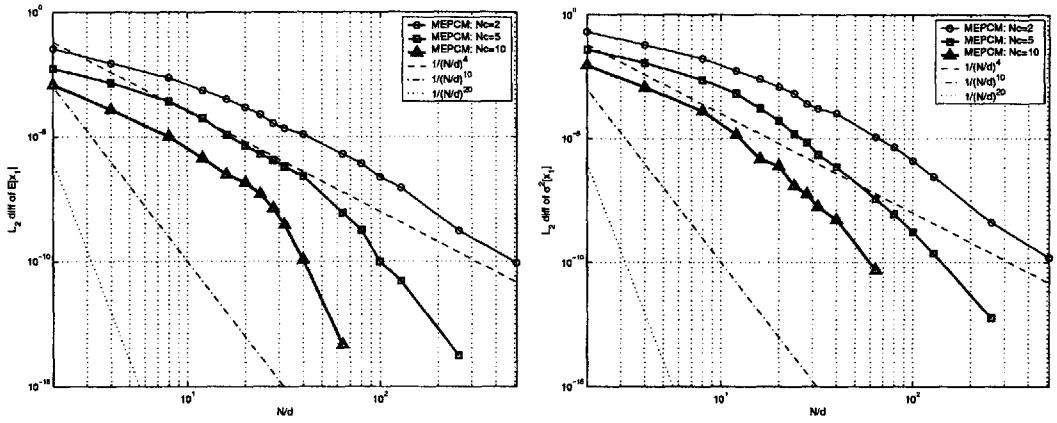

Figure 4-80: The L_2 norm error of mean (left) and variance (right) solutions as a function of N/d, using the MEPCM, exhibit the algebraic convergence rate of $O((N/d)^{-4})$ for $Nc = 2$, $O((N/d)^{-10})$ for $Nc = 5$, and $O((N/d)^{-20})$ for $Nc = 10$.

Owing to the smoothness and continuity of system solutions, the Nc-convergence of PCM exhibits an exponential convergence rate of $O(e^{-0.03(Nc/d)})$, as shown in Figure 4-81 below. The computational cost per mean accuracy is a measurement of the efficiency of these stochastic algorithms. The PCM yields the smallest computing time per accuracy. In this case, the N-convergence of the multi-element technique can improve the accuracy of the solution significantly, but we need a large Nc to see a faster computational time in the uniform MEPCM.

4.3.3 For the three dimensional random process as the stochastic input

Figure 4-82 shows the stochastic responses of all coupled states in the case when a parametric uncertainty in the rotor resistance becomes a time-dependent variable,

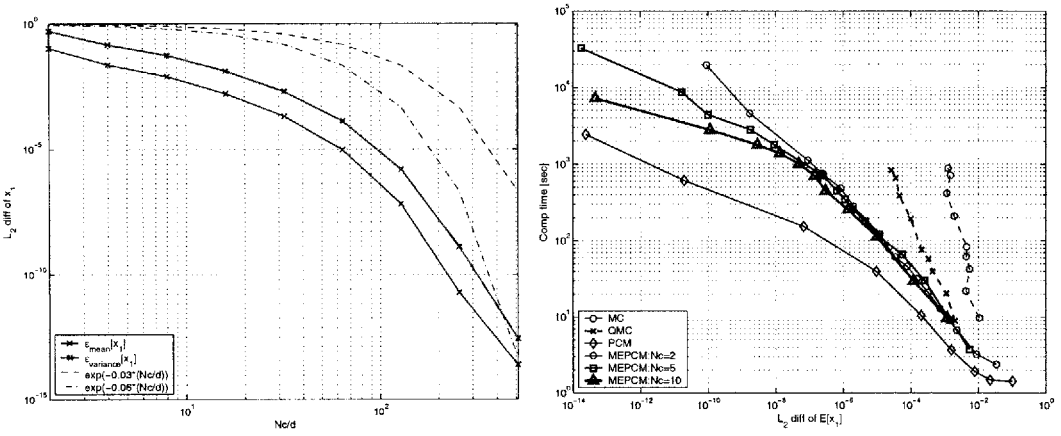

Figure 4-81: The Nc-convergence of mean and variance solutions using PCM (left) and the computational time of MC, QMC, PCM, uniform MEPCM (right).

which is correlated in time. With a slow varying r_r', statistical responses are not much different from those in Figure 4-72.

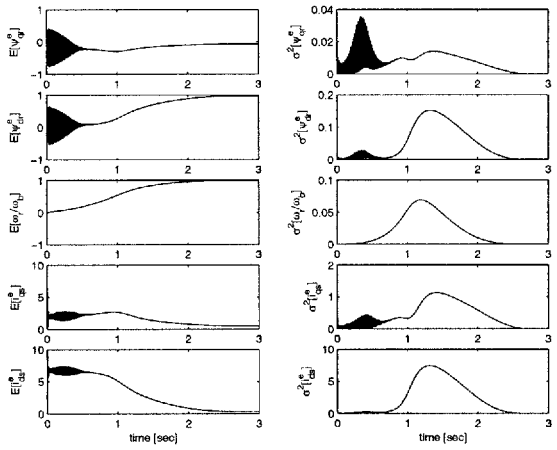

Figure 4-82: The reference stochastic mean (left column) and variance (right column) solutions of five state variables in per unit of the 200-hp induction machine, obtained from MEgPC with $p = 1$ and $N/d = 70$.

In the case of a three dimensional random process (with d=KL=3) with $t \in [0, 3]$ seconds, the accuracy and efficiency are also examined and compared among these stochastic algorithms: 1) MC and QMC, 2) full-grid uniform and adaptive MEPCM, and 3) uniform MEgPC. The reference solution in this case is obtained from the MEgPC with p=1 and total N of 343,000. According to Figure 4-83, the MC and QMC with NN=[10^3,$\cdots$,8x10^4] still yield the linear convergence rates of $O(NN^{-1/2})$

and $O(NN^{-1})$ within the accuracy range of [10^{-2},10^{-5}] similar to those with one random dimension. This confirms an advantage of the Monte Carlo method that it is insensitive to the random dimension, but its convergence rate is linear and limited to a power factor up to 1. Figure 4-84 and 4-85 show the results of the uniform MEPCM and uniform MEgPC with N=[8,...,1000]. The convergence rates of $O((N/d)^{-4})$ for [$Nc = 2$ or $p = 1$] and $O((N/d)^{-10})$ for [$Nc = 5$ or $p = 4$], also agree with the N/d convergence relation, found in the Kraichnan-Orszag Sections 4.1.8 with continuity in stochastic solutions and those in Sections 4.3.1 and 4.3.2.

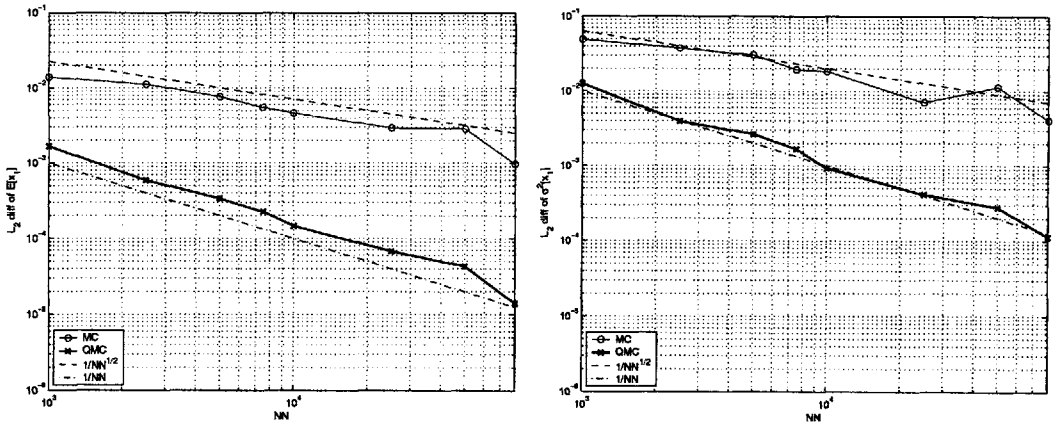

Figure 4-83: The L_2 norm error of mean (left) and variance (right) solutions as a function of realization (NN) exhibit the algebraic convergence rate of $O(NN^{-1/2})$ using pseudo-Monte Carlo and of $O(NN^{-1})$ using quasi-Monte Carlo.

Again, the multi-element technique of gPC and PCM with uniformly distributed elements exhibits both asymptotic and non-asymptotic convergence ranges, as shown in Figure 4-84 and 4-85. The rates of convergence for the uniform MEgPC and MEPCM are respectively on the order of $O((N/d)^{-2(p+1)})$ and $O((N/d)^{-2Nc})$ with a non-stationary random input. Note that both p and Nc in the uniform MEgPC and MEPCM are normalized by the random dimension. Likewise, the Nc-convergence of the PCM in Figure 4-86 yields an exponential convergence rate of $O(e^{-0.5(Nc/d)})$.

The convergence rate of MEPCM can be further improved by using the adaptive criterion to decompose the random space in three dimensions. Figure 4-86 shows that the adaptive MEPCM with $Nc = 5$ and θ_1= [0.5, 0.05, 0.01, 0.001, 0.0005, 0.0001, 0.00005] yields the L_2 error convergence rate of $O(N^{-2})$, as shown in Figure 4-86. As

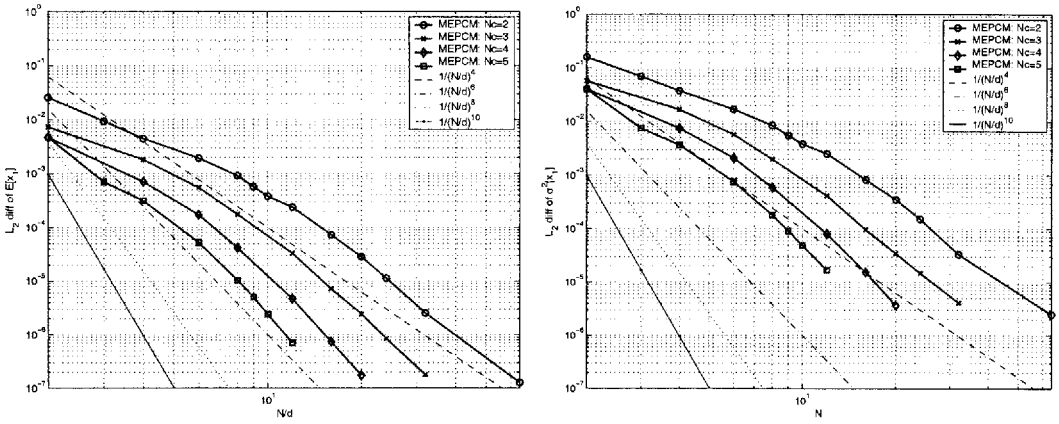

Figure 4-84: The L_2 norm errors of mean (left) and variance (right) solutions as a function of N/d, using the uniform MEPCM, exhibit the algebraic convergence rate of $O(N^{-4})$ for $Nc = 2$ and $O(N^{-10})$ for $Nc = 5$.

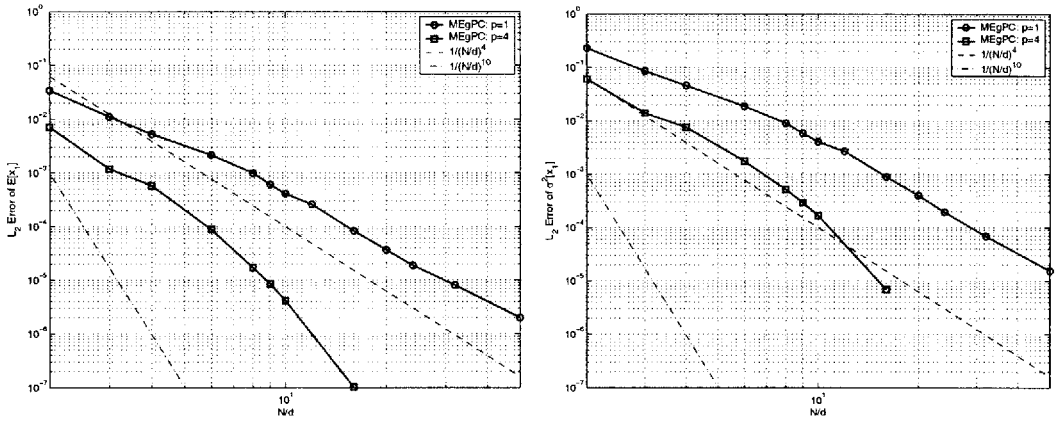

Figure 4-85: The L_2 norm errors of mean (left) and variance (right) solutions as a function of N/d, using the uniform MEgPC, exhibit the algebraic convergence rate of $O(N^{-4})$ for $p = 1$ and $O(N^{-10})$ for $p = 4$.

a result, the computational efficiency of the adaptive MEPCM surpasses that of the uniform MEPCM and approaches that of the single-element PCM, which is the best algorithm in terms of the numerical efficiency per accuracy.

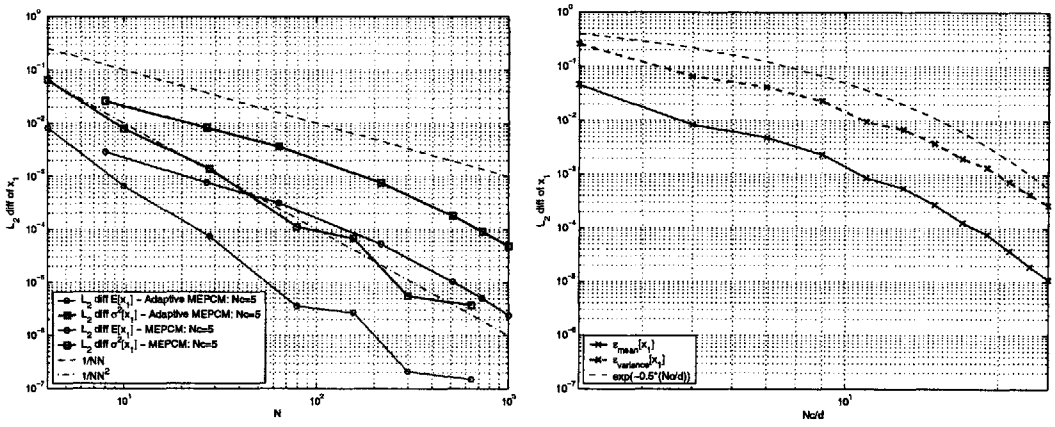

Figure 4-86: The comparison of the convergence rate of mean and variance solutions between the adaptive MEPCM and uniform MEPCM (left) and the exponential Nc-convergence of the single-element PCM.

For a random multi-dimension, the computational costs of PCM and gPC increase proportional to Nc^d nodal points and $(p+d)!/p!d!$ modes, respectively. Since the accuracy of the PCM and gPC is consequently governed by Nc and p and the relationship of $Nc = p + 1$ for the same level of accuracy is still held in the larger dimension, the computational cost of gPC grows much faster than that of PCM as we require the higher accuracy of solutions. If $Nc = 5$ and $p = 4$, the PCM and gPC require a calculation of the solution at 125 nodal points and from 56 modes in three dimensions. However, the gPC needs to compute the Galerkin projection of polynomial chaos basis, consuming more computing time. With this reasoning, the computational cost of the uniform MEgPC with $p = [1, 4]$ is even larger than that of the uniform MEPCM with $Nc = [2, 5]$, as illustrated in Figure 4-87

4.4 AC power distribution with propulsion drive

When the system becomes more complex as in the shipboard power system, the order of the mathematical model increases tremendously. We will investigate the perfor-

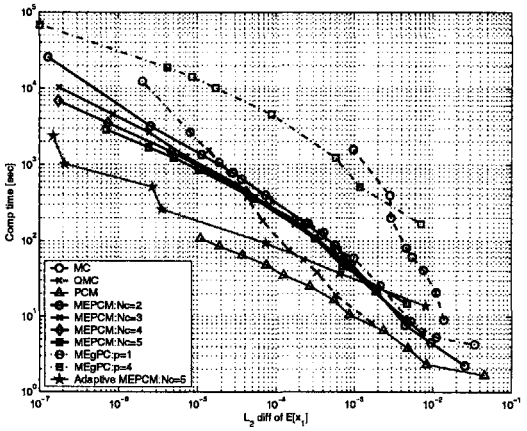

Figure 4-87: The computing time versus x_1 mean accuracy using MC, QMC, PCM, uniform MEPCM with $Nc = [2, 3, 4, 5]$, uniform MEgPC with $p = [1, 4]$, and adaptive MEPCM with $Nc = 5$.

mance of the best stochastic algorithms from Monte Carlo and Collocation approaches with a large-scale system. This section considers two different configurations of the shipboard power system. In the first configuration, the AC power generation system is connected to a main three-phase radial bus, which supplies the electrical power to two induction motors. This configuration in Figure 4-88, representing the power distribution system of a DDG-51 Navy destroyer [38], uses the first type of interconnection, discussed in Section 2.3. The entire system consists of a 3.125MW Synchronous Machine (SM) driven by a simplified version of the Allison 501 gas turbine/governor, the IEEE Type 2 voltage regulator and exciter for controlling generated voltage from the generator, an RL tie-line, and 200-hp and 150-hp Induction Machines (IM). Containing the nonlinearity in both polynomial and trigonometric forms, this model is composed of 26-order ODEs.

In the second configuration, the second type of interconnection, explained in Section 2.3, is considered because an average model of power converter can be included for the induction machine drive. Figure 5-89 displays a one-line diagram of all components: a 59 MW synchronous generator driven by ideal or constant-speed prime mover, a simplified voltage regulator/exciter, and a 50-hp induction machine with power converter drive using the constant torque technique. A mechanical torque load applied on the motor shaft is proportional to motor speed squared to mimic the load

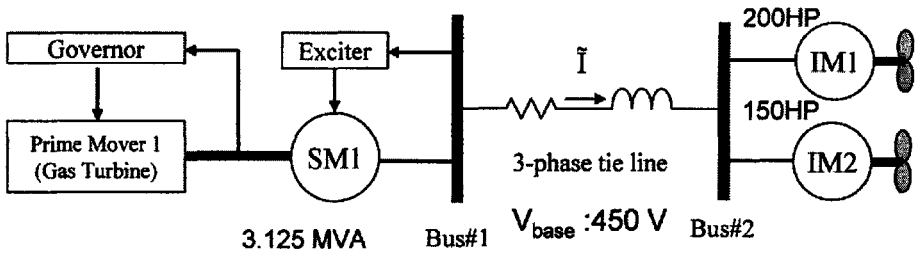

Figure 4-88: A one-line diagram of the first configuration of the AC power distribution with two open-loop induction machines for studying the stochastic analysis with 6 dimensional random variables.

characteristic of propellers. This model, obtained from the detail model in the 2003 ONR challenge problem [27], represents the Naval Combat Survivability testbeds located at Purdue and University of Missouri at Rolla. Including both continuous and discontinuous nonlinearities, the total number of states in this configuration is 30.

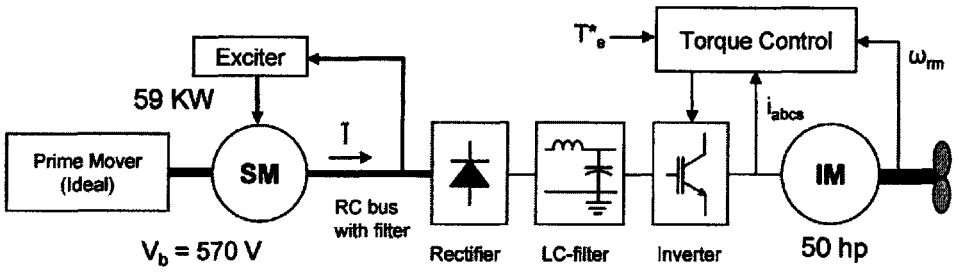

Figure 4-89: A one-line diagram of the second configuration of the AC power distribution with the closed-loop induction machine for studying the stochastic analysis with 31 dimensional random variables.

4.4.1 Results for Six stochastic inputs

In this case, six independent random variables in the system of Figure 4-88 include $[r'_{kq}, r'_{fd}, r'_{kd}]$ of SM, r'_r of both IM1 and IM2, and r_t of tie line. All of these random variables, associated with the uniform distribution, are assumed to vary within plus and minus 10 percent of their nominal values. For this system simulation, the generator is assumed to be initially in its steady-state condition and then suddenly two induction machines start from rest at zero second. Therefore, a start-up transient of

two motors, similar to the previous section, as well as an interaction among electric machines can be seen in Figure 4-90 for $t \in [0, 3]$ seconds. At first, the speed of the SM drops and then the exciter compensates for an error in the bus voltage by speeding up the generator before bringing the SM's speed back to its steady-state operation of 1 per unit. In the first second, the start-up transient of both IMs dies out. After that the interactions between SM and IMs are illustrated in the responses of the q-axis stator flux linkage of all machines. The variance of all states of both IMs contains a high peak right before reaching the steady state. This characteristic implies that the open-loop response, especially right after the start-up transient, is sensitive to the parameter variation. With the closed-loop control of the exciter, the responses of SM's variance have a smaller peak magnitude compared to those of IMs.

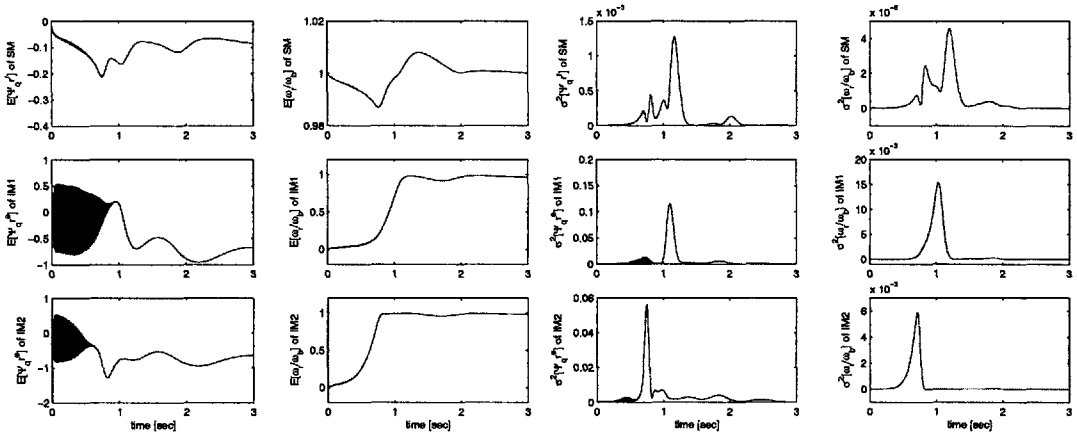

Figure 4-90: The reference stochastic mean (first two columns) and variance (third and fourth columns) solutions of the q-axis stator flux linkage and normalized rotor speed of SM, IM1, and IM2 in per unit, obtained from QMC with $NN = 1,200,000$.

To study the numerical performance of stochastic algorithms-QMC, full- and sparse-grid PCM, and sparse-grid uniform MEPCM-with this large-scale system in the first configuration, the convergence rate and computational efficiency are again considered. In this case, the reference solution for the L_2 error computation is obtained from the QMC with $NN = 1,200,000$, which requires 13,736 seconds of the computational time. With NN between 10^3 and 6x10^4, the QMC yields an algebraic convergence rate of the SM q-axis stator flux linkage (Ψ^r_{qr}) mean and variance so-

lutions on the order of $O(NN^{-1})$, shown in Figure 4-91. The error convergences of the same state using the full- and sparse-grid PCMs are shown in Figure 4-92. The rate of convergence per random dimension using both PCMs is still exponential on the order of $O(e^{-1.5(Nc/d)})$ or $O(e^{-1.5(Level/d)})$. Notice that the L_2 error of the sparse-grid PCM starts to saturated at $Level/d = 7$ because the accuracy limitation of the reference solution has been reached. From the efficiency aspect, the computing time per variance accuracy of all algorithms, illustrated in Figure 4-91, can be used for the performance comparison among these stochastic algorithms. For this large-scale system, the computational cost of the sparse-grid PCM is an order of magnitude less than that of the full-grid PCM for the same accuracy. Furthermore, the sparse-grid PCM becomes more efficient than the QMC in the high-accuracy region. Unlike the results with the small model in the last section, the sparse-grid uniform MEPCM with $Level = [2, 3]$ improves the accuracy with a much higher computational cost than the single-element sparse-grid PCM.

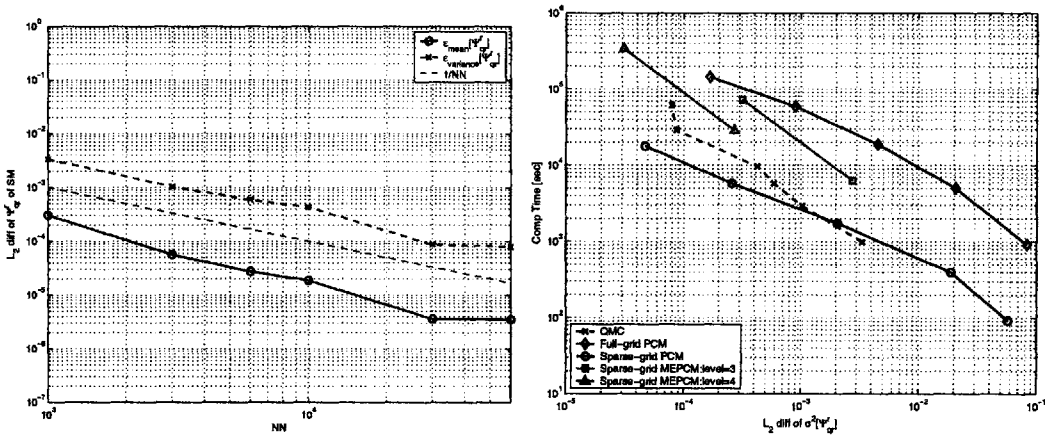

Figure 4-91: For six-dimensional random dimensions, the x_1 or ψ_{qr}^r statistical error convergence rates as a function of NN are in the order of $O(NN^{-1})$ using QMC (left) and The computational time per accuracy of these stochastic algorithms (right).

4.4.2 Results for thirty-one stochastic inputs

To demonstrate the capability of the sparse-grid PCM for handling a large random-dimension problem, all twenty nine parameters in SM, IM, RC bus, and Rectifier,

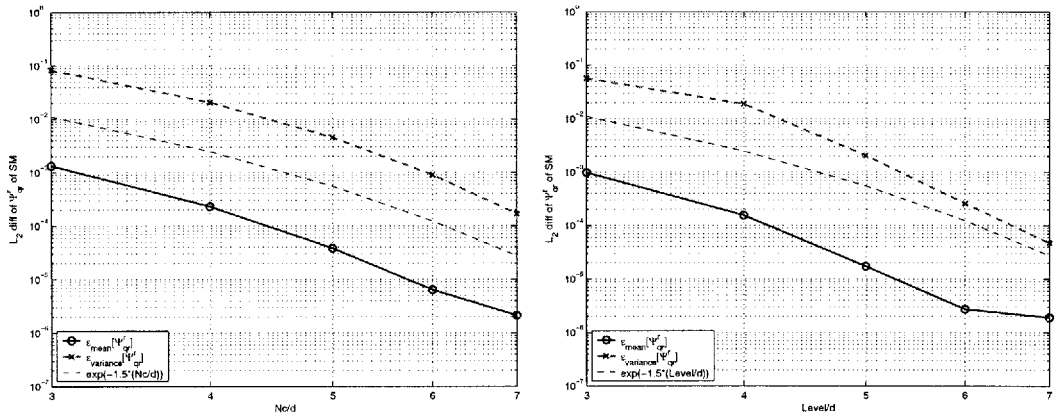

Figure 4-92: For six-dimensional random dimensions, the x_1 or ψ_{qr}^r statistical error convergence rates as a function of Nc are in the order of $O(e^{-3.2(Nc/d)})$ using the full-grid PCM (left) and of$O(e^{-1.5(Level/d)})$ using the sparse-grid PCM (right).

LC-filter, and Inverter and a mechanical torque load in the system of Figure 5-89 are assumed to be independent uniform random variables with 1 percent variation from their mean values, which are the nominal values. All the nominal values of these thirty parameters can be found in Appendix B. Furthermore, the performance of the sparse-grid PCM can be compared with that of the quasi-Monte Carlo method in the large dimension. The scenario of this simulation is that initially the synchronous generator is operating near its steady-state value and the induction machine and its torque controller is disconnected from the inverter with a switch, then at 0.35 seconds we suddenly turn on the switch to connect the induction machine and its controller with the power converter with a ramp torque command. However, with this constant-slip torque controller, we no longer experience a large start-up current from the induction machine as in the previous configuration without the propulsion drive, which can be indirectly observed from no large fluctuation in the statistical values of both current and voltage of the power converter in Figure 4-94. Due to a time limitation, the stochastic response of this system is considered between [0,0.5] seconds.

Figure 4-93 and 4-94 show the stochastic responses of the synchronous generator and the power converter, respectively. From these two figures, both the quasi-Monte Carlo with $NN = 1,000$ and sparse-grid PCM with $level = 3$ can accurately capture

the dynamics of the stochastic responses comparing to a reference solution, which obtained from the quasi-Monte Carlo with $NN = 10,000$. However, the enlargement of the generator's stochastic response, ψ_{qs}^e, reveals a minor discrepancy of the sparse-grid PCM's results from the quasi-Monte Carlo results, because of the small magnitude of $\sigma^2[\psi_{qs}^e]$.

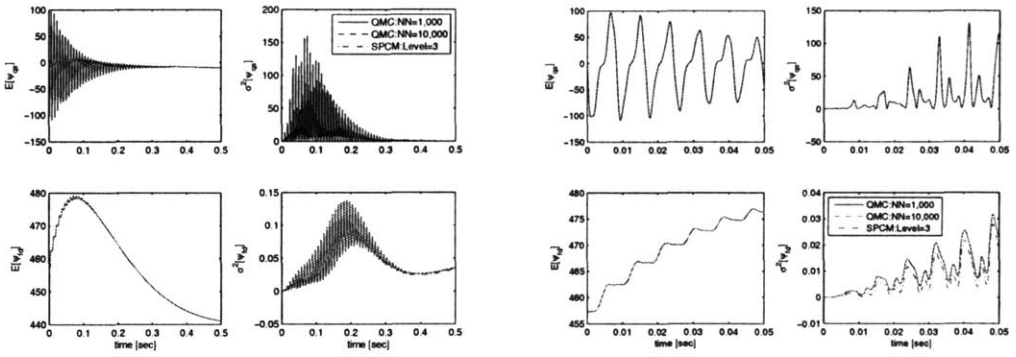

Figure 4-93: Comparison of the stochastic mean and variance solutions of the q-axis stator flux linkage (ψ_{qs}^e) and d-axis field-winding rotor flux linkage (ψ_{qs}^e) of SM-(First and Second Columns) and their enlargements-(Third and Fourth Columns), among from QMC with $NN = 10,000$ (Reference Solution), QMC with $NN = 1,000$, and sparse-grid PCM with $Level = 3$.

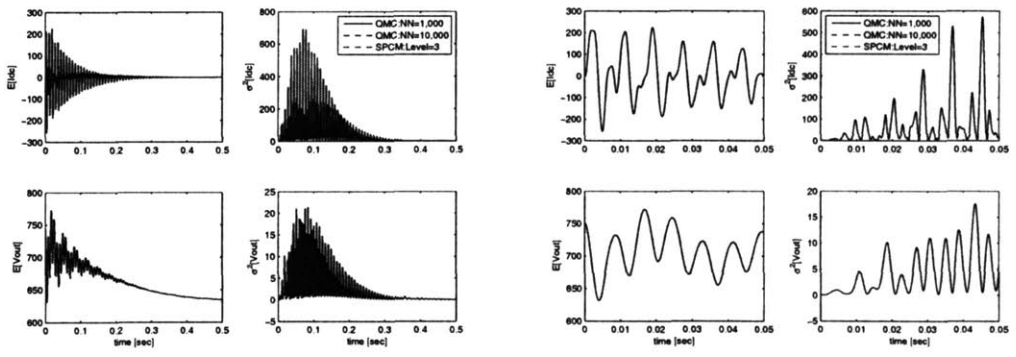

Figure 4-94: Comparison of the stochastic mean and variance solutions of the dc current in the rectifier (I_{dc}) and the capacitor voltage in the LC-link filter (V_{out})-(First and Second Columns) and their enlargements-(Third and Fourth Columns), among from QMC with $NN = 10,000$ (Reference Solution), QMC with $NN = 1,000$, and sparse-grid PCM with $Level = 3$.

To directly compare the accuracy of the solution from these two methods, Figure 4-

95 shows the ϵ_{mean} and ϵ_{var} of all state variables for the results from QMC with $NN = 1,000$ and sparse-grid PCM with $Level = [2,3]$. The ϵ_{mean}, obtained from the sparse-grid PCM with $Level = 3$ is more accurate than that from QMC with $NN = 1,000$ and vice versa for the ϵ_{var}. Notice the large ϵ_{var} are from the first seven states, corresponding to the variables of the synchronous generator. All state variables of SM exhibit a fast transient dynamics within the first fraction of a second and their variance has a small magnitude. These two reason causes the sparse-grid to quickly lost its accuracy to capture a small variation precisely and to handle a large number of oscillation in the function, as time progresses. While the variance magnitude of other state variables are about the same order of magnitude as their mean values. We summarize the accuracy ($\sum_{j=1}^{30}(\epsilon_{mean}, \epsilon_{var})$) and computational time of the QMC and sparse-grid PCM. Note that for a comparison, the computing time for the reference solution is 347,700 seconds.

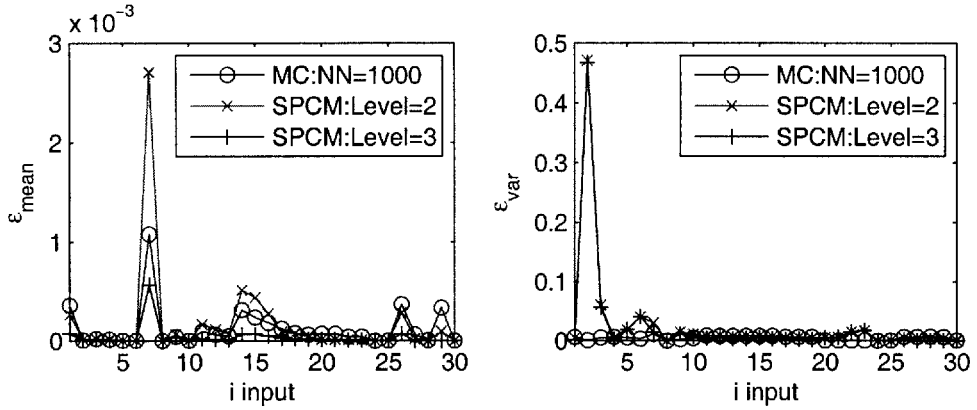

Figure 4-95: For thirty-dimensional random dimensions, the statistical error $(\epsilon_{mean}, \epsilon_{var})$ for all thirty state variables from the results of the QMC and sparse-grid PCM, comparing with the reference solution.

Table 4.4: Summary of the accuracy and computational time of the QMC and sparse-grid PCM

Method	ϵ_{mean}	ϵ_{var}	**Computing time [sec]**
QMC:NN=1,000	0.0037	0.1367	36,717
Sparse-grid PCM:Level=2	0.0053	0.7698	87,554
Sparse-grid PCM:Level=3	0.0011	0.6907	1,355,700

Chapter 5

Sensitivity Analysis

Studying how the uncertainties of parameters, external disturbances, and inputs propagate through to the outputs of a system is known as sensitivity or uncertainty analysis. Sensitivity analysis is valuable especially for examining the extreme or worst case in a complex system and estimating the robustness and reliability of the system against uncertainties. To reduce the risk of equipment damage and the time-consuming nature of experimental set-up, we can perform sensitivity analysis on mathematical models, which can closely match the characteristics of physical systems.

In the literature, sensitivity analysis has been studied from two different perspectives – ranking the inputs' significance or evaluating the outputs' tolerance limit –, when the inputs are known to vary within a specified range. In the first approach, sensitivity analysis provides information on which inputs have more influence on the system outputs and on how strong is the coupling or interaction among inputs. Two main classes of techniques for ranking these inputs in sensitivity studies are local and global methods. The local approach [21], [48], which relies on a partial derivative of output with respect to input, is used to measure the sensitivity around a local operating point. When the system has strong nonlinearity and the input uncertainties are contained within a wide range, the local sensitivity does not provide full information to the system operators. On the other hand, the global approach examines the sensitivity from the entire range of the parameter variations. The screening methods,

which are included in the global methods, rank the important factors and their interaction among a large number of system parameters. These screening techniques are based on "One-at-A-Time" (OAT) perturbation of parameters, which directly yields the main input effect without input interaction. Several screening methods have been proposed in the literature, for example, the Morris method [39], [51], Cotter's method [17], factorial experimentation [7], and iterated fractional factorial design [50]. Different techniques have their strengths and weaknesses. The Morris method can efficiently identify the sensitive parameters when a system has a large number of inputs or parameters. Only the worst-case analysis of a system is examined for the upper and lower bounds of system variables in Cotter's method. In factorial experimentation, all combinations of inputs' interactions as well as the main effects are evaluated at the same time, which requires intensive computation. Iterated fractional factor design reduces this large input-combination computation by evaluating only important combinations. As a result, the sensitivity indices might be biased. Other global sensitivity analysis techniques are regression analysis [51], and ANOVA decomposition [53], etc. All of these techniques rank the importance of each input uncertainty to the system outputs. The regression analysis is limited because of the required prior knowledge about the structure of the system. Similarly, the ANOVA decomposition requires the system to be expressed in an orthogonal decomposition, which is not applicable to general functions or systems.

The second category of sensitivity analysis is tolerance analysis. In contrast to ranking the significance of inputs, this kind of sensitivity analysis works in terms of the tolerance limit or probability of failure when one or more inputs are known to fluctuate within a specific range due to environment variation or random noise. Using a mathematical model of the system, the tolerance limit has been examined using worst-case analysis and root-sum-square analysis [8]. However, most systems are nonlinear; therefore, the maximum and minimum of worst cases cannot truly capture the tolerance limits of the system. Boyd [8] used the Monte Carlo method to specify the tolerance limits of linear electronic circuits, while Hockenberry [21] studied tolerance limits using the full-grid PCM with only a single random variable.

In this chapter, four new sensitivity analysis techniques for ranking the inputs' significance and the nonlinear and coupling effects of inputs are introduced and then the performance and limitations of each approach are investigated with both static functions and systems of differential equations. Two different approaches - 1) gradient-based sensitivity and 2) variance-based sensitivity - are developed in this section. Then, sensitivity results from both approaches are compared against that of the Morris method. Section 5.1 briefly explains the concept and advantages of the Morris method [39]. Next, the Monte Carlo Sampling and Collocation methods, based on an "One-At-a-Time" (OAT) randomized gradient approximation, are explained in detail. Furthermore, two new techniques - variance and inverse variance methods - based on an OAT variance calculation are introduced and applied to the problem of parameter screening as well. All sensitivity algorithms developed here are based on stochastic solutions with inputs and parameters varying with their random space; thus, these algorithms can be further applied with correlated random inputs or parameters as well.

5.1 Parameter Screening

Practically, when the system has hundreds or thousands of input parameters $[x_1, \ldots, x_k]$, it is almost impossible to fully investigate all combinations of input parameters. Therefore, parameter screening is needed to examine which inputs have the most effect on the output and to rank those inputs accordingly, so that the smallest number of further experimental designs can focus only on the sensitive set of parameters. To investigate the One-At-a-Time (OAT) global sensitivity, an elementary effect of i input on j output (EE_i^j) is defined as the approximated gradient. Basically, EE_i^j is a ratio of the difference in outputs $y_j(\mathbf{x})$ over Δ when only i input deviates from its nominal value with Δ magnitude. This definition of EE_i^j is identical to that of Morris [39]. The EE_i^j can be formulated as the following:

$$EE_i^j = \frac{y_j(x_1, x_2, \ldots, x_i + \Delta, \ldots, x_k) - y_j(x_1, x_2, \ldots, x_i, \ldots, x_k)}{\Delta}, \qquad (5.1)$$

where x_i with $i = 1, \ldots, k$ is contained within a domain of variation. For y_j outputs with $j = 1, \ldots, n$, we need a total of $n \times k$ computations of EE_i^j. Using the local gradient computation, when $\partial y_j / \partial x_i$ is equal to 1) zero, 2) a non-zero constant, or 3) a non-constant function of input parameter/s, the effects of x_i on y_j are 1) negligible, 2) linear and additive, or 3) nonlinear and coupled, respectively. The numerically approximated gradient can capture all the above effects, called the elementary or first-order effect. If all x except x_i are fixed at their nominal values, the EE_i^j can only rank the input parameter according to the first-order or elementary effect without specifying any influence of the interaction among inputs. By randomizing all values of $\mathbf{x}$ in computing EE_i^j, the interaction effects can be discovered from the variation of the EE_i^j distribution. With this concept in mind, we present the gradient-based methods - Morris, Monte Carlo Sampling, and Collocation methods - and the variance-based method, then compare their accuracy and efficiency among these approaches.

5.1.1 Morris Method

The Morris method considers the OAT EE_i^j to identify the significant first-order and interaction effects of input parameters with only a few evaluations of EE_i, which is proportional to k input. The basic methodology of this approach is to randomly select an initial condition and construct a randomized trajectory in a high-dimension input space for r trials. Thus, the mean and standard deviation of EE_i^j resulting from i input dimension consequently represent the first-order effect of i input and interaction of other inputs with the i input. Originally, all input parameters in the Morris method [39] are assumed to be independent uniformly distributed; nevertheless, the normal distribution can be applicable to parameters in this method as well [12]. Unlike the regression analysis, the input interaction requires a high-order polynomial approximation in the input-output relation, which leads to more computational cost for better accuracy. However, the Morris method becomes more efficient when $k \gg n$.

The procedure to construct the OAT randomized trajectory can be described as the following. First, each input dimension of the k-dimensional hypercube is divided into a grid with p uniform space, $[0, 1/(p-1), 2/(p-1), \ldots, 1]$, such that the initial

condition, $\mathbf{x}^*$, can be randomly assigned to one of these grid points. According to Morris, the value of Δ is set as $p/(2(p-1))$ using an even p value and $p > 2$ such that Δ optimally covers the k-dimensional p-level random space with an equal probability. And the randomized trajectory is contained within the range of input variation.

Second, a $(k+1) \times k$ $\mathbf{B}$ matrix, a lower-triangular matrix, is expressed in the following form:

$$B_{ij} = \begin{cases} 0 & \text{for } i \leq j \\ 1 & \text{for } i > j \end{cases} \tag{5.2}$$

Each row of the $\mathbf{B}$ matrix is different from its adjacent row by only one element; therefore, the row difference of the $\mathbf{B}$ matrix times Δ, called $\Delta\mathbf{B}$, forms the deterministic trajectory of the elementary effect, as shown in Figure 5-1. To construct an OAT randomized matrix, $\mathbf{B}^*$, from $\mathbf{B}$ matrix, Morris [39] proposed the following formulation:

$$\mathbf{B}^* = (\mathbf{J}_{k+1,1}\mathbf{x}^* + (\Delta/2)[(2\mathbf{B} - \mathbf{J}_{k+1,k})\mathbf{D}^* + \mathbf{J}_{k+1,k}])\mathbf{P}^*, \tag{5.3}$$

where $\mathbf{x}^*$ is the random initial vector in a k dimension, $\mathbf{D}^*$ is a k-dimensional diagonal matrix with each element equal to either +1 or -1 with equal probability, $\mathbf{P}^*$ is a $k \times k$ random permutation of an identity matrix, and $\mathbf{J}$ is a matrix with all elements equal to 1. The role of $\mathbf{P}^*$ matrix is to guarantee an equal probability of the random elementary effect in each input direction. The last step is to construct r trials of this randomized $\mathbf{B}^*$ matrix such that the r random trajectories can be obtained from the row difference of $\mathbf{B}^*$, called $\Delta\mathbf{B}^*$ matrix. To distinguish between the row difference of $\mathbf{B}$, $\Delta\mathbf{B}$, and the row difference of $\mathbf{B}^*$, $\Delta\mathbf{B}^*$, we show one of the r trajectories from $\Delta\mathbf{B}$ and $\Delta\mathbf{B}^*$ for $p = 4$ in Figure 5-1. In this case, $\Delta\mathbf{B}^*$ is

$$\mathbf{B}^* = \begin{pmatrix} 1 & 1 & 2/3 \\ 1/3 & 1 & 2/3 \\ 1/3 & 1 & 0 \\ 1/3 & 1/3 & 0 \end{pmatrix}. \tag{5.4}$$

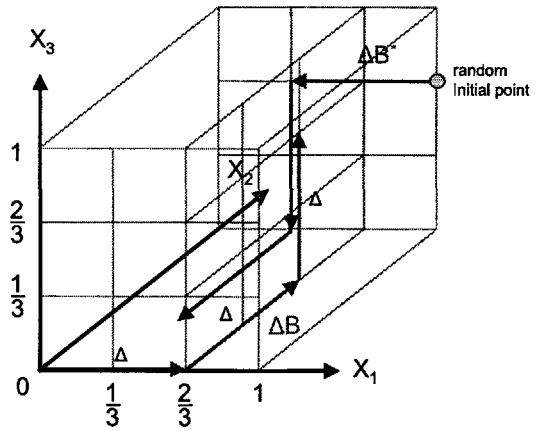

Figure 5-1: The trajectories from $\Delta\mathbf{B}$ and $\Delta\mathbf{B}^*$ for $p = 4$

The total computational cost consists of two parts: generating the randomized trajectory in the order of $O(r \times k)$ and evaluating the EE_i for one output using the randomized trajectories in the order of $O(r \times (k+1))$. The computing cost of the randomized trajectories is shown in Figure 5-2 as a function of the number of realizations (NN) and the input dimensions (k). This plot reveals the exponential cost of forming the randomized trajectories as the number of inputs increases.

Note that, as we increase the p-level in this k dimensional space, the value of Δ approaches $1/2$. This minimum Δ of $1/2$ seems to constrain the randomized trajectory on the boundary more than in the interior of the input domain. Thus, the approximated gradient in the Morris method is described in the global sense, which cannot be compared with the partial derivative around the operating point in the local sense. To avoid averaging out the effects from the i input in the EE_i^j computation, we use the absolute difference of the j output, as shown below.

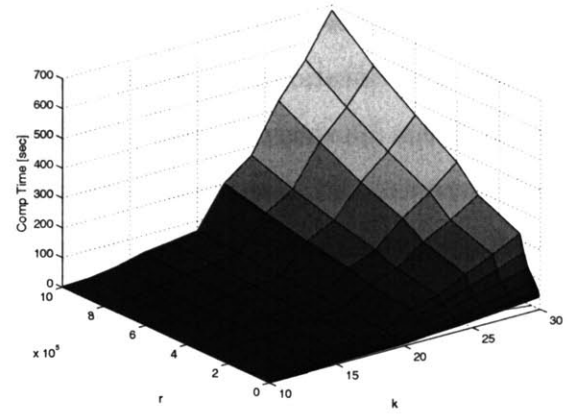

Figure 5-2: The computational cost of generating randomized trajectories as a function of NN and k.

$$EE_i^j = \frac{|y_j(x_1, x_2, \ldots, x_i + \Delta, \ldots, x_k) - y_j(x_1, x_2, \ldots, x_i, \ldots, x_k)|}{\Delta}. \quad (5.5)$$

The Morris method was first developed for ranking the sensitivity of a multi-input function, called a static function. To extend the capability of the Morris method for solving Ordinary Differential Equations (ODE), we can view the computation of the elementary effect at each time step as a random perturbation in each input dimension with fixed length Δ. Due to the requirement of random trajectory generated in this approach, $(k+1)\times r$ deterministic ODE must be solved at the random initial condition. Then, at each time step we can compute the statistics of EE_i^j as in the static function.

5.1.2 Monte Carlo Sampling Method

Instead of computing the statistics of the EE_i from the randomized trajectories on the p-level grid in the Morris method, the Monte Carlo Sampling method can be used to randomly generate the NN initial conditions in the k-dimensional inputs, and then the elementary effect in each direction can be computed at these NN random initial points. The mean of each i elementary effect or $E[EE_i^j]$ can be directly used to rank input parameters. In addition, $\sigma[EE_i^j]$ can specify the respective influences of inputs' interaction and nonlinearity on the output. To obtain smooth convergence in the result, the same random realizations in the small NN case are reused in the

large NN case. The main advantage of this approach is that the EE_i computation is not constrained on the p-level grid location as it is in the Morris method. Therefore, in a system with large inputs, this approach should be more efficient than the Morris method because no construction of the randomized trajectories is required and the input domain is covered more thoroughly to examine the input interaction. However, a large number of realizations (NN) is needed to guarantee the convergence of the EE_i^j statistics.

To demonstrate this methodology, Figure 5-3 shows 9 realizations of a random initial condition and direction in the EE_i computation with fixed Δ in a three-dimensional input space. The total evaluation of output for k elementary effects is on the order of $O(NN \times k)$ for the k inputs; therefore, the accuracy of $E[EE_i^j]$ and $\sigma[EE_i^j]$ depends on the convergence characteristic of the Monte Carlo method, $1/\sqrt{NN}$ and $1/NN$ for pseudo- and quasi-random sampling techniques, respectively.

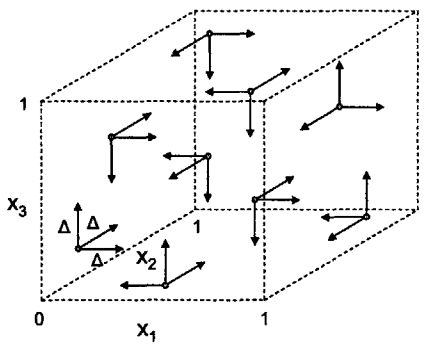

Figure 5-3: With 9 realizations, the random direction and initial condition in each direction of a three-dimensional input space are used for computing the EE_i for $i = 1, 2, 3$ with a fixed Δ.

Because of the simple structure of this technique, the sensitivity analysis of any static function can be easily implemented. Furthermore, applying this technique to analyze the sensitivity of ODE requires solving only NN ODE problems. At each time step, we perturb the system inputs one at a time with a fixed Δ. Similar to a maximum limit of the Δ magnitude in the Morris method, which equals $\frac{1}{2}$ for an input range between $[0, 1]$, we assign the Δ magnitude to be half of the input range.

If Δ is greater than $\frac{1}{2}$ of the input range, the distribution of EE_i^j might be misleading due to possible strong nonlinearity present in the system, and the value of $x_i + \Delta$ in EE_i^j computation can exceed the input range. If $x_i \pm \Delta$ is outside the inputs' range, the perturbation direction with Δ must be reversed such that the input variation is confined within the specified range.

5.1.3 Collocation Method

To further improve the accuracy and efficiency of this parameter screening technique, the initial condition of the EE_i^j computation can be selected at the collocation points instead of at the random sampling points; thus, the PCM technique should give us an advantage in computing the statistics of EE_i^j. The procedure for this approach is similar to the Monte Carlo Sampling method. First, we specify a distance of Δ in computing the EE_i^j and the level of accuracy or the number of collocation points, using either the full-grid or sparse-grid PCM. Second, the elementary effect in each i-input direction is calculated at the collocation point with a random direction of Δ. Lastly, the mean and standard deviation of EE_i are found from the quadrature, as described in Section 3.4. Again, $E[EE_i^j]$ and $\sigma[EE_i^j]$ consequently represent the first-order effect and the nonlinear and coupling effect of inputs. As shown in Section 4.1, when all parameters in the system are deterministic and only external input or systems' parameter is stochastic, we can expect an exponential convergence rate in statistical results. On the other hand, with random direction of Δ in the gradient computation of EE_i^j, the convergence rate of the EE_i^j statistics is not necessary an exponential when a function is non-monotonic. As shown in the next section, the statistical convergence becomes algebraic, but the rate is still faster than that of the Monte Carlo Sampling method.

To illustrate the concept of this method, Figure 5-4 shows how we combined the approximated gradient calculation with the full-grid collocation method. The computational cost of using the PCM depends on the input dimension, which is described by $O(N_c^k \times k)$ for the full-grid PCM where N_c is a number of collocation points per random dimension and by $O(n(L,k) \times k)$ for the sparse-grid PCM where $n(L,k)$ is

a number of collocation points at level, L, in k input dimensions. Similar to the constraint in the Morris method, most of the collocation points are on the boundary of the input domain; therefore, using the sparse-grid PCM with this technique cannot thoroughly explore an input interaction. To extend this technique to study the sensitivity of ODE, we need to solve N_c^k ODEs at each time step.

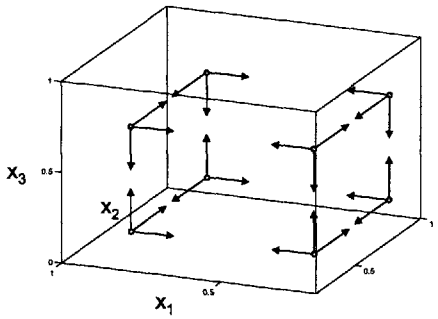

Figure 5-4: With 8 collocation points or $N_c = 2$ of the full-grid PCM, the approximated gradient, EE_i for $i = 1, 2, 3$, with a fixed Δ is computed at the collocation points with a random direction along each dimension in a three-dimensional input space.

5.1.4 Variance Method

The Variance method introduced here directly takes advantage of the efficiency and accuracy of the PCM to identify each input sensitivity and input interaction. This method relies on a variation of the output when only one input is a random variable instead of using the approximated gradient to measure the sensitivity of each input. Note that here we use the standard deviation as a sensitivity index when we refer to the Variance method. First, let us define the variance effect (VEE_i), closely related to the EE_i, of each input on the output, $y^j(x_1, \ldots, x_k)$ for $j = 1, \ldots, n$, as the following:

$$\begin{aligned} VEE_i^j &= E_{x_{i \neq j}}[\sigma_{x_i}[y^j(\mathbf{x})]] \\ &= \int_{x_1} \cdots \int_{x_{i-1}} \int_{x_{i+1}} \cdots \int_{x_k} \sigma_{x_i}[y^j(\mathbf{x})] dx_1 \cdots dx_{i-1} dx_{i+1} \cdots dx_k, \end{aligned} \tag{5.6}$$

where σ_{x_i} denotes the standard deviation of the j output ($y^j(\mathbf{x})$) when only x_i input is a random variable and the other inputs are fixed at the collocation points in the $k-1$ input dimension. $E_{x_{i\neq j}}[\,]$ represents an expectation of all other inputs except the x_i input. Formulating an OAT variation of each input in this way, the interaction of the x_i input with the others, called IEE_i, can be described by

$$\begin{aligned} IEE_i^j &= \sigma_{x_{i\neq j}}[\sigma_{x_i}[y^j(\mathbf{x})]] \qquad (5.7) \\ &= \sqrt{\int_{x_1}\cdots\int_{x_{i-1}}\int_{x_{i+1}}\cdots\int_{x_k}(\sigma_{x_i}[y^j(\mathbf{x})]-VEE_i)^2 dx_1\cdots dx_{i-1}dx_{i+1}\cdots dx_k}. \end{aligned}$$

Again, $\sigma_{x_{i\neq j}}[\,]$ denotes a standard deviation of all other inputs except the x_i input. The magnitude of IEE_i can only specify the coupling of the i parameters without taking into account the nonlinearity of the x_i term. Therefore, an exponential convergence of both VEE_i and IEE_i can be expected with use of the full-grid PCM in each dimension for low and medium input dimensions when the system responses are smooth and continuous. However, the efficiency of the sparse-grid PCM is not applicable to this method, especially for computing $\sigma_{x_{i\neq j}}[\,]$, because the collocation points of the sparse-grid PCM are not distributed evenly per direction in the input domain. The evenly distributed collocation points of the full-grid PCM allow for a thorough exploration of the interaction of the x_i input with the other inputs.

Figure 5-5 demonstrates how to obtain the elementary and coupling effects from the standard deviation of each x_i input in the case of three input parameters. The computational cost to obtain VEE_i is approximately $O(N_c^k \times k)$, which is the same order of magnitude as that of the Collocation method. Nevertheless, this Variance method yields a more accurate sensitivity solution than the two previous methods for the low input dimensions due to error only in its stochastic solution.

This technique can be further applied to compute the sensitivity of input parameters in a system of ODEs by solving N_c ODEs for one input at each time step; thus, with k inputs, we need to solve the total ODEs of N_c^k for the OAT sensitivity as well as parameter interaction. Similar to a static function case, we compute the standard deviation of the system integration with respect to the x_i using one-dimensional

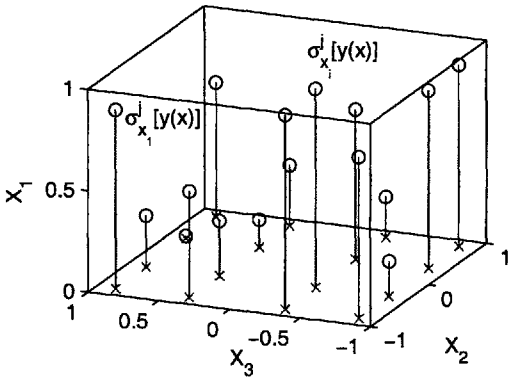

Figure 5-5: With $N_c = 4$ in the full-grid PCM, the standard deviation of the x_1 input is computed at the full-grid collocation points, where x_2 and x_3 are assumed to be independent random variables, such that the elementary effect and interaction of x_1 with the other inputs can be uncovered.

full-grid PCM, while all other inputs are fixed at the collocation points of the $k-1$-dimensional full-grid PCM. Then, we compute the standard deviation of σ_{x_i} with respect to $x_{i \neq j}$ for measuring the parameter interaction.

5.1.5 Inverse Variance Method

Consider a dual concept of the Variance method just described. This technique examines the inverse of how unimportant each input parameter is in the system output, $y^j(x_1, \ldots, x_k)$, which is related to the first-order effect. Let us define the first-order effect of the x_i input as $IVEE_i$, described in the following equation:

$$IVEE_i^j = \frac{1}{E_{x_i}[\sigma_{x_{i \neq j}}[y^j(\mathbf{x})]]}, \tag{5.8}$$

where the denominator is defined as

$$E_{x_i}\Big(\sqrt{\int_{x_1} \cdots \int_{x_{i-1}} \int_{x_{i+1}} \cdots \int_{x_n} \big(y(\mathbf{x}|x_1, \ldots, x_{i-1}, x_{i+1}, \ldots, x_k \in \xi) - E_{x_{i \neq j}}[y(\mathbf{x})]\big)^2 dx_1 \cdots dx_{i-1} dx_{i+1} \cdots dx_k}\Big),$$

where $\sigma_{x_{i \neq j}}[y^j(\mathbf{x})]$ is the standard deviation of the output when all inputs except the i input are random variables, which is described as the negligible effect of the x_i input

on the output. $E_{x_i}[\ ]$ represents the expectation of the i input. An inverse of the $E_{x_i}[\sigma_{x_{i\neq j}}[f(\mathbf{x})]]$ specifies the important effect of the x_i input. Likewise the coupling effect of the i input with the other inputs can be examined from the $IIEE_i$, defined below:

$$IIEE_i^j = \sigma_{x_i}[\sigma_{x_{i\neq j}}[y^j(\mathbf{x})]], \tag{5.9}$$

where $\sigma_{x_i}[\ ]$ stands for the standard deviation of the i input. Likewise, the $IIEE_i$ can only capture the coupling effect of i input with the others, not the nonlinearity associated with x_i. According to these definitions, the sparse-grid PCM can be directly employed for computing $\sigma_{x_{i\neq j}}[\ ]$, especially for large input dimensions. Owing to the efficiency of the full-grid PCM in a small input dimension, $E_{x_i}[\ ]$ and $\sigma_{x_i}[\ ]$ can be computed with the Gauss quadrature. Therefore, this technique can provide a fast convergence of $IVEE_i$ and $IIEE_i$ accuracy with less computational cost, particularly in the high input dimension. The total computational cost is in the order of $\mathrm{O}(n(L,k-1)\times Nc\times k)$, where $n(L,k-1)$ is a number of collocation point at level, L, in $k-1$ input dimension. Thus, the computational cost of this method should be several orders of magnitude smaller than that of the Variance method when k is large.

To explain the concept of this method in a three-dimensional input space, Figure 5-6 shows how to obtain the effect of excluding the x_1 input by considering the standard deviation of x_2 and x_3 with fixed x_1 at the full-grid collocation points. The inverse of the mean of $\sigma_{x_2,x_3}[f(\mathbf{x}/x_1 \text{ is fixed}, x_2=\xi_1, x_3=\xi_2)]$ with respect to x_1 can be used to rank the significance of the x_1 input. Moreover, the standard deviation of this quantity with respect to x_1 identifies the coupling effect of x_1 with the other inputs.

Because of the indirect measurement of the input sensitivity in this technique, the input sensitivity of the dynamical system, particularly the input interaction, cannot be captured accurately, if we consider the entire length of time. Nevertheless, at each time step, this technique still can provide the ranking of the input's influence. Thus, this technique is more suitable for the sensitivity analysis of static functions than the

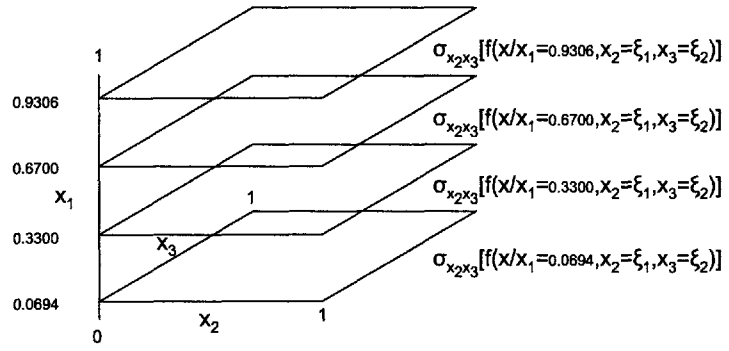

Figure 5-6: For the full-grid PCM with $Nc = 4$ in the first direction, the standard deviation of x_2 and x_3 inputs is computed at the sparse-grid collocation points, where the x_1 is assumed to be fixed at the full-grid collocation point. The inverse of the mean of σ_{x_2,x_3} with respect to x_1 can identify the elementary effect of x_1, while the standard deviation of σ_{x_2,x_3} with respect to x_1 specifies the coupling effect of x_1 with the others.

ODE.

5.2 Comparison of Sensitivity Analysis on Static Functions

In this section, let us consider examples of 8 static functions and a complex function with 12 input parameters, modified from the Morris paper. In all static function examples, the accuracy of each algorithm is improved by increasing the governing parameter, as shown in Table 5.1.

5.2.1 Linear Static Function

The first linear static function is

$$y_1 = 63x_1 - 70x_2 + 15x_3 \text{ for } 0 < x_i < 1. \tag{5.10}$$

Table 5.1: The range of parameters that controls the accuracy of each sensitivity analysis algorithm

Method	Range of the governing parameter
Morris with $p = 16$ or $\Delta = \frac{8}{15}$	r=[50, 10^2, $5x10^2$, 10^3, $5x10^3$, 10^4, $3x10^4$, $8x10^4$, 10^5, $3x10^5$, $8x10^5$]
MC Sampling with $\Delta = \frac{1}{2}$	NN=[10, 10^2, $5x10^2$, 10^3, $5x10^3$, 10^4, $5x10^4$, 10^5, $5x10^5$, 10^6]
Collocation with $\Delta = \frac{1}{2}$	Nc/d=[2,8,10,20,30,40,50,60,70,80,100,120]
Variance	Nc/d=[2,6,10, 14,20,30,40,50,60,80,100,120]
Inverse Variance	$Nc = 8$ and $Level$=[2,3,4,5,6,7,8,9]

Due to the linearity of this function, the EE_i, which approximates the gradient computation in the global domain, should yield the same result as the local method, which computes the sensitivity index from the partial derivative of y with respect to x_i. For this function, $[E[|\frac{\partial y_1}{\partial x_1}|], E[|\frac{\partial y_1}{\partial x_2}|], E[|\frac{\partial y_1}{\partial x_3}|]]|_{x_i \subset U[0,1]} = [63, -70, 15]$ using the Monte Carlo method with a million realizations. As mentioned earlier, the estimated mean and standard deviation of EE_i can consequently rank the importance of each input to the output and identify both a nonlinearity of the i input and an interaction of that input with the others, respectively. Therefore, the plot of $\sigma[EE_i]$ versus $E[EE_i]$ can capture both of these effects. The bottom-right and top-left corners of this plot consequently represent the linear and additive effects as well as the nonlinear and coupling effects, while the origin of this plot denotes negligible or no interaction effects. Using the gradient approximation methods, Morris method with $p = 16$ or $\Delta = \frac{8}{15}$, and Monte Carlo Sampling and Collocation method with $\Delta = \frac{1}{2}$, the magnitudes of $E[EE_1, EE_2, EE_3]$ are [63, 70, 15], which agrees with the first-order derivative of the function, as shown in Figure 5-7. The lines, linked between results with two different accuracy levels, show some variation when we increase the number of trials, realizations, and collocation points. The standard deviations of EE_i are very small because of the linearity of the function. The results from the Variance and Inverse Variance methods with $Nc = 8$, shown in Figure 5-8, provide the same input ranking according to the relative magnitude of VEE_i and $IVEE_i$ and identify no coupling effect because the magnitude of IEE_i and $IIEE_i$ is so small.

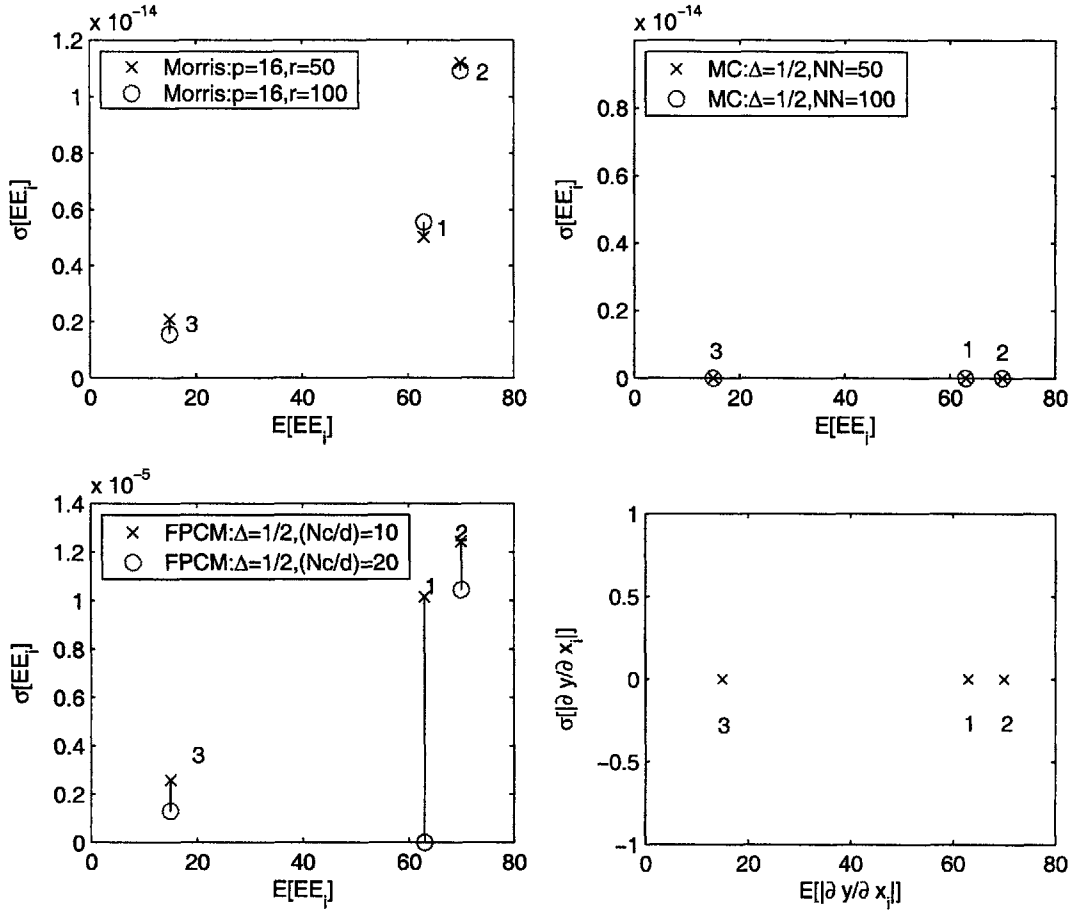

Figure 5-7: Function (y_1): the mean and standard deviation of EE_i from the Morris method with $p = 16$ and $r = 50$ to 100 (top-left), from the Monte Carlo Sampling with $\Delta = 1/2$ and $NN = 50$ to 100 (top-right), the Collocation method with $\Delta = 1/2$ and $Nc = 10$ to 20 (bottom-left), and from the statistics of the absolute partial derivative ($|\partial y/\partial x_i|$) (bottom-right).

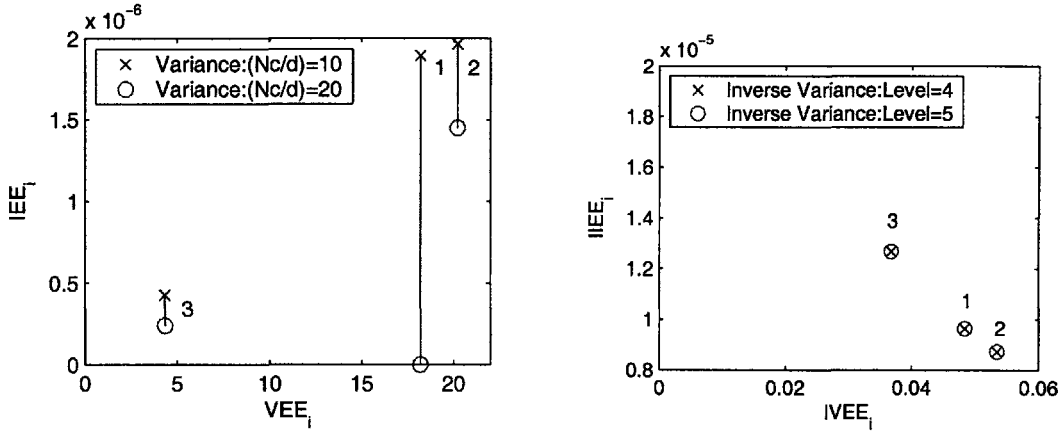

Figure 5-8: Function (y_1): the mean and standard deviation of EE_i from the Variance method with $Nc/d = 10$ to 20 (left) and from the Inverse Variance method with $Nc = 8$ and $Level = 4$ to 5 (right).

5.2.2 Nonlinear Static Function without Parameters' Interaction

The second static function is used to test these algorithms for the input nonlinearity without any coupling. Consider the nonlinear polynomial function expressed in the following form:

$$y_2 = 63x_1^4 - 70x_2^3 + 15x_3 \text{ for } 0 < x_i < 1. \tag{5.11}$$

Figure 5-9 illustrates that the techniques based on the approximated gradient, Morris method with $p = 16$ or $\Delta = \frac{8}{15}$, and Monte Carlo Sampling and Collocation methods with $\Delta = \frac{1}{2}$, rank the elementary effect of inputs in the following order: 2,1,3. This order also agrees with the mean value of the first-order derivative evaluated within the random uniform range, U[0,1], $[E[|\frac{\partial y_2}{\partial x_1}|], E[|\frac{\partial y_2}{\partial x_2}|], E[|\frac{\partial y_2}{\partial x_3}|]]|_{x_i \subset U[0,1]} = [63.17, 69.91, 15.00]$. $[\sigma[|\frac{\partial y_2}{\partial x_1}|], \sigma[|\frac{\partial y_2}{\partial x_2}|], \sigma[|\frac{\partial y_2}{\partial x_3}|]]|_{x_i \subset U[0,1]} = [71.57, 62.58, 0]$, which rank the nonlinearity of inputs in the same order of $\sigma[EE_i]$ for $i = 1, 2, 3$ in the Morris, Monte Carlo sampling, and Collocation methods. $\sigma[EE_1]$ is slightly higher than $\sigma[EE_2]$; this relation implies that the distribution of EE_i can capture the nonlinear characteristics of inputs. All results in Figure 5-9 converge to correct positions for

given parameters, $(r, NN, (Nc/d))$. Without using the approximated gradient, both Variance and Inverse Variance methods can also identify the important ranking of inputs in the same order: 2,1,3; however, IEE_i and $IIEE_i$ do not capture the input nonlinearity effect, which is shown by their very small magnitude in Figure 5-10.

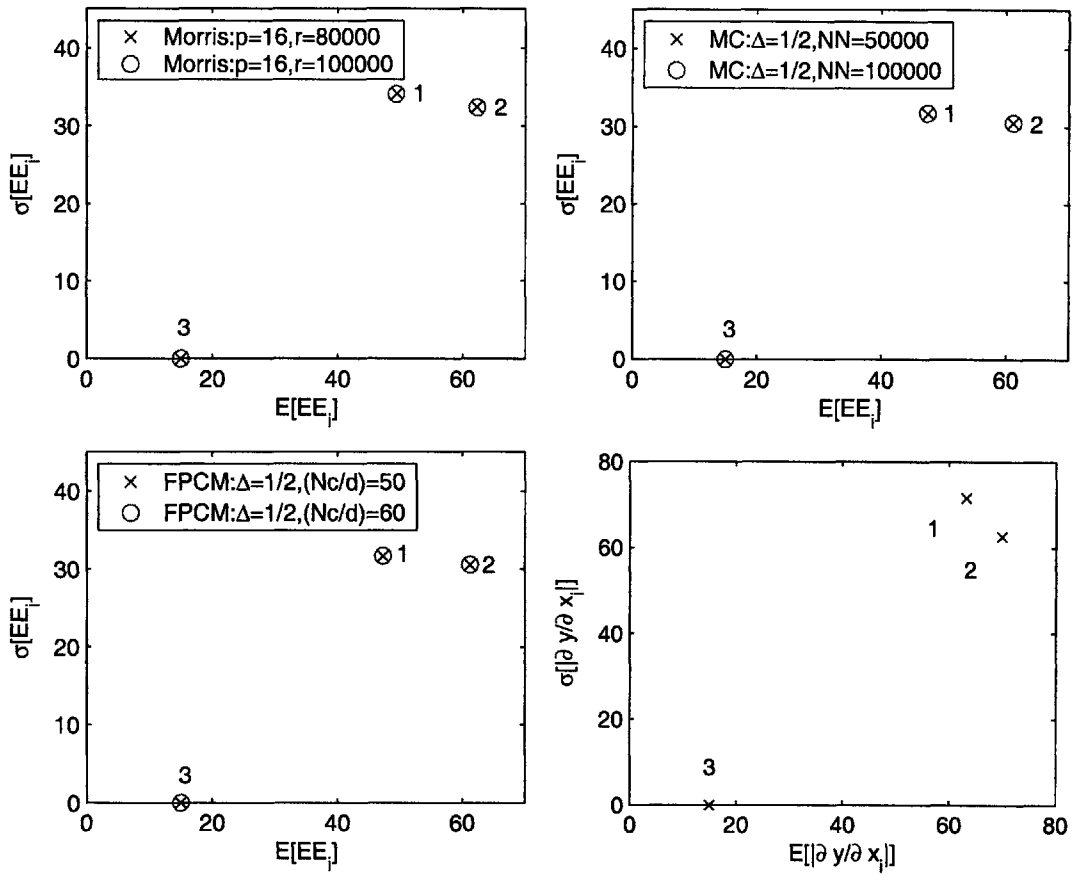

Figure 5-9: Function (y_2): the mean and standard deviation of EE_i from the Morris method with $p = 16$ and $r = 80,000$ to $100,000$ (top-left), from the Monte Carlo Sampling with $\Delta = 1/2$ and $NN = 50,000$ to $100,000$ (top-right), the Collocation method with $\Delta = 1/2$ and $Nc = 10$ to 20 (bottom-left), and from the statistics of the absolute partial derivative $(|\partial y/\partial x_i|)$ (bottom-right).

Moreover, to show the convergence characteristics of all these sensitivity analysis techniques, we need to define a difference in the results between using low and high accuracy levels - r, NN, or (Nc/d) - in each technique. With n multiple inputs, the RMS values of the difference in $E[EE_i]$ and $\sigma[EE_i]$ at different level (L) are defined

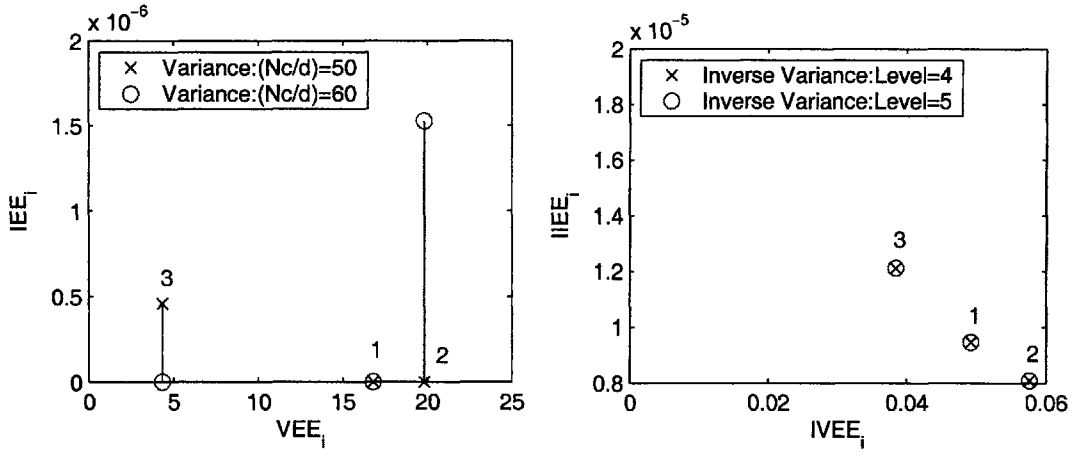

Figure 5-10: Function (y_2): the mean and standard deviation of EE_i from the Variance method with $Nc/d = 10$ to 20 (left) and from the Inverse Variance method with $Nc = 8$ and $Level = 4$ to 5 (right).

as the following:

$$RMS(\Delta E[EE_i]) = \sqrt{\sum_{i=1}^{n} \left(E^L[EE_i] - E^{L-1}[EE_i]\right)^2}, \tag{5.12}$$

$$RMS(\Delta\sigma[EE_i]) = \sqrt{\sum_{i=1}^{n} \left(\sigma^L[EE_i] - \sigma^{L-1}[EE_i]\right)^2} \tag{5.13}$$

where $E^L[EE_i]$ and $E^{L-1}[EE_i]$ are the mean of the i elementary effect of the high and low accuracy level, respectively. This definition can be applicable for the variance and inverse variance methods by replacing $(E[EE_i], \sigma[EE_i])$ with either (VEE_i, IEE_i) or $(IVEE_i, IIEE_i)$. The smaller value of these RMS differences indicates a convergence of our sensitivity indices in each technique. Thus, we can plot the RMS difference versus the computing cost, which reflects a total number of the function evaluations as well as the simplicity of the algorithms' structure. In Figure 5-11, we compare the convergence performance among Morris, Monte Carlo Sampling, and Collocation methods. The Collocation method yields the best result convergence among these three techniques, while the convergence of the Monte Carlo Sampling and Morris methods is comparable, except that an additional computing cost is needed for generating the random trajectories in the Morris method. As expected, the convergence

characteristics of both Variance and Inverse Variance methods, as shown in Figure 5-12, are extremely fast due to the exponential convergence rate of the PCM. The sensitivity indices of these variance methods approach their final values by using only a few collocation points.

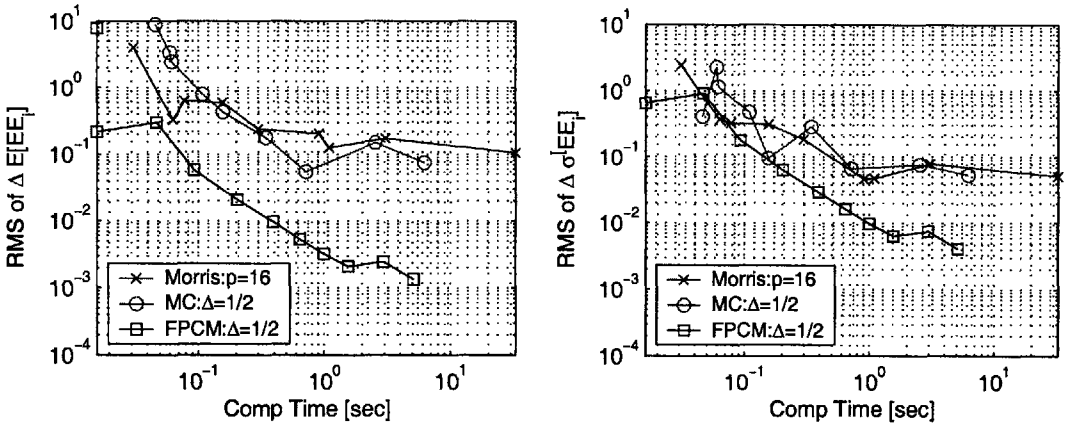

Figure 5-11: Function (y_2): the convergence characteristic of $RMS(\Delta E[EE_i])$ and $RMS(\Delta\sigma[EE_i])$, using the Morris, Monte Carlo Sampling, and Collocation methods based on the approximated gradient computation, is plotted versus the computational time.

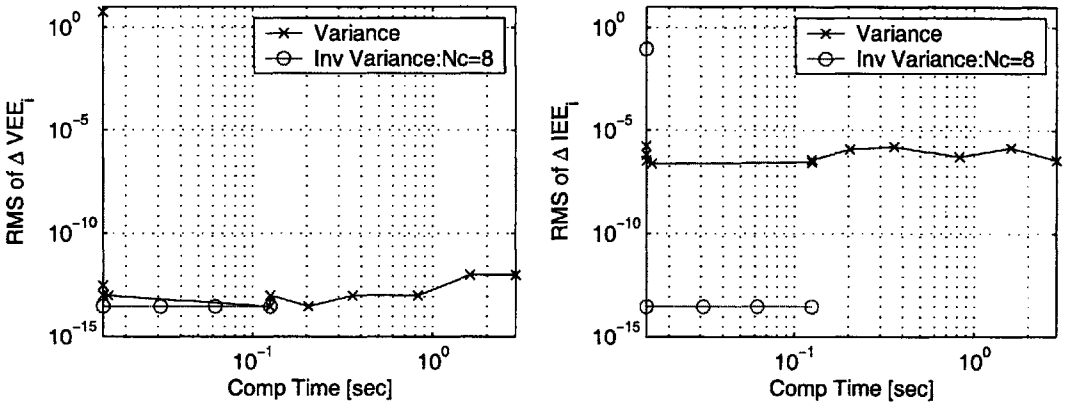

Figure 5-12: Function (y_2): the convergence characteristic of $RMS(\Delta VEE_i)$ and $RMS(\Delta IEE_i)$ using the Variance and Inverse Variance based on the statistical computation is plotted versus the computational time.

5.2.3 Nonlinear Static Function with Parameters' Interaction

Let us consider the case where the inputs are strongly coupled and have only quadratic nonlinearity, which is expressed in the third static function below:

$$y_3 = x_1^2 + x_2^2 + 4x_2x_3 + x_1x_3 \text{ for } 0 < x_i < 1. \tag{5.14}$$

Using the approximated gradient, Morris with $p = 16$, Monte Carlo Sampling and Collocation methods with $\Delta = \frac{1}{2}$ rank the significance of these 3 inputs in the following order: 2,3,1, as illustrated in Figure 5-13, because of a large coefficient in the third term. This ranking can also be easily discovered from the first-order partial derivative. The mean and standard deviation of the $|\partial y_3/\partial x_i|$ are shown in Figure 5-13 as well. $[E[|\frac{\partial y_3}{\partial x_1}|], E[|\frac{\partial y_3}{\partial x_2}|], E[|\frac{\partial y_3}{\partial x_3}|]]|_{x_i \subset U[0,1]} = [1.50, 3.00, 2.50]$ and $[\sigma[|\frac{\partial y_3}{\partial x_1}|], \sigma[|\frac{\partial y_3}{\partial x_2}|], \sigma[|\frac{\partial y_3}{\partial x_3}|]]|_{x_i \subset U[0,1]} = [0.65, 1.29, 1.19]$. The $\sigma[|\frac{\partial y_3}{\partial x_i}|]$ captures the nonlinearity effect of inputs, but not the coupling effect. The coupling effect is as important as the inputs' nonlinearity in this function; therefore, the $\sigma[|\frac{\partial y_3}{\partial x_i}|]$ for $i = 1, 2, 3$ fail to identify this coupling effect as effectively as the $\sigma[EE_i]$ of the Morris, Sampling, and Collocation methods. In Figure 5-14, both variance and inverse variance methods correctly rank the inputs' significance and the interaction among them. Notice that the $IIEE_i$ tends to separate the input coupling more clearly than the IEE_i.

To compare the convergence performance of the algorithms based on the approximated gradient, the RMS differences of mean and standard deviation of EE_i are plotted versus the computational time, as shown in Figure 5-15. In this three-dimensional problem, the convergence rate of RMS($\Delta E[EE_i]$) using the Collocation method is about an order of magnitude faster than those of Morris and Monte Carlo Sampling methods. Due to the monotonicity and smoothness of this function, the $E[EE_i]$ from the Collocation method converges to $[1.5, 3, 2.5]$ up to the machine precision within a fraction of a second. Similar to the previous example, the results of both Variance and Inverse Variance methods converge extremely fast using only $Nc = 14$ and $Level = 4$, respectively, as illustrated in Figure 5-16. Again, a reason for this fast convergence

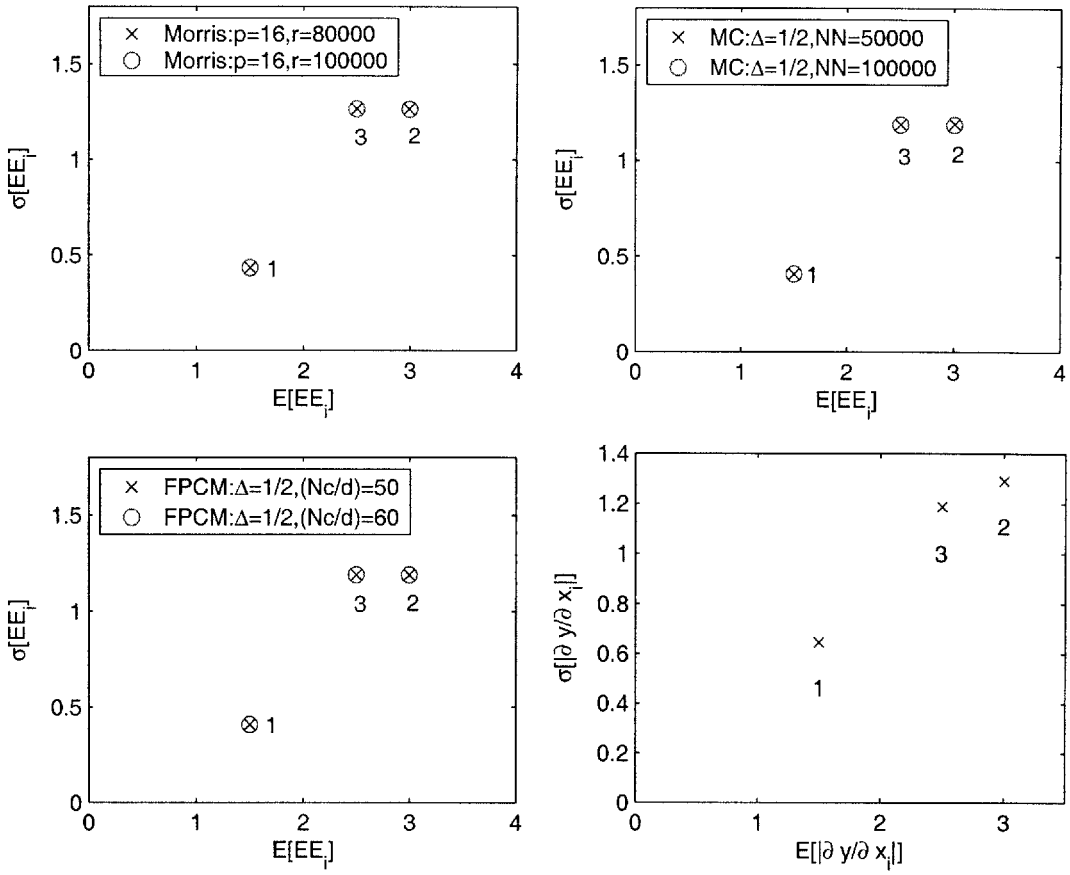

Figure 5-13: Function (y_3): the mean and standard deviation of EE_i from the Morris method with $p = 16$ and $r = 80,000$ to $100,000$ (top-left), from the Monte Carlo Sampling with $\Delta = 1/2$ and $NN = 50,000$ to $100,000$ (top-right), the Collocation method with $\Delta = 1/2$ and $Nc = 10$ to 20 (bottom-left), and from the statistics of the absolute partial derivative ($|\partial y/\partial x_i|$) (bottom-right).

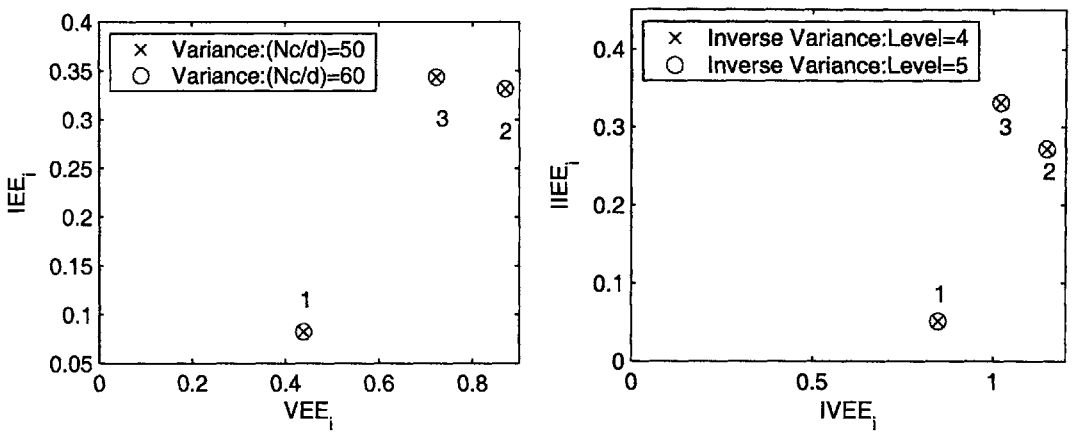

Figure 5-14: Function (y_3): the mean and standard deviation of EE_i from the Variance method with $Nc/d = 10$ to 20 (left) and from the Inverse Variance method with $Nc = 8$ and $Level = 4$ to 5 (right).

depends on the exponential convergence rate of both full- and sparse-grid PCMs.

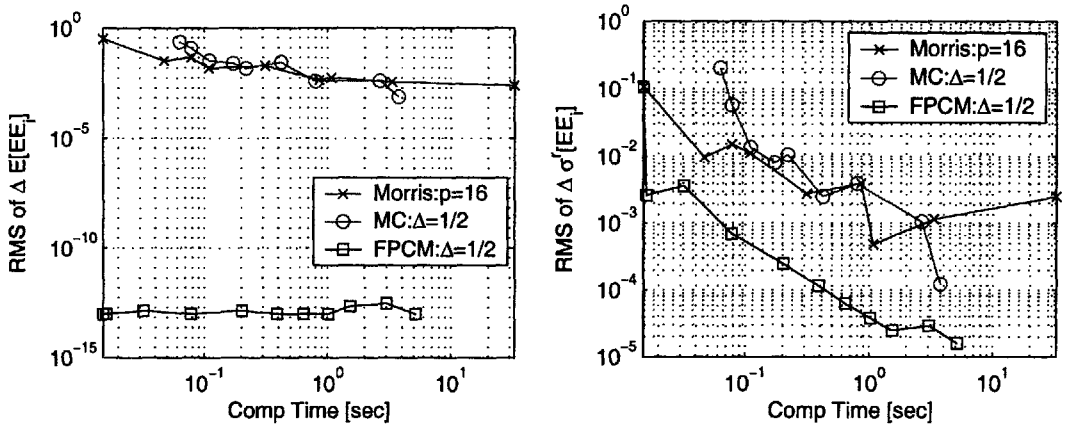

Figure 5-15: Function (y_3): the convergence characteristic of $RMS(\Delta E[EE_i])$ and $RMS(\Delta\sigma[EE_i])$, using the Morris, Monte Carlo Sampling, and Collocation methods based on the approximated gradient computation, is plotted versus the computational time.

When the function is no longer monotonic and has the same coupling as the last function, we again examine the convergence performance as well as the ranking of sensitivity indices among these algorithms. The fourth static nonlinear function (y_4) is given by the equation below:

$$y_4 = x_1^2 + x_2^2 - 4x_1x_2 + x_1x_3 \text{ for } 0 < x_i < 1. \tag{5.15}$$

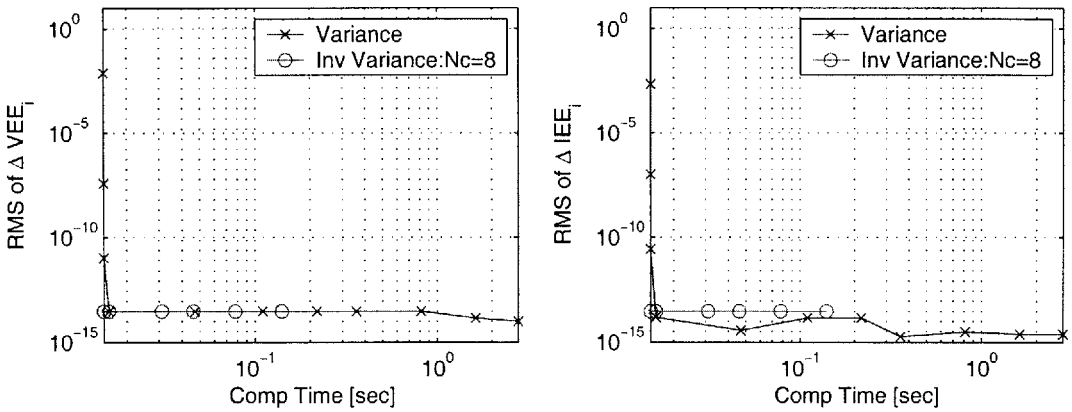

Figure 5-16: Function (y_3): the convergence characteristic of $RMS(\Delta VEE_i)$ and $RMS(\Delta IEE_i)$ using the Variance and Inverse Variance based on the statistical computation is plotted versus the computational time.

All techniques based on the approximated gradient calculation yield the same ranking of input significance ($E[EE_i]$) and of inputs' interaction and nonlinearity effect ($\sigma[EE_i]$), as shown in Figure 5-17. x_2 is the most sensitive parameter because of a large coefficient in the third term and there is no cancellation from the fourth term. For x_1, there is a cancellation between the third and fourth terms, which make the output less sensitive to x_1. With the same quadratic nonlinearity and no cancellation of the coupling effect in the third and fourth terms as in x_1, x_2 is ranked the first for the input interaction and then x_1 and x_3. Also, the mean and standard deviation of the absolute value of the partial derivative can rank both the significance and interaction of inputs as well. Using the magnitude of OAT variance, the variance method yields the same ranking of the inputs' sensitivity and interaction. However, the inverse variance fails to identify the coupling effect, owing to the cancellation of the coupling effect in x_2 input.

From the convergence performance aspect, the sensitivity index of the Collocation method gains about an order of magnitude in accuracy better than those results of the Morris and Monte Carlo Sampling methods, as shown in Figure 5-19. For this nonmonotonic function, the convergence characteristic of the Variance method is degraded; however, an exponential convergence rate using the full-grid PCM is applicable, as illustrated in Figure 5-20. The rapid convergence characteristics of

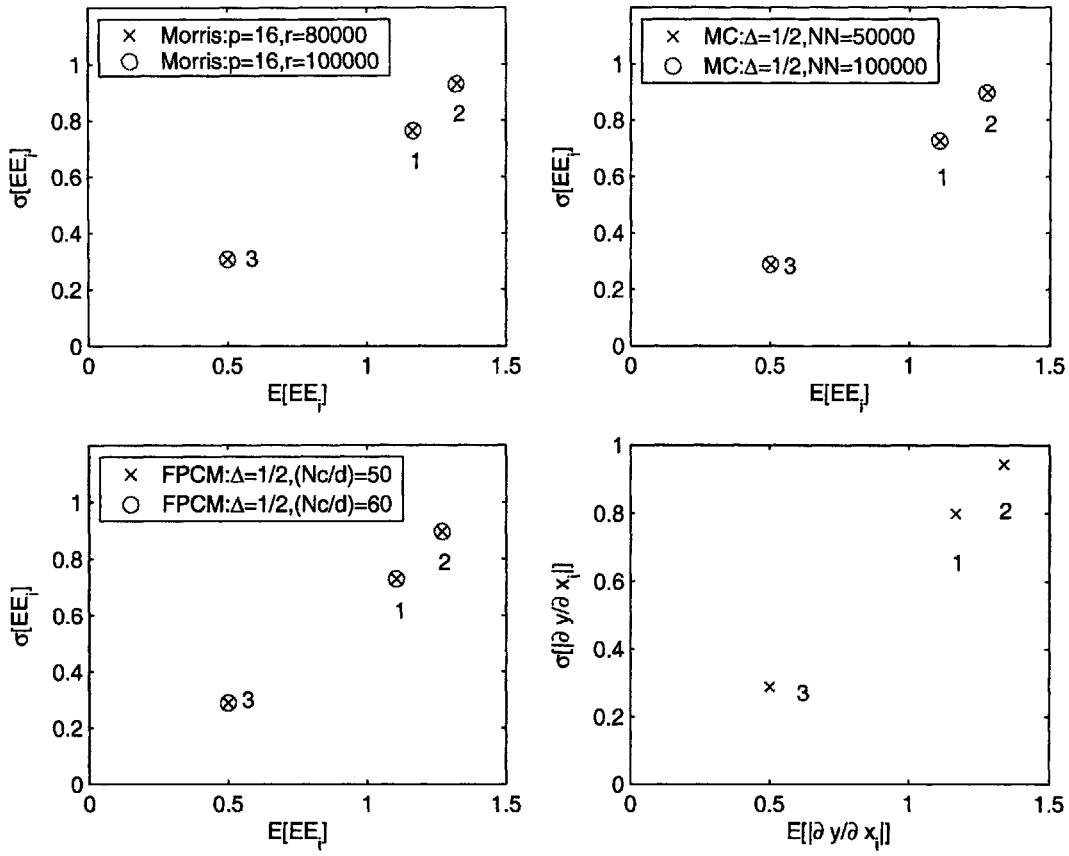

Figure 5-17: Function (y_4): the mean and standard deviation of EE_i from the Morris method with $p = 16$ and $r = 80,000$ to $100,000$ (top-left), from the Monte Carlo Sampling with $\Delta = 1/2$ and $NN = 50,000$ to $100,000$ (top-right), the Collocation method with $\Delta = 1/2$ and $Nc = 10$ to 20 (bottom-left), and from the statistics of the absolute partial derivative ($|\partial y/\partial x_i|$) (bottom-right).

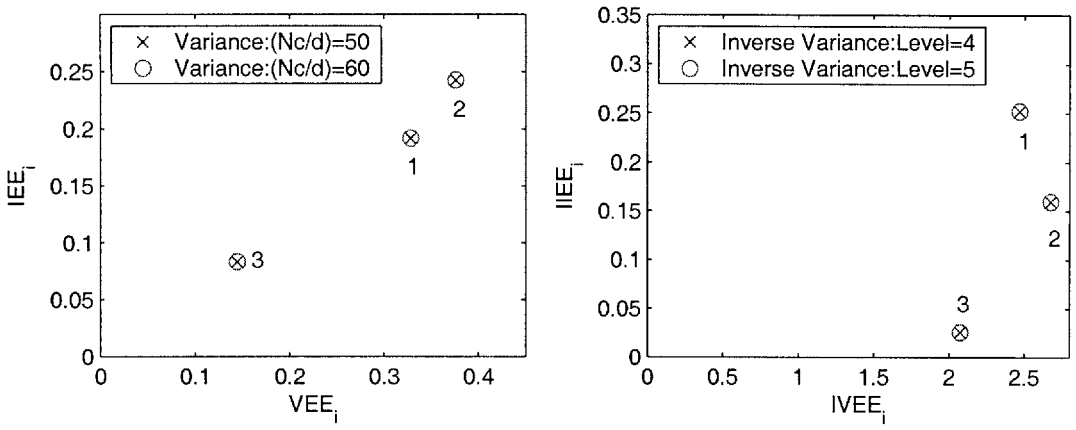

Figure 5-18: Function (y_4): the mean and standard deviation of EE_i from the Variance method with $Nc/d = 10$ to 20 (left) and from the Inverse Variance method with $Nc = 8$ and $Level = 4$ to 5 (right).

the Inverse Variance method are not affected by this nonmonotonic property of the function.

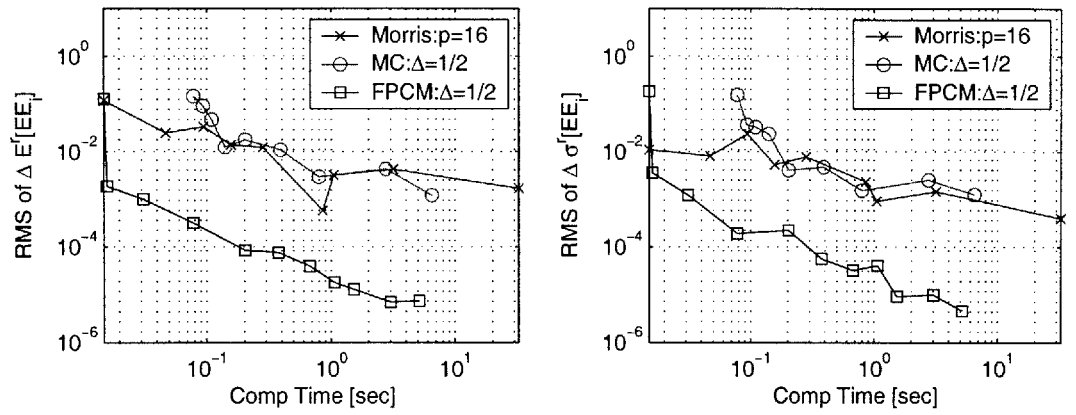

Figure 5-19: Function (y_4): the convergence characteristic of $RMS(\Delta E[EE_i])$ and $RMS(\Delta\sigma[EE_i])$, using the Morris,Monte Carlo Sampling, and Collocation methods based on the approximated gradient computation, is plotted versus the computational time.

In the fifth example, we increase the coefficients of only the nonlinear terms in the static nonlinear function (y_5), as expressed by the equation below:

$$y_5 = 10x_1^2 + 20x_2^2 + 4x_1x_2 + x_1x_3 \text{ for } 0 < x_i < 1. \tag{5.16}$$

The techniques, relying on the gradient computation, rank x_2 as the most sensitive

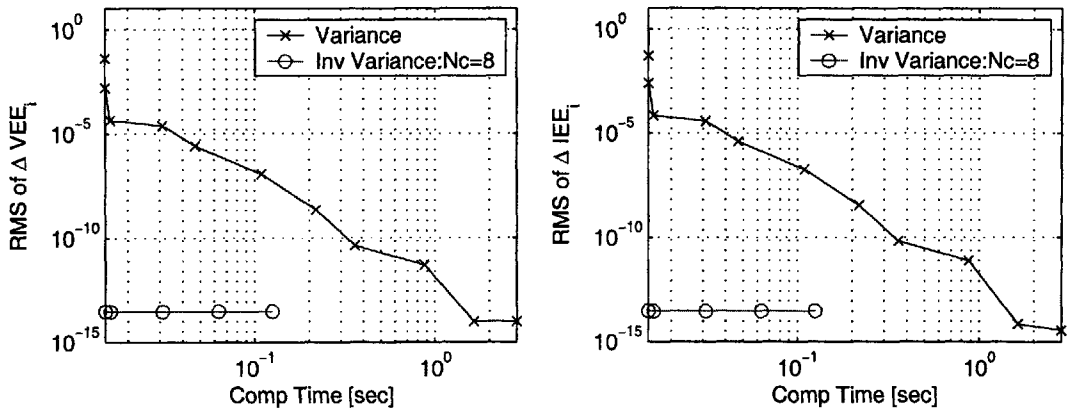

Figure 5-20: Function (y_4): the convergence characteristic of $RMS(\Delta VEE_i)$ and $RMS(\Delta IEE_i)$ using the Variance and Inverse Variance based on the statistical computation is plotted versus the computational time.

and coupled parameter, as expected. The results from the Morris method with $p = 16$, Monte Carlo Sampling and Collocation methods with $\Delta = \frac{1}{2}$, shown in Figure 5-21, agree with one another as well as with the $E[|\partial y/\partial x_i|]$ and $\sigma[|\partial y/\partial x_i|]$. Both Variance and Inverse Variance methods provide the same ranking of the input sensitivity; nevertheless, these two approaches do not emphasize the nonlinearity of the inputs, like that in the y_2 function. Thus, IEE and IIEE exhibit that the x_1 input has the largest interaction among inputs, which can be observed directly from the function. Then, the x_2 and x_3 are ranked the second and third in the coupling effect, according to the Variance and Inverse Variance methods.

In terms of the numerical performance, the convergence results of all algorithms are the same as those in the third example with y_3. The results from the Collocation method converge faster than those from the Morris and Monte Carlo Sampling methods by approximately an order of magnitude. Both Variance and Inverse Variance methods provide a rapid convergence of the results up to the machine precision.

In the sixth function below, both the nonlinearity and coupling of inputs become prominent:

$$y_6 = 63x_1^5x_2 - 70x_2^3x_3^2 + 15x_1x_2x_3 \text{ for } 0 < x_i < 1, \tag{5.17}$$

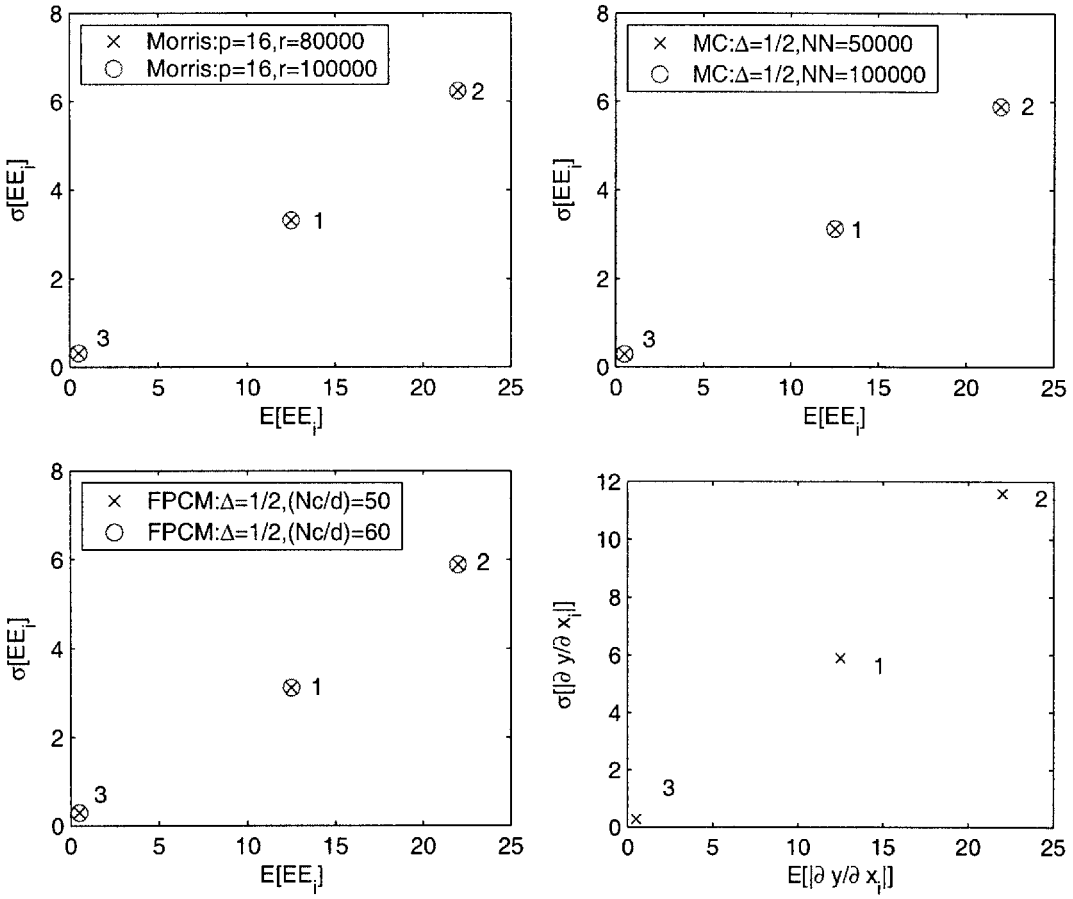

Figure 5-21: Function (y_5): the mean and standard deviation of EE_i from the Morris method with $p = 16$ and $r = 80,000$ to $100,000$ (top-left), from the Monte Carlo Sampling with $\Delta = 1/2$ and $NN = 50,000$ to $100,000$ (top-right), the Collocation method with $\Delta = 1/2$ and $Nc = 10$ to 20 (bottom-left), and from the statistics of the absolute partial derivative ($|\partial y/\partial x_i|$) (bottom-right).

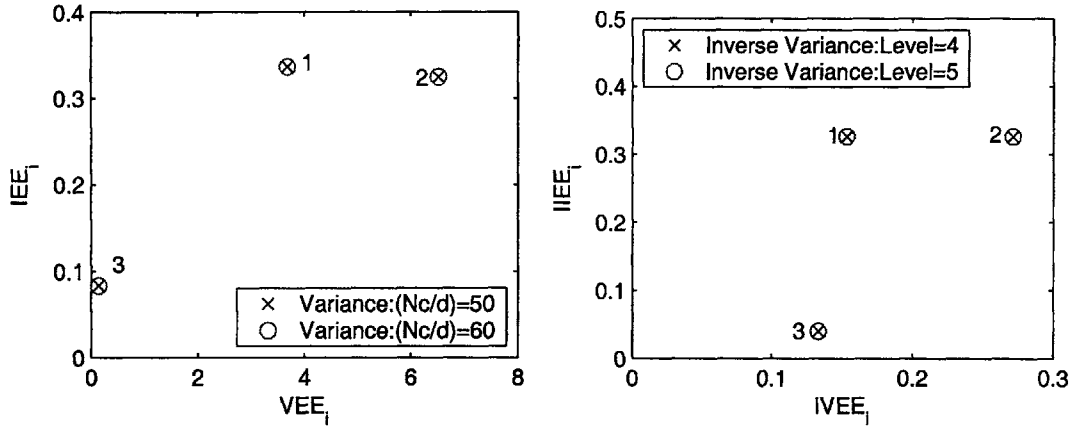

Figure 5-22: Function (y_5): the mean and standard deviation of EE_i from the Variance method with $Nc/d = 10$ to 20 (left) and from the Inverse Variance method with $Nc = 8$ and $Level = 4$ to 5 (right).

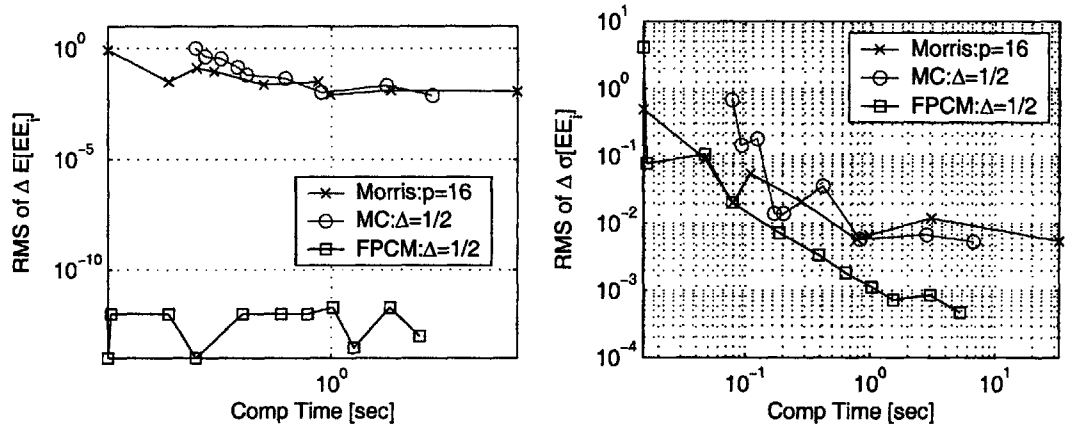

Figure 5-23: Function (y_5): the convergence characteristic of $RMS(\Delta E[EE_i])$ and $RMS(\Delta\sigma[EE_i])$, using the Morris,Monte Carlo Sampling, and Collocation methods based on the approximated gradient computation, is plotted versus the computational time.

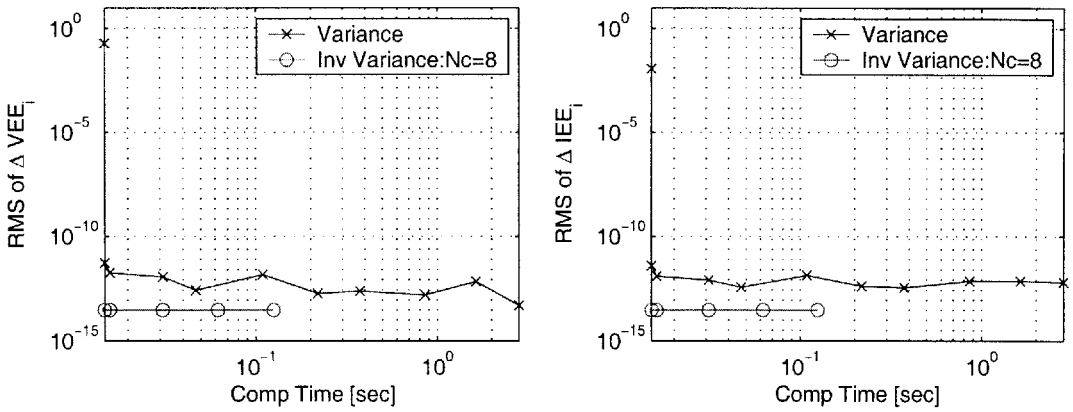

Figure 5-24: Function (y_5): the convergence characteristic of $RMS(\Delta VEE_i)$ and $RMS(\Delta IEE_i)$ using the Variance and Inverse Variance based on the statistical computation is plotted versus the computational time.

All the gradient computing algorithms, Morris with $p = 16$, Monte Carlo Sampling and Collocation methods with $\Delta = \frac{1}{2}$, provide the same ranking for the significance of the inputs' influence on the output as well as inputs' interaction, as shown in Figure 5-25. The first input (x_1) is the most sensitive due to the fifth order polynomial, while the sensitivities of x_2 and x_3 are ranked second and third. Again, the mean and standard deviation of the first-order derivatives with respect to each input of this function evaluated within the random uniform range, U[0,1], $[E[|\frac{\partial y_6}{\partial x_1}|], E[|\frac{\partial y_6}{\partial x_2}|], E[|\frac{\partial y_6}{\partial x_3}|]]|_{x_i \subset U[0,1]}$, are $[35.30, 24.65, 14.85]$. The magnitude of the local derivative fails to correctly rank the importance of input due to a strong coupling of inputs. Nevertheless, $[\sigma[|\frac{\partial y}{\partial x_1}|], \sigma[|\frac{\partial y}{\partial x_2}|], \sigma[|\frac{\partial y}{\partial x_3}|]]|_{x_i \subset U[0,1]}$ are $[52.67, 30.50, 22.96]$, which yield the relative magnitude similar to the distribution of EE_i using the approximated gradient method. The standard deviation of EE_1 is larger than those of EE_2 and EE_3 due to the higher order polynomials. The coupling effect of the second and third inputs in the second term gives a comparable importance in the distribution of EE_2 and EE_3.

Due to the high-order polynomial nonlinearity and nonmonotonicity of this function, the results from all algorithms based on the gradient computation converge more slowly than those in the previous three examples of static function with only quadratic nonlinearity, as seen from the upward shift of RMS($\Delta E[EE_i]$) and RMS($\Delta \sigma[EE_i]$)

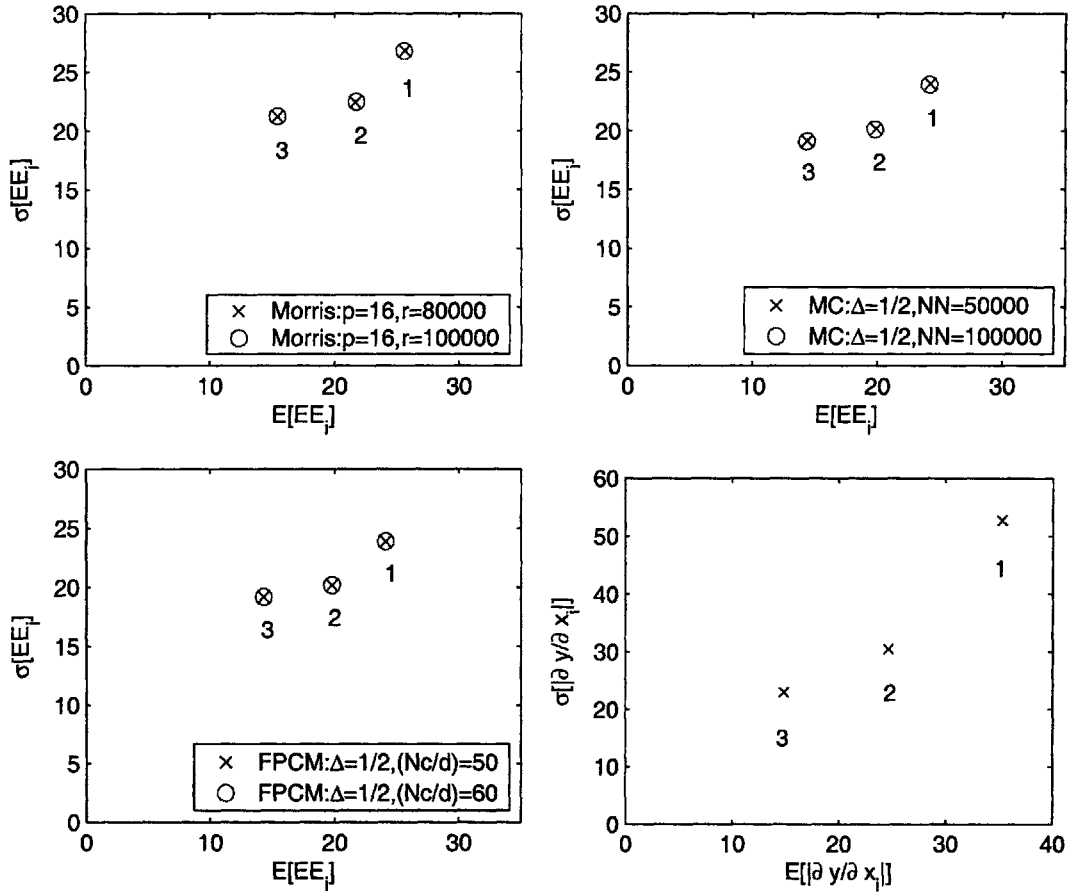

Figure 5-25: Function (y_6): the mean and standard deviation of EE_i from the Morris method with $p = 16$ and $r = 80,000$ to $100,000$ (top-left), from the Monte Carlo Sampling with $\Delta = 1/2$ and $NN = 50,000$ to $100,000$ (top-right), the Collocation method with $\Delta = 1/2$ and $Nc = 10$ to 20 (bottom-left), and from the absolute partial derivative ($|\partial y/\partial x_i|$) (bottom-right).

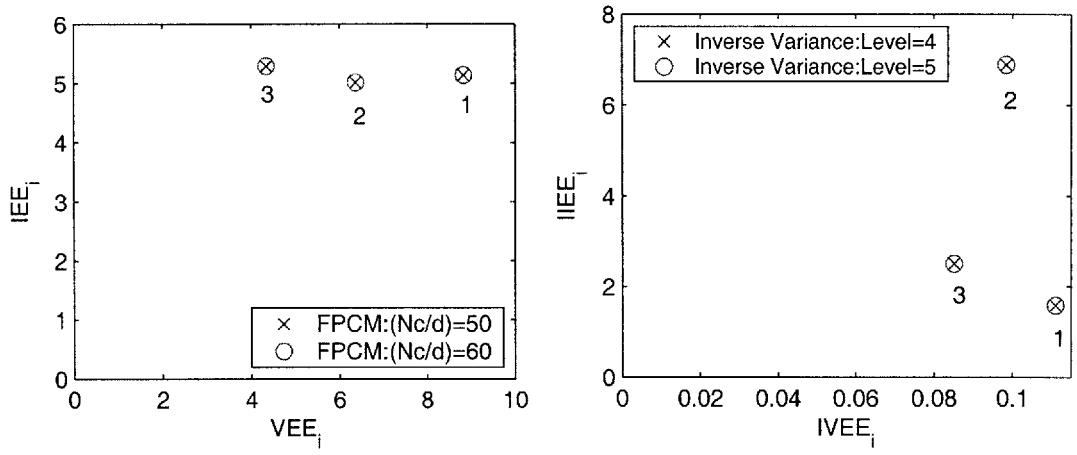

Figure 5-26: Function (y_6): the mean and standard deviation of EE_i from the Variance method with $Nc/d = 10$ to 20 (left) and from the Inverse Variance method with $Nc = 8$ and $Level = 4$ to 5 (right).

curves in Figure 5-27. In Figure 5-28, the variance method also exhibits a slower convergence characteristic, which is still an exponential rate; however, the rapid convergence of the results using the inverse variance method is insensitive to the strong nonlinearity and nonmonotonicity.

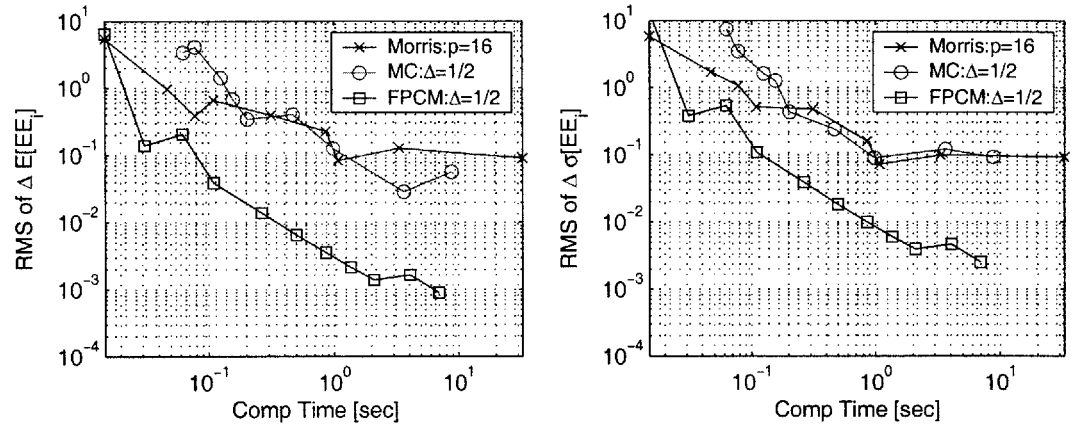

Figure 5-27: Function (y_6): the convergence characteristic of $RMS(\Delta E[EE_i])$ and $RMS(\Delta\sigma[EE_i])$, using the Morris,Monte Carlo Sampling, and Collocation methods based on the approximated gradient computation, is plotted versus the computational time.

Before considering the performance and characteristics of these sensitivity analysis algorithms with more complex functions, the key properties of each algorithm are

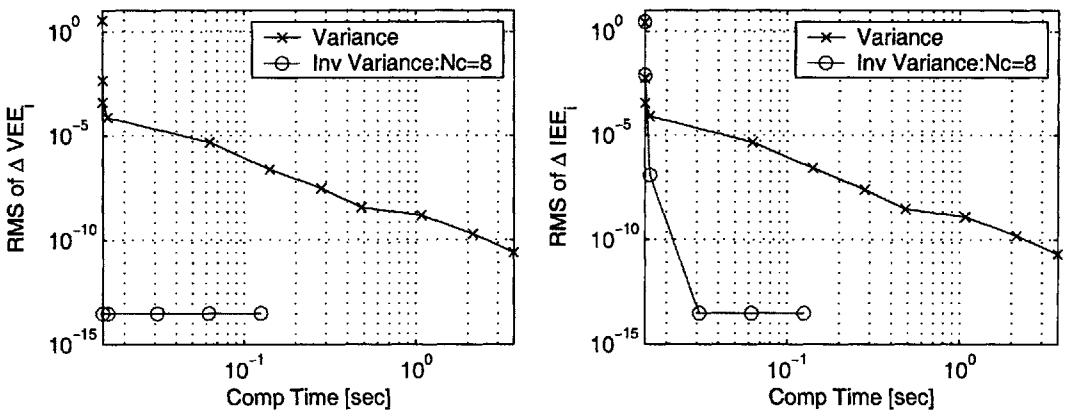

Figure 5-28: Function (y_6): the convergence characteristic of $RMS(\Delta VEE_i)$ and $RMS(\Delta IEE_i)$ using the Variance and Inverse Variance based on the statistical computation is plotted versus the computational time.

summarized in the following list:

- Morris and Monte Carlo Sampling Methods: $E[EE_i]$ and $\sigma[EE_i]$ can correctly rank the sensitivity of the input parameters and rank the influence of the nonlinearity and coupling effect in each input, respectively, for any type of nonlinear and non/monotonic functions. The sensitivity indices converge slowly with an algebraic rate; however, this algebraic rate is applicable for any kind of function.

- Collocation Methods: $E[EE_i]$ and $\sigma[EE_i]$ can rank the inputs' sensitivity as well as the effect of nonlinearity and coupling of inputs, which closely match the sensitivity index of the Morris and Sampling methods quantitatively. The algebraic convergence of its sensitivity index is superior than those of Morris and Sampling methods in a small input-dimension problem and is not sensitive to strong nonlinearity or coupling effect.

- Variance Methods: The relative magnitude of VEE_i can rank the sensitivity of inputs. The magnitude of IEE_i captures only the coupling of inputs. It does not include the inputs' nonlinearity because of the OAT variance measurement of a single random variable. Using the efficiency of the full-grid PCM, the convergence rate of the sensitivity index is exponential in a small dimension problem; nevertheless, this rate is sensitive to the function's monotonicity.

- Inverse Variance Methods: The relative magnitude of $IVEE_i$ can correctly rank

Table 5.2: Comparison on the computational cost of all sensitivity analysis techniques

Method	Computing Cost
Morris	$O(r \times (k+1))+c(r \times k)$
Monte Carlo Sampling	$O(NN \times k)$
Collocation	$O(N_c^k \times k)$,
Variance	$O(N_c^k \times k)$,
Inverse Variance	$O(n(L, k-1) \times N_c \times k)$,

the sensitivity of inputs as well. Similar to the variance method, the magnitude of $IIEE_i$ can capture only the coupling of inputs, but not the inputs' nonlinearity. Furthermore, the value of $IIEE_i$ is also sensitive to the function's monotonicity due to the possibility of cancellation effect in computing the standard deviation of the $n-1$ inputs in the n-dimensional problem. The main advantage of this technique is its rapid convergence rate of the sensitivity index and its independence in convergence characteristic from any kind of the inputs' nonlinearity.

The computational costs of all sensitivity analysis algorithms are summarized in Table 5.2 below. The Morris and Monte Carlo Sampling methods require about the same order of magnitude in the computing cost, except that an additional cost, $c()$, for generating randomized trajectories in the Morris method. Similarly, the computational cost of the Collocation and Variance methods is identical; however, the accuracy of sensitivity indices is different because of their measured sensitivity characteristics.

5.2.4 Modified Morris's Function

In a more complex system, the last static function considered in this section, a modified function from the original test problem with 20 inputs in the Morris paper [39] is considered only for 6 and 12 inputs because the other 8 inputs $(x_{11}, \ldots, x_{20})$ have a negligible effect, as mentioned by Morris [39]. This modified Morris function is suitable for testing the sensitivity of large-dimensional inputs with strong coupling among the inputs. The modified Morris function with n inputs is given in the equation

Table 5.3: The values of β coefficients for the modified Morris functions

β **coefficients for** $n = 6$ **inputs**	β **coefficients for** $n = 12$ **inputs**
$\beta_0 = 1,$	$\beta_0 = 1,$
$\beta_i = 20, \text{for} i = 1, 2, 3$	$\beta_i = 20, \text{for} i = 1, \cdots, 10$
$\beta_{i,j} = -15, \text{for} i, j = 1, 2,$	$\beta_{i,j} = -15, \text{for} i, j = 1, \cdots, 6,$
$\beta_{i,j,k} = -10, \text{for} i, j, k = 1,$	$\beta_{i,j,k} = -10, \text{for} i, j, k = 1, \cdots, 5,$

below:

$$y = \beta_0 + \sum_{i}^{n} \beta_i w_i + \sum_{i<j}^{n} \beta_{i,j} w_i w_j + \sum_{i<j<k}^{n} \beta_{i,j,k} w_i w_j w_k \tag{5.18}$$

where $w_i \in [0, 1]$ or $w_i \in [-1, 1]$. The values of (β) coefficients are given in Table 5.3.

The rest of β_i and $\beta_{i,j}$ are assigned zero-mean unit-variance random numbers, associated with the normal distribution. The other coefficients of $\beta_{i,j,k}$ are set to be zero. For the case when $w_i \in [0, 1]$, the Morris method with $p = 16$ or $\Delta = \frac{8}{15}$, and Monte Carlo Sampling and Collocation methods with $\Delta = \frac{1}{2}$ can classify the sensitivity of inputs according to $E[EE_i]$ and $\sigma[EE_i]$ into three distinct groups: (1,2,3);(4);(5,6), as shown in Figure 5-29. The quantitative results from these three techniques agree with one another. The second group of inputs, (4), exhibits only a strong elementary effect with a minor interaction with the other inputs. In contrast, the first group, (1,2,3), shows a strong coupling and a small sensitivity on the output. Lastly, the (5,6) group has a small effect on the output. In Figure 5-30, the magnitude of VEE_i and IEE_i of the Variance method also relatively ranks the significance of inputs to the output as well as their coupling effect in the same order as those of the Morris, Sampling and Collocation methods. In the case of the Inverse Variance method, the magnitude of $IVEE_i$, [0.1366, 0.1393, 0.1377, 0.2781, 0.1343, 0.1342], can rank the elementary effect of inputs correctly as well; however, the magnitude of $IIEE_i$ does not yield the same order of inputs' coupling effect as those of the other techniques. Because of the nonmonotonicity of this modified Morris function, we can

expect the results from $IIEE_i$ to be different, as we show in those three-dimensional static functions.

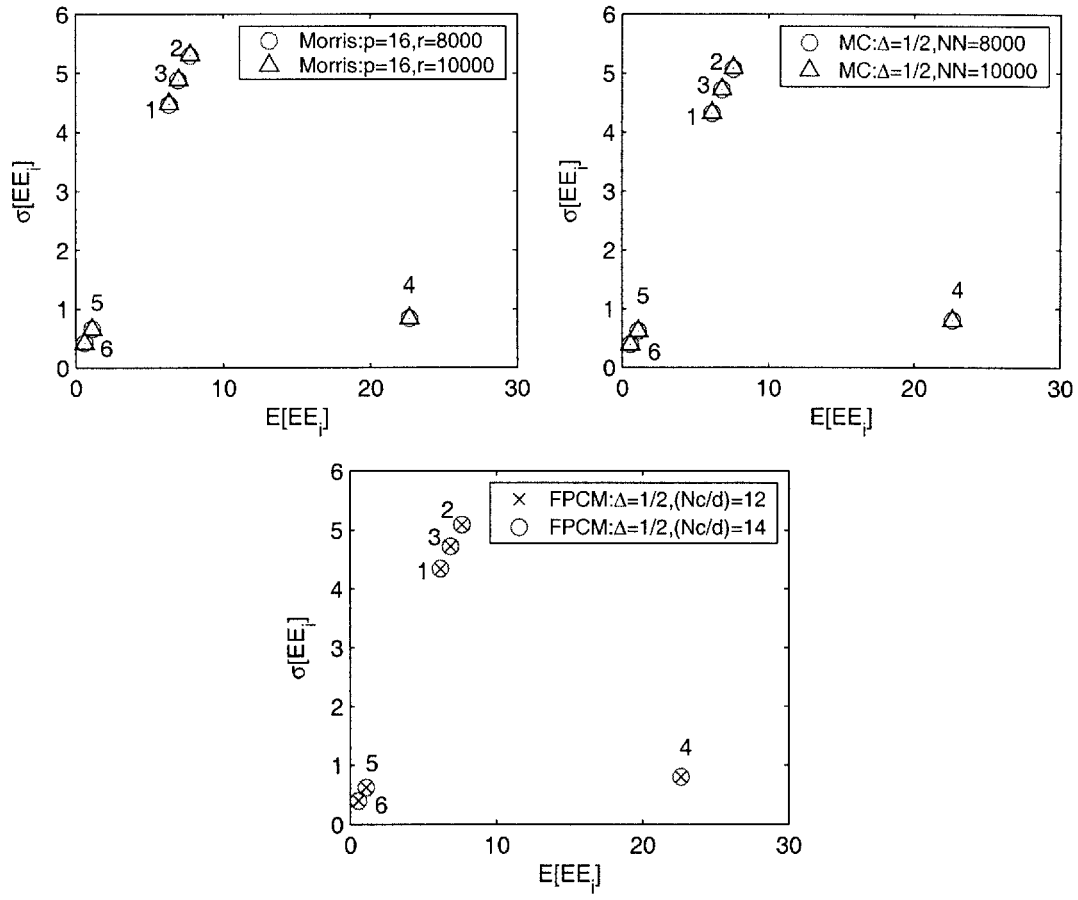

Figure 5-29: For the modified Morris function with 6 inputs and $w_i \in [0, 1]$: the mean and standard deviation of EE_i from the Morris method with $p = 16$ and $r = 8000$ to $10,000$ (top-left), from the Monte Carlo Sampling with $\Delta = 1/2$ and $NN = 8000$ to $10,000$ (top-right), and the Collocation method with $\Delta = 1/2$ and $Nc = 12$ to 14 (bottom).

In terms of the convergence performance, all methods based on the gradient computation exhibit the same order of magnitude in the convergence of the sensitivity results, as shown in Figure 5-31. Because of the dimension dependence of the full-grid PCM, the fast convergence performance of the Collocation method, shown in the previous three-dimensional static function, is degraded as the input dimension increases to 6. In the presence of the nonmonotonic and large-dimension inputs, the convergence of sensitivity results in the Variance method becomes comparable with

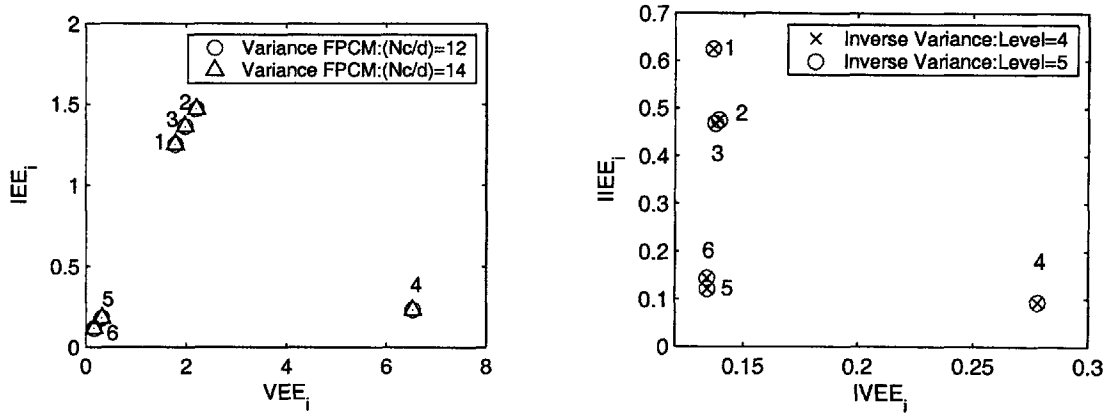

Figure 5-30: For the modified Morris function with 6 inputs and $w_i \in [0, 1]$: the mean and standard deviation of EE_i from the Variance method with $Nc/d = 12$ to 14 (left) and from the Inverse Variance method with $Nc = 12$ and $Level = 4$ to 5 (right).

those of the gradient computation. On the other hand, the superior performance in convergence of the Inverse Variance methods is still held for this function.

When $w_i \in [-1, 1]$, the sensitivity index from the 6 inputs again clusters into three groups in the $E[EE_i]$ versus $\sigma[EE_i]$ plots, shown in Figure 5-32 using the Morris method with $p = 16$ as well as the Monte Carlo Sampling and Collocation methods with $\Delta = \frac{1}{2}$. However, the (1,2,3) group now becomes more sensitive than the 4 input and has a stronger interaction with the other inputs, which are located on the top right of the $E[EE_i]$ versus $\sigma[EE_i]$ plot. Moreover, the magnitude of $E[EE_i]$ also switches between the 5 and 6 inputs. The change of the sensitivity index establishes that the inputs' range is another important factor when there are strong coupling effects among inputs, as in this modified Morris function. A similar ranking of the inputs' influence on the output as well as of the coupling effect can be obtained using either Variance or Inverse Variance methods, as illustrated in Figure 5-33. Note that the results from the Variance method closely match those of the technique using the gradient; however, the relative distance between (1,2,3) and 4 input groups using the Inverse Variance method differs slightly from the other methods.

Similar to the previous example, the sensitivity indices of all methods based on the gradient computation converge at about the same order of magnitude, as shown in Figure 5-34. The convergence performance of the variance method is also compa-

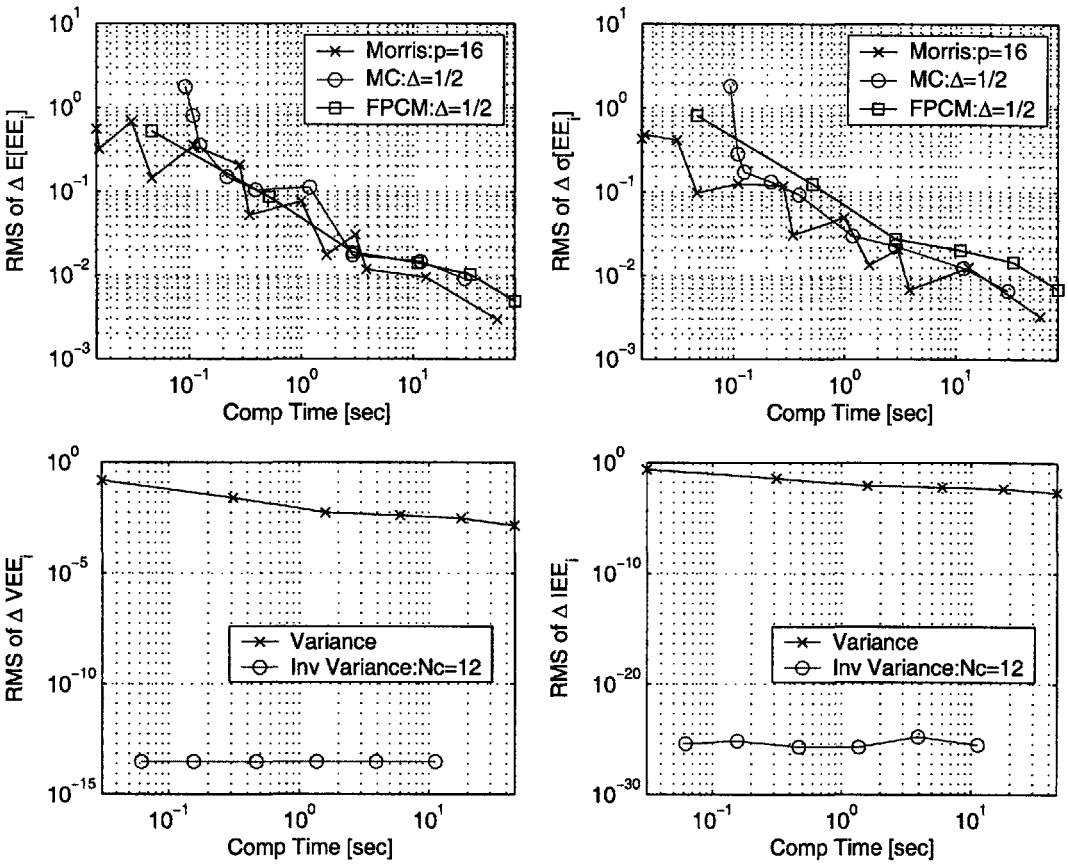

Figure 5-31: For the modified Morris function with 6 inputs and $w_i \in [0, 1]$: the convergence characteristics, plotted versus the computational time, for $RMS(\Delta E[EE_i])$ (Top-Left) and $RMS(\Delta\sigma[EE_i])$ (Top-Right) using the Morris, Monte Carlo Sampling, and Collocation methods and $RMS(\Delta VEE_i)$ (Bottom-Left) and $RMS(\Delta IEE_i)$ (Bottom-Right) using the Variance and Inverse Variance methods.

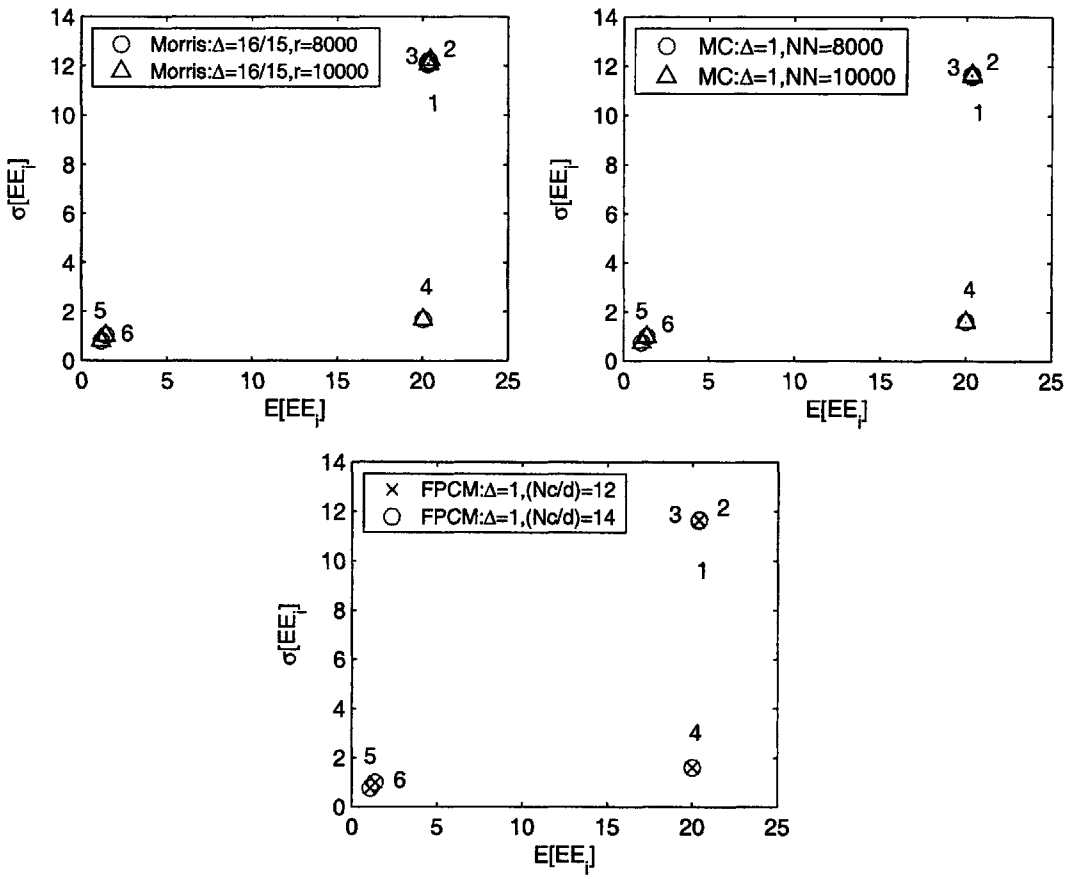

Figure 5-32: For the modified Morris function with 6 inputs and $w_i \in [-1, 1]$: the mean and standard deviation of EE_i from the Morris method with $p = 16$ and $r = 8000$ to $10,000$ (top-left), from the Monte Carlo Sampling with $\Delta = 1/2$ and $NN = 8000$ to $10,000$ (top-right), and the Collocation method with $\Delta = 1/2$ and $Nc = 12$ to 14 (bottom).

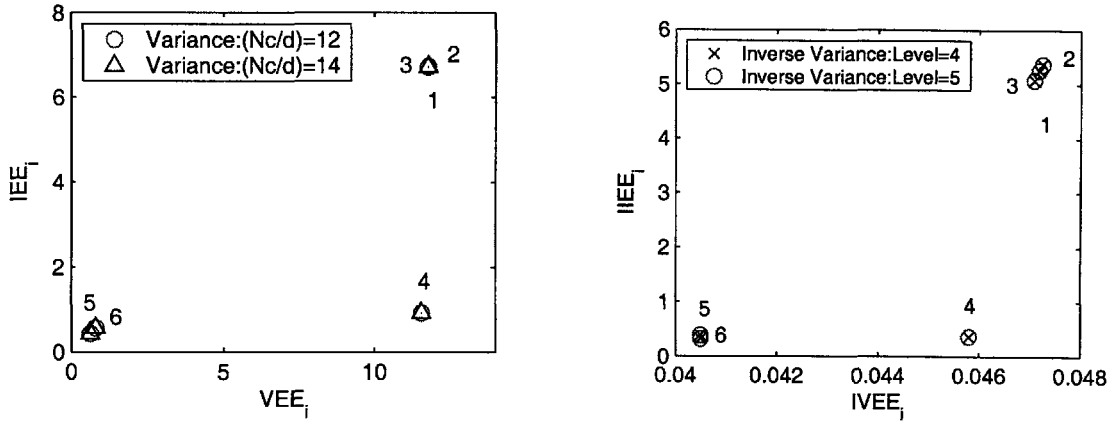

Figure 5-33: For the modified Morris function with 6 inputs and $w_i \in [-1, 1]$: the mean and standard deviation of EE_i from the Variance method with $Nc/d = 12$ to 14 (left) and from the Inverse Variance method with $Nc = 12$ and $Level = 4$ to 5 (right).

rable with those using the gradient when the function consists of the nonmonotonic terms and large-input dimensions. Again, the inverse variance method still provides superior performance in the convergence of results. Consequently, the convergence of all algorithms is not affected by varying the input range.

Lastly, when we increase the random dimension of inputs in the modified Morris function to 12, the inputs are clustered into four distinct groups: (1,2,3,4,5),(6),(7,8,9,10), and (11,12) according to their sensitivity to the output and coupling. With this more complicated function, the three methods we are now considering - the Morris method with $p = 16$, Monte Carlo Sampling, and Collocation methods with $\Delta = \frac{1}{2}$ (see Figure 5-35) consequently rank the first-order effect ($E[EE_i]$) and the input coupling effect ($\sigma[EE_i]$) of all inputs in the same order as the VEE_i and IEE_i of the Variance and Inverse Variance methods (see Figure 5-36). Although the magnitudes of $IIEE_i$ are closely packed together, the $IIEE_i$, [4.20, 4,27, 4.29, 4.16, 4.17, 2.22, 0.06, 0.031, 0.034, 0.005, 0.046, 0.022], is still able to rank the coupling effects of inputs correctly. Thus, these results exhibit that all algorithms can identify the inputs' sensitivity accurately for any static function.

In terms of the convergence performance for the 12-dimensional input problem, the Morris, Monte Carlo Sampling, and Collocation methods provide the same order

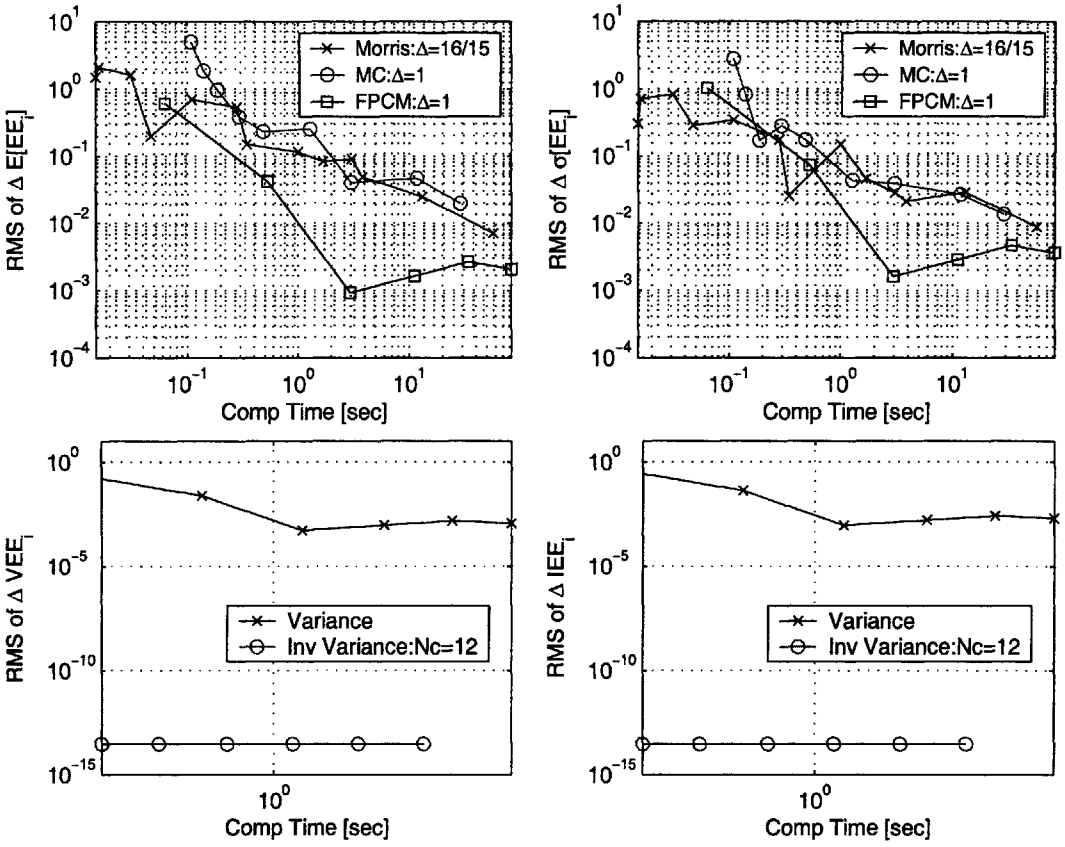

Figure 5-34: For the modified Morris function with 6 inputs and $w_i \in [-1, 1]$: the convergence characteristics, plotted versus the computational time, for $RMS(\Delta E[EE_i])$ (Top-Left) and $RMS(\Delta\sigma[EE_i])$ (Top-Right) using the Morris, Monte Carlo Sampling, and Collocation methods and $RMS(\Delta VEE_i)$ (Bottom-Left) and $RMS(\Delta IEE_i)$ (Bottom-Right) using the Variance and Inverse Variance methods.

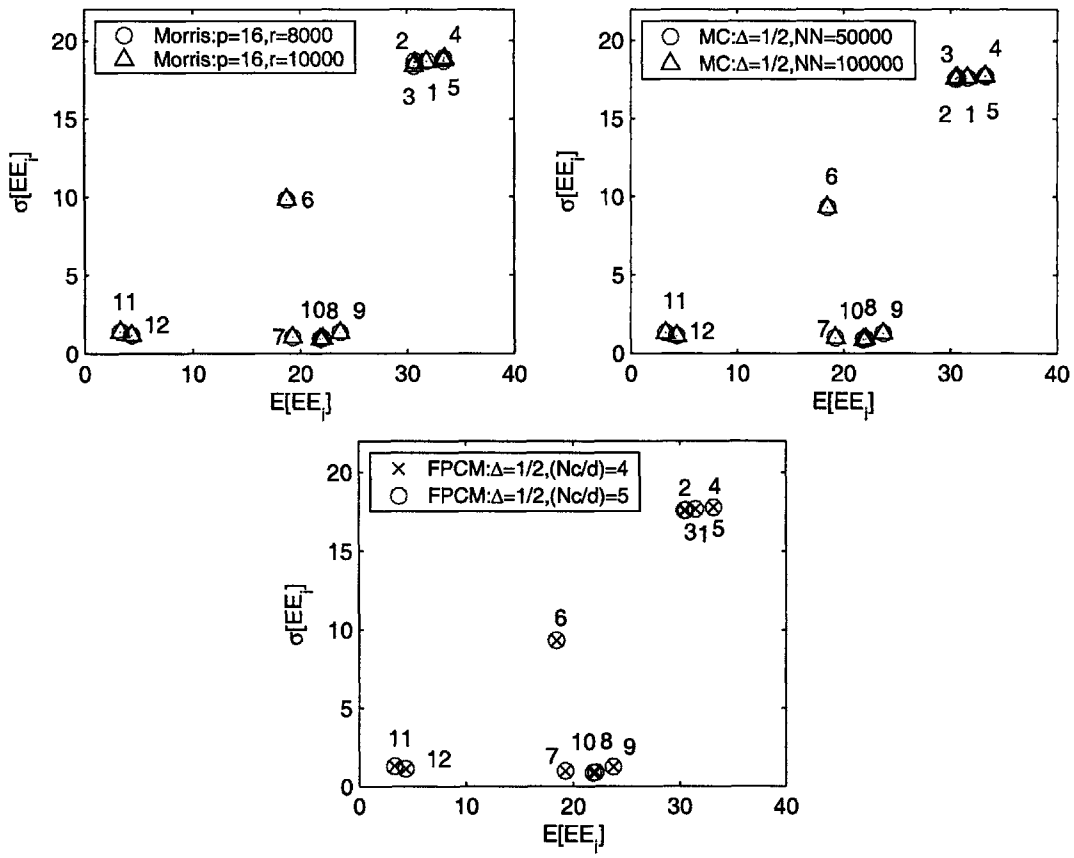

Figure 5-35: For the modified Morris function with 12 inputs and $w_i \in [0, 1]$: the mean and standard deviation of EE_i from the Morris method with $p = 16$ and $r = 8000$ to $10,000$ (top-left), from the Monte Carlo Sampling with $\Delta = 1/2$ and $NN = 8000$ to $10,000$ (top-right), and the Collocation method with $\Delta = 1/2$ and $Nc = 12$ to 14 (bottom).

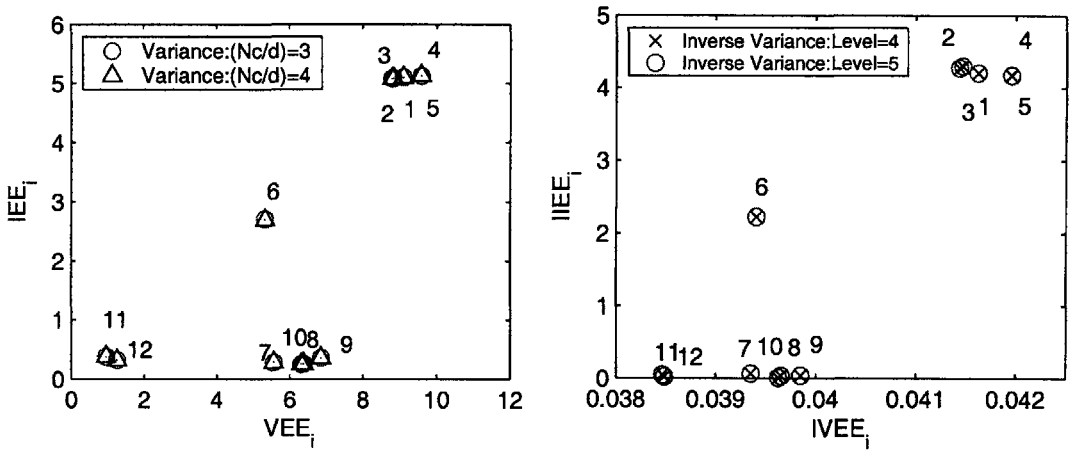

Figure 5-36: For the modified Morris function with 12 inputs and $w_i \in [0,1]$: the mean and standard deviation of EE_i from the Variance method with $Nc/d = 12$ to 14 (left) and from the Inverse Variance method with $Nc = 12$ and $Level = 4$ to 5 (right).

of magnitude in their convergence accuracy, as shown in Figure 5-37. Owing to an increase of the input dimension, the Collocation method using the full-grid PCM is computed with (Nc/d)=[2,3,4,5] such that the computing time is contained within a range similar to those of the Morris and Monte Carlo Sampling methods. The results from the Variance method with (Nc/d)=[2,3,4,5] shows a similar convergence, parallel with the Collocation method, which is related to the convergence characteristic of the full-grid PCM. Despite the large input dimension, the results using the Inverse Variance method still converge to the machine precision within a fraction of a second. In the next few sections, we extend the capability of these algorithms to analyze the input sensitivity of the ODE systems within a given time interval.

5.3 Comparison of Sensitivity Analysis on ODE

To demonstrate that these sensitivity algorithms can be applicable to the ODEs, we systematically tested the parametric sensitivity and interaction of the system on various linear and nonlinear ODEs, including the first-order ODE , Duffing's oscillator with a constant forcing, open-loop induction machine with the infinite bus in Section 4.3, and the AC power distribution with open- and close-loop propulsion drive.

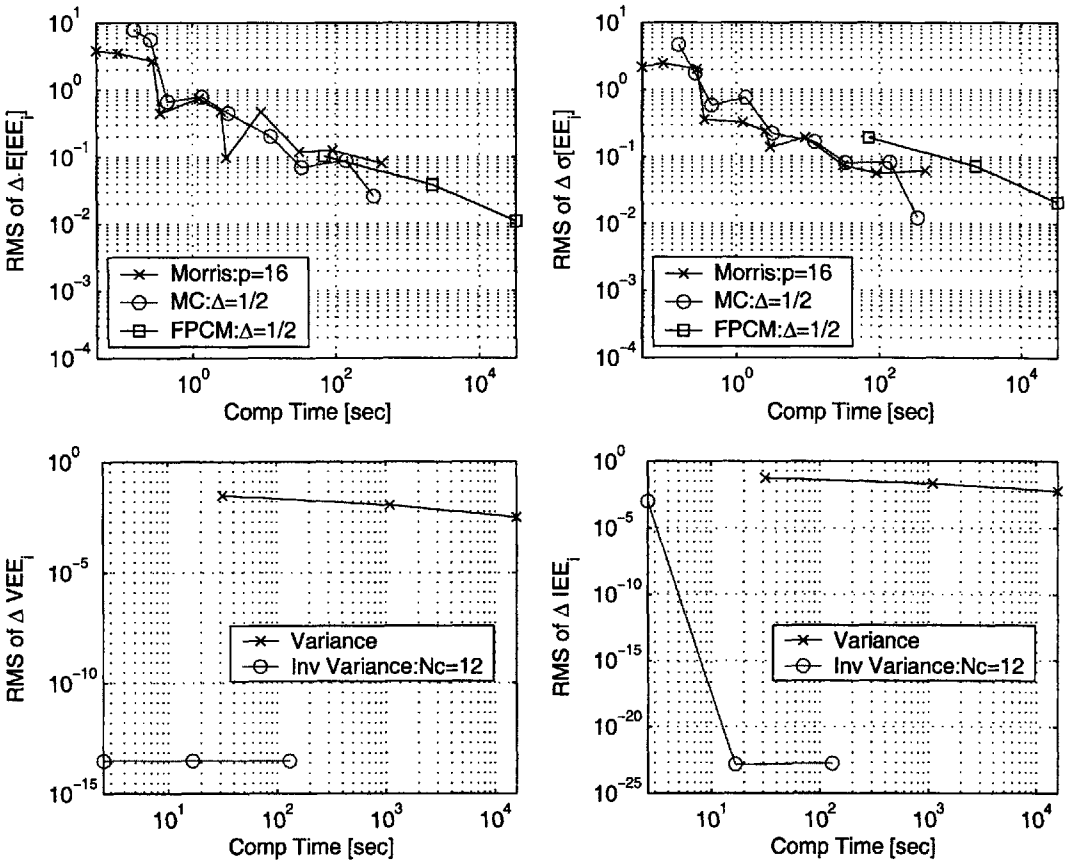

Figure 5-37: For the modified Morris function with 12 inputs and $w_i \in [0, 1]$: the convergence characteristics, plotted versus the computational time, for $RMS(\Delta E[EE_i])$ (Top-Left) and $RMS(\Delta\sigma[EE_i])$ (Top-Right) using the Morris, Monte Carlo Sampling, and Collocation methods and $RMS(\Delta VEE_i)$ (Bottom-Left) and $RMS(\Delta IEE_i)$ (Bottom-Right) using the Variance and Inverse Variance methods.

Due to the time dependency of the systems' response, we show that the sensitivity of one parameter can dominate that of the other parameters only within a certain time interval. In addition, the convergence characteristics of these algorithms are evaluated and compared against one another. First, we define the sensitivity index as $E[EE_i]$ using the Morris, Sampling, and Collocation methods or VEE_i using the Variance method. The interaction index, denoted by D_{σ_i}, is defined as a time-average distance between the origin to the curve of $\sigma[EE_i]$ versus $E[EE_i]$ or of VEE_i versus IEE_i. Note that the original Morris method is designed for testing the parameters' sensitivity of the static function only, and thus we also extend the capability of the Morris method to handle ODE systems.

5.3.1 Linear first-order ODE

First, we consider the simplest ODE, which is identical to that in Section 4.1.1 of Chapter 4, again written below. This equation is used as a reference for a comparison of the sensitivity indices' magnitude between the deterministic gradient-based methods and the stochastic variance-based method.

$$\frac{dy}{dt} = -ky \text{ with } y(0) = y_0 = 2 \tag{5.19}$$

where the decay coefficient k assumes to be a uniform random variable with $\bar{k} = 5$ and $\sigma_k = 0.4$. The deterministic solution of this equation is $y(t) = y_0 e^{-kt}$. As a result, the local derivative of $y(t)$ with respect to k is expressed as the following:

$$\frac{dy}{dk} = -y_0 t e^{-kt}. \tag{5.20}$$

The closed-form statistical solution of the ratio of σ_y over σ_k, which derived in Section 4.1.1., is again rewritten below.

$$\frac{\sigma_y}{\sigma_k} = \sqrt{\frac{y_0^2 e^{-2kt}}{2}\left(\frac{(e^{-2\sigma_k t} - e^{2\sigma_k t})}{2\sigma_k t} + \frac{(e^{\sigma_k t} - e^{-\sigma_k t})^2}{2\sigma_k^2 t^2}\right)}. \tag{5.21}$$

The deterministic sensitivity index, $E[EE_k]$, from the gradient-based methods is plotted overlaying the local derivative, $\frac{dy}{dk}$, shown on the left of Figure ??. Similarly, the stochastic sensitivity index, $\frac{\sigma_y}{\sigma_k}$, from the Variance method is directly superimposed on the closed-form statistical solution, $\frac{\sigma_y}{\sigma_k}$, shown on the right of Figure ??. Both the gradient-based and Variance methods well agree with their analytical solutions. Notice that a scaling factor between the absolute local derivative and the statistical solution at the initial point or zero second is $\sqrt{3}$. This scaling factor can be discovered analytically from the ratio of $|\frac{dy}{dk}|$ over $\frac{\sigma_y}{\sigma_k}$ by using an approximation of the exponential series.

$$\begin{aligned}
\frac{|\frac{dy}{dk}|}{\frac{\sigma_y}{\sigma_k}} &= \frac{2(\sigma_k t)^2}{\sqrt{\sigma_k t(e^{2\sigma_k t} - e^{-2\sigma_k t}) - (e^{\sigma_k t} - e^{-\sigma_k t})^2}}, \\
&= \frac{2(\sigma_k t)^2}{\sqrt{2 + e^{2\sigma_k t}(\sigma_k t - 1) - e^{-2\sigma_k t}(1 + \sigma_k t)}} \\
&\approx \frac{2(\sigma_k t)^2}{\sqrt{2 + \sum_{i=0}^{4} \frac{(2\sigma_k t)^i}{i!}(\sigma_k t - 1) - \sum_{i=0}^{4} \frac{(-2\sigma_k t)^i}{i!}(1 + \sigma_k t)}} \\
&\approx \frac{2(\sigma_k t)^2}{\frac{2}{\sqrt{3}}(\sigma_k t)^2}.
\end{aligned} \tag{5.22}$$

However, the absolute ratio of the local derivative over the statistical solution varies as time progresses, as shown in Figure 5-39. The bigger the magnitude of σ_k is, the larger the deviation of $|(\frac{dy}{dk})/(\frac{\sigma_y}{\sigma_k})|$ as a function of time becomes. Nevertheless, the $\frac{\sigma_y}{\sigma_k}$ curve changes slightly as the σ_k increase.

The multiplicative uncertainty in k also induces the interaction with the state variable, which can be captured by the variation of the gradient in the Morris, MC Sampling, and Collocation methods in Figure 5-40. The interaction of k with y is evolved with time, as shown in the $\sigma[EE_k]$ versus $E[EE_k]$ plot. However, the Variance method cannot identify the parameter's interaction in a one-dimensional problem.

Second, we consider another simple first-order ODE with an exponential decay rate (k) and a constant forcing function (c), as expressed below:

$$\frac{dy}{dt} = -ky + c \text{ with } y(0) = y_0 = 2 \tag{5.23}$$

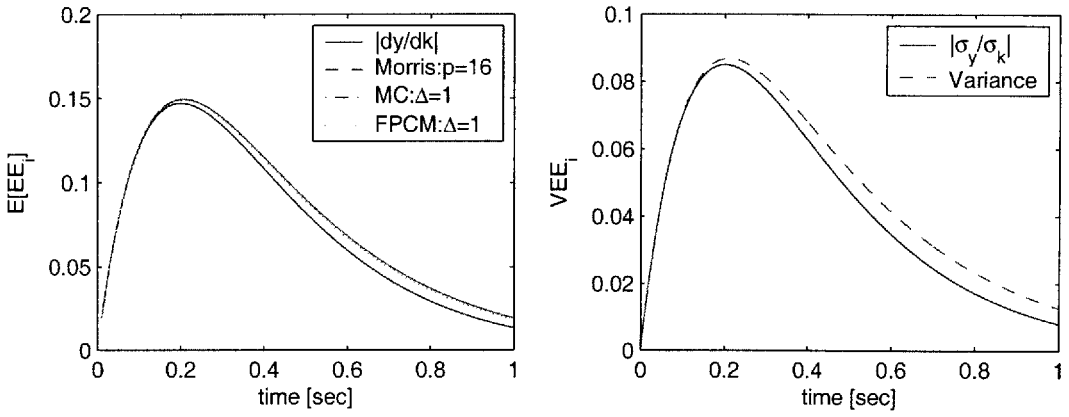

Figure 5-38: For the linear ODE $dy/dt = -ky$: the mean of EE_k (left) from the Morris with $p = 16$ and $r = 50000$, Monte Carlo Sampling with $\Delta = 1$ and $NN = 50000$, and Collocation with $\Delta = 1$ and $Nc = 30$ method with $\sigma_k = 0.4$ are compared with the absolute local derivative of y with respect to k and the VEE_k (right) from the Variance method are compared with the statistical solution $|\frac{\sigma_y}{\sigma_k}|$.

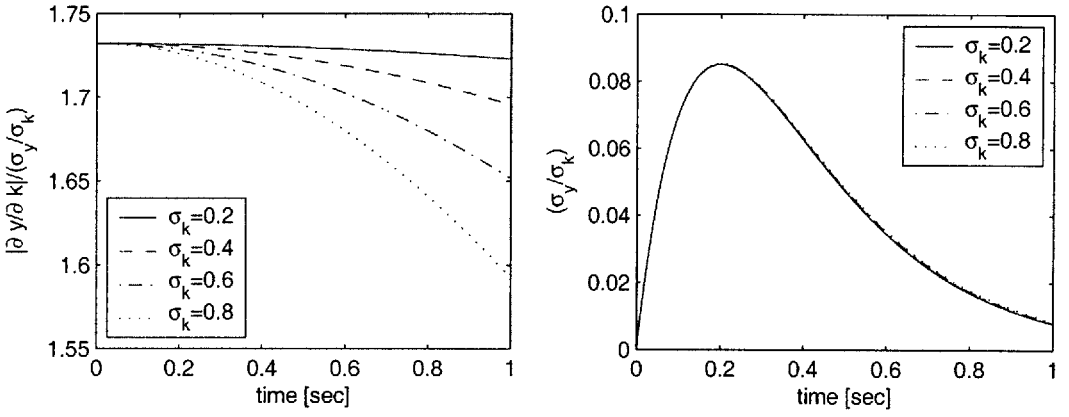

Figure 5-39: For the linear ODE $dy/dt = -ky$: the absolute ratio of the local derivative over the statistical solution (left) and the statistical solution $|\frac{\sigma_y}{\sigma_k}|$ for various σ_k.

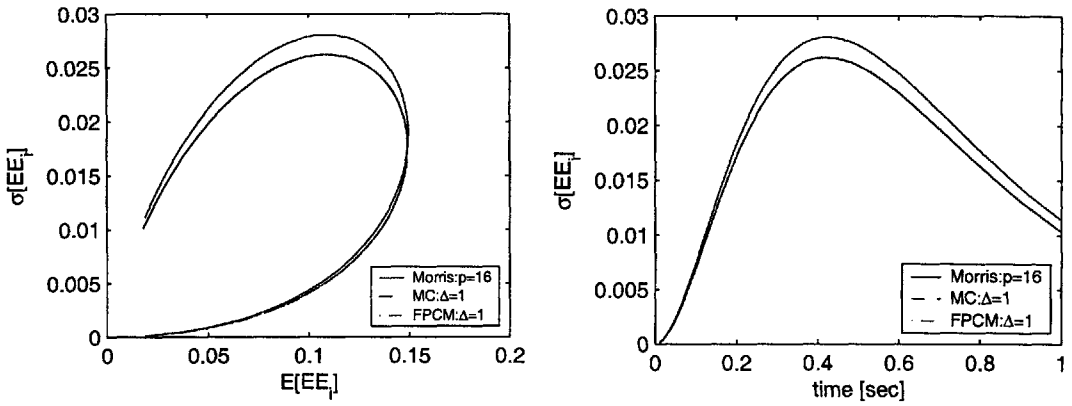

Figure 5-40: For the linear ODE $dy/dt = -ky$: the $\sigma[EE_k]$ as a function of time (left) and the plot of $\sigma[EE_k]$ versus $E[EE_k]$ (right), using the Morris method with $p = 16$ and $r = 50000$ (solid-line), the Monte Carlo Sampling with $\Delta = \frac{1}{2}$ and $NN = 50000$ (dash-line), and Collocation method with $\Delta = \frac{1}{2}$ and $Nc/d = 30$ (dot-line).

With this ODE, two different conditions – 1) k is a fixed constant of 5 and c is an uniform random variable with $\bar{c} = 2$ and $\sigma_c = 0.4$ and 2) both k and c are independent uniform random variables with $\bar{k} = 5$, $\bar{c} = 2$, and σ_k and σ_c are 0.4 – are considered in this system. The first condition is for studying the sensitivity and interaction effects of the additive uncertainty, c, alone, while the second condition shows how the multiplicative uncertainty, k, induces the interaction effect in the additive term. The deterministic solution and its local derivatives with respect to k and c can be derived as the following equations below, which can be used as the reference solutions of the time-dependent sensitivity indices.

$$y = y_0 - (y_0 - \frac{c}{k})(1 - e^{-kt}), \tag{5.24}$$

$$\frac{\partial y}{\partial c} = \frac{1}{k}(1 - e^{-kt}). \tag{5.25}$$

For the first condition, the closed-form statistical solution of the ratio of σ_y over σ_c, can be derived as the following:

$$\frac{\sigma_y}{\sigma_c} = \frac{1}{\sqrt{3}k}(1 - e^{-kt}). \tag{5.26}$$

Due to the linearity and additive uncertainty of this system, the absolute ratio of the

local derivative and statistical solution is just $\sqrt{3}$; however, this ratio is not always constant as in the case of nonlinear systems and other types of uncertainties, e.g. multiplicative and rational functions. For this linear system, Figure 5-41 shows that $\frac{\partial y}{\partial c}$ is exactly identical to $E[EE_c]$ from the Morris method, Sampling, and Collocation methods. Moreover, $\frac{\sigma_y}{\sigma_c}$ from the Variance method is also precisely matched with the closed-form statistical solution, illustrated in Figure 5-41.

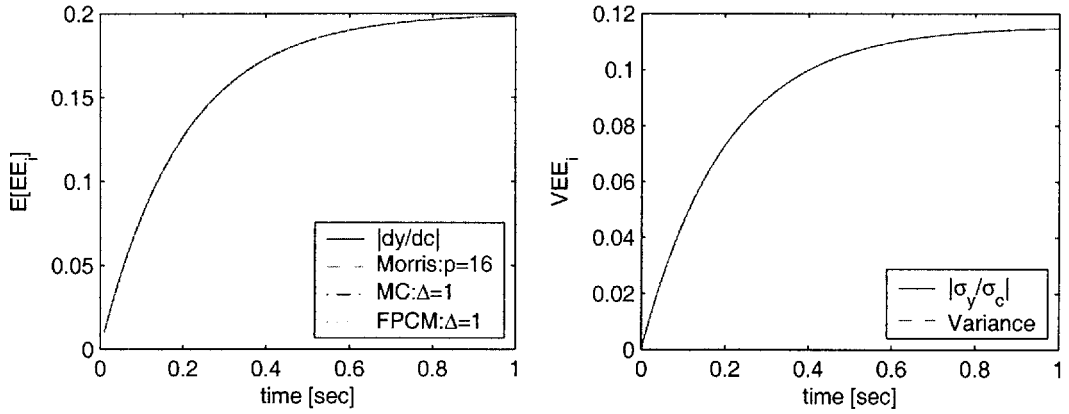

Figure 5-41: For the linear ODE $dy/dt = -ky + c$ with only c as a uniform random variable: the mean of EE_c (left) from the Morris with $p = 16$ and $r = 50000$, Monte Carlo Sampling with $\Delta = 1$ and $NN = 50000$, and Collocation with $\Delta = 1$ and $Nc = 30$ method with $\sigma_c = 0.4$ are compared with the absolute local derivative of y with respect to c and the VEE_c (right) from the Variance method are compared with the statistical solution $|\frac{\sigma_y}{\sigma_c}|$.

Since the additive uncertainty is not directly coupled with other parameter and state; thus, there is no interaction from c, as shown in the $\sigma[EE_c]$ of Figure 5-42 using the Morris, Sampling, and Collocation methods.

For the second condition, when both k and c are independently uniform random variables, the closed-form statistical solution of $\frac{\sigma_y}{\sigma_k}$ and $\frac{\sigma_y}{\sigma_c}$ become very complex, as

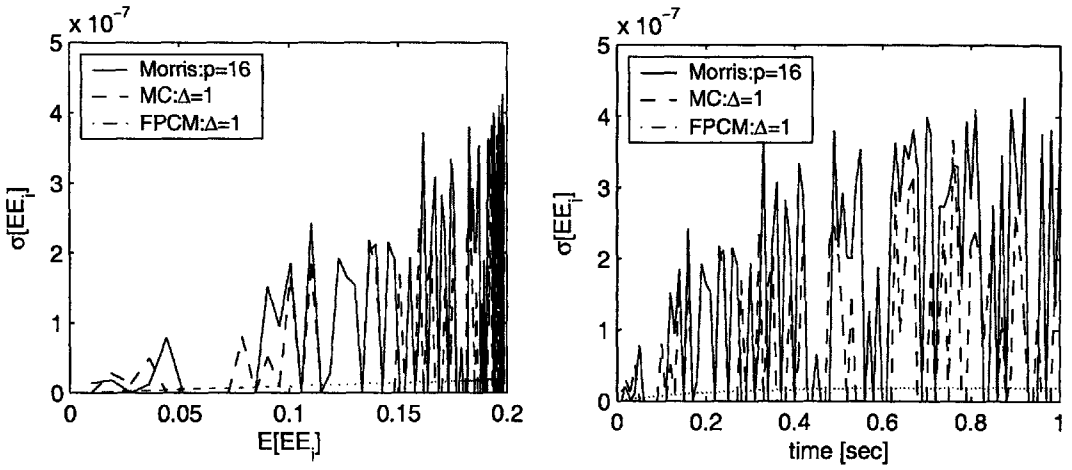

Figure 5-42: For the linear ODE $dy/dt = -ky$: the $\sigma[EE_k]$ as a function of time (left) and the plot of $\sigma[EE_k]$ versus $E[EE_k]$ (right), using the Morris method with $p = 16$ and $r = 50000$ (solid-line), the Monte Carlo Sampling with $\Delta = \frac{1}{2}$ and $NN = 50000$ (dash-line), and Collocation method with $\Delta = \frac{1}{2}$ and $Nc/d = 30$ (dot-line).

shown below:

$$\begin{aligned}\frac{\sigma_y}{\sigma_k} &= \int_{-1}^{1} \frac{1}{2}\Big(y_0 e^{-(\bar{k}+\sigma_k\xi)t} + \frac{c}{\bar{k}+\sigma_k\xi}(1-e^{-(\bar{k}+\sigma_k\xi)t}) \\ &\quad + \frac{y_0 e^{-\bar{k}t}}{2\sigma_k t}(e^{-\sigma_k t} - e^{\sigma_k t}) - \frac{c}{2\sigma_k}\ln\Big|\frac{\bar{k}+\sigma_k}{\bar{k}-\sigma_k}\Big| \\ &\quad + \frac{c}{2}e^{-\bar{k}t}\int_{-1}^{1}\frac{e^{-\sigma_k t\zeta}}{\bar{k}+\sigma_k\zeta}d\zeta\Big)^2 d\xi, \text{ and} \end{aligned} \tag{5.27}$$

$$\frac{\sigma_y}{\sigma_c} = \frac{1}{\sqrt{3}k}(1-e^{-kt}). \tag{5.28}$$

Using the gradient-based sensitivity algorithms, the $E[EE_i]$ and $\sigma[EE_i]$ curves as a function of time are plotted overlaying the local derivatives, as shown in Figure 5-43. The parametric sensitivity of the decay rate, k, and forcing function, c, from the Morris, Sampling, and Collocation methods is closely matched with the local derivatives for this linear system. The magnitude of k and c sensitivity curves indicates that if there is one percent change in these parameters, the output's peaks are 0.17 and 0.2 percent, respectively. Moreover, the sensitivity curves of $E[\frac{\sigma_y}{\sigma_{x_i}}]$ from the Variance method, illustrated in Figure 5-44, yields similar characteristics as its local derivatives, except that the magnitude of these curves are again scaled down. The absolute

ratio of the local derivatives over the solution from the Variance method for k and c are exponential decreasing, shown in Figure 5-45. Furthermore, when we decrease the range of variation in k and c to 20 percent or when σ_k and σ_c are 0.2, all these sensitivity algorithms still provide slightly different sensitivity curves because of the linearity of this system.

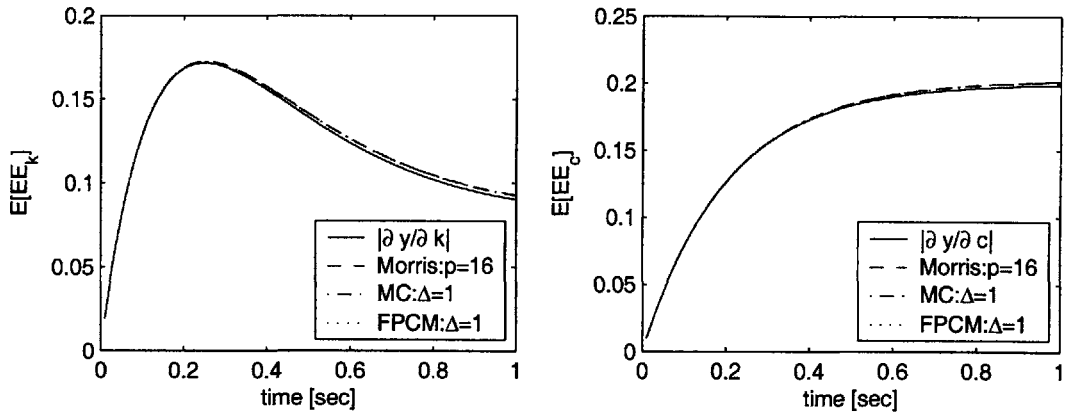

Figure 5-43: For the linear ODE $dy/dt = -ky + c$: the mean of EE_k (left) and EE_c (right) from the Morris with $p = 16$, Monte Carlo Sampling with $\Delta = 1$, and Collocation with $\Delta = 1$ method with $\sigma_k = \sigma_c = 0.2$ are compared with the absolute local derivative of y with respect to k and c.

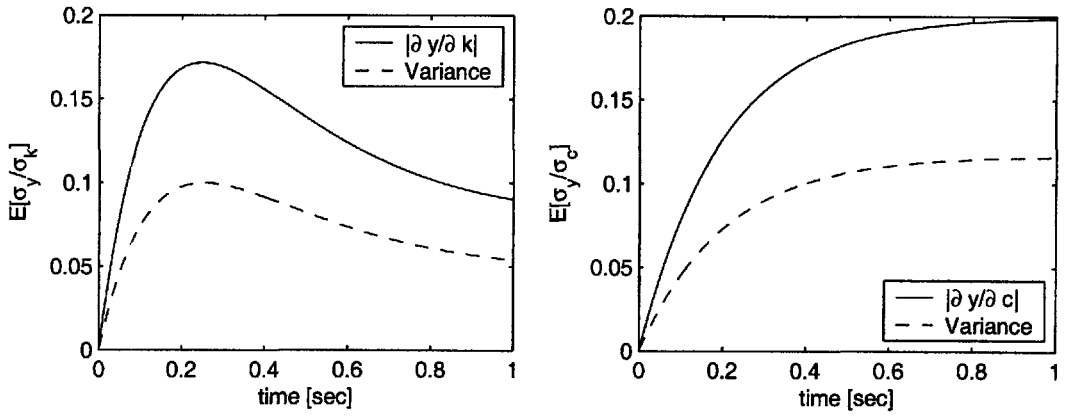

Figure 5-44: For the linear ODE $dy/dt = -ky + c$: the mean of $\frac{\sigma_y}{\sigma_k}$ (left) and $\frac{\sigma_y}{\sigma_c}$ (right) from the Variance method with $\sigma_k = \sigma_c = 0.2$ are compared with the absolute local derivative of y with respect to k and c.

However, the sensitivity of the multiplicative term, k, should have a larger influence on the system output than that of the additive term, c. To correctly rank the

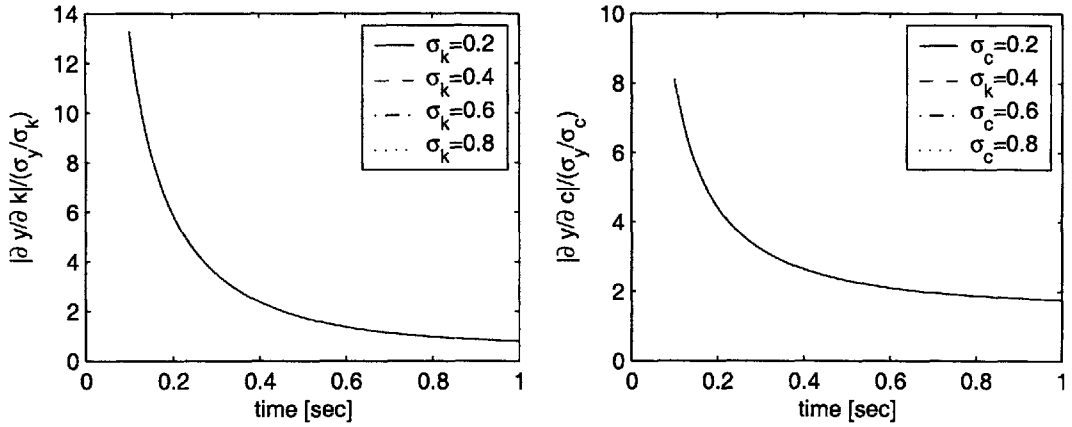

Figure 5-45: For the linear ODE $dy/dt = -ky + c$: the absolute ratio of the local derivative over the solution from the Variance method for k (left) and c (right) for various σ_k and σ_c.

parameters' sensitivity, the approximated gradient must be normalized by $k/\|y\|_\infty$ or $c/\|y\|_\infty$ to avoid including the parameters' scaling. Figure 5-46 shows the normalized $E[EE_i]$ and $\sigma[EE_i]$, which represent the parameters' sensitivity and interaction ranking, using the Morris, MC Sampling, and Collocation methods. Notice that the normalized $E[EE_i]$ rank k to be more important than c and the peak magnitude of $E[EE_k]$ is 2.14 times larger than that of $E[EE_c]$ within 0 to 1 second. From Figure 5-46, the parameter interaction with other parameters and output can be seen from the plot of $\sigma[EE_i]$ versus $E[EE_i]$. The D_{σ_k} and D_{σ_c} are respectively 0.321 and 0.164 for $\sigma_k = \sigma_c = 0.2$. When σ_k and σ_c are increased to 0.4, only the $\sigma[EE_i]$ curve is affected by this increase in the parameter variation. Therefore, D_{σ_k} and D_{σ_c} are consequently 0.344 and 0.170 for $\sigma_k = \sigma_c = 0.4$. Also, the mean values of σ_y/σ_{x_i} need to be normalized by $x_i/\|y\|_\infty$ to correctly identify the parameters' significance, as shown in Figure 5-47. Notice that IEE_k and IEE_c are exactly on top of each other; however, the plot of IEE_i versus VEE_i shows a larger interaction effect of k than that of c. The $[D_{\sigma_k}, D_{\sigma_c}]$ are [0.185,0.094] for $\sigma_{x_i} = 0.2$ and [0.198,0.097] for $\sigma_{x_i} = 0.4$. In the presence of the multiplicative uncertainty, the interaction effect of the additive uncertainty is non-zero.

Third, let us further investigate another first-order ODE without an interaction

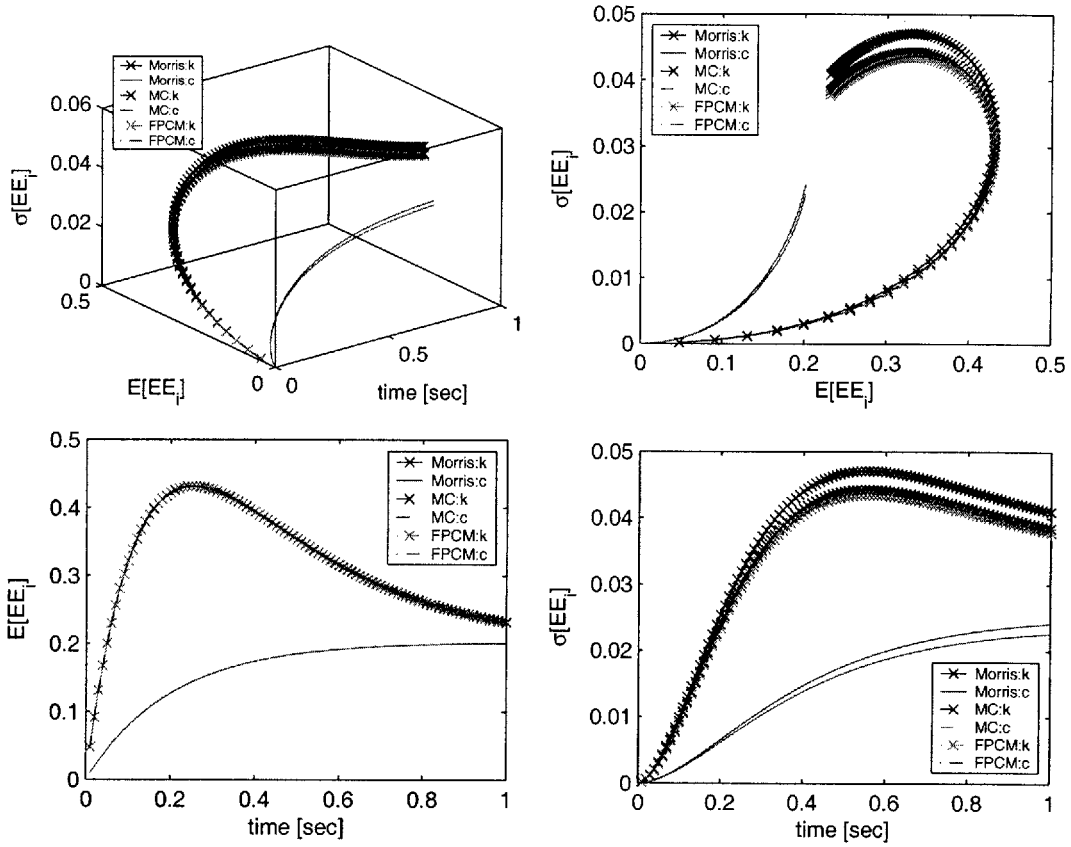

Figure 5-46: For the linear ODE $dy/dt = -ky + c$: the normalized $E[EE_i]$ and $\sigma[EE_i]$ of k and c as a function of time, $t \in [0, 1]$ second, using the Morris method with $p = 16$ and $r = 50000$ (solid-line), the Monte Carlo Sampling with $\Delta = \frac{1}{2}$ and $NN = 50000$ (dash-line), and Collocation method with $\Delta = \frac{1}{2}$ and $Nc/d = 10$ (dot-line) in three dimension (Top-Left), the Side view (Top-Right) for emphasizing the first-order effect, the Top view (Bottom-Left) for emphasizing the inputs' interaction effect, and the Front view (Bottom-Right).

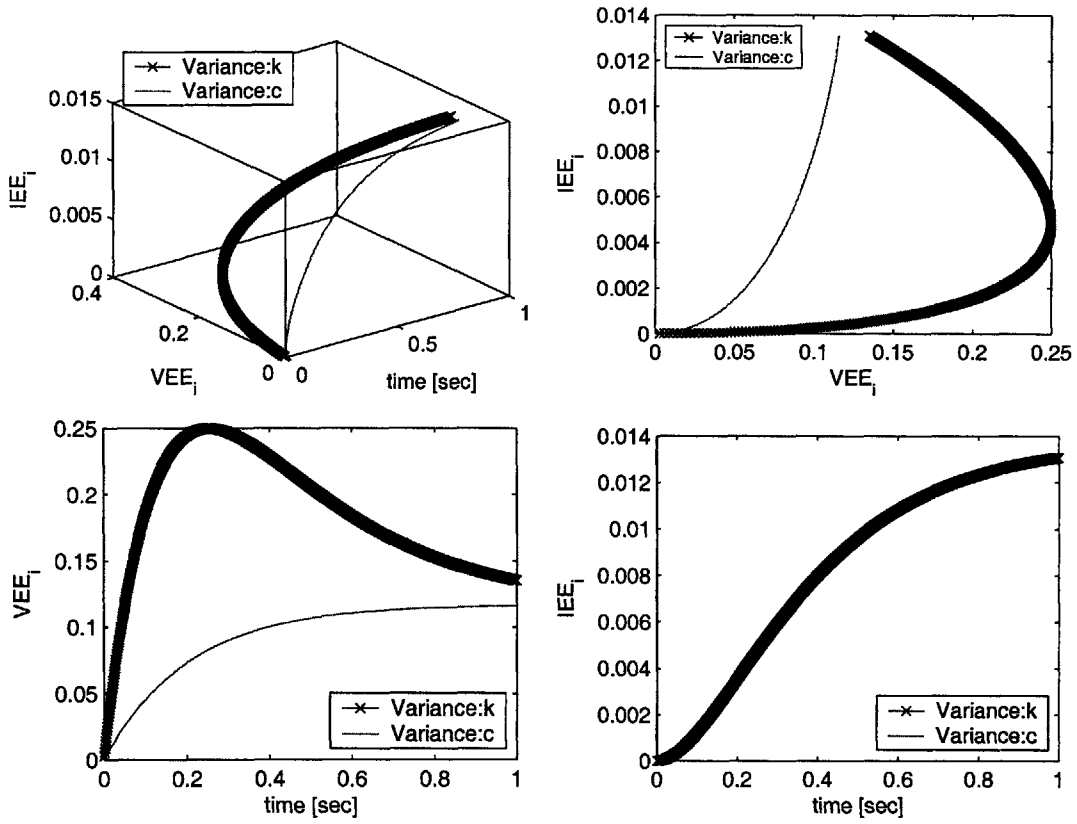

Figure 5-47: For the linear ODE $dy/dt = -ky + c$: the normalized $E[\frac{\sigma_y}{\sigma_{x_i}}]$ and $\sigma[\frac{\sigma_y}{\sigma_{x_i}}]$ of k and c as a function of time, $t \in [0, 1]$ second, using the Variance method with $Nc/d = 20$ in three dimension (Top-Left), the Side view (Top-Right) for emphasizing the first-order effect, the Top view (Bottom-Left) for emphasizing the inputs' interaction effect, and the Front view (Bottom-Right).

between state and parameters, as written in the following equation:

$$\frac{dy}{dt} = -k - b - c \text{ with } y(0) = 2 \tag{5.29}$$

where k, b, and c are random variables with mean values of 4, 2, and 3, respectively. This ODE is for testing the base-line reference of the interaction index using the Morris method and our sensitivity algorithms. Using the Morris method in Figure 5-48, the significance of parameters is ranked according to this order (k,b,c), corresponding to the magnitude of each parameter. Since there is no interaction in each parameter, the magnitudes of $\sigma[EE_i]$ are very small. Similarly, the ranking of parameters' importance using the Variance method, shown in Figure 5-49, provides the same relative order in the normalized VEE_i and no interaction among parameters can be seen from a small magnitude of the normalized IEE_i. This again confirms that in the absent of the multiplicative uncertainty, the additive uncertainty leads to zero interaction.

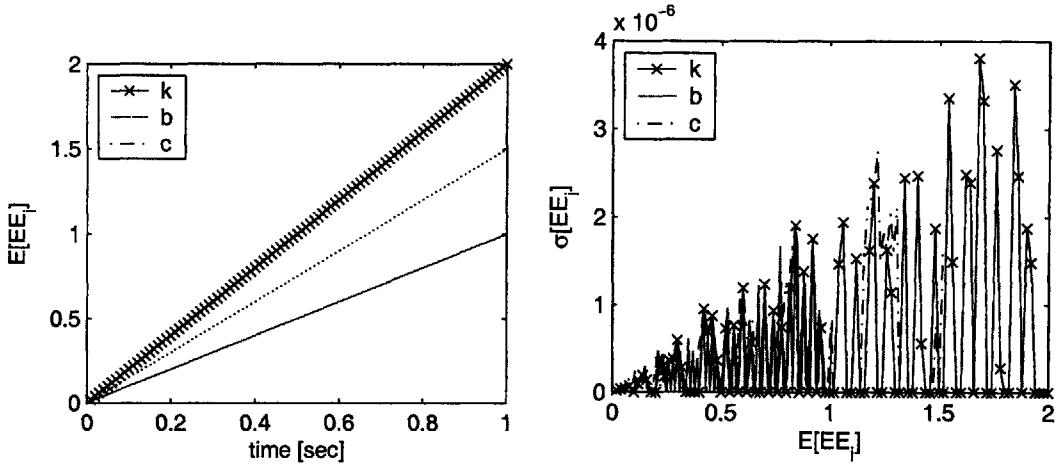

Figure 5-48: For the linear ODE $dy/dt = -k - b - c$: the normalized $E[EE_i]$ and $\sigma[EE_i]$ of k, b, and c as a function of time, $t \in [0, 1]$ second, using the Morris method with $p = 16$ and $r = 80000$ to emphasize the first-order effect (Left) and to emphasize the inputs' interaction effect (Right).

Fourth, to evaluate the effectiveness of the interaction index using the Morris method and our sensitivity algorithms, we look at another first-order ODE, shown below:

$$\frac{dy}{dt} = -kcy + c \text{ with } y(0) = 2 \tag{5.30}$$

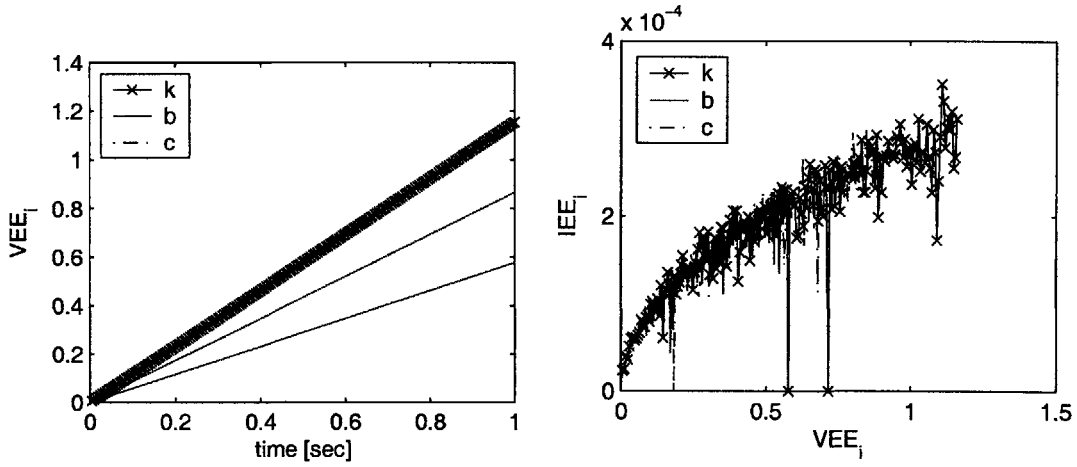

Figure 5-49: For the linear ODE $dy/dt = -k - b - c$: the normalized $E[\frac{\sigma_y}{\sigma_{x_i}}]$ and $\sigma[\frac{\sigma_y}{\sigma_{x_i}}]$ or VEE_i and IEE_i of k, b, and c as a function of time, $t \in [0, 1]$ second, using the Variance method with $Nc/d = 30$ to emphasize the first-order effect (Left) and to emphasize the inputs' interaction effect (Right).

where k and c are random variables with mean values of 5 and 2, respectively. σ_{x_i} is set to be 0.4. From Figure 5-50, k has a larger influence on the output than c, which is unexpected because there are two terms of c in the above equation. However, the cancellation of the multiplicative and additive terms c decreases its sensitivity index. Similarly, the interaction index also indicates that k has a stronger coupling effect than c with $y(t)$. The $[D_{\sigma_k}, D_{\sigma_c}]$ are [0.210,0.114] for $\sigma_{x_i} = 0.4$. Using the Variance method, we obtain similar sensitivity characteristics and parameters' coupling effect, as shown in Figure 5-51. Notice that the plot of normalized VEE_i versus IEE_i contains more curvature than that of $E[EE_i]$ versus $\sigma[EE_i]$; nevertheless, the interaction index of the Variance method yields the same relative magnitude of k and c, where $[D_{\sigma_k}, D_{\sigma_c}]$ are [0.120,0.065] for $\sigma_{x_i} = 0.4$.

5.3.2 Duffing's oscillator

Now, let us consider a nonlinear Duffing's oscillator with a constant forcing function, which consists of two state variables: position (y) and velocity ($\frac{dy}{dt}$) as expressed in the equation below,

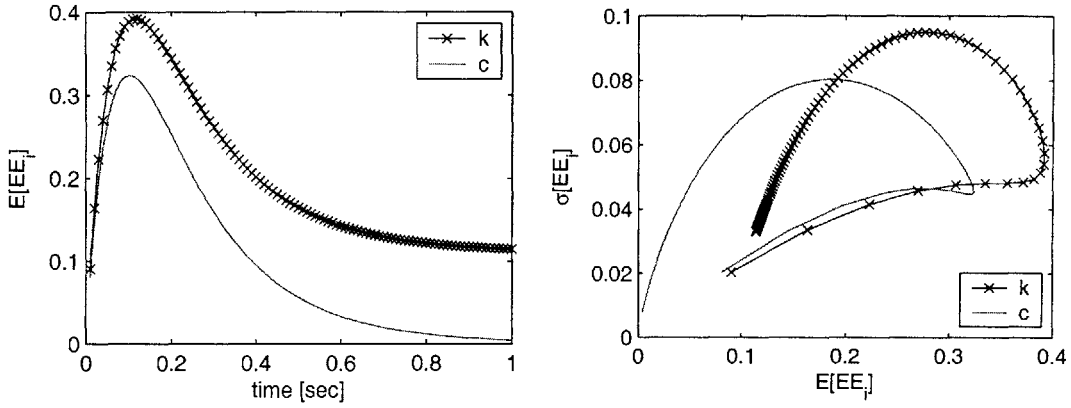

Figure 5-50: For the linear ODE $dy/dt = -kcy + c$: the normalized $E[EE_i]$ and $\sigma[EE_i]$ of k and c as a function of time, $t \in [0, 1]$ second, using the Morris method with $p = 16$ and $r = 80000$ to emphasize the first-order effect (Left) and to emphasize the inputs' interaction effect (Right).

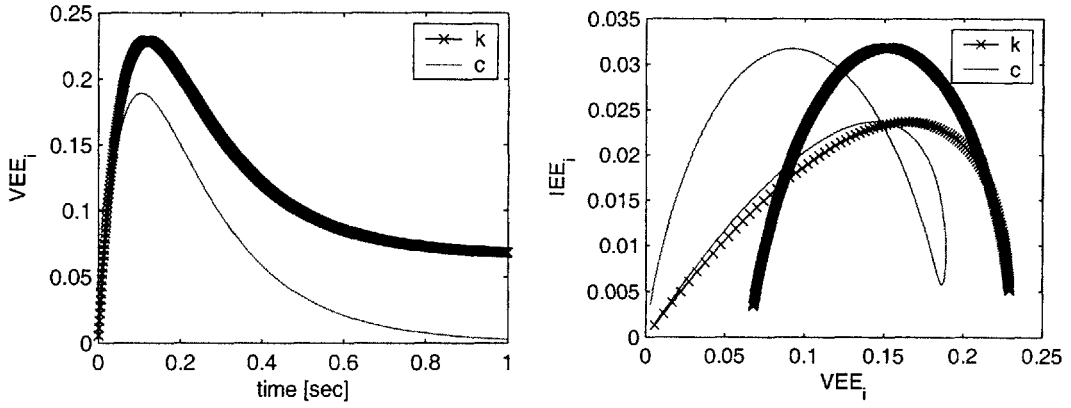

Figure 5-51: For the linear ODE $dy/dt = -kcy + c$: the normalized $E[\frac{\sigma_y}{\sigma_{x_i}}]$ and $\sigma[\frac{\sigma_y}{\sigma_{x_i}}]$ or VEE_i and IEE_i of k and c as a function of time, $t \in [0, 1]$ second, using the Variance method with $Nc/d = 30$ to emphasize the first-order effect (Left) and to emphasize the inputs' interaction effect (Right).

$$\frac{dy^2}{dt} + 2\eta\omega\frac{dy}{dt} + \omega^2 y + \epsilon\omega^2 y^3 = 1.0, \text{ with } \frac{dy(0)}{dt} = 0; y(0) = 2, \tag{5.31}$$

where η, ω, and ϵ are a damping coefficient, a natural frequency, and a coefficient of the cubic nonlinearity, which can represent a hardening nonlinear spring. All η, ω, and ϵ are assumed to be independent uniform random variables with mean of 2 and standard deviation of 0.2 for unbiased weighting of this nonlinear ODE. From this nonlinear system, ω is the most influential parameter due to the quadratic nonlinearity and strong couplings with the other two parameters and the output. However, this might not be the case for all times between [0,1] second. As shown in Figure 5-52, the trajectories of normalized $E[EE_i]$ and $\sigma[EE_i]$ for these three parameters are plotted as a function of time using the Morris method with $p = 16$, the Monte Carlo Sampling and Collocation methods with $\Delta = \frac{1}{2}$, which are based on the gradient computation. Note that the normalized $E[EE_i]$ and $\sigma[EE_i]$ trajectories from the Monte Carlo and Collocation methods are identical, and also closely match with that of the Morris method. From the plot of normalized $E[EE_i]$ versus time, the sensitivity effect of ω is dominant at the first quarter of a second and again after 0.6 second; the damping effect of η surpasses that of ω only between 0.35 and 0.6 second. These characteristics occur because of the cubic nonlinearity in the last term of the equation. As expected, the coupling effect of ω is stronger than those of the η and ϵ for the entire range of time, illustrated in the plots of $\sigma[EE_i]$ versus time and $\sigma[EE_i]$ versus $E[EE_i]$. The $[D_{\sigma_\omega}, D_{\sigma_\eta}, D_{\sigma_\epsilon}]$ are [0.472,0.285,0.235] using the Morris method with $\sigma_{x_i} = 0.2$, which is similar to the interaction indices obtained from the Sampling and Collocation methods. The interaction of ω is twice as that of ϵ on average. In addition, we can consider the ranking of inputs' first-order and coupling effects at a specified time, as shown in Figure 5-53 for t=$[\frac{1}{3}, \frac{2}{3}]$ second. The results using the MC Sampling and Collocation methods precisely overlay each other, while their relative magnitude matches that of the Morris method.

Now, the VEE_i and IEE_i trajectories of η, ω, and ϵ are plotted in Figure 5-54 using the Variance method. These trajectories resemble those in Figure 5-52,

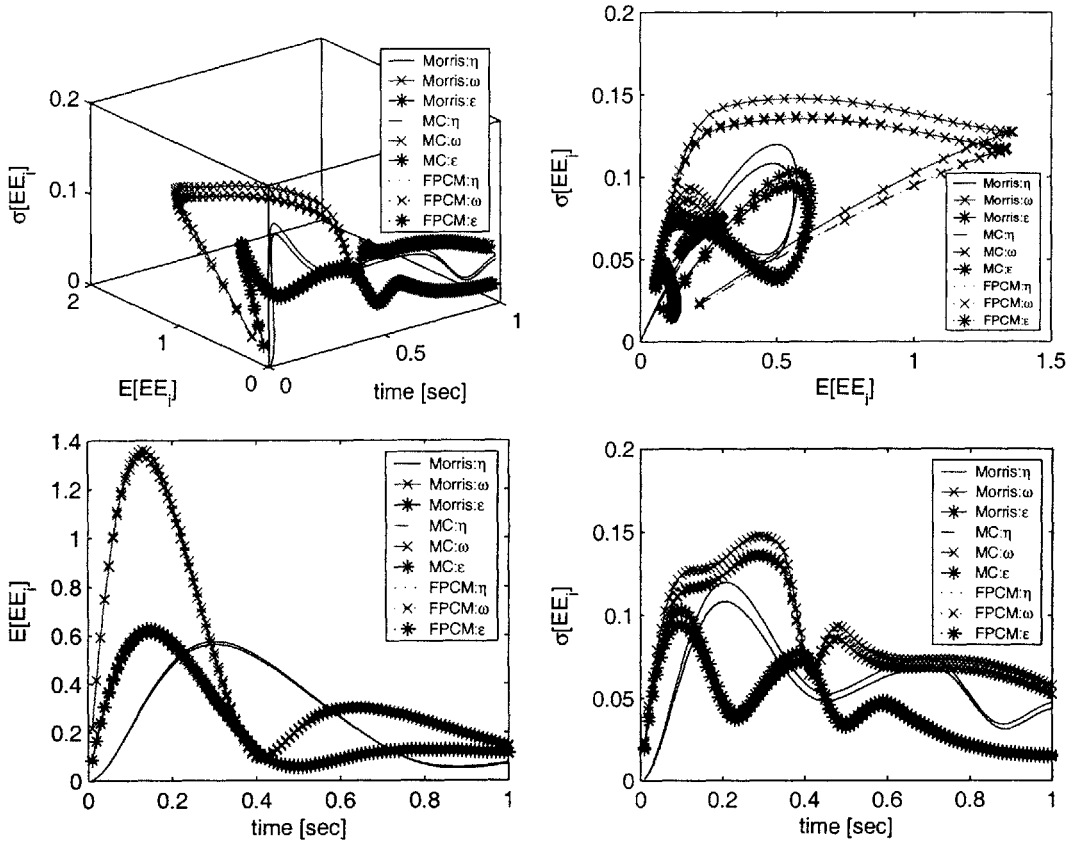

Figure 5-52: For a $\frac{dy}{dt}$ variable, the $E[EE_i]$ and $\sigma[EE_i]$ of η, ω, and ϵ as a function of time, $t \in [0, 1]$ second, using the Morris method with $p = 16$ and $r = 5,000$ (solid-line), the Monte Carlo Sampling with $\Delta = \frac{1}{2}$ (dash-line), and Collocation method with $\Delta = \frac{1}{2}$ (dot-line) in three dimensions (Top-Left), the Side view (Top-Right) for emphasizing the first-order effect, the Top view (Bottom-Left) for emphasizing the inputs' interaction effect, and the Front view (Bottom-Right).

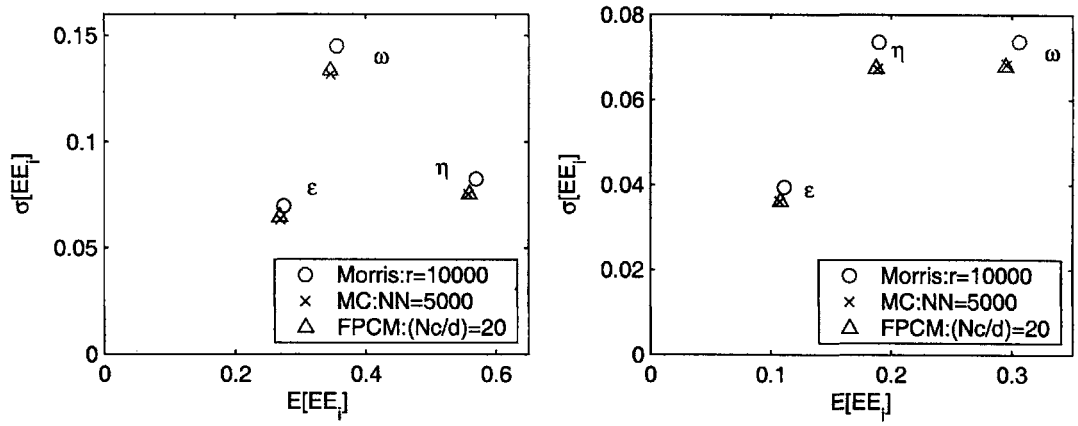

Figure 5-53: The mean and standard deviation of EE_i from the Morris method, the Monte Carlo Sampling and, the Collocation method in the last figure, when time is fixed at $\frac{1}{3}$ and $\frac{2}{3}$ second.

obtained using the gradient-based sensitivity. In particular, the relative magnitude of the first-order effect, VEE_i, is the same as that of $E[EE_i]$. However, the trajectories of IEE_ω and $\sigma[EE_\omega]$ are slightly different during [0,0.5] second since the IEE_i of the Variance method does not include the nonlinear effect. As seen in Figure 5-52, the trajectory of $\sigma[EE_\omega]$ is larger than those of $\sigma[EE_{\eta,\epsilon}]$ at all times due to the quadratic nonlinearity of ω and the coupling with the cubic nonlinearity output. After 0.5 second, when the system reaches its steady state, the characteristics of the IEE_i and $\sigma[EE_i]$ trajectories become very similar. The plots of $\sigma[EE_i]$ versus $E[EE_i]$ and of IEE_i and VEE_i reveal another perspective. The $\sigma[EE_i]$ versus $E[EE_i]$ plot shows that the interaction and nonlinear effects of ω dominate those of η and ϵ, while the IEE_i and VEE_i plot, which emphasizes the interaction effect more, shows that η can be more important in certain time ranges than ω because of its direct interaction with the $\frac{dy}{dt}$ state variable. The $[D_{\sigma_\omega}, D_{\sigma_\eta}, D_{\sigma_\epsilon}]$ are [0.360,0.173,0.159] using the Variance method with $\sigma_{x_i} = 0.2$. These interaction indices show that the coupling effect of ω is almost two times larger than that of ϵ. Likewise, the plot of VEE_i and IEE_i can be taken from the slice of the trajectory plot at a particular time, as shown in Figure 5-57 for t=$[\frac{1}{3}, \frac{2}{3}]$ second. The relative magnitude of VEE_i and IEE_i plots at these two time slices are identical to those of $E[EE_i]$ and $\sigma[EE_i]$ plots.

From the convergence performance aspect, we need to redefine the $RMS(\Delta E[EE_i])$

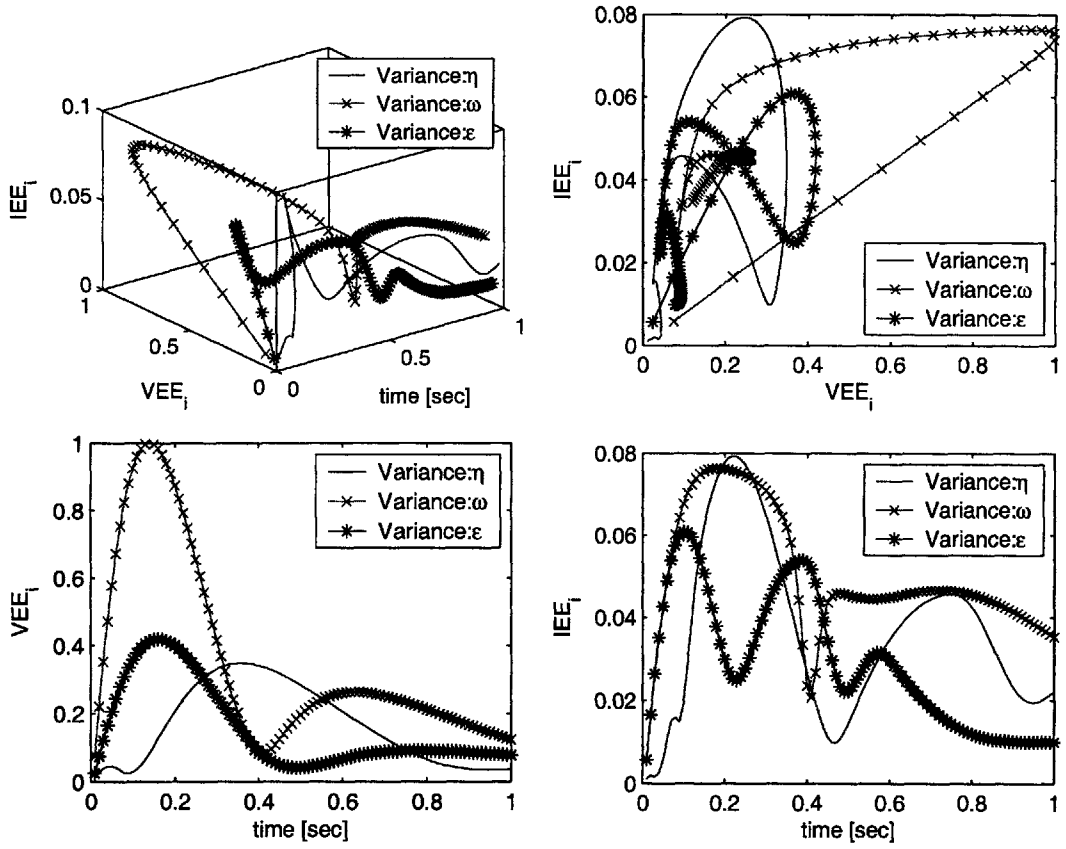

Figure 5-54: For a $\frac{dy}{dt}$ variable, the VEE_i and IEE_i of η, ω, and ϵ as a function of time, $t \in [0, 1]$ second, using the Variance method with $(Nc/d) = 20$ in three dimensions (Top-Left), the Side view (Top-Right) for emphasizing the first-order effect, the Top view (Bottom-Left) for emphasizing the inputs' interaction effect, and the Front view (Bottom-Right).

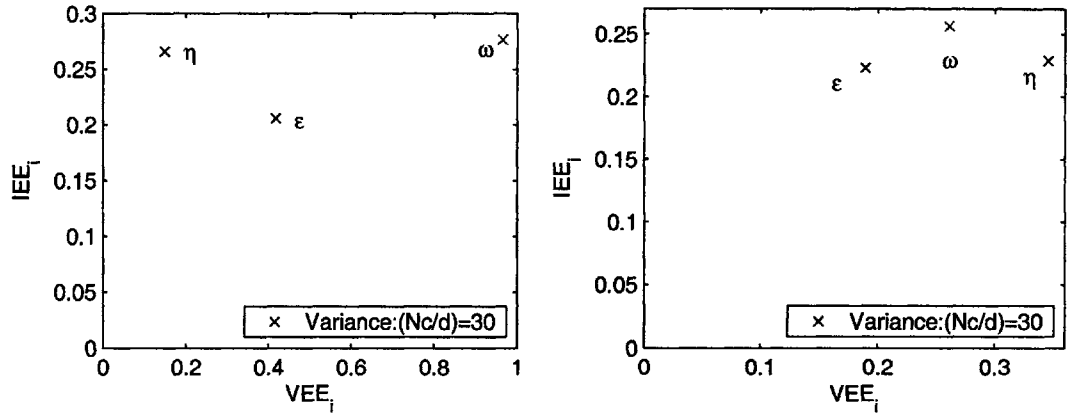

Figure 5-55: The mean and standard deviation of EE_i from the Variance method in the last figure, when time is fixed at $\frac{1}{3}$ and $\frac{2}{3}$ second.

and $RMS(\Delta\sigma[EE_i])$ to take into account the third dimension of time. The L_2 norm is employed in $RMS(\|\Delta E[EE_i]\|_2)$ and $RMS(\|\Delta\sigma[EE_i]\|_2)$ to sum the $\Delta E[EE_i]$ and $\Delta\sigma[EE_i]$ over time as shown in the equations below:

$$RMS(\|\Delta E[EE_i]\|_2) = \sqrt{\sum_{i=1}^{n} \left(\|E^L[EE_i] - E^{L-1}[EE_i]\|_2\right)^2}, \tag{5.32}$$

$$RMS(\|\Delta\sigma[EE_i]\|_2) = \sqrt{\sum_{i=1}^{n} \left(\|\sigma^L[EE_i] - \sigma^{L-1}[EE_i]\|_2\right)^2} \tag{5.33}$$

For this Duffing's oscillator with three input parameters, the convergence of the Morris and Sampling methods, measured by $RMS(\|\Delta E[EE_i]\|_2)$ and $RMS(\|\Delta\sigma[EE_i]\|_2)$, is comparable in both accuracy and computing cost, while the results' convergence using the Collocation method is about an order of magnitude faster than those of the Morris and Sampling methods, as shown in Figure 5-56. Similar to the example of the monotonic static function, the Variance method exhibits an exponential convergence of $RMS(\|\Delta VEE_i\|_2)$ and $RMS(\|\Delta IEE_i\|_2)$. Similar to the convergence study in Chapter 4, the exponential convergence rate of the full-grid collocation is faster than the algebraic convergence rate of the Monte Carlo method for the same computing cost in low- and medium-dimensional problems.

Let us consider Duffing's oscillator with a sinusoidal forcing function, described below, from the stochastic analysis perspective. In this case, the phase of the forcing function is assumed to be a uniform random variable, $\phi = \bar{\phi} + \sigma_\phi \xi$, where $\bar{\phi} = 0$ and $\xi \in [-1, 1]$.

$$\frac{dy^2}{dt} + 2\eta\omega\frac{dy}{dt} + \omega^2 y + \epsilon\omega^2 y^3 = Asin(2\pi ft + \phi), \text{ with } \frac{dy(0)}{dt} = 0; y(0) = 2, \tag{5.34}$$

where η, ω, and ϵ are just constants of 2, the magnitude and frequency of the forcing function are 2 and 1, respectively. The four different ranges of random phase shift, $\sigma_\phi = 0, \pi/4, \pi/2$, and π, are considered for the stochastic analysis using the full-grid PCM with $Nc = 100$. Figure 5-57 shows the statistical results with the random phase shift. Surprisingly, as the fluctuation of random phase shift approaches π, the mean

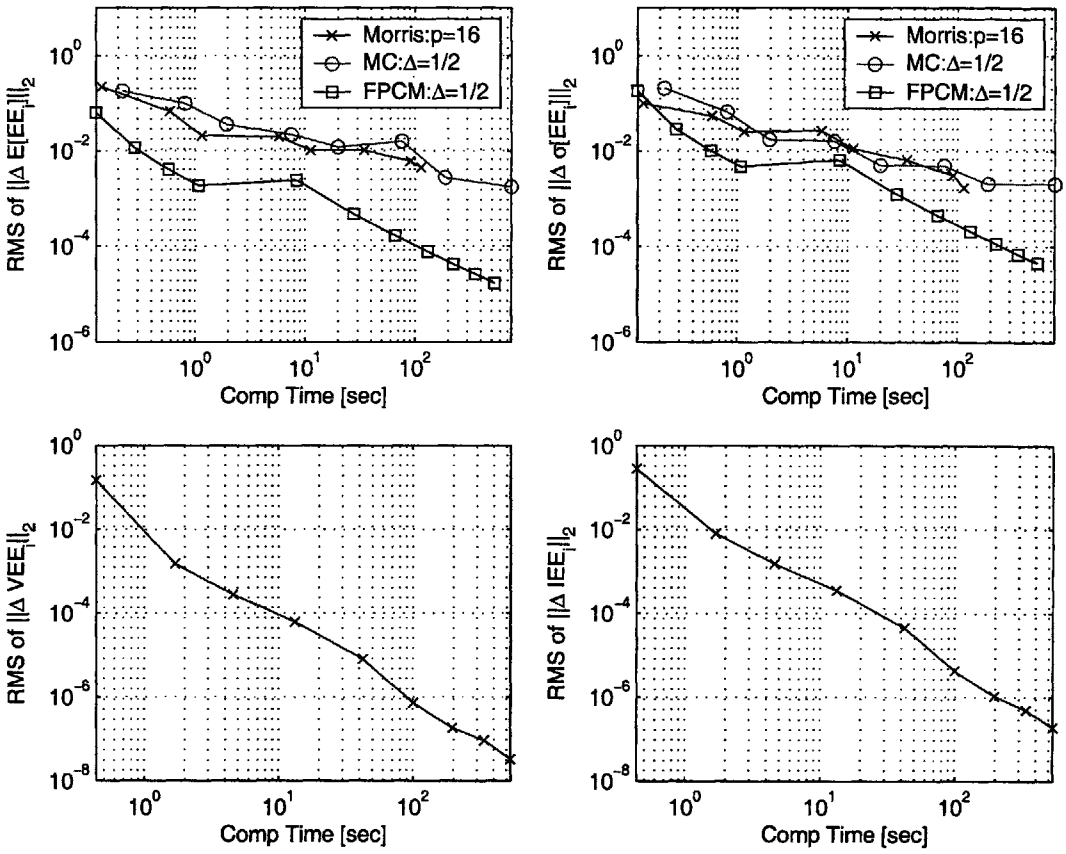

Figure 5-56: The convergence characteristics of $RMS(\|\Delta E[EE_i]\|_2)$ (Top-Left) and $RMS(\|\Delta\sigma[EE_i]\|_2)$ (Top-Right) using the Morris, Monte Carlo Sampling, and Collocation methods and $RMS(\|\Delta VEE_i\|_2)$ (Bottom-Left) and $RMS(\|\Delta IEE_i\|_2)$ (Bottom-Right) using the Variance methods are plotted versus the computational time.

solutions of both y and dy/dt become zero. Nevertheless, the variance solutions of both y and dy/dt in the transient region become larger as σ_ϕ increases.

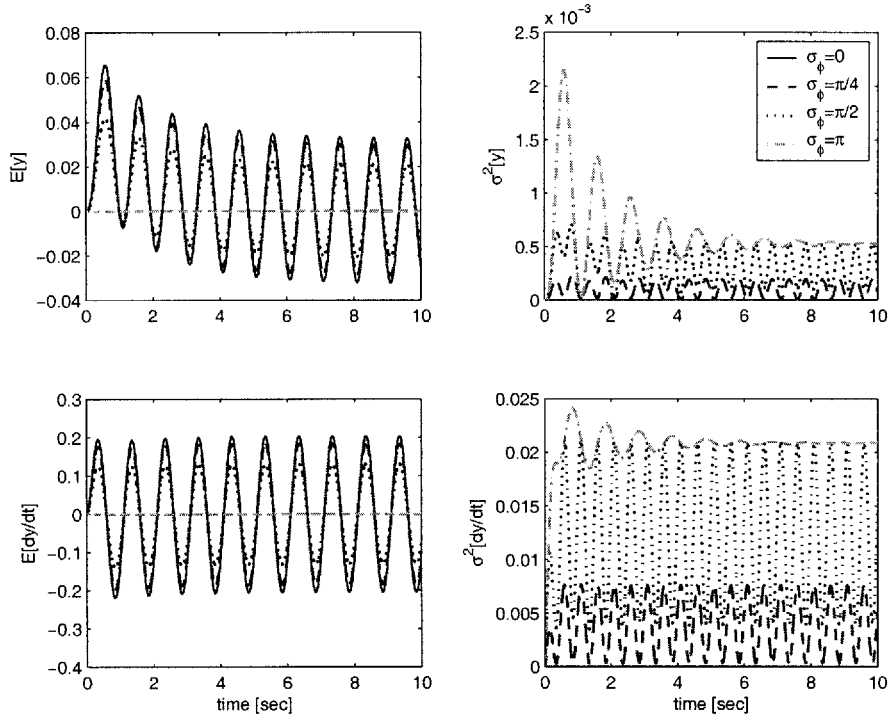

Figure 5-57: The stochastic solutions of the position and velocity of Duffing's oscillator with the four different variations of random phase shift, $\sigma_\phi = 0, \pi/4, \pi/2$, and π.

5.3.3 An open-loop induction machine with an infinite bus

In this section, we investigate how these three sensitivity algorithms rank the significance and interaction of inputs and what effects a large number of inputs and states have on the convergence performance of these algorithms, when the system of ODEs and number of input parameters are increased and all input parameters are strongly coupled with other inputs as well as state variables of the induction machine with an infinite bus (see Figure 4-70 in Chapter 4.3). Because of the five coupled output variables, $[\psi'^e_{qr}, \psi'^e_{dr}, \omega_r, i'^e_{qt}, i'^e_{dt}]$, the trajectories of 10 input parameters, including $[r_s, x_{ls}, x_m, x'_{lr}, r'_r, r_t, L_t, M_t, T_{load}, H]$, are shown only for the d-axis tie line current or i'^e_{dt} state, using the Morris method with $p = 16$, shown in Figure 5-58. All these inputs are assumed to be independent random variables with 10 percent variation from their

mean or nominal values. These results have the same relative magnitude of $E[EE_i]$ and $\sigma[EE_i]$ as those obtained from the Monte Carlo sampling and Collocation methods with $\Delta = \frac{1}{2}$, which are omitted. As seen in the $E[EE_i]$ versus time plot below, the $i_{dt}^{'e}$ is very sensitive to multiple inputs, especially x_{ls} and $x_{lr}^{'}$ in the first second and $r_r^{'}$ right before reaching the synchronous speed. These sensitivity indices agree with multiple time constants associated with the induction machine. In the first second, the stator and rotor windings attempt to accelerate the rotor up to speed; therefore, the reactance of these windings, x_{ls} and $x_{lr}^{'}$, should be the most sensitive parameters during the electrical transient regime. After the electrical transient dies out, the rotor inertia, H, and mechanical torque load, T_{load}, also have significant influence on the tie line or stator current during [1,2] seconds, where the mechanical time constant dominates, as we can see from the 1.2 and 0.6 magnitude of $E[EE_i]$. In terms of input coupling, all these five parameters $(r_r^{'}, x_{ls}, x_{lr}^{'}, H, T_{load})$ exhibit strong interaction with other inputs. Again, at each time step, the $\sigma[EE_i]$ versus $E[EE_i]$ plot can be used to directly rank the inputs' sensitivity as well as interaction, as shown in Figure 5-59. Notice that r_t, L_t, and M_t from the tie line and x_m from the induction machine have almost a negligible effect on this $i_{dt}^{'e}$ output because the infinite bus absorbs all variations in the tie line's parameters. The mutual flux leakage, x_m, is usually about 100 times larger than the flux leakage of the stator and rotor windings; thus, with the same percentage of fluctuation, x_m is less sensitive than x_{ls} and $x_{lr}^{'}$. Moreover, the coupling effect of some inputs using the Monte Carlo and Collocation methods is slightly different from $\sigma[EE_i]$ of the Morris method.

Using the Variance method, the normalized sensitivity trajectories of these 10 inputs can also indicate which inputs have larger impact on the output, such as $i_{dt}^{'e}$, as shown in Figure 5-60. Both plots of VEE_i and IEE_i versus time yield the same relative magnitude and ranking of all inputs as those using the Morris methods in Figure 5-58; the sensitivity from the stochastic results can be used to confirm the sensitivity from the deterministic result, using the gradient computation. The dynamic ODEs of this electric machine are mostly composed of quadratic nonlinearities and rational functions. Thus, the propagation of uncertainty in complicated ODEs can

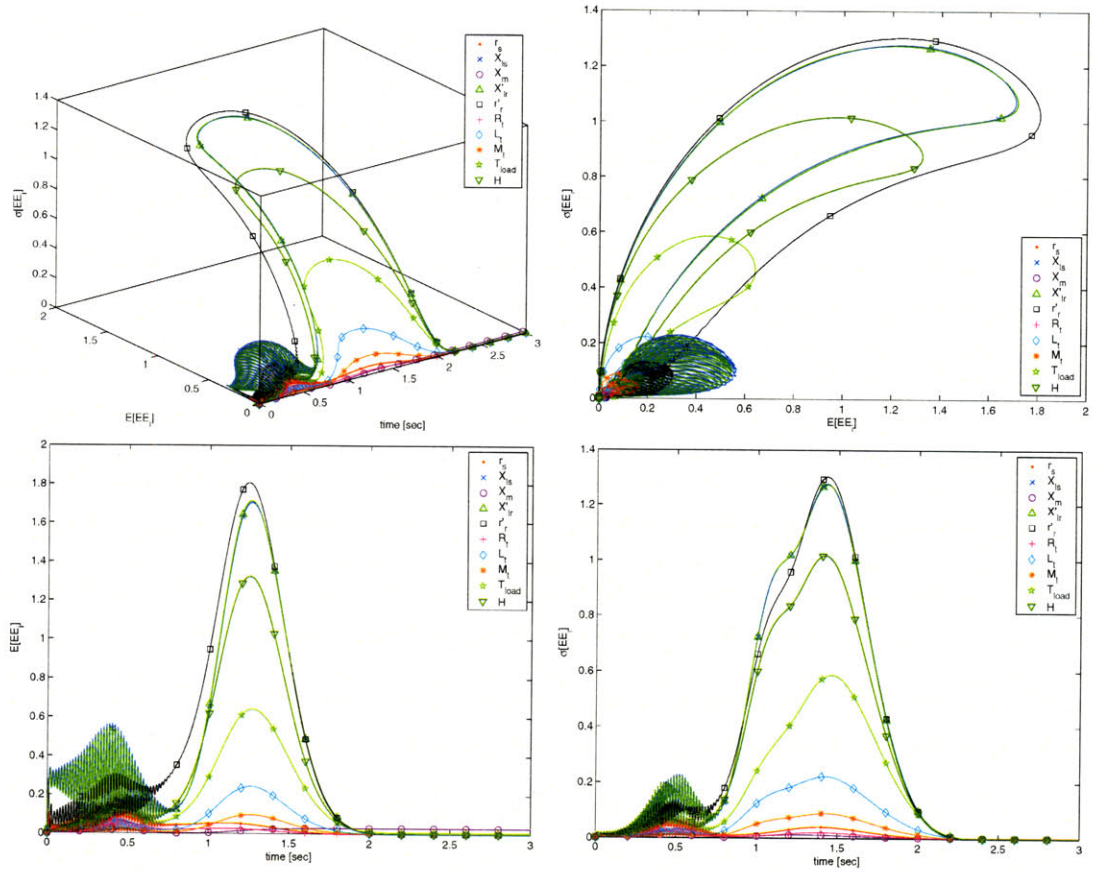

Figure 5-58: For the y_5 or i'^{e}_{dt} state variable, the $E[EE_i]$ and $\sigma[EE_i]$ trajectories of all 10 input parameters as a function of time, $t \in [0, 3]$ second, using the Morris method with $p = 16$ and $r = 80,000$ in three dimension (Top-Left), the Side view (Top-Right) for emphasizing the first-order effect, the Top view (Bottom-Left) for emphasizing the inputs' interaction effect, and the Front view (Bottom-Right).

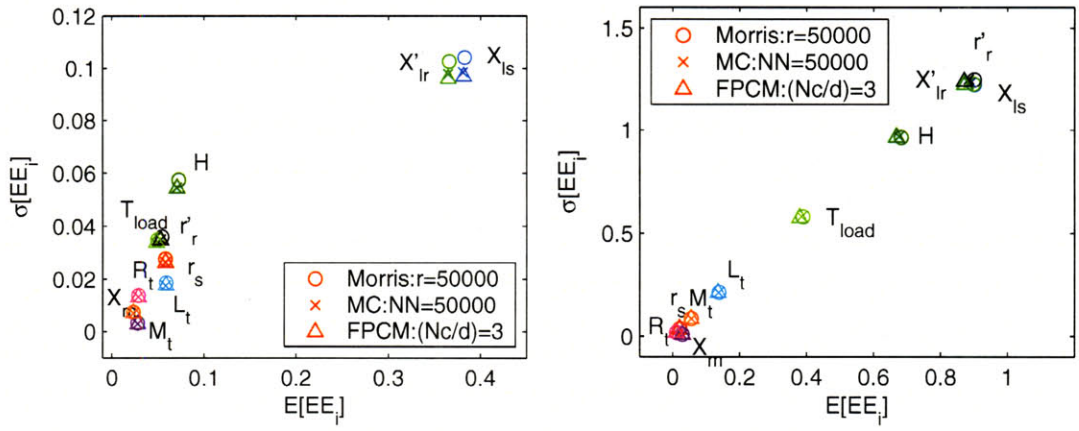

Figure 5-59: The mean and standard deviation of EE_i from the Morris method, the Monte Carlo Sampling, and the Collocation method in the last figure, when time is fixed at 0.3 and 1.5 seconds, where the electrical and mechanical transients dominate, respectively.

be used for detecting the parameters' sensitivity as well. Furthermore, the slices of the IEE_i versus VEE_i plot from the sensitivity trajectories (see Figure 5-61) at the particular times of 0.3 and 1.5 seconds can be precisely compared with those from the gradient-based sensitivity algorithms, in Figure 5-59. Again, the relative magnitude of parameters in the IEE_i versus VEE_i plots agrees well with that of parameters in the $\sigma[EE_i]$ versus $E[EE_i]$ plots.

Figure 5-62 reveals the convergence performance of all techniques based on the gradient computation. Again, using the $RMS(\|\Delta E[EE_i]\|_2)$ and $RMS(\|\Delta\sigma[EE_i]\|_2)$ as the convergence measurement, the convergence rates of both Morris and Monte Carlo Sampling methods are in the same order of magnitude. The convergence performance of the Collocation method is still much better than those two methods in this system with a large-input dimension because the faster convergence rate of the full-grid PCM. However, the standard deviation of the outputs' stochastic variation of the Variance method does not converge as quickly as that of the Collocation method, as shown in Figure 5-63 because of different characteristics of the Variance method.

To summarize the i input sensitivity on all j system outputs over the entire time interval in a two-dimensional figure, we need to define an average sensitivity index as the $(ES_{2,(j,i)})$ and an average interaction index as the $(SS_{2,(j,i)})$, using the L_2 norm

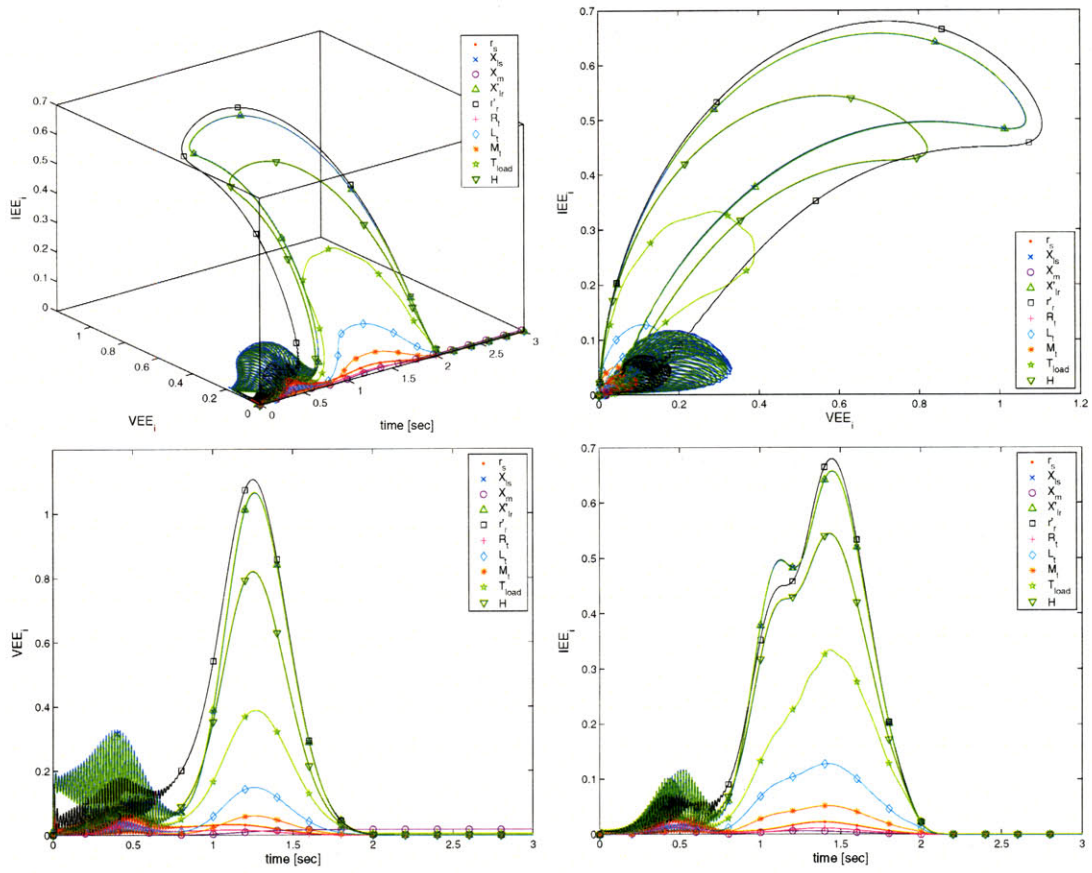

Figure 5-60: For a y_5 variable or i'^{e}_{dt}, the VEE_i and IEE_i trajectories of all 10 input parameters as a function of time, $t \in [0, 3]$ second, using the Variance method with $(Nc/d) = 20$ in three dimensions (Top-Left), the Side view (Top-Right) for emphasizing the first-order effect, the Top view (Bottom-Left) for emphasizing the inputs' interaction effect, and the Front view (Bottom-Right).

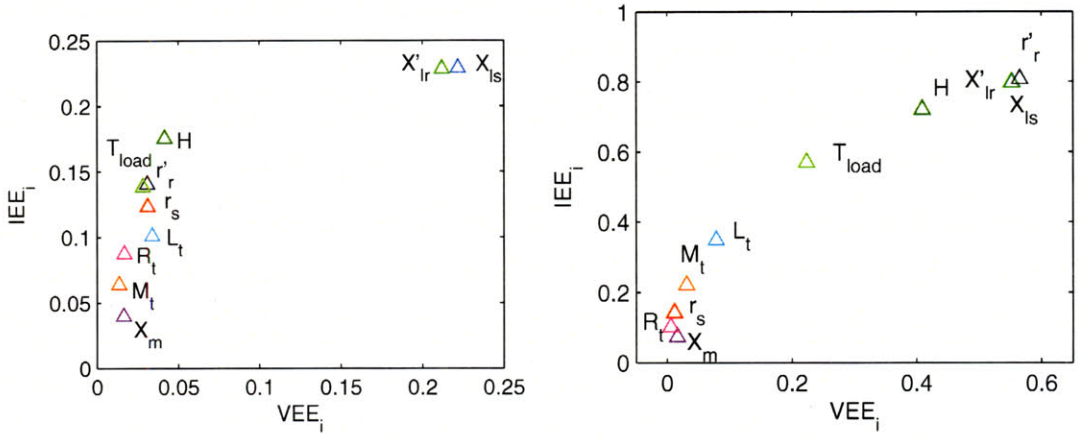

Figure 5-61: The mean and standard deviation of EE_i from the Variance method in the last figure, when time is fixed at 0.3 and 1.5 seconds, where the electrical and mechanical transients dominate, respectively.

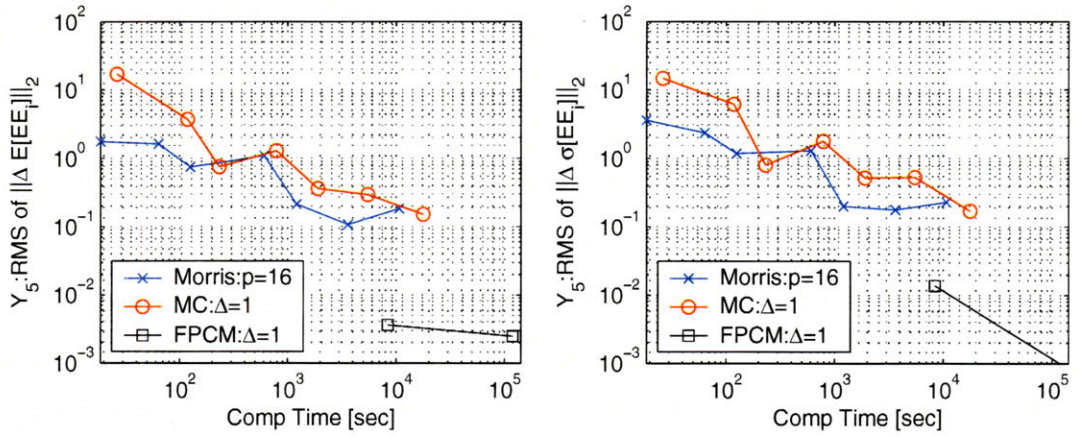

Figure 5-62: The convergence characteristic of $RMS(\|\Delta E[EE_i]\|_2)$ and $RMS(\|\Delta\sigma[EE_i]\|_2)$ using the Morris, Monte Carlo Sampling, and Collocation methods based on the approximated gradient computation is plotted versus the computational time.

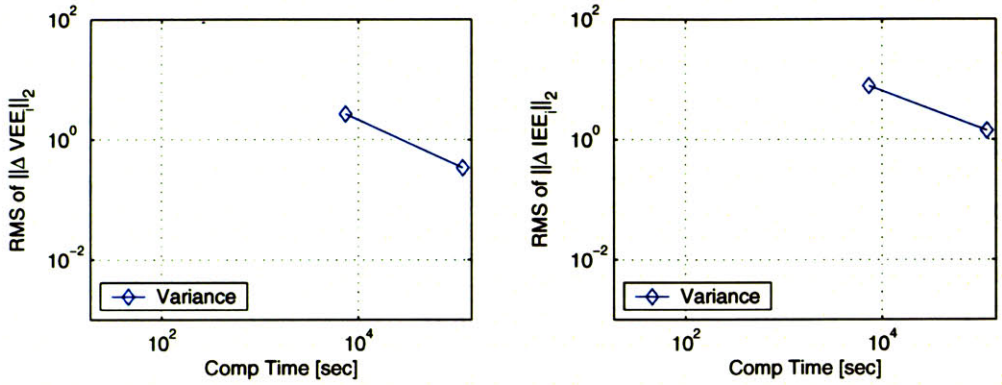

Figure 5-63: The convergence characteristics of $RMS(\|\Delta VEE_i\|_2)$ and $RMS(\|\Delta IEE_i\|_2)$ using the Variance and Inverse Variance methods, based on the statistical computation, is plotted versus the computational time.

as the following:

$$ES_{2,(j,i)} = \|E[EE_i]\|_2 \text{ and } SS_{2,(j,i)} = \|\sqrt{E[EE_i]^2 + \sigma[EE_i]^2}\|_2. \tag{5.35}$$

Nevertheless, because some parameters might have strong influences only within a specified time interval, the peak sensitivity $((ES_{\infty,(j,i)}))$ and interaction indices $((SS_{\infty,(j,i)}))$, defined below, must be considered along with the $(ES_{2,(j,i)})$ and $(SS_{2,(j,i)})$.

$$ES_{\infty,(j,i)} = \|E[EE_i]\|_\infty \text{ and } SS_{\infty,(j,i)} = \|\sqrt{E[EE_i]^2 + \sigma[EE_i]^2}\|_\infty. \tag{5.36}$$

Therefore, all the normalized sensitivity trajectories of the induction machines with 5 coupled outputs and 10 input parameters can be summed up in the following plot of $ES_{2,(j,i)}$ for ranking the input sensitivity and of $SS_{2,(j,i)}$ for ranking the input interaction. All algorithms exhibit the same order of magnitude of $ES_{2,(j,i)}$ and $SS_{2,(j,i)}$ on average between 0 and 3 seconds, as shown in Figures 5-64 and 5-65, respectively. Notice that the y_2 or ψ'^e_{dr} output is the most sensitive, particularly to the electrical parameters, among all the outputs. The peak magnitude of $ES_{\infty,(j,i)}$ is about 2.6 times that of $ES_{2,(j,i)}$ and both interaction indices, $SS_{2,(j,i)}$ and $SS_{\infty,(j,i)}$, exhibit a similar ranking to their sensitivity indices.

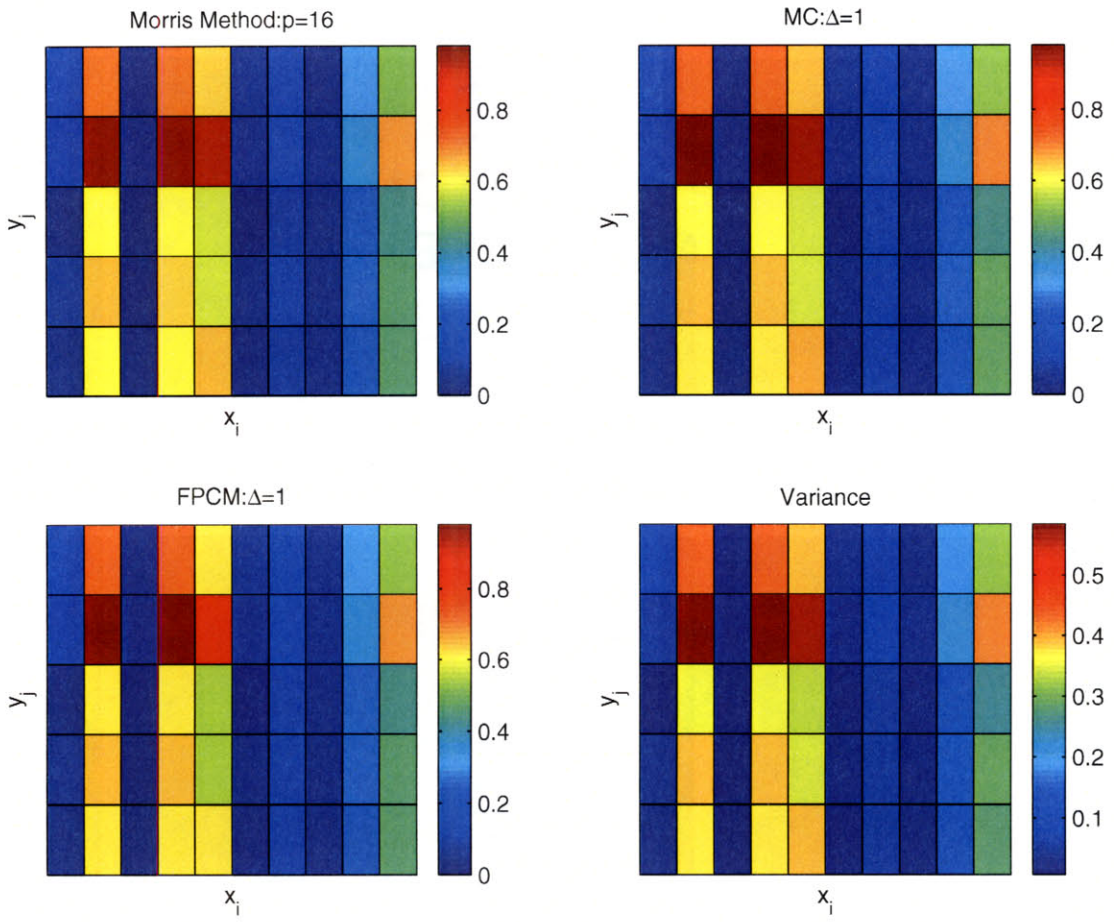

Figure 5-64: The $ES_{2,(j,i)}$ plots using Morris, MC Sampling, Collocation, and Variance methods for ranking the input sensitivity. Note that the order of x_i inputs on the x-axis are $[r_s, x_{ls}, x_m, x'_{lr}, r'_r, r_t, L_t, M_t, T_{load}, H]$ from left to right and the order of y_j outputs on the y-axis are $[\psi'^{e}_{qr}, \psi'^{e}_{dr}, \omega_r, i'^{e}_{qt}, i'^{e}_{dt}]$ from top to bottom.

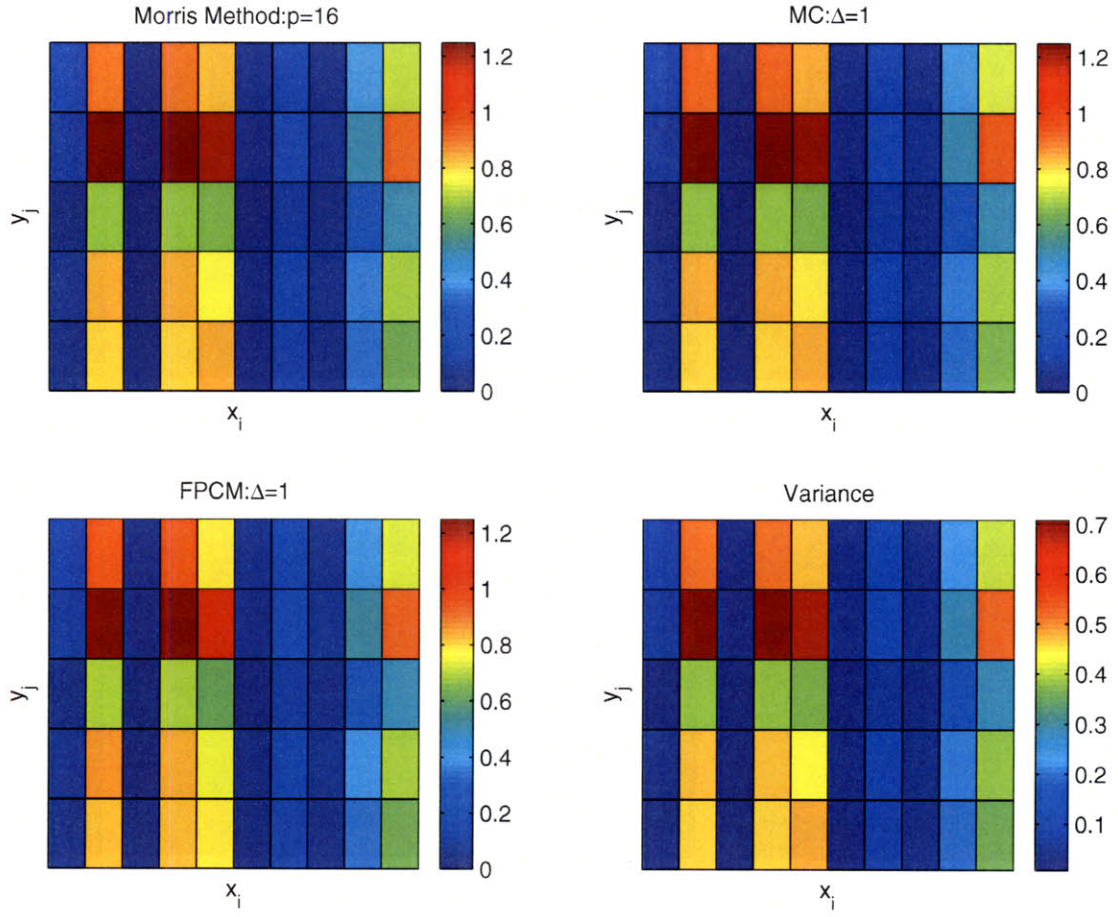

Figure 5-65: The $SS_{2,(j,i)}$ plots using Morris, MC Sampling, Collocation, and Variance methods for ranking the input coupling or interaction. Note that the order of x_i inputs on the x-axis are $[r_s, x_{ls}, x_m, x_{lr}^{'}, r_r^{'}, r_t, L_t, M_t, T_{load}, H]$ from left to right and the order of y_j outputs on the y-axis are $[\psi_{qr}^{'e}, \psi_{dr}^{'e}, \omega_r, i_{qt}^{'e}, i_{dt}^{'e}]$ from top to bottom.

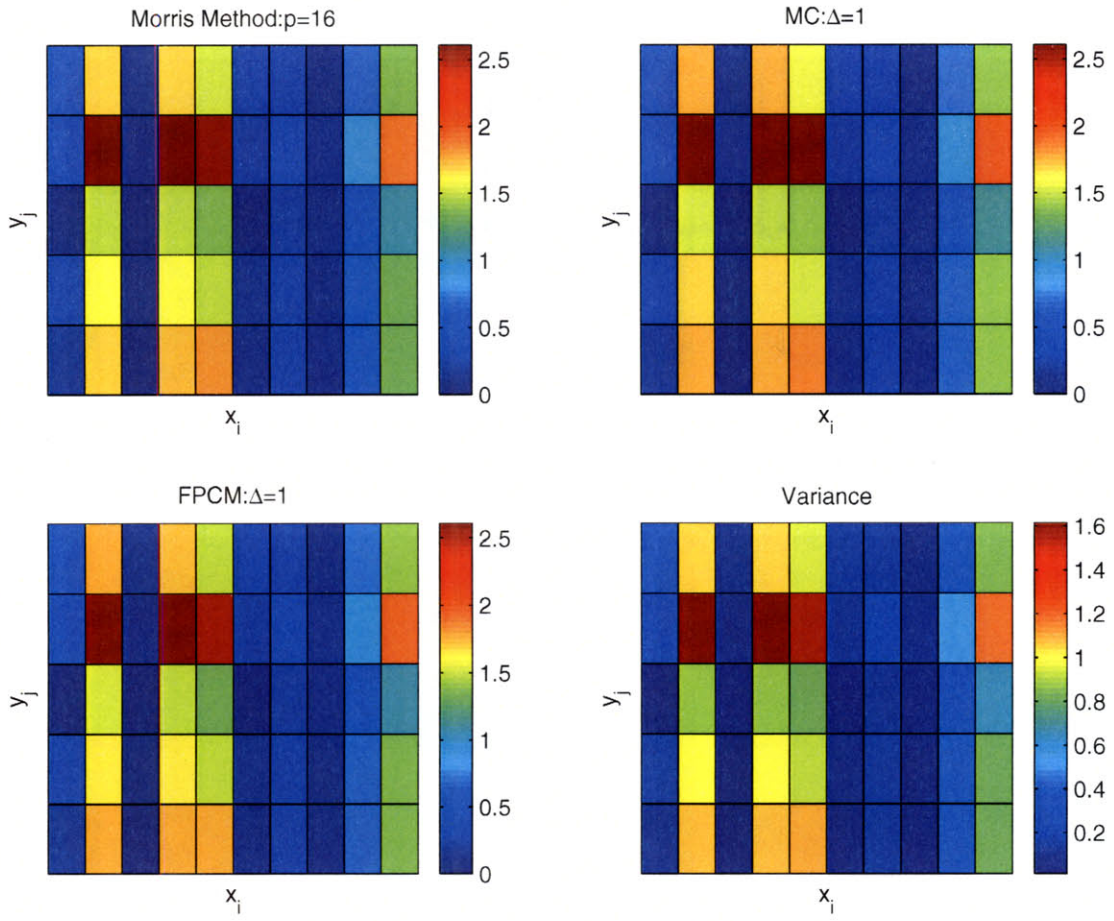

Figure 5-66: The $ES_{\infty,(j,i)}$ plots using Morris, MC Sampling, Collocation, and Variance methods for ranking the input sensitivity. Note that the order of x_i inputs on the x-axis are $[r_s, x_{ls}, x_m, x'_{lr}, r'_r, r_t, L_t, M_t, T_{load}, H]$ from left to right and the order of y_j outputs on the y-axis are $[\psi'^e_{qr}, \psi'^e_{dr}, \omega_r, i'^e_{qt}, i'^e_{dt}]$ from top to bottom.

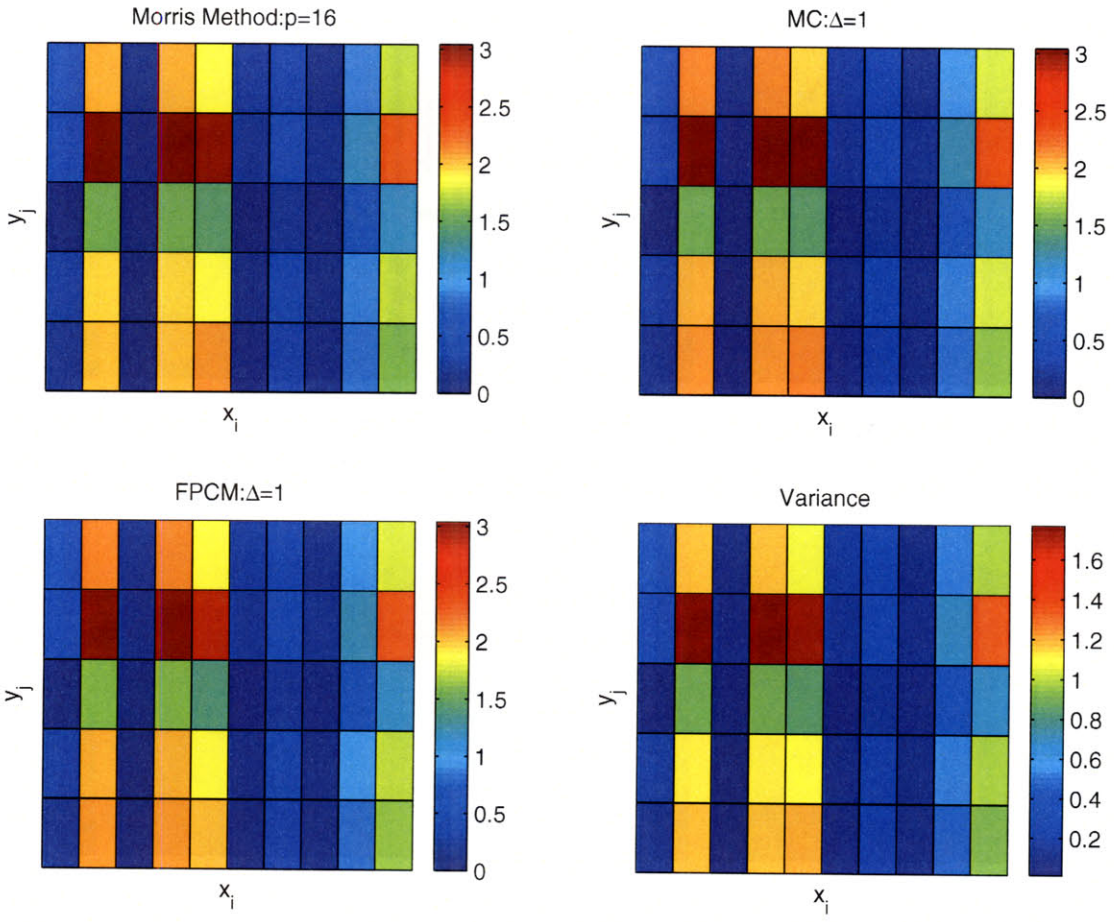

Figure 5-67: The $SS_{\infty,(j,i)}$ plots using Morris, MC Sampling, Collocation, and Variance methods for ranking the input coupling or interaction. Note that the order of x_i inputs on the x-axis are $[r_s, x_{ls}, x_m, x'_{lr}, r'_r, r_t, L_t, M_t, T_{load}, H]$ from left to right and the order of y_j outputs on the y-axis are $[\psi'^e_{qr}, \psi'^e_{dr}, \omega_r, i'^e_{qt}, i'^e_{dt}]$ from top to bottom.

5.3.4 AC power distribution with open-loop propulsion system

We can extend the ability of these four sensitivity algorithms further to deal with a large-scale complex system of the power distribution and propulsion units in the integrated electric ship system. Actually, this system is similar to the system described in Figure 5-89 of Section 4.4, except that the power converter and the constant-slip current controller of the induction are removed to simplify the system in an open-loop configuration. The one-line diagram of this system is shown in Figure 5-68 below,

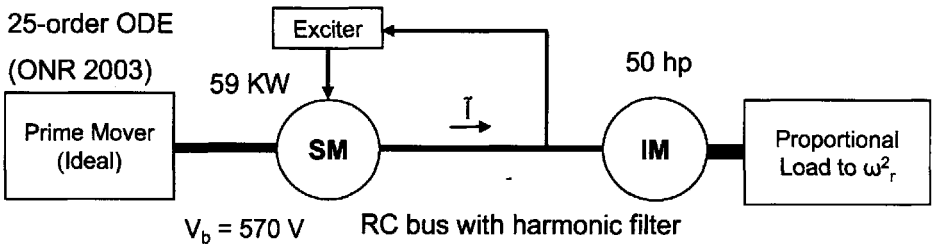

Figure 5-68: A one-line diagram of the second configuration of the AC power distribution with the open-loop induction machine for studying the sensitivity analysis with 24 parameters.

where the mechanical torque load is modeled as a proportional torque load to the square of the motor speed with α_{load} coefficient, which is similar to the propeller load. The scenario of this simulation is that the 59 kW generator is initially operated around its steady-state condition and then the 50-hp induction motor is suddenly turned on at zero second; thus, the start-up transient dynamics of the induction motor must be taken into account. Also, both electrical and mechanical time constants of the synchronous generator and the induction motor are the focus in this sensitivity study. With this particular proportional torque load, the electrical transient responses die out within the first second, while the mechanical time constant is about 6 seconds before approaching steady-state values. There are a total of 24 parameters (12 in the 59 kW synchronous generator and exciter, 7 in the 50-hp induction motor, and 5 in the RC bus connecting between the generator and motor) and 25 state variables.

The nominal values of all parameters are given in Appendix B. These parameters are assumed to be random variables with σ_{x_i} as the percent variation from their mean or nominal values of each parameter.

To study the parametric sensitivity for all state variables, we employ only the Monte Carlo Sampling methods with $\Delta = 1$ to perform the sensitivity analysis for $t \in [0, 1]$ and $t \in [0, 12.4]$ seconds, where the electrical and mechanical time constants dominate, respectively. All parameters are assumed to be independent uniform random variables, $X_i = \bar{x}_i + \sigma_{x_i}\xi$, where $\xi \in [-1, 1]$. Moreover, three different ranges of the parameter variation, $\sigma_{x_i} = 0.1$, 0.3, and 0.5, are compared against one another in this study because the sensitivity and interaction effects of this nonlinear system do not scale up linearly.

For $t \in [0, 1]$ second and $\sigma_{x_i} = 0.1$, Figure 5-69 and 5-70 show the normalized sensitivity time traces of the a-phase current of the harmonic filter($I_{a,filter}$) or y_{14} state and the IM's rotor angular velocity (ω_r) or y_{24} state, respectively. These two plots consider only the sensitivity time traces of $I_{a,filter}$ and ω_r to the the 7 induction machine's and 3 bus's parameters. Each input parameter influences each state variable differently. The $I_{a,filter}$ is highly sensitive to only the harmonic filter capacitor, C_f, as seen from a large gradient magnitude within the first fraction of second. This peak gradient of $I_{a,filter}$ to C_f approaches a small steady-state value very quickly. The large and sudden peak of $I_{a,filter}$ sensitivity occurs because of two reasons: 1) a large three-phase current from the bus is required to start the induction machine from rest and 2) C_f is directly influence a change in power drawn from the RC bus. However, ω_r is sensitive to both electrical parameters: stator and rotor resistances (r_s,r_r') and mechanical parameter: rotor inertia (J).

To see how L_f of the harmonic filter and r_r' of the IM's rotor windings influence the three-phase RC-bus current ($I_{a,b,c,filter}$) and the magnetic flux linkage of the IM's stator and rotor windings (ψ_{qds} and ψ'_{qdr}), L_f and r_r' are varied by $\pm$ 10 percent from their nominal values in a deterministic simulation. Then, we compare these responses with the deterministic responses when L_f and r_r' are at their maximum and minimum bounds, as shown in Figure 5-71 and 5-72. Figure 5-71 shows that the increase in

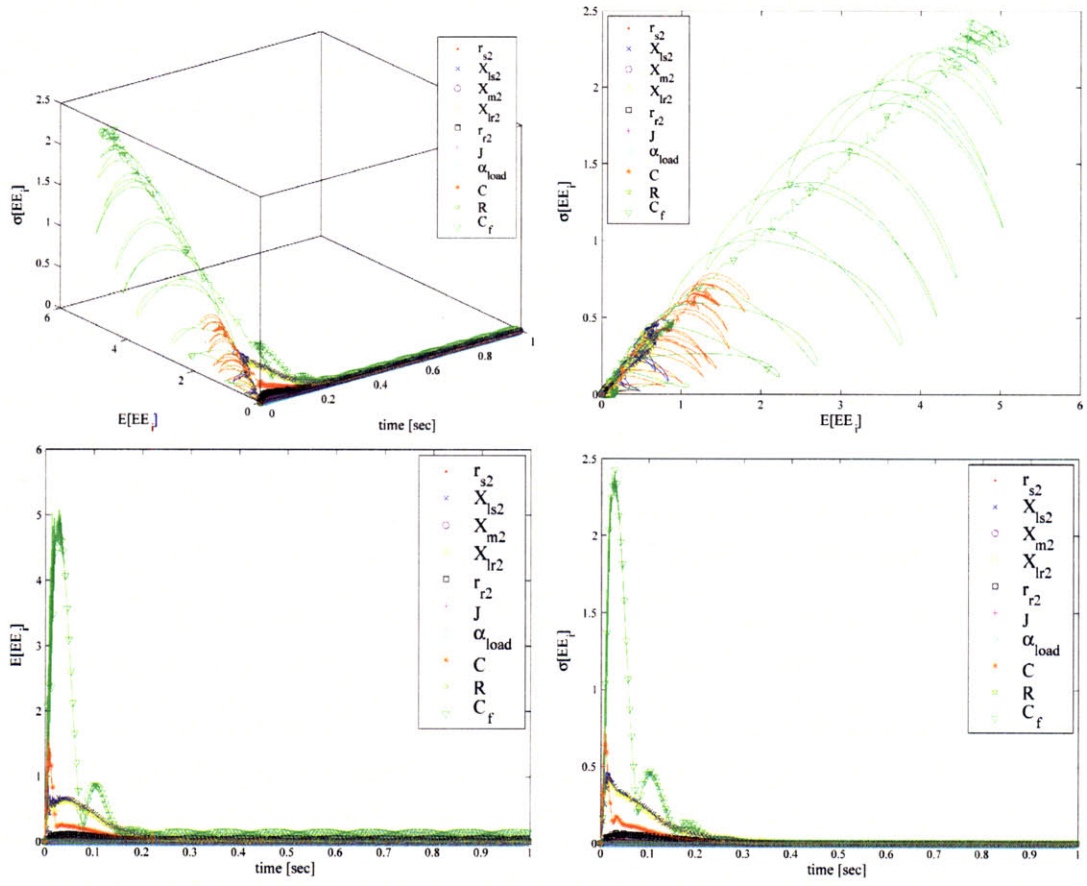

Figure 5-69: For a y_{14} variable or $I_{a,filter}$ of the harmonic filter, the normalized $E[EE_i]$ and $\sigma[EE_i]$ trajectories of the 7 induction machine parameters and 3 bus parameters as a function of time, $t \in [0, 1]$ second, using the MC Sampling method with $NN = 1,000$ and $\sigma_{x_i} = 0.1$ in three dimensions (Top-Left), the Side view (Top-Right) for emphasizing the first-order effect, the Top view (Bottom-Left) for emphasizing the inputs' interaction effect, and the Front view (Bottom-Right).

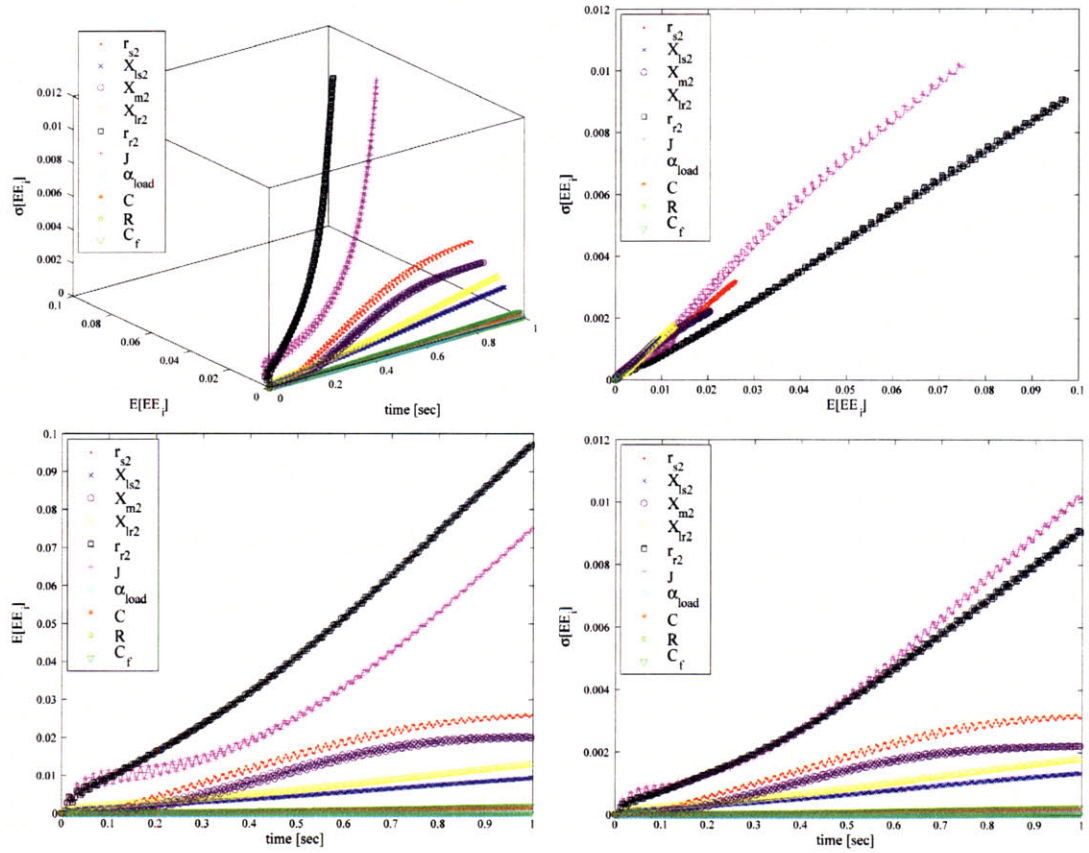

Figure 5-70: For a y_{24} variable or ω_r of the IM, the normalized $E[EE_i]$ and $\sigma[EE_i]$ trajectories of the 7 induction machine parameters and 3 bus parameters as a function of time, $t \in [0, 1]$ second, using the MC Sampling method with $NN = 1,000$ and $\sigma_{x_i} = 0.1$ in three dimensions (Top-Left), the Side view (Top-Right) for emphasizing the first-order effect, the Top view (Bottom-Left) for emphasizing the inputs' interaction effect, and the Front view (Bottom-Right).

L_f leads to a slower response of the $I_{a,b,c,filter}$ and vice versa, which further induces a phase shift in $I_{a,b,c,filter}$, especially in the high-frequency region in the first fraction of a second. On the other hand, the change in r'_r only increases or decreases the magnitude of the IM's ψ_{qds} and ψ'_{qdr}, as shown in Figure 5-72.

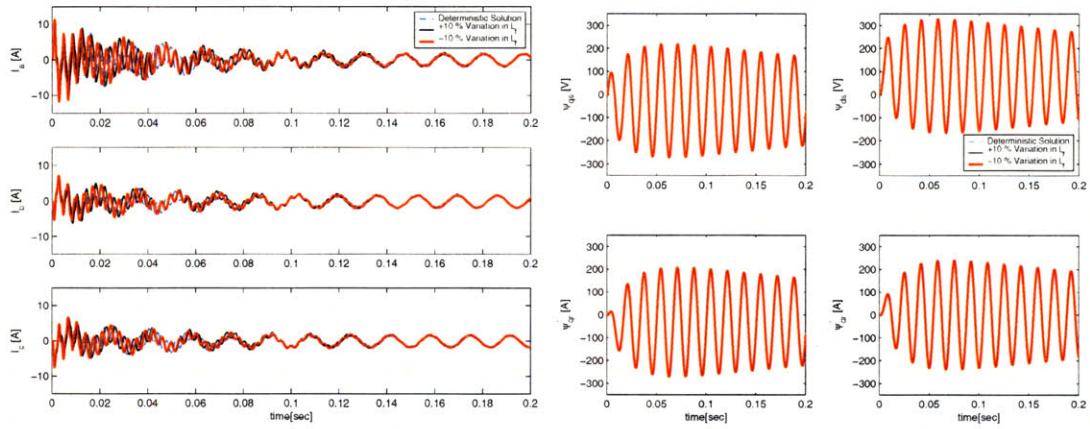

Figure 5-71: For 10 percent increase in L_f, the deterministic responses of $I_{a,b,c,filter}$, ψ_{qds}, and ψ'_{qdr} with and without change in the L_f nominal values.

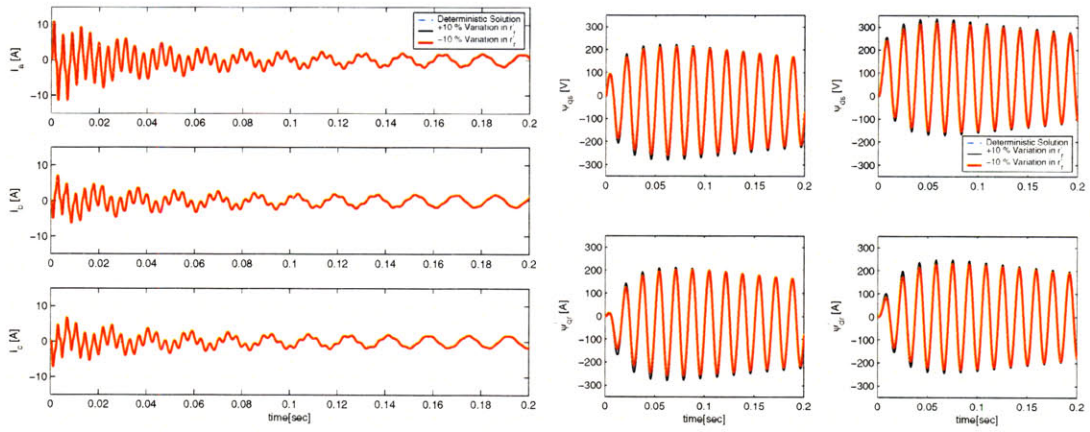

Figure 5-72: For 10 percent increase in r'_r, the deterministic responses of $I_{a,b,c,filter}$, ψ_{qds}, and ψ'_{qdr} with and without change in the r'_r nominal values.

Due to a large number of inputs and outputs, we can summarize all these results in the plots of $ES_{2,(i,j)}$ and $SS_{2,(j,i)}$ (See Figure 5-73) for examining the average sensitivity and interaction effects over a specified time interval, respectively. To capture the maximum magnitude of the sensitivity and interaction effects, $ES_{\infty,(i,j)}$ and $SS_{\infty,(j,i)}$ (See Figure 5-74) must be considered along with $ES_{2,(i,j)}$ and $SS_{2,(j,i)}$. The $ES_{2,(i,j)}$

reveals that the three-phase currents (I_a, I_b, I_c) of the harmonic filter in the RC bus are the most sensitive variables among all 25 states and they are very sensitive to C_f and L_f because the harmonic filter is tuned to reduce high harmonic frequency and the RC bus subjects to large high-frequency start-up current of the IM. Moreover, most state variables are sensitive to the IM's parameters, which implies a direct interaction among the SM, IM, and RC bus. Similarly, $ES_{\infty,(i,j)}$ or the peak sensitivity indices show the same agreement that $I_{a,b,c,filter}$ are the three most sensitive state variables to L_f and C_f with large maximum gradient as well as average gradient.

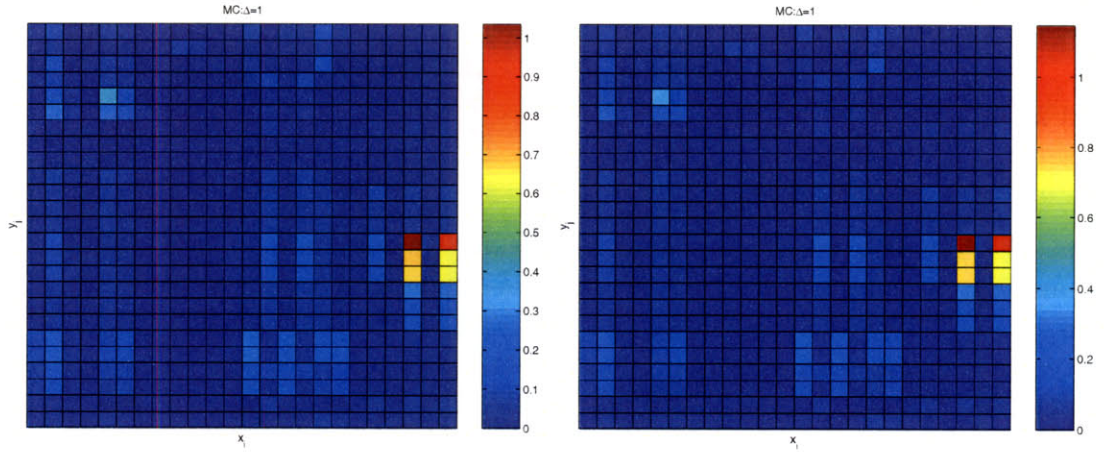

Figure 5-73: The $ES_{2,(j,i)}$ plot (Left) and $SS_{2,(j,i)}$ plot (Right) using the Monte Carlo Sampling method with $NN = 1,000$ for ranking the input sensitivity for $\sigma_{x_i} = 0.1$ and $t \in [0, 1]$ second. Note that the order of x_i inputs on the x-axis are [r_s, X_{ls}, X_{md}, X_{mq}, r_{fd}, X_{fd}, r_{kd}, X_{lkd}, r_{kq1}, X_{lkq1},r_{kq2}, X_{lkq2}, r_{s2}, X_{ls2}, X_{m2}, X_{lr2}, r_{r2}, J, α_{load}, C, R, C_f, r_f, L_f] from left to right and the order of y_j states or outputs on the y-axis are [ψ^e_{qs}, ψ'^e_{kq1}, ψ'^e_{kq2}, ψ^e_{ds}, ψ'^e_{fd}, ψ'^e_{kd}, ψ^e_{0s}, θ, e'_{xfd}, VF, V_{an}, V_{bn}, V_{cn}, i_a, i_b, i_c, V_{c1}, V_{c2}, V_{c3},ψ^e_{qs}, ψ'^e_{qr}, ψ^e_{ds}, ψ'^e_{dr}, ψ^e_{0s}, ω_r] from top to bottom.

The normalized sensitivity time traces of ω_r for $t \in [0, 1]$ and $\sigma_{x_i} = 0.3$ in Figure 5-76 is slightly larger than those for $\sigma_{x_i} = 0.1$ in Figure 5-70. Even though, there is a small increase in the $E[EE_{24}]$ magnitude, the peak magnitude of $\sigma[EE_{24}]$ grows by three times. Little change in the ω_r sensitivity occurs because the transient dynamics of the mechanical component still gradually increase within this time range. While the fast dynamics of the electrical transient, such as in y_{14} or $I_{a,filter}$, are strongly dominated during the IM's start-up acceleration, the frequency of the normalized sensitivity trajectories of $I_{a,filter}$ becomes higher and its peak magnitude drops more

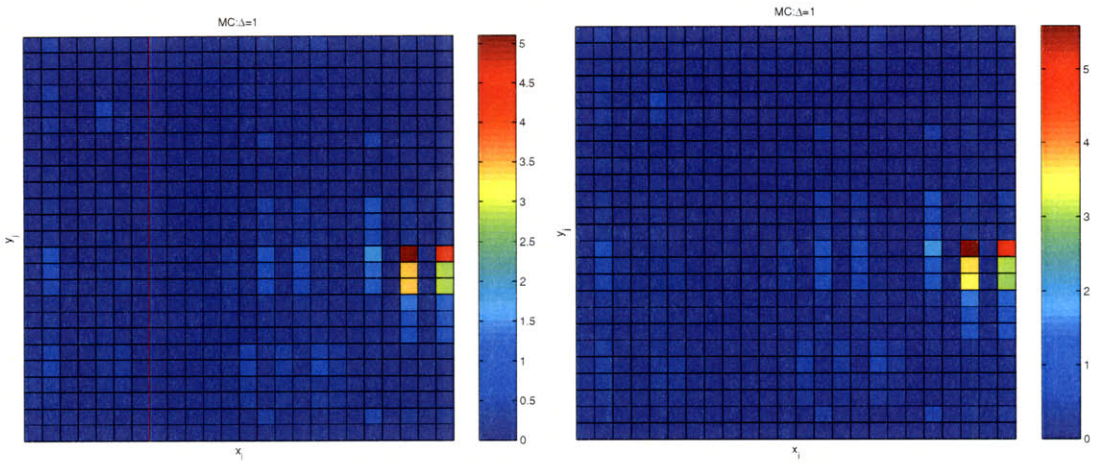

Figure 5-74: The $ES_{\infty,(j,i)}$ plot (Left) and $SS_{\infty,(j,i)}$ plot (right) using the Monte Carlo Sampling method with $NN = 1,000$ for ranking the input sensitivity for $\sigma_{x_i} = 0.1$ and $t \in [0, 1]$ second. Note that the order of x_i inputs on the x-axis are [r_s, X_{ls}, X_{md}, X_{mq}, r_{fd}, X_{fd}, r_{kd}, X_{lkd}, r_{kq1}, X_{lkq1},r_{kq2}, X_{lkq2}, r_{s2}, X_{ls2}, X_{m2}, X_{lr2}, r_{r2}, J, α_{load}, C, R, C_f, r_f, L_f] from left to right and the order of y_j states or outputs on the y-axis are [ψ^e_{qs}, $\psi^{'e}_{kq1}$, $\psi^{'e}_{kq2}$, ψ^e_{ds}, $\psi^{'e}_{fd}$, $\psi^{'e}_{kd}$, ψ^e_{0s}, θ, $e^{'}_{xfd}$, VF, V_{an}, V_{bn}, V_{cn}, i_a, i_b, i_c, V_{c1}, V_{c2}, V_{c3},ψ^e_{qs}, $\psi^{'e}_{qr}$, ψ^e_{ds}, $\psi^{'e}_{dr}$, ψ^e_{0s}, ω_r] from top to bottom.

quickly as σ_{x_i} increases from 0.1 to 0.3, as shown in Figure 5-75. This reduction of the mean value as the percent variation increases is caused by the cancellation of the response ensembles due to the phase shift in the dynamic responses, which is explained in Section 5.3.2. The magnitude of $\sigma[EE_{14}]$ also decreases; this phase shifting of $I_{a,filter}$ must be caused by the interaction with other states or parameters. Unlike, the random phase shift in the inputs of the duffing's oscillator does not cause a reduction in the variance magnitude.

Similarly, we again change the nominal values of both L_f of the harmonic filter and r'_r of the IM by $\pm$ 30 percent and then investigate the difference between the deterministic minimum- and maximum-bound responses of the three-phase RC-bus current ($I_{a,b,c,filter}$) and the magnetic flux linkage of the IM's stator and rotor windings (ψ_{qds} and ψ'_{qdr}), as illustrated in Figure 5-77 and 5-78. With 30 percent variation in L_f from its nominal value, $I_{a,b,c,filter}$ are even slower than those with 10 percent variation in L_f; thus, the phase shift of the high-frequency $I_{a,b,c,filter}$ become more significant. On the contrary, the 30 percent increase in r'_r only enlarges the magnitude of the IM's

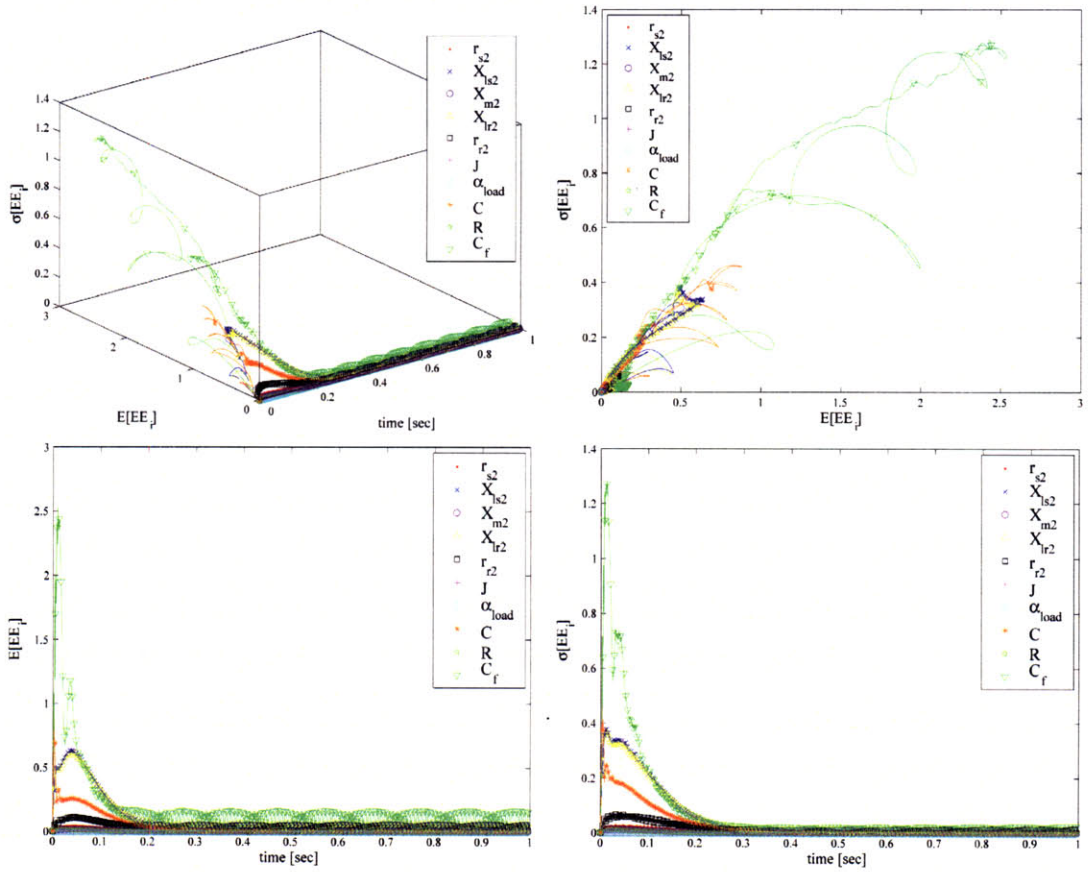

Figure 5-75: For a y_{14} variable or $I_{a,filter}$ of the harmonic filter, the normalized $E[EE_i]$ and $\sigma[EE_i]$ trajectories of the 7 induction machine parameters and 3 bus parameters as a function of time, $t \in [0, 1]$ second, using the MC Sampling method with $NN = 2,500$ and $\sigma_{x_i} = 0.3$ in three dimensions (Top-Left), the Side view (Top-Right) for emphasizing the first-order effect, the Top view (Bottom-Left) for emphasizing the inputs' interaction effect, and the Front view (Bottom-Right).

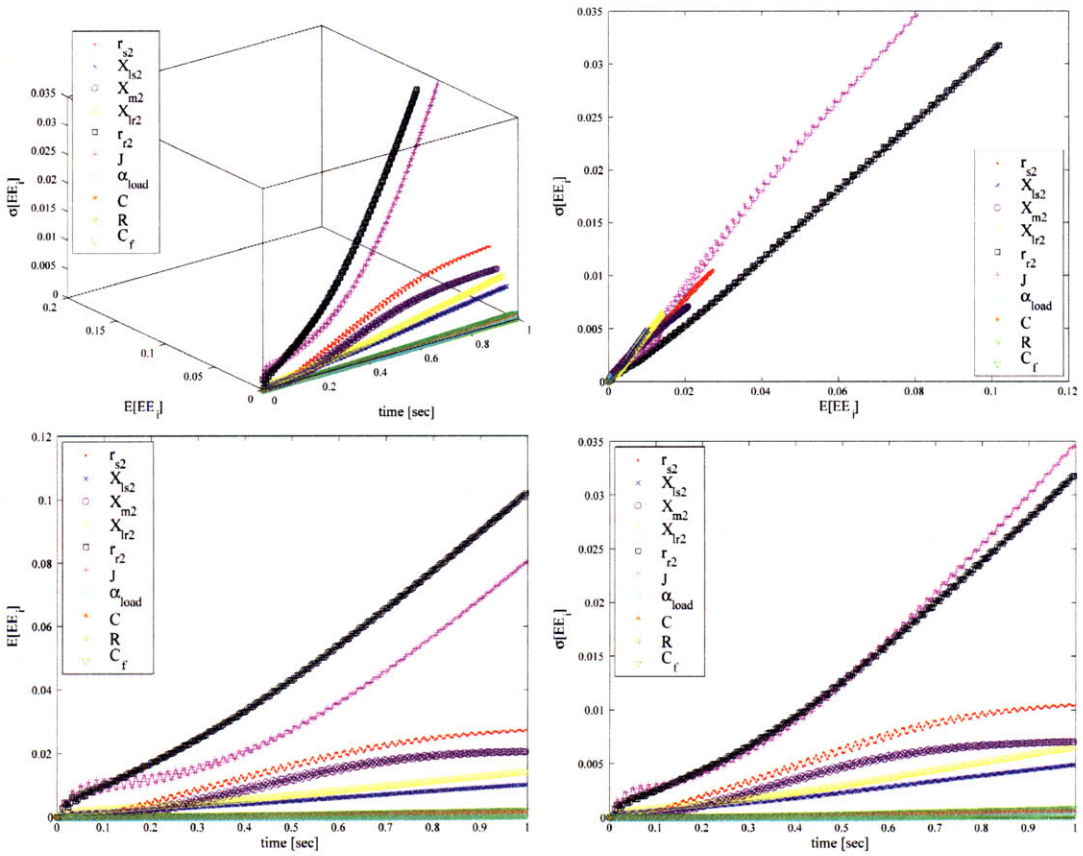

Figure 5-76: For a y_{24} variable or ω_r of the IM, the normalized $E[EE_i]$ and $\sigma[EE_i]$ trajectories of the 7 induction machine parameters and 3 bus parameters as a function of time, $t \in [0, 1]$ second, using the MC Sampling method with $NN = 2,500$ and $\sigma_{x_i} = 0.3$ in three dimensions (Top-Left), the Side view (Top-Right) for emphasizing the first-order effect, the Top view (Bottom-Left) for emphasizing the inputs' interaction effect, and the Front view (Bottom-Right).

ψ_{qds} and ψ'_{qdr} without any phase shifting, which directly leads to an increase in the magnitude of ω_r sensitivity.

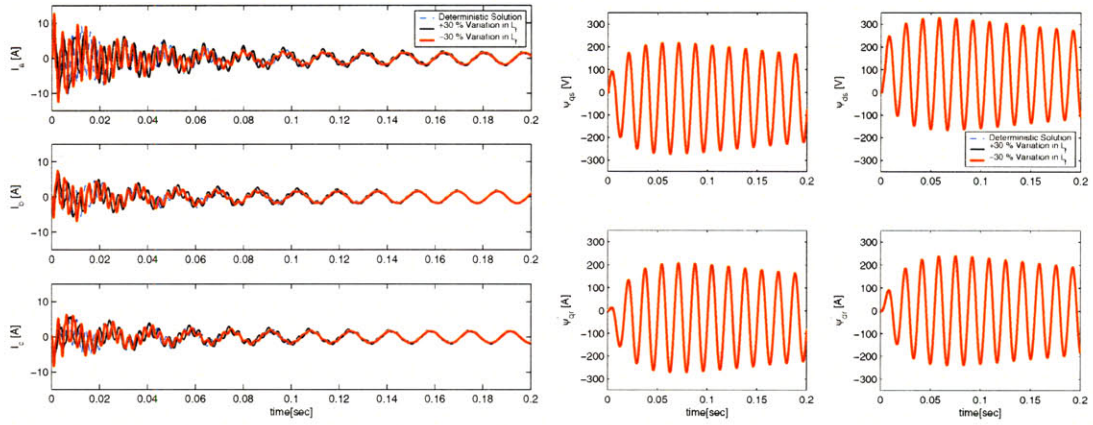

Figure 5-77: For 30 percent increase in L_f, the deterministic responses of $I_{a,b,c,filter}$, ψ_{qds}, and ψ'_{qdr} with and without change in the L_f nominal values.

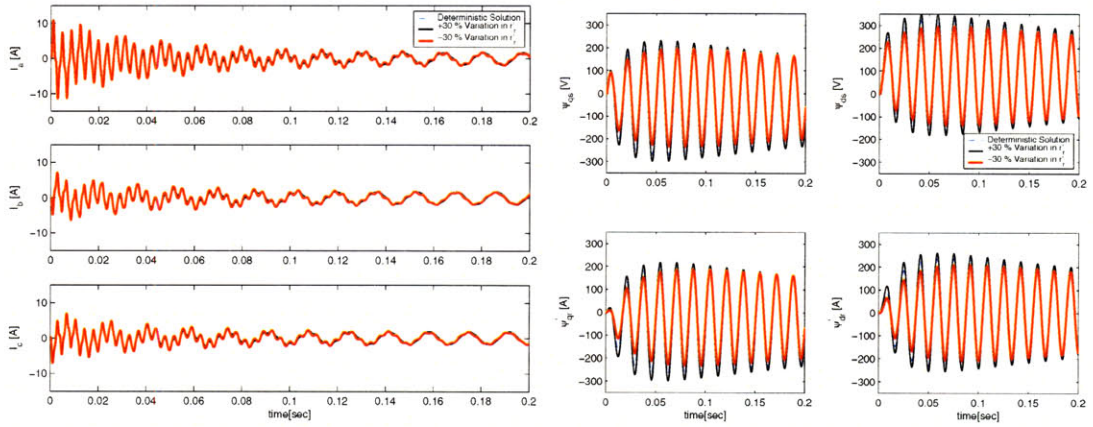

Figure 5-78: For 30 percent increase in r'_r, the deterministic responses of $I_{a,b,c,filter}$, ψ_{qds}, and ψ'_{qdr} with and without change in the r'_r nominal values.

Again, to summarize all sensitivity and interaction of all states to all input parameters in one plot, both $(ES_{2,(j,i)}, SS_{2,(j,i)})$ and $(ES_{\infty,(j,i)}, SS_{\infty,(j,i)})$ plots reveal the overall picture of both of these effects over the time range of $[0, 1]$ second and at a specified peak location, respectively. As the percent variation of parameters increases, both (X_{ls},r_{fd}) of the SM's parameters and (r_{s2},X_{m2},r_{r2},J) of the IM's parameters consequently exhibit large influences on (ψ_{kd},ψ_{fd}) of the SM's states and (ψ^e_{qs}, ψ'^e_{qr}, ψ^e_{ds}, ψ'^e_{dr}) of the IM's states, seen Figure 5-79. Notice that on average, all

state variables of this system become more sensitive to the large parameter variation and the variation of IM's parameters can have some effect on the generator states and vice versa. Thus, the overall sensitivity plots imply direct machine interactions between the generator and the motor. Note that all state variables in this system with the open-loop propulsion are not sensitive to the load coefficient, α_{load}, within this time frame. However, the peak sensitivity and interaction indices in Figure 5-80 show only a slight difference in the parameter ranking from those in Figure 5-74, except the higher peak magnitude of $I_{a,b,c,filter}$.

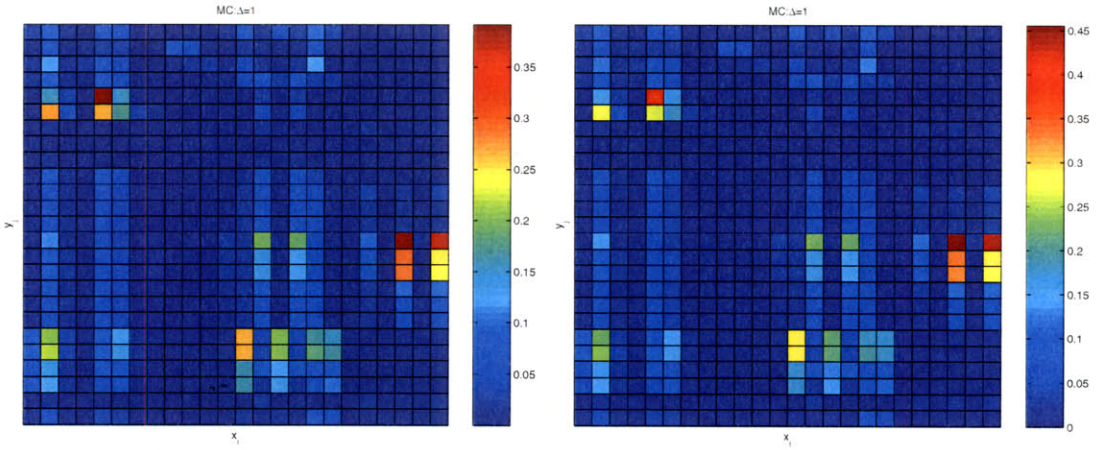

Figure 5-79: The $ES_{2,(j,i)}$ plot (Left) and $SS_{2,(j,i)}$ plot (right) using the Monte Carlo Sampling method with $NN = 2,500$ for ranking the input sensitivity for $\sigma_{x_i} = 0.3$ and $t \in [0, 1]$ second. Note that the order of x_i inputs on the x-axis are [r_s, X_{ls}, X_{md}, X_{mq}, r_{fd}, X_{fd}, r_{kd}, X_{lkd}, r_{kq1},X_{lkq1},r_{kq2}, X_{lkq2}, r_{s2}, X_{ls2}, X_{m2}, X_{lr2}, r_{r2}, J, α_{load}, C, R, C_f, r_f, L_f] from left to right and the order of y_j states on the y-axis are [ψ^e_{qs}, ψ'^e_{kq1}, ψ'^e_{kq2}, ψ^e_{ds}, ψ'^e_{fd}, ψ'^e_{kd}, ψ^e_{0s}, θ, e'_{xfd}, VF, V_{an}, V_{bn}, V_{cn}, i_a, i_b, i_c, V_{c1}, V_{c2}, V_{c3},ψ^e_{qs}, ψ'^e_{qr}, ψ^e_{ds}, ψ'^e_{dr}, ψ^e_{0s}, ω_r] from top to bottom.

As we further increase the percent variation of all parameters' fluctuation to 50 percent to examine the free acceleration of the induction machine, the sensitivity of the mechanical state, ω_r, becomes larger as time progresses (see Figure 5-82), while the sensitivity of the electrical state, $I_{a,filter}$, to C_f is even more sudden with a smaller gradient magnitude than that with $\sigma_{x_i} = 0.3$ occurring within 0.1 second (see Figure 5-81). Again, the cancellation of the phase shift responses due to variations in C_f and L_f leads to decrease in the magnitude of the sensitivity time traces. However, the magnitude of $E[EE_{14}]$ to other parameters remains constant.

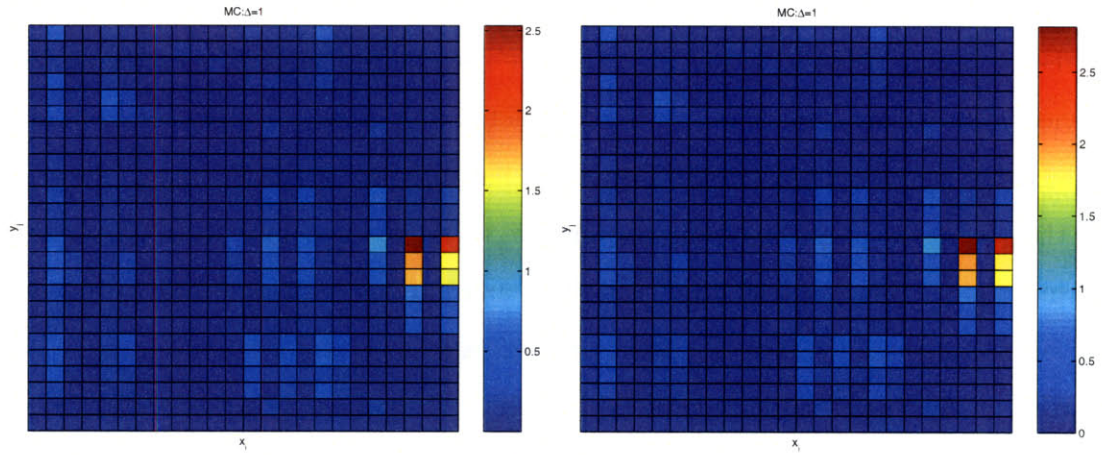

Figure 5-80: The $ES_{\infty,(j,i)}$ plot (Left) and $SS_{\infty,(j,i)}$ plot (Right) using the Monte Carlo Sampling method with $NN = 2,500$ for ranking the input sensitivity for $\sigma_{x_i} = 0.3$ and $t \in [0, 1]$ second. Note that the order of x_i inputs on the x-axis are [r_s, X_{ls}, X_{md}, X_{mq}, r_{fd}, X_{fd}, r_{kd}, X_{lkd}, r_{kq1}, X_{lkq1},r_{kq2}, X_{lkq2}, r_{s2}, X_{ls2}, X_{m2}, X_{lr2}, r_{r2}, J, α_{load}, C, R, C_f, r_f, L_f] from left to right and the order of y_j states or outputs on the y-axis are [ψ^e_{qs}, $\psi^{'e}_{kq1}$, $\psi^{'e}_{kq2}$, ψ^e_{ds}, $\psi^{'e}_{fd}$, $\psi^{'e}_{kd}$, ψ^e_{0s}, θ, $e^{'}_{xfd}$, VF, V_{an}, V_{bn}, V_{cn}, i_a, i_b, i_c, V_{c1}, V_{c2}, V_{c3},ψ^e_{qs}, $\psi^{'e}_{qr}$, ψ^e_{ds}, $\psi^{'e}_{dr}$, ψ^e_{0s}, ω_r] from top to bottom.

As the peak magnitude of the $I_{a,filter}$ sensitivity drops, the plots of $(ES_{2,(j,i)}, SS_{2,(j,i)})$ with σ_{x_i}=0.5 (see Figure 5-83) are closely matched with those with σ_{x_i}=0.3. Similarly, the peak sensitivity and interaction indices, $(ES_{\infty,(j,i)}, SS_{\infty,(j,i)})$ (see Figure 5-84) reveal that there is strong coupling between the SM, IM, and RC bus. Particularly, some SM's and IM's parameters have a significant impact on all state variables of the entire system, while all RC bus's parameters only affect its state variables.

For $t \in [0, 12.4]$ second where the mechanical time constant is dominated, the normalized sensitivity trajectories of $I_{a,filter}$ of the harmonic filter and ω_r of the IM in Figure 5-85 and 5-86 are compared to those with $t \in [0, 1]$ second in Figure 5-75 and 5-76. We can see that C_f, $r^{'}_r$, and J have the strongest influence on the $I_{a,filter}$ and the interaction index of $r^{'}_r$ and J overwhelms that of other parameters. The sensitivity of $I_{a,filter}$ to $r^{'}_r$ and J, particularly after 2 seconds, confirms directly interaction between the RC bus and induction motor even more. The sensitivity time traces of ω_r to $r^{'}_r$ and J reach a peak gradient magnitude of 0.7, which is almost 7 time larger than that in the short time frame, then approach zero steady-state values within three times of the mechanical time constant. Moreover, the rotor speed also becomes

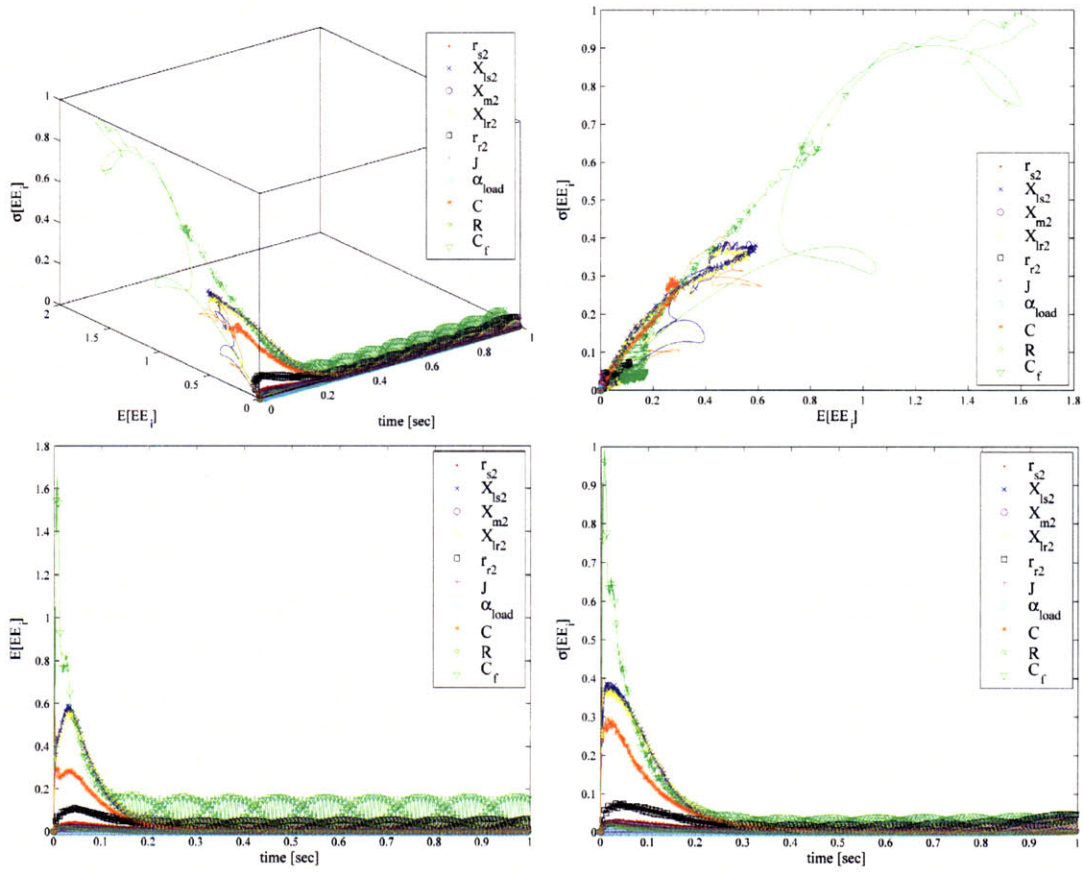

Figure 5-81: For a y_{14} variable or $I_{a,filter}$ of the harmonic filter, the normalized $E[EE_i]$ and $\sigma[EE_i]$ trajectories of the 7 induction machine parameters and 3 bus parameters as a function of time, $t \in [0, 1]$ second, using the MC Sampling method with $NN = 5,000$ and $\sigma_{x_i} = 0.5$ in three dimensions (Top-Left), the Side view (Top-Right) for emphasizing the first-order effect, the Top view (Bottom-Left) for emphasizing the inputs' interaction effect, and the Front view (Bottom-Right).

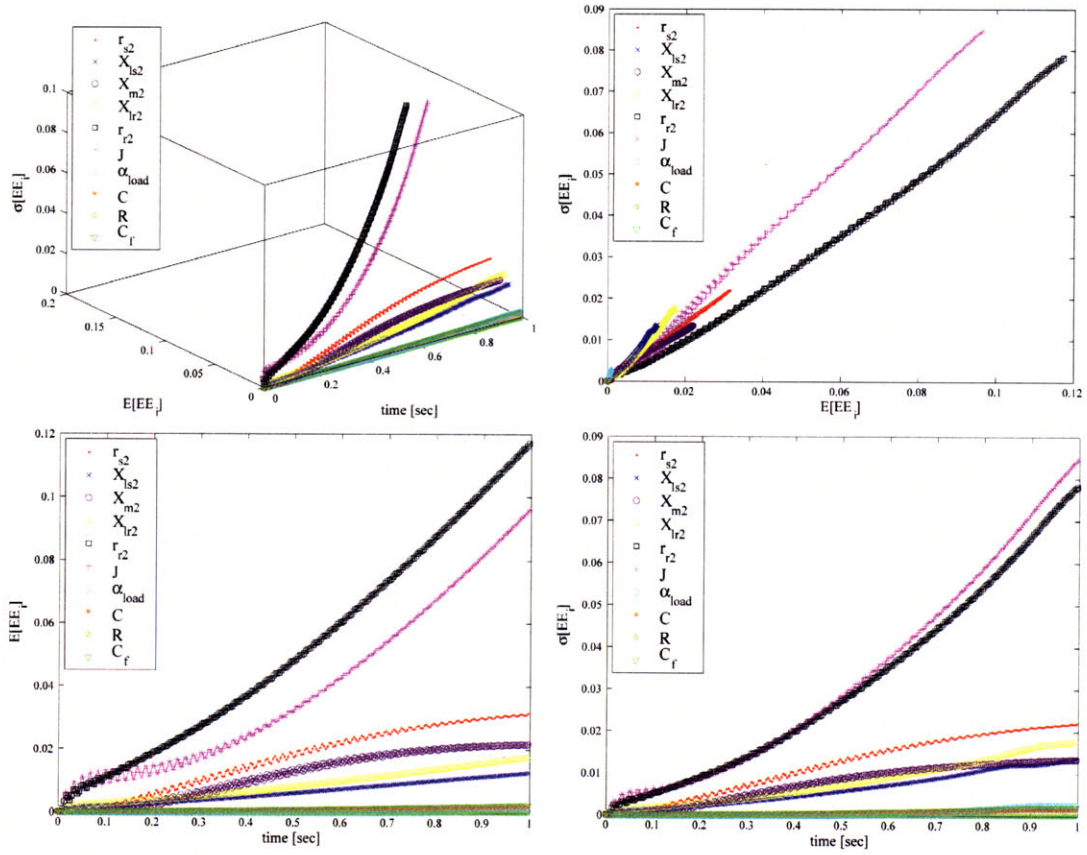

Figure 5-82: For a y_{24} variable or ω_r of the IM, the normalized $E[EE_i]$ and $\sigma[EE_i]$ trajectories of the 7 induction machine parameters and 3 bus parameters as a function of time, $t \in [0, 1]$ second, using the MC Sampling method with $NN = 5,000$ and $\sigma_{x_i} = 0.5$ in three dimensions (Top-Left), the Side view (Top-Right) for emphasizing the first-order effect, the Top view (Bottom-Left) for emphasizing the inputs' interaction effect, and the Front view (Bottom-Right).

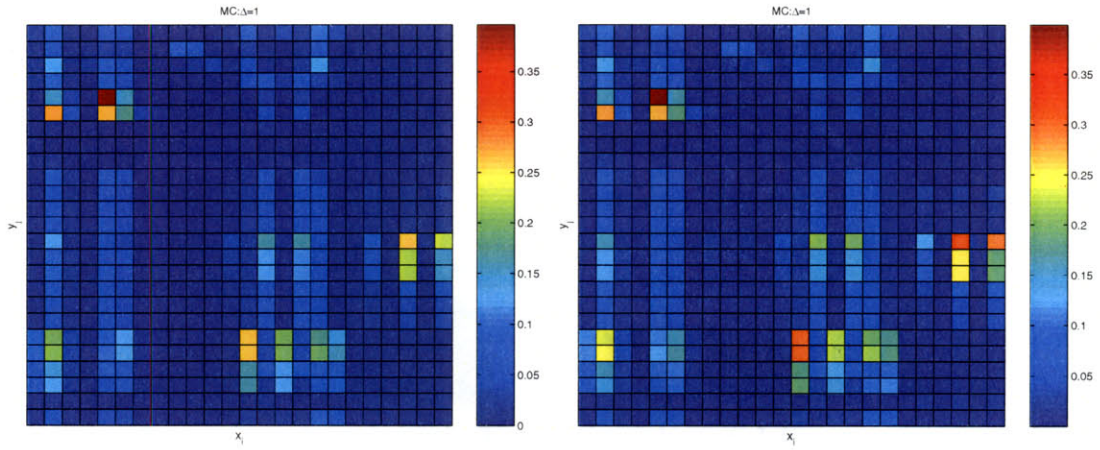

Figure 5-83: The $ES_{2,(j,i)}$ plot (Left) and $SS_{2,(j,i)}$ plot (Right) using the Monte Carlo Sampling method with $NN = 5,000$ for ranking the input sensitivity for $\sigma_{x_i} = 0.5$ and $t \in [0, 1]$ second. Note that the order of x_i inputs on the x-axis are [r_s, X_{ls}, X_{md}, X_{mq}, r_{fd}, X_{fd}, r_{kd}, X_{lkd}, r_{kq1}, X_{lkq1},r_{kq2}, X_{lkq2}, r_{s2}, X_{ls2}, X_{m2}, X_{lr2}, r_{r2}, J, α_{load}, C, R, C_f, r_f, L_f] from left to right and the order of y_j states or outputs on the y-axis are [ψ^e_{qs}, $\psi^{'e}_{kq1}$, $\psi^{'e}_{kq2}$, ψ^e_{ds}, $\psi^{'e}_{fd}$, $\psi^{'e}_{kd}$, ψ^e_{0s}, θ, $e^{'}_{xfd}$, VF, V_{an}, V_{bn}, V_{cn}, i_a, i_b, i_c, V_{c1}, V_{c2}, V_{c3},ψ^e_{qs}, $\psi^{'e}_{qr}$, ψ^e_{ds}, $\psi^{'e}_{dr}$, ψ^e_{0s}, ω_r] from top to bottom.

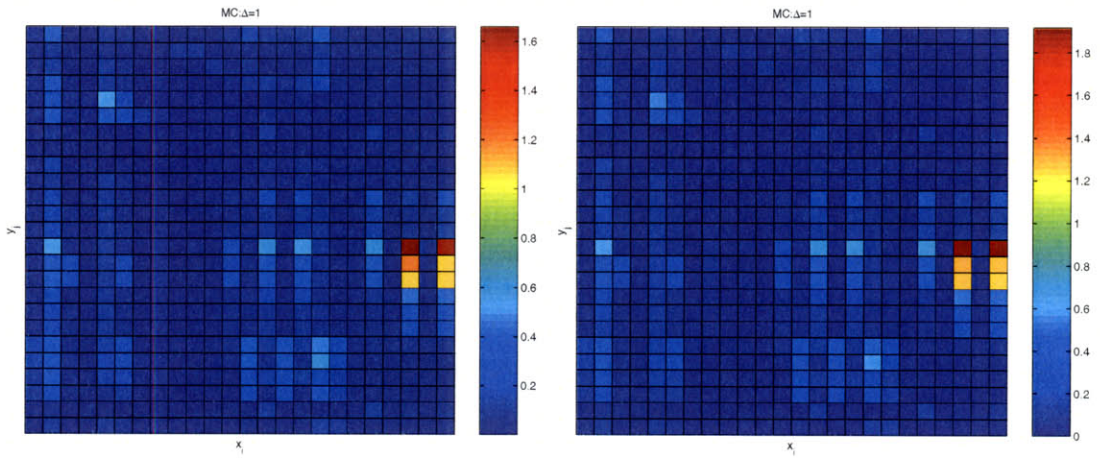

Figure 5-84: The $ES_{\infty,(j,i)}$ plot (Left) and $SS_{\infty,(j,i)}$ plot (Right) using the Monte Carlo Sampling method with $NN = 5,000$ for ranking the input sensitivity for $\sigma_{x_i} = 0.5$ and $t \in [0, 1]$ second. Note that the order of x_i inputs on the x-axis are [r_s, X_{ls}, X_{md}, X_{mq}, r_{fd}, X_{fd}, r_{kd}, X_{lkd}, r_{kq1}, X_{lkq1},r_{kq2}, X_{lkq2}, r_{s2}, X_{ls2}, X_{m2}, X_{lr2}, r_{r2}, J, α_{load}, C, R, C_f, r_f, L_f] from left to right and the order of y_j states or outputs on the y-axis are [ψ^e_{qs}, $\psi^{'e}_{kq1}$, $\psi^{'e}_{kq2}$, ψ^e_{ds}, $\psi^{'e}_{fd}$, $\psi^{'e}_{kd}$, ψ^e_{0s}, θ, $e^{'}_{xfd}$, VF, V_{an}, V_{bn}, V_{cn}, i_a, i_b, i_c, V_{c1}, V_{c2}, V_{c3},ψ^e_{qs}, $\psi^{'e}_{qr}$, ψ^e_{ds}, $\psi^{'e}_{dr}$, ψ^e_{0s}, ω_r] from top to bottom.

more sensitive to the load coefficient, α_{load}, after 2 seconds. This phenomenon implies that each parameter can have a different influence according to the time scale.

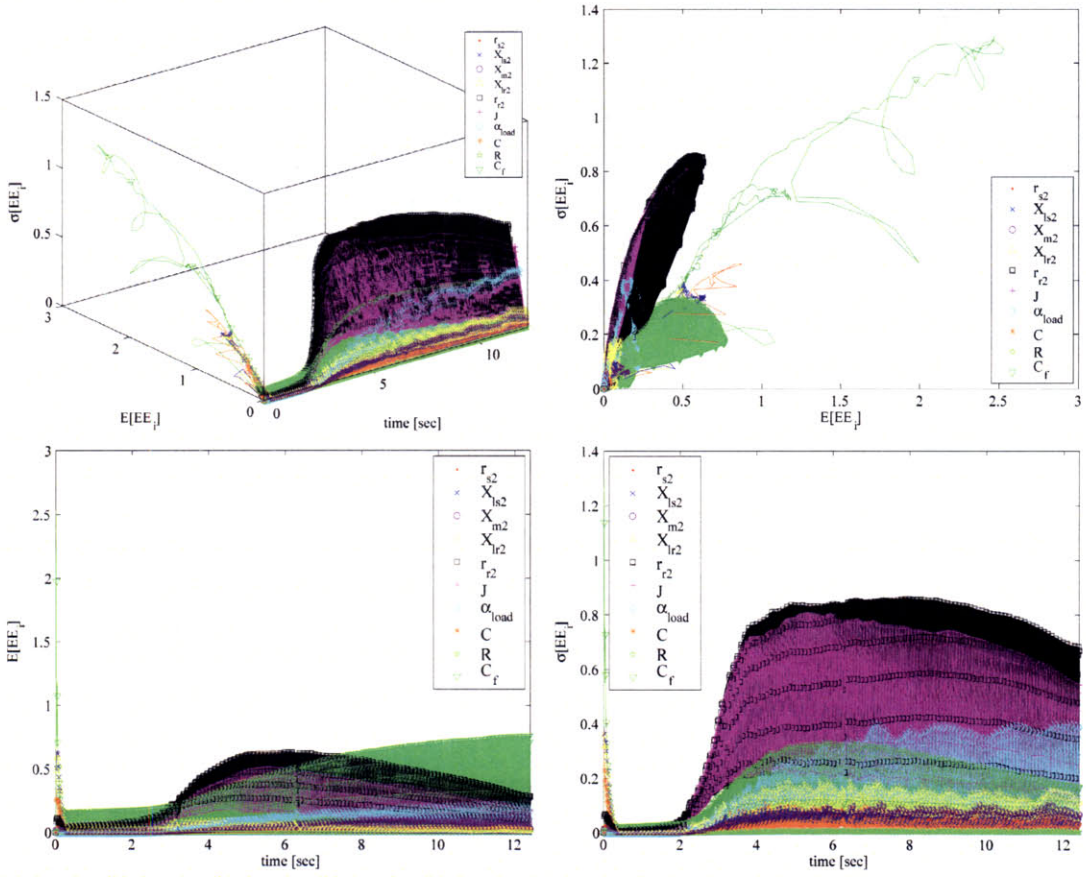

Figure 5-85: For a y_{14} variable or $I_{a,filter}$ of the harmonic filter, the normalized $E[EE_i]$ and $\sigma[EE_i]$ trajectories of the 7 induction machine parameters and 3 bus parameters as a function of time, $t \in [0, 12.4]$ seconds, using the MC Sampling method with $NN = 1,000$ and $\sigma_{x_i} = 0.3$ in three dimension (Top-Left), the Side view (Top-Right) for emphasizing the first-order effect, the Top view (Bottom-Left) for emphasizing the inputs' interaction effect, and the Front view (Bottom-Right).

A large number of parameters' sensitivity to these systems with $\sigma_{x_i} = 0.3$ can be summarized in the plots of $(ES_{2,(j,i)}, SS_{2,(j,i)})$ and $(ES_{\infty,(j,i)}, SS_{\infty,(j,i)})$. From $ES_{2,(j,i)}$ and $SS_{2,(j,i)}$ plots in Figure 5-87, only three parameters - r_{fd} of the SM and $r_r^{'}$ and J of the IM - have distinct impacts on all state variables of this system. The reasons that these three parameters are more sensitive than other parameters are: 1) the rotor inertia directly governs the mechanical time constant, 2) the rotor resistance of IM has a direct influence on the generated rotor flux and the motor operation, 3)

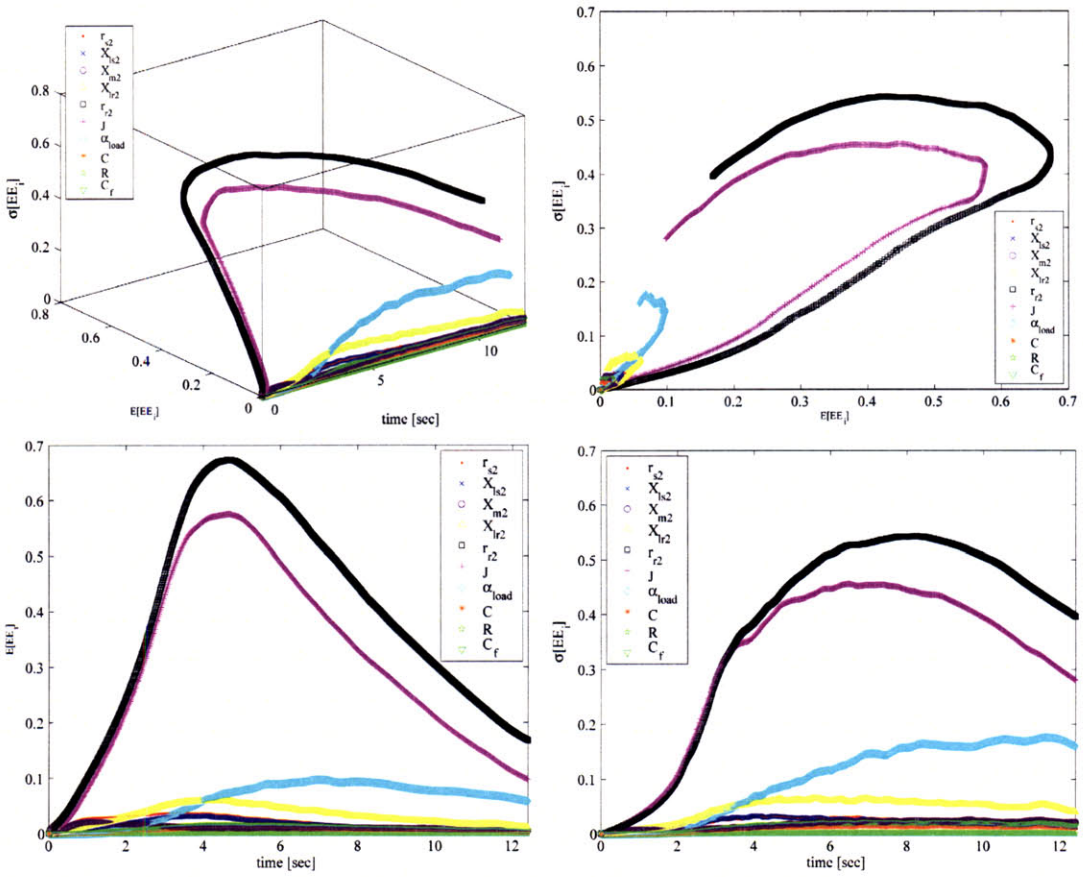

Figure 5-86: For a y_{24} variable or ω_r of the IM, the normalized $E[EE_i]$ and $\sigma[EE_i]$ trajectories of the 7 induction machine parameters and 3 bus parameters as a function of time, $t \in [0, 12.4]$ seconds, using the MC Sampling method with $NN = 1,000$ and $\sigma_{x_i} = 0.3$ in three dimension (Top-Left), the Side view (Top-Right) for emphasizing the first-order effect, the Top view (Bottom-Left) for emphasizing the inputs' interaction effect, and the Front view (Bottom-Right).

the rotor field winding of SM, which is connected to the voltage feedback from the exciter/voltage regulator, can amplify the propagation of uncertainties. Therefore, a small variation in r_{fd} of the SM can lead to a large fluctuation in the bus voltage. However, if we consider only the peak magnitude of the sensitivity and interaction indices, $ES_{\infty,(j,i)}$ and $SS_{\infty,(j,i)}$, in Figure 5-88 within $t \in [0, 12.4]$ seconds, the sudden peak gradients of L_f and C_f are still much larger than the gradually increasing gradient of r_{fd}, $r_r^{'}$ and J. Thus, the peak sensitivity of electrical transient is very important, especially for the high-frequency transient like in the start-up dynamics of the electric machine.

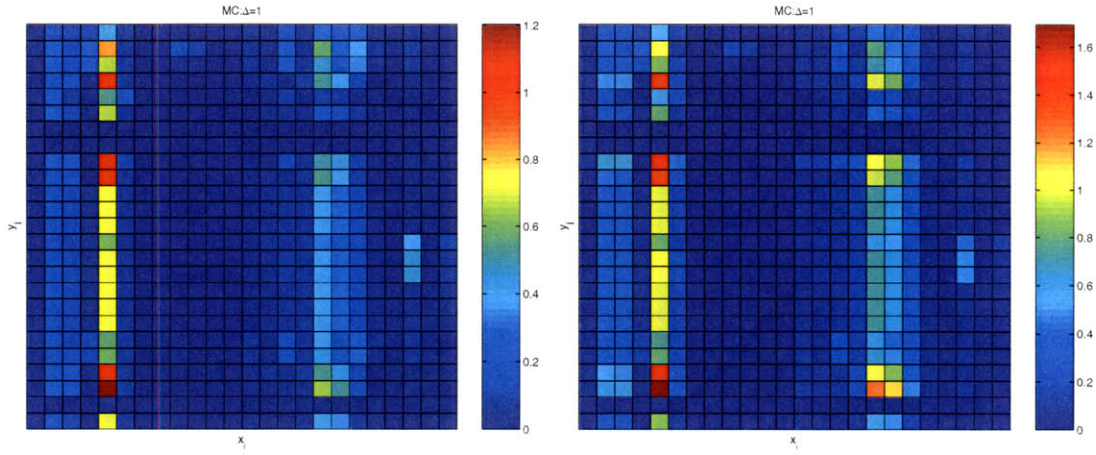

Figure 5-87: The $ES_{2,(j,i)}$ plot (Left) and $SS_{2,(j,i)}$ plot (Right) using the Monte Carlo Sampling method for ranking the input sensitivity for $\sigma_{x_i} = 0.3$ and $t \in [0, 12.4]$ seconds. Note that the order of x_i inputs on the x-axis are [r_s, X_{ls}, X_{md}, X_{mq}, r_{fd}, X_{fd}, r_{kd}, X_{lkd}, r_{kq1}, X_{lkq1},r_{kq2}, X_{lkq2}, r_{s2}, X_{ls2}, X_{m2}, X_{lr2}, r_{r2}, J, α_{load}, C, R, C_f, r_f, L_f] from left to right and the order of y_j states on the y-axis are [ψ^e_{qs}, $\psi^{'e}_{kq1}$, $\psi^{'e}_{kq2}$, ψ^e_{ds}, $\psi^{'e}_{fd}$, $\psi^{'e}_{kd}$, ψ^e_{0s}, θ, $e^{'}_{xfd}$, VF, V_{an}, V_{bn}, V_{cn}, i_a, i_b, i_c, V_{c1}, V_{c2}, V_{c3},ψ^e_{qs}, $\psi^{'e}_{qr}$, ψ^e_{ds}, $\psi^{'e}_{dr}$, ψ^e_{0s}, ω_r] from top to bottom.

5.3.5 AC power distribution with closed-loop propulsion system

Instead of the free acceleration of the induction machine as in the previous example, the power converter and constant-slip current control, in Section 2.2.1, controls the electromagnetic torque of the 50-hp induction machine, connected to the same 59

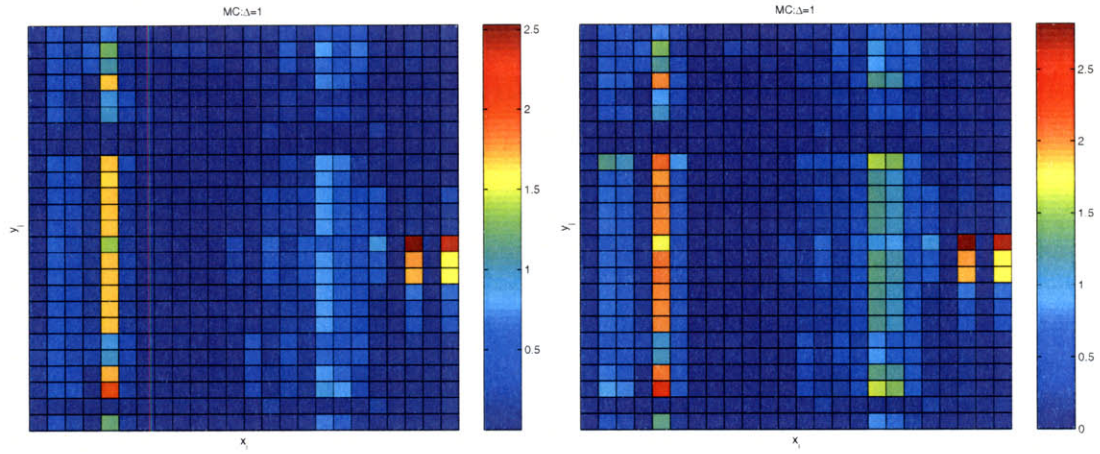

Figure 5-88: The $ES_{\infty,(j,i)}$ plot (Left) and $SS_{\infty,(j,i)}$ plot (Right) using the Monte Carlo Sampling method for ranking the input sensitivity for $\sigma_{x_i} = 0.3$ and $t \in [0, 12.4]$ seconds. Note that the order of x_i inputs on the x-axis are [r_s, X_{ls}, X_{md}, X_{mq}, r_{fd}, X_{fd}, r_{kd}, X_{lkd}, r_{kq1}, X_{lkq1},r_{kq2}, X_{lkq2}, r_{s2}, X_{ls2}, X_{m2}, X_{lr2}, r_{r2}, J, α_{load}, C, R, C_f, r_f, L_f] from left to right and the order of y_j states or outputs on the y-axis are [ψ^e_{qs}, ψ'^e_{kq1}, ψ'^e_{kq2}, ψ^e_{ds}, ψ'^e_{fd}, ψ'^e_{kd}, ψ^e_{0s}, θ, e'_{xfd}, VF, V_{an}, V_{bn}, V_{cn}, i_a, i_b, i_c, V_{c1}, V_{c2}, V_{c3},ψ^e_{qs}, ψ'^e_{qr}, ψ^e_{ds}, ψ'^e_{dr}, ψ^e_{0s}, ω_r] from top to bottom.

kW synchronous machine through the three-phase RC bus, as shown in Figure 5-89 below. The high-dimensional stochastic analysis of this system has been demonstrated in Section 4.4.2.

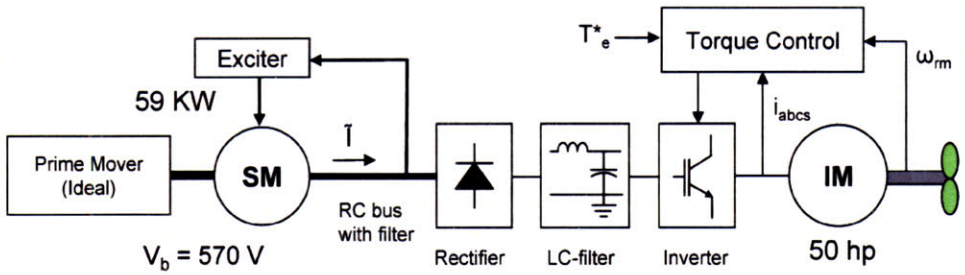

Figure 5-89: A one-line diagram of the third configuration of the AC power distribution with the closed-loop control of induction machine for studying the sensitivity analysis with 31 parameters.

In this study, we assume that the generator initially operates at its rated speed in its steady-state condition and then at zero seconds the induction machine with the controller is suddenly turned on. The torque command to the controller is kept constant at 2 N-m during $t \in [0, 1.62]$ seconds. In this system, there are 30 state

variables and 31 parameters, which include 7 additional parameters: (L_c, R_{dc}, L_{dc}, C_{dc}) of the 6-pulse full-wave rectifier and (R_L, L_L, C_L) of the DC-link filter. Similarly, in this complex nonlinear system, three different ranges of parameters' variations, σ_{x_i} = 0.1, 0.3, and 0.5, are also considered in the sensitivity analysis to investigate the influence of each parameter at different fluctuation levels and to compare with the sensitivity results in the previous section.

First, let us consider the case with $\sigma_{x_i} = 0.1$ and $t \in [0, 0.2]$ second, where the electrical time constant is dominated. Using the Monte Carlo Sampling method with $\Delta = 1$ to perform the sensitivity analysis, Figure 5-90 shows the normalized sensitivity trajectories of the IM's ω_r and the RC bus's $I_{a,filter}$ to 7 parameters of the induction machine and 3 parameters of the RC bus. $I_{a,filter}$ is very sensitive to both C of the RC bus and to C_f of the harmonic filter. The controller draws more power to maintain a constant torque of the IM, while the exciter/voltage regulator attempts to keep the bus voltage at a rated voltage; thus, a small change in the bus's and harmonic filter's capacitors, governing the bus voltage, has a significant impact on the entire system. The interaction of C and C_f with state variables is strong during the start-up transient of this system and then becomes weaker, approaching 0.05, as the electrical transient dies out within 0.2 second. Furthermore, only J and α_{load} have a strong influence on the normalized sensitivity trajectories of the induction machine's ω_r, while other parameters have negligible effect, as shown in Figure 5-91. The constant-slip current controller makes the propulsion system sensitive only to its mechanical component; thus, the performance of the closed-loop propulsion is much better than that of the open-loop propulsion in terms of the sensitivity to electrical components of the SM, bus, and IM itself. These characteristics confirm that the controller becomes very active in controlling the generated magnetic flux in the IM and its interaction.

Second, when the parameters' variation increases to 30 percent from their nominal values or $\sigma_{x_i} = 0.3$, the sensitivity of $I_{a,filter}$ in Figure 5-92 to C_f slightly decreases, while the sensitivity of this state to C and R of the RC bus increases at least 50 percent as time progresses. This decrease in the peak magnitude of the $I_{a,filter}$ sensitivity

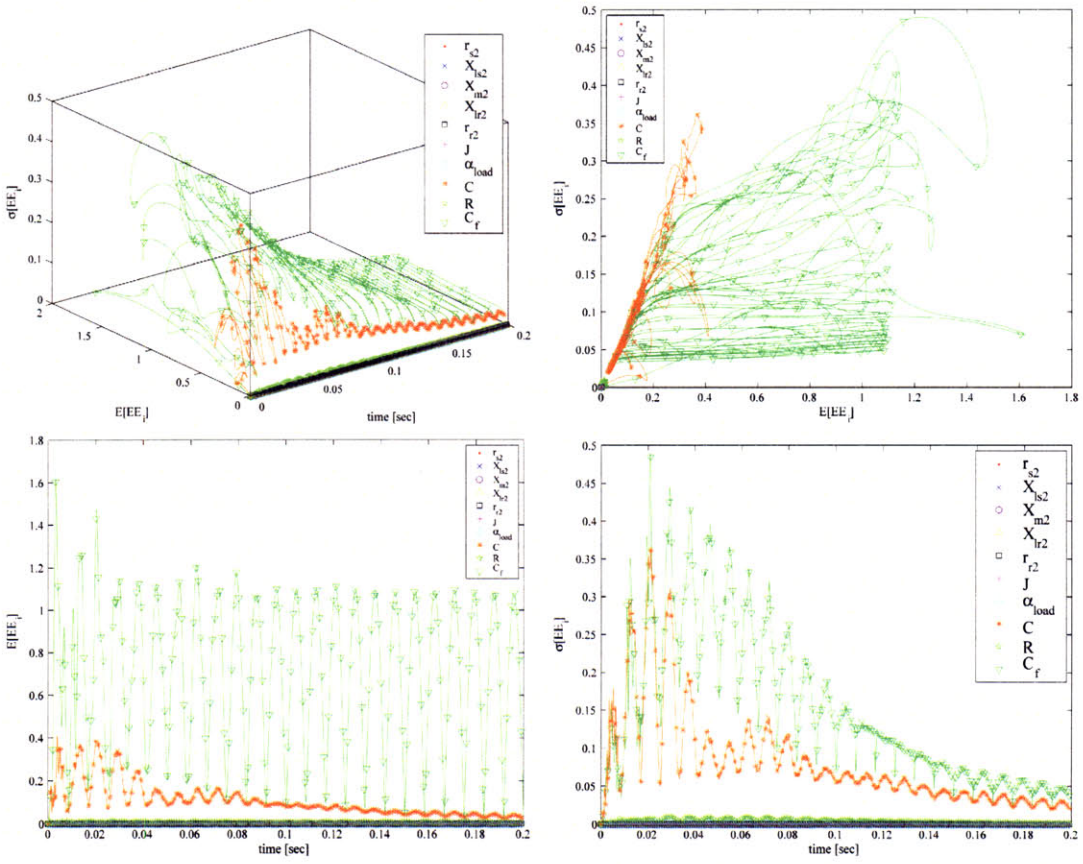

Figure 5-90: For a y_{14} variable or $I_{a,filter}$ of the harmonic filter, the normalized $E[EE_i]$ and $\sigma[EE_i]$ trajectories of the 7 induction machine parameters and 3 bus parameters as a function of time, $t \in [0, 0.2]$ second, using the MC Sampling method with $NN = 1,000$ and $\sigma_{x_i} = 0.1$ in three dimensions (Top-Left), the Side view (Top-Right) for emphasizing the first-order effect, the Top view (Bottom-Left) for emphasizing the inputs' interaction effect, and the Front view (Bottom-Right).

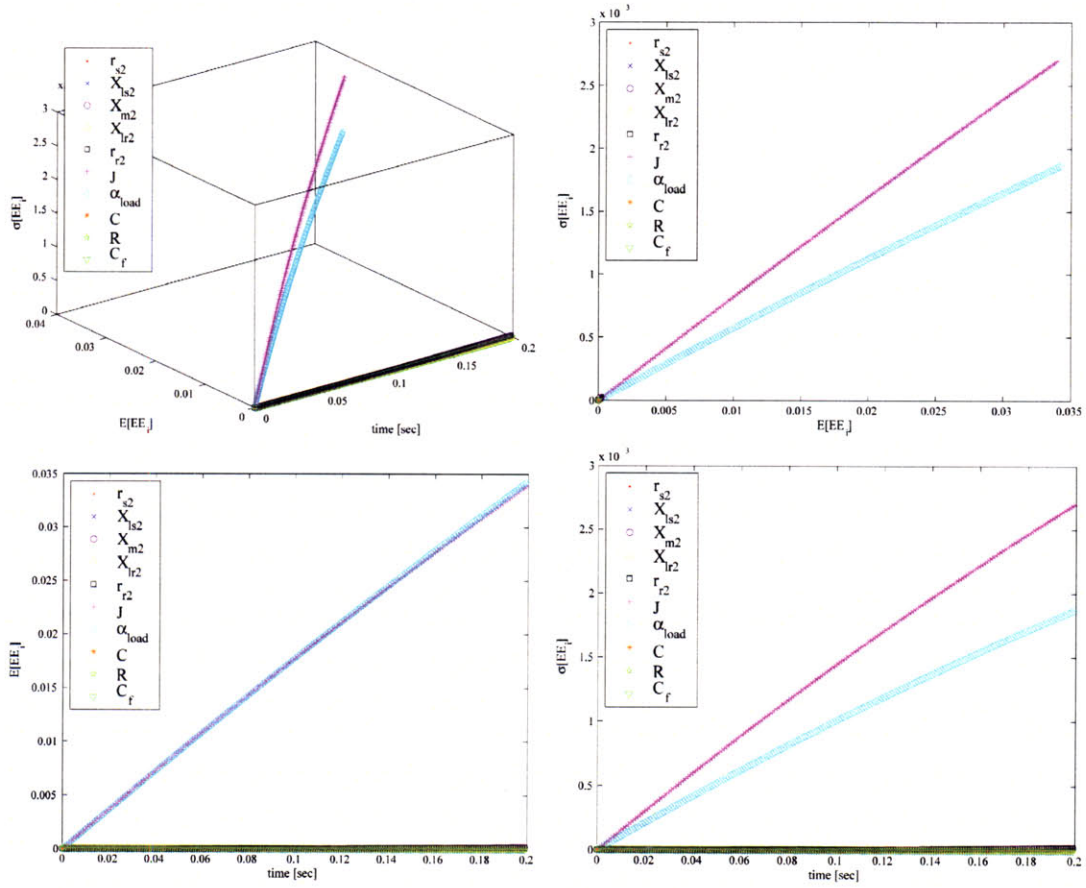

Figure 5-91: For a y_{25} variable or ω_r of the IM, the normalized $E[EE_i]$ and $\sigma[EE_i]$ trajectories of the 7 induction machine parameters and 3 bus parameters as a function of time, $t \in [0, 0.2]$ second, using the MC Sampling method with $NN = 1,000$ and $\sigma_{x_i} = 0.1$ in three dimensions (Top-Left), the Side view (Top-Right) for emphasizing the first-order effect, the Top view (Bottom-Left) for emphasizing the inputs' interaction effect, and the Front view (Bottom-Right).

index is again caused by the phase shift of the responses due to a variation in C_f. For the sensitivity of ω_r in Figure 5-93, only J and α_{load} still have a strong influence with only a minor increase in the magnitude of sensitivity; however, the interaction indices of J and α_{load} on ω_r grow by three times compared to the case with $\sigma_{x_i} = 0.1$. This implies that the feedback controller performs very well so that electromechanical torque, controlled by induced electromagnetic flux of stator and rotor windings, is almost insensitive to any electrical parameters.

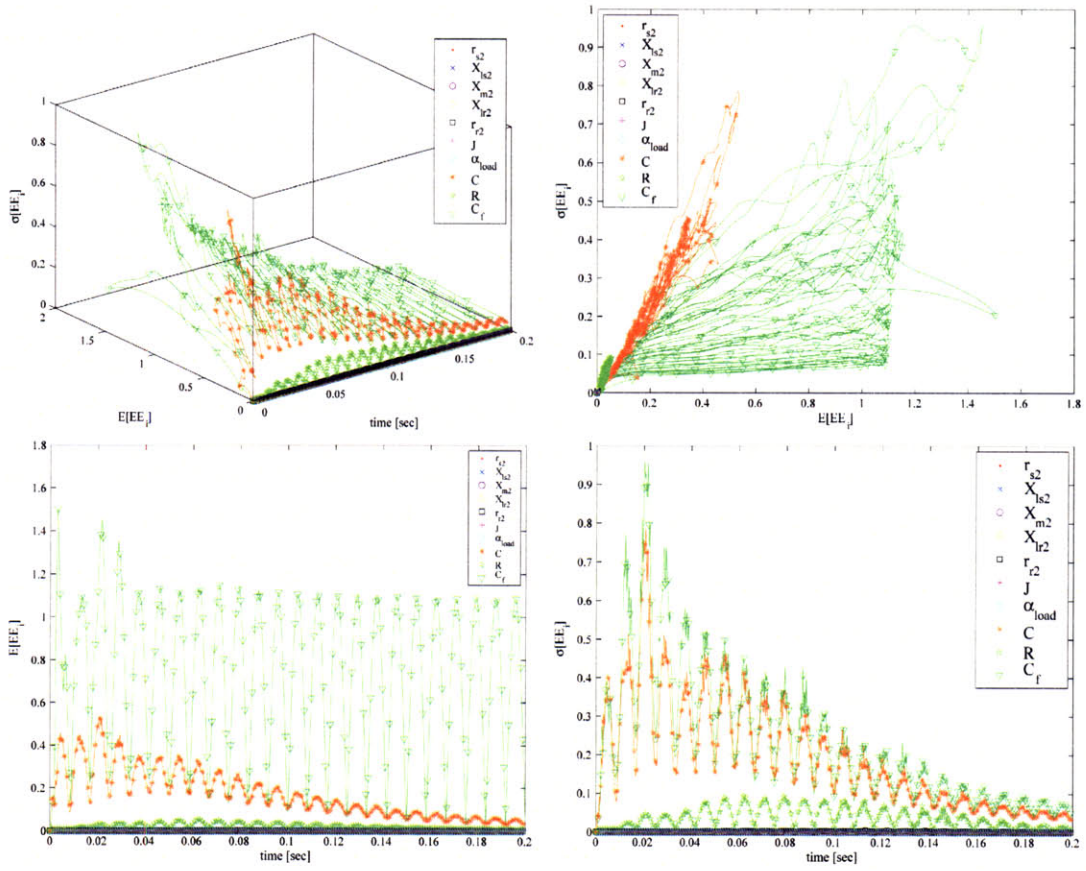

Figure 5-92: For a y_{14} variable or $I_{a,filter}$ of the harmonic filter, the normalized $E[EE_i]$ and $\sigma[EE_i]$ trajectories of the 7 induction machine parameters and 3 bus parameters as a function of time, $t \in [0, 0.2]$ second, using the MC Sampling method with $NN = 3,000$ and $\sigma_{x_i} = 0.3$ in three dimensions (Top-Left), the Side view (Top-Right) for emphasizing the first-order effect, the Top view (Bottom-Left) for emphasizing the inputs' interaction effect, and the Front view (Bottom-Right).

Third, parameters' variation of 50 percent from their nominal values or $\sigma_{x_i} = 0.5$, the normalized sensitivity trajectories of $I_{a,filter}$ and ω_r are again shown in Figure 5-94

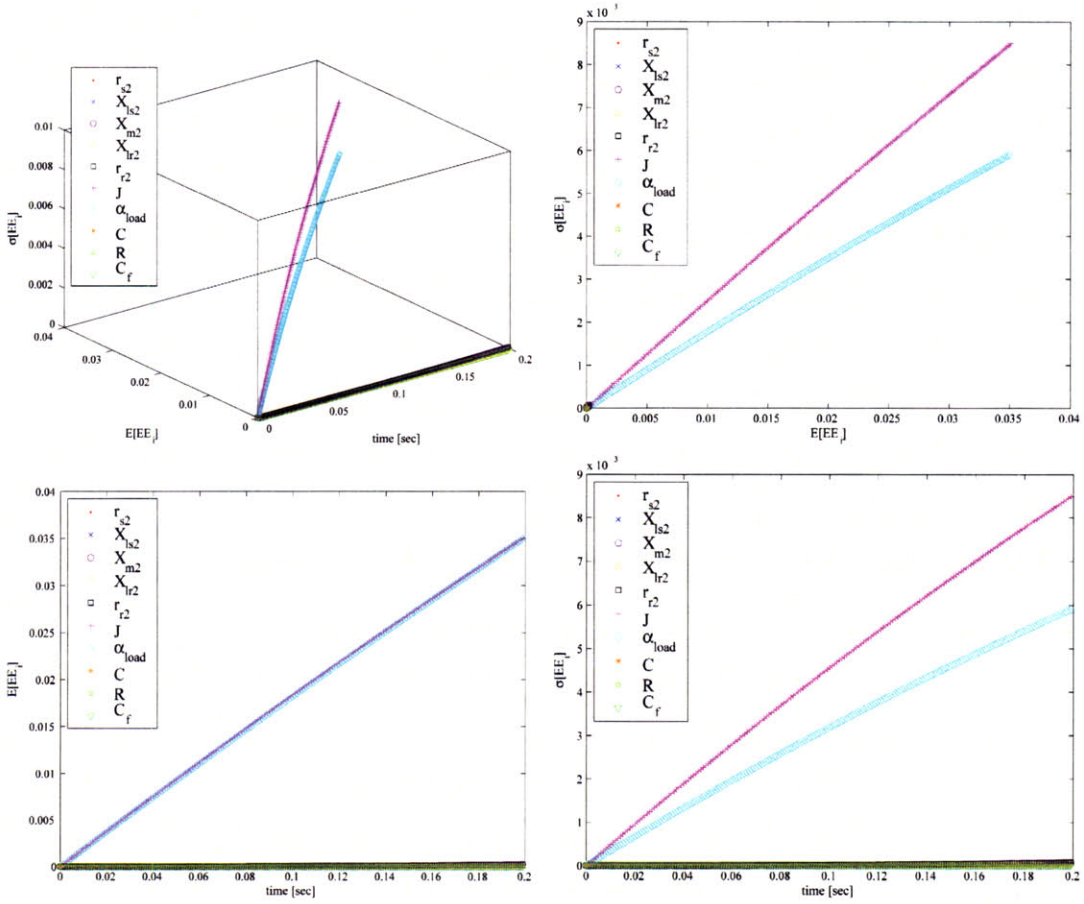

Figure 5-93: For a y_{25} variable or ω_r of the IM, the normalized $E[EE_i]$ and $\sigma[EE_i]$ trajectories of the 7 induction machine parameters and 3 bus parameters as a function of time, $t \in [0, 0.2]$ second, using the MC Sampling method with $NN = 3,000$ and $\sigma_{x_i} = 0.3$ in three dimensions (Top-Left), the Side view (Top-Right) for emphasizing the first-order effect, the Top view (Bottom-Left) for emphasizing the inputs' interaction effect, and the Front view (Bottom-Right).

and 5-95, respectively. The peak magnitude of $I_{a,filter}$ sensitivity to C_f drops slightly, while the steady-state magnitude of its sensitivity to C_f is about the same as in the previous two cases. On the other hand, both sensitivity and interaction indices of $I_{a,filter}$ to other parameters significantly increase, particularly to C and R of the RC bus. The sensitivity trajectories of ω_r to J and α_{load} again increase somewhat, while J and α_{load} exhibit stronger interaction with ω_r and other states.

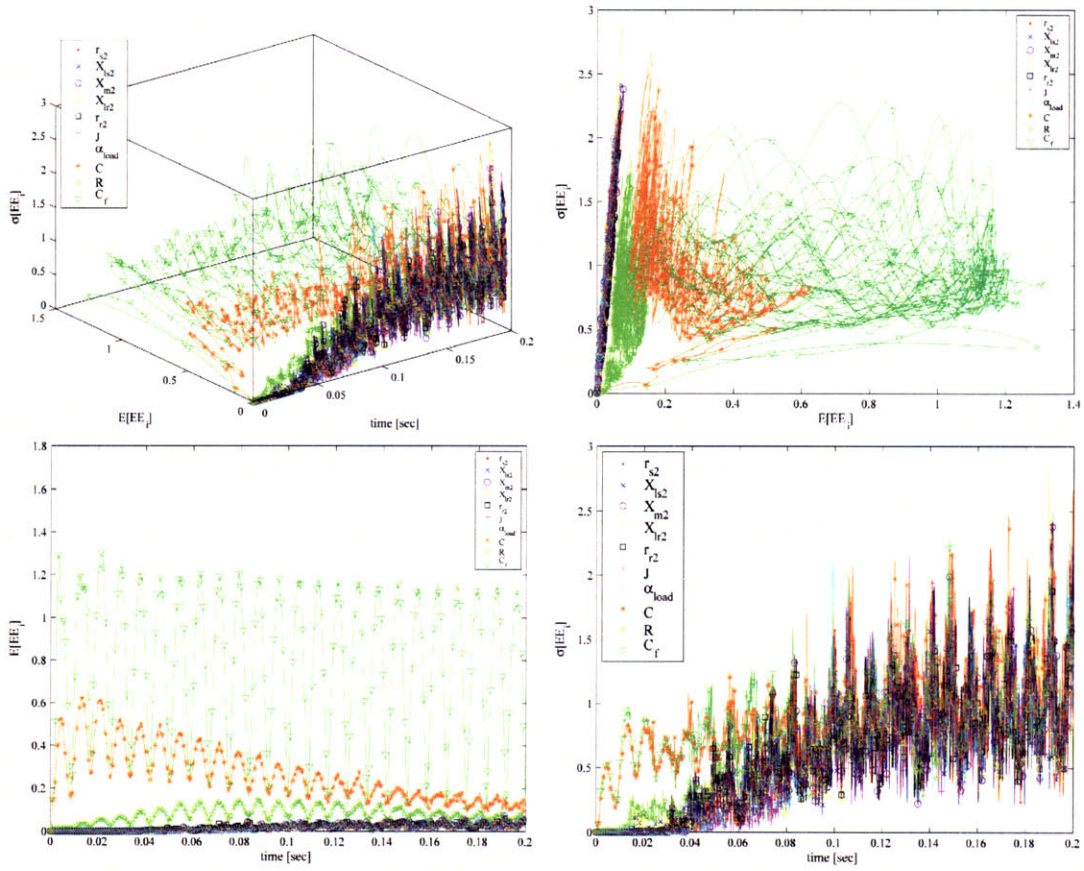

Figure 5-94: For a y_{14} variable or $I_{a,filter}$ of the harmonic filter, the normalized $E[EE_i]$ and $\sigma[EE_i]$ trajectories of the 7 induction machine parameters and 3 bus parameters as a function of time, $t \in [0, 0.2]$ second, using the MC Sampling method with $NN = 5,000$ and $\sigma_{x_i} = 0.5$ in three dimensions (Top-Left), the Side view (Top-Right) for emphasizing the first-order effect, the Top view (Bottom-Left) for emphasizing the inputs' interaction effect, and the Front view (Bottom-Right).

To summarize the ranking of parameters' sensitivity with increasing percent variation of parameters, $\sigma_{x_i} = 0.1$, 0.3, and 0.5, $ES_{2,(j,i)}$ is plotted versus parameters of the synchronous generator (see Figure 5-96), the induction machine (see Figure 5-98),

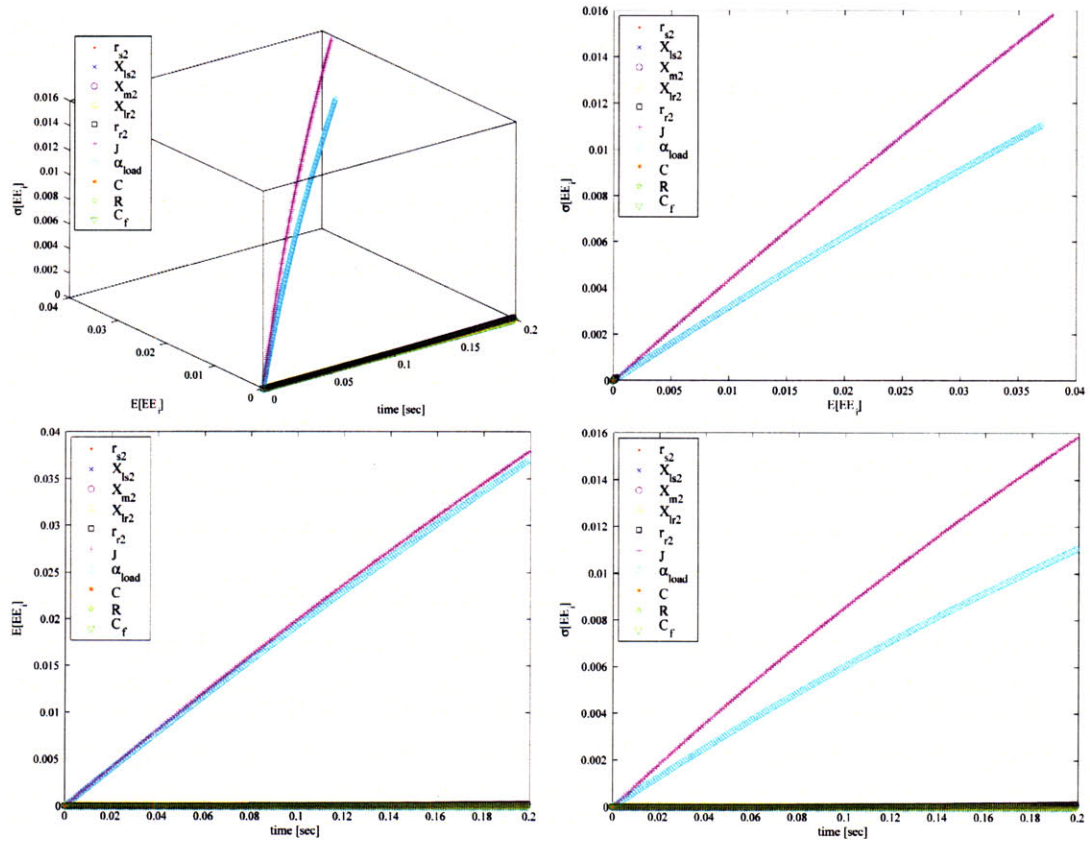

Figure 5-95: For a y_{25} variable or ω_r of the IM, the normalized $E[EE_i]$ and $\sigma[EE_i]$ trajectories of the 7 induction machine parameters and 3 bus parameters as a function of time, $t \in [0, 0.2]$ second, using the MC Sampling method with $NN = 5,000$ and $\sigma_{x_i} = 0.5$ in three dimensions (Top-Left), the Side view (Top-Right) for emphasizing the first-order effect, the Top view (Bottom-Left) for emphasizing the inputs' interaction effect, and the Front view (Bottom-Right).

the RC bus (see Figure 5-97), and the power converter (see Figure 5-99). Figure 5-96 shows that the peak sensitivity of ψ_{0s}^{e} to X_{ls} dominates the entire sensitivity domain due to the SM's parameters and this peak sensitivity of ψ_{0s}^{e} to X_{ls} decreases as the percent variation of parameters increases. This phenomenon again occurs because of the phase shifting in the large start-up transient response of ψ_{0s}^{e}. This phase shifting in the ψ_{0s}^{e} response implies that the average ψ_{0s}^{e} can be amplified or cancelled each other out, particularly during the first fraction of a second. The ψ_{0s}^{e} represents a balancing operation of the generator; thus, there are a lot of change in the balancing operation as the percent variation increases. Similarly, the average sensitivity of all state variables to the RC bus's parameter is dominated by the sensitivity of ψ_{0s}^{e} to C, C_f, and L_f and becomes smaller as the percent variation increases. The phase shifting in the ψ_{0s}^{e} response causes by the same reason as in the previous situation.

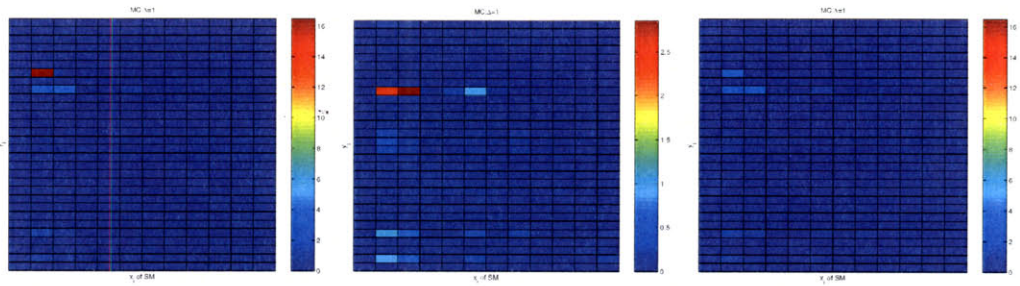

Figure 5-96: The $ES_{2,(j,i)}$ plots using the Monte Carlo Sampling method for ranking the input sensitivity with $\sigma_{x_i} = 0.1$ (Left), 0.3 (Middle), and 0.5 (Right). Note that the order of the **synchronous generator's parameters** (x_i) on the x-axis are [r_s, X_{ls}, X_{md}, X_{mq}, r_{fd}, X_{fd}, r_{kd}, X_{lkd},) r_{kq1}, X_{lkq1},r_{kq2}, X_{lkq2}] from left to right and the order of y_j outputs on the y-axis are [ψ_{qs}^{e}, $\psi_{kq1}^{'e}$, $\psi_{kq2}^{'e}$, ψ_{ds}^{e}, $\psi_{fd}^{'e}$, $\psi_{kd}^{'e}$, ψ_{0s}^{e}, θ, $e_{xfd}^{'}$, VF, V_{an}, V_{bn}, V_{cn}, i_a, i_b, i_c, V_{c1}, V_{c2}, V_{c3},ψ_{qs}^{e}, $\psi_{qr}^{'e}$, ψ_{ds}^{e}, $\psi_{dr}^{'e}$, ψ_{0s}^{e}, ω_r] from top to bottom.

For the average sensitivity to the IM's parameters in Figure 5-98, we can see a substantial increase in the sensitivity of the controller's state variables as the percent variation becomes larger. This increase in the controller's sensitivity means that the controller's variables become more active to correct any discrepancy in the IM's output torque from the commanded torque. The maximum magnitude in the controller's sensitivity is 24 percent variation in the voltage across the rectifier's capacitor due to 50 percent increase in either X_{m2} or $r_r^{'}$ of the induction machine. Likewise, the

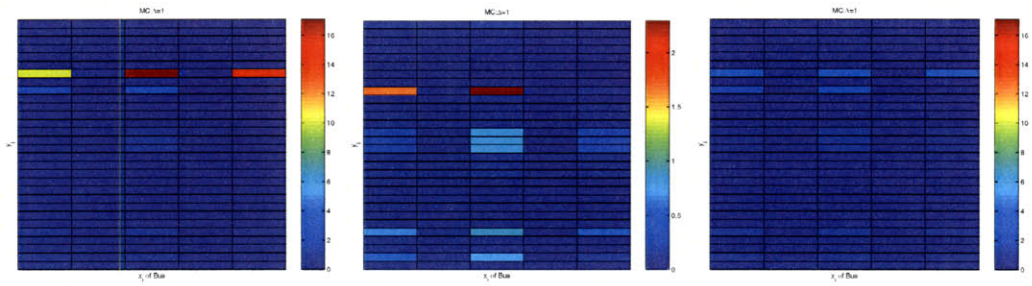

Figure 5-97: The $ES_{2,(j,i)}$ plots using the Monte Carlo Sampling method for ranking the input sensitivity with $\sigma_{x_i} = 0.1$ (Left), 0.3 (Middle), and 0.5 (Right). Note that the order of the **RC bus's parameters** (x_i) on the x-axis are [C, R, C_f, r_f, L_f] from left to right and the order of y_j outputs on the y-axis are [ψ^e_{qs}, ψ'^e_{kq1}, ψ'^e_{kq2}, ψ^e_{ds}, ψ'^e_{fd}, ψ'^e_{kd}, ψ^e_{0s}, θ, e'_{xfd}, VF, V_{an}, V_{bn}, V_{cn}, i_a, i_b, i_c, V_{c1}, V_{c2}, V_{c3},ψ^e_{qs}, ψ'^e_{qr}, ψ^e_{ds}, ψ'^e_{dr}, ψ^e_{0s}, ω_r] from top to bottom.

larger the percent variation is, the greater the average sensitivity indices of all states to the power converter's parameters (see Figure 5-99) become, especially to L_c of the tie line, C_{dc} of the rectifier, and (L_f,C_f) of the DC-link filter. Again, this increase in the controller's sensitivity indices confirms the effectiveness of the controllers in the presence of the parameter fluctuation.

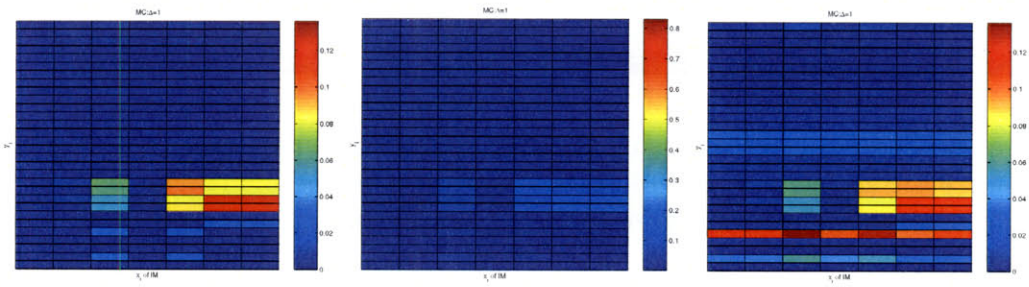

Figure 5-98: The $ES_{2,(j,i)}$ plots using the Monte Carlo Sampling method for ranking the input sensitivity with $\sigma_{x_i} = 0.1$ (Left), 0.3 (Middle), and 0.5 (Right). Note that the order of the **induction machine's parameters** (x_i) on the x-axis are [r_{s2}, X_{ls2}, X_{m2}, X_{lr2}, r_{r2}, J, α_{load}] from left to right and the order of y_j outputs on the y-axis are [ψ^e_{qs}, ψ'^e_{kq1}, ψ'^e_{kq2}, ψ^e_{ds}, ψ'^e_{fd}, ψ'^e_{kd}, ψ^e_{0s}, θ, e'_{xfd}, VF, V_{an}, V_{bn}, V_{cn}, i_a, i_b, i_c, V_{c1}, V_{c2}, V_{c3},ψ^e_{qs}, ψ'^e_{qr}, ψ^e_{ds}, ψ'^e_{dr}, ψ^e_{0s}, ω_r] from top to bottom.

When the simulation time is lengthened to 1.62 seconds, where the mechanical time constant is dominated, the sensitivity trajectories of $I_{a,filter}$ to C_f are still much larger than other parameters as they approach steady-state oscillation, as shown in Figure 5-100. Nevertheless, the sensitivity index of C on $I_{a,filter}$ diminishes very

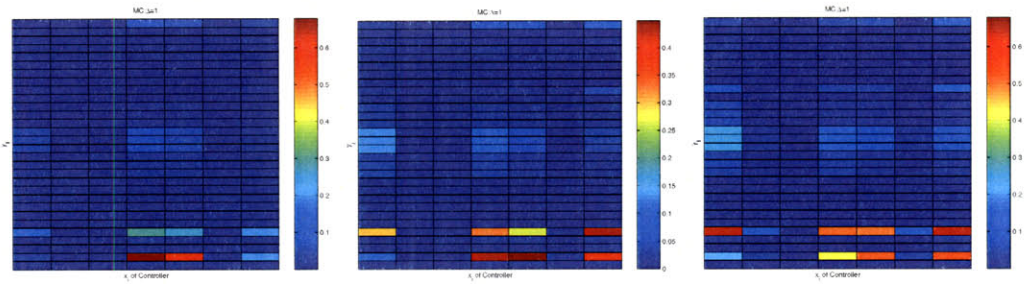

Figure 5-99: The $ES_{2,(j,i)}$ plots using the Monte Carlo Sampling method for ranking the input sensitivity with $\sigma_{x_i} = 0.1$ (Left), 0.3 (Middle), and 0.5 (Right). Note that the order of the **power converter's parameters** (x_i) on the x-axis are [L_c, r_{dc}, L_{dc}, C_{dc}, L_{filt}, r_{filt}, C_{filt}] from left to right and the order of y_j outputs on the y-axis are [ψ^e_{qs}, $\psi^{'e}_{kq1}$, $\psi^{'e}_{kq2}$, ψ^e_{ds}, $\psi^{'e}_{fd}$, $\psi^{'e}_{kd}$, ψ^e_{0s}, θ, $e^{'}_{xfd}$, VF, V_{an}, V_{bn}, V_{cn}, i_a, i_b, i_c, V_{c1}, V_{c2}, V_{c3},ψ^e_{qs}, $\psi^{'e}_{qr}$, ψ^e_{ds}, $\psi^{'e}_{dr}$, ψ^e_{0s}, ω_r] from top to bottom.

quickly as time approaches 0.4 second. The interaction index of C persists in time up to 0.4 second, similar to that of C_f. For the sensitivity of ω_r, both J and α_{load}, exhibiting the same order of the sensitivity magnitude, become even more dominant than other parameters, as shown in Figure 5-101. Again, J interacts with other parameters and states more than α_{load} and the sensitivity and interaction indices of ω_r to X_{m2}, governing the interaction between stator and rotor windings of the IM, increase as time reaches 1.62 seconds. These characteristics show that the constant-slip controller well controls the induction motor and the controller's action increases sensitivity to the mutual reactance, which is directly used in the maximum torque per current calculation of the constant-slip controller.

To make a comparison on a different time scale, the overall view can be examined from the $ES_{2,(j,i)}$ plots with $t \in [0, 0.2]$ for electrical time constant and $t \in [0, 1.62]$ for mechanical time constant. The average sensitivity to the generator's parameters in Figure 5-102 and to the bus's parameters in Figure 5-103 are very similar between these two different time scales. Figure 5-105 shows the average sensitivity indices of all state variables to only the power converter parameters. Only currents are sensitive to both capacitors and inductors of the rectifier and the DC-link filter (L_c, C_{dc}, L_{filter}, C_{filter}) when both electrical and mechanical time constants are dominated. However, in a short time frame, the currents of the power converter are more sensitive

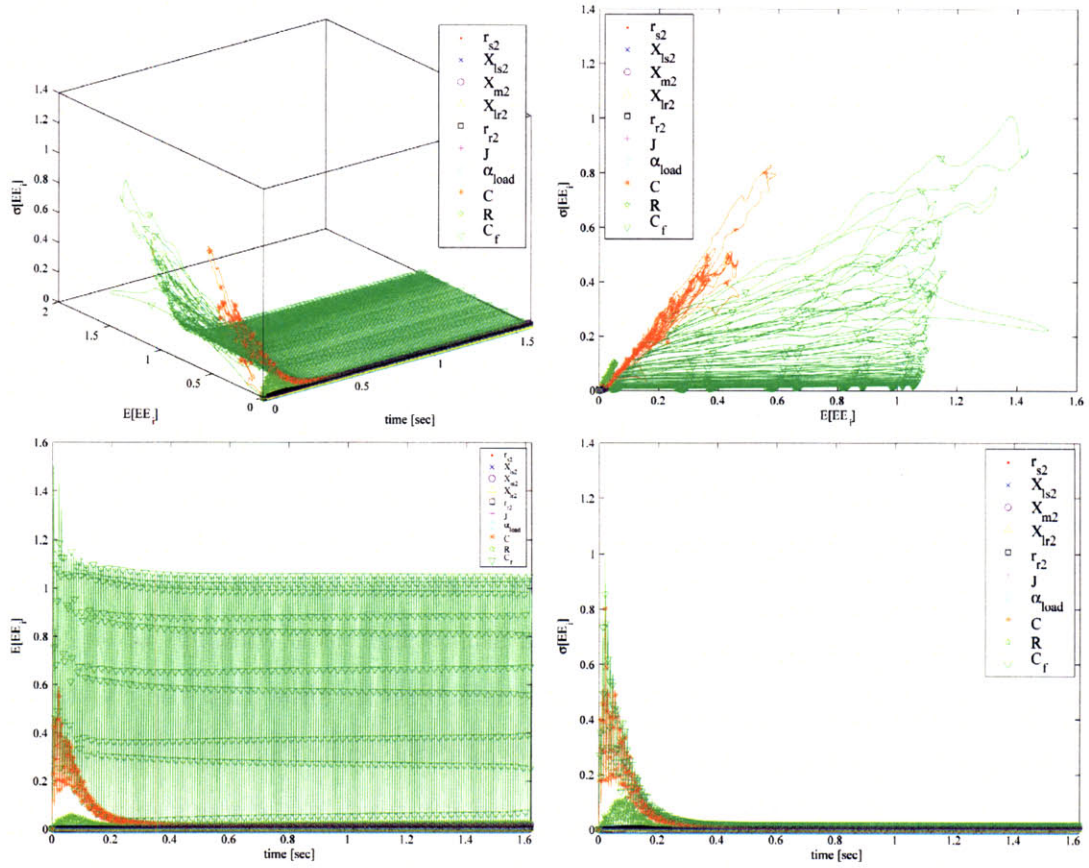

Figure 5-100: For a y_{14} variable or $I_{a,filter}$ of the harmonic filter, the normalized $E[EE_i]$ and $\sigma[EE_i]$ trajectories of the 7 induction machine parameters and 3 bus parameters as a function of time, $t \in [0, 1.62]$ seconds, using the MC Sampling method with $NN = 3,000$ and $\sigma_{x_i} = 0.3$ in three dimension (Top-Left), the Side view (Top-Right) for emphasizing the first-order effect, the Top view (Bottom-Left) for emphasizing the inputs' interaction effect, and the Front view (Bottom-Right).

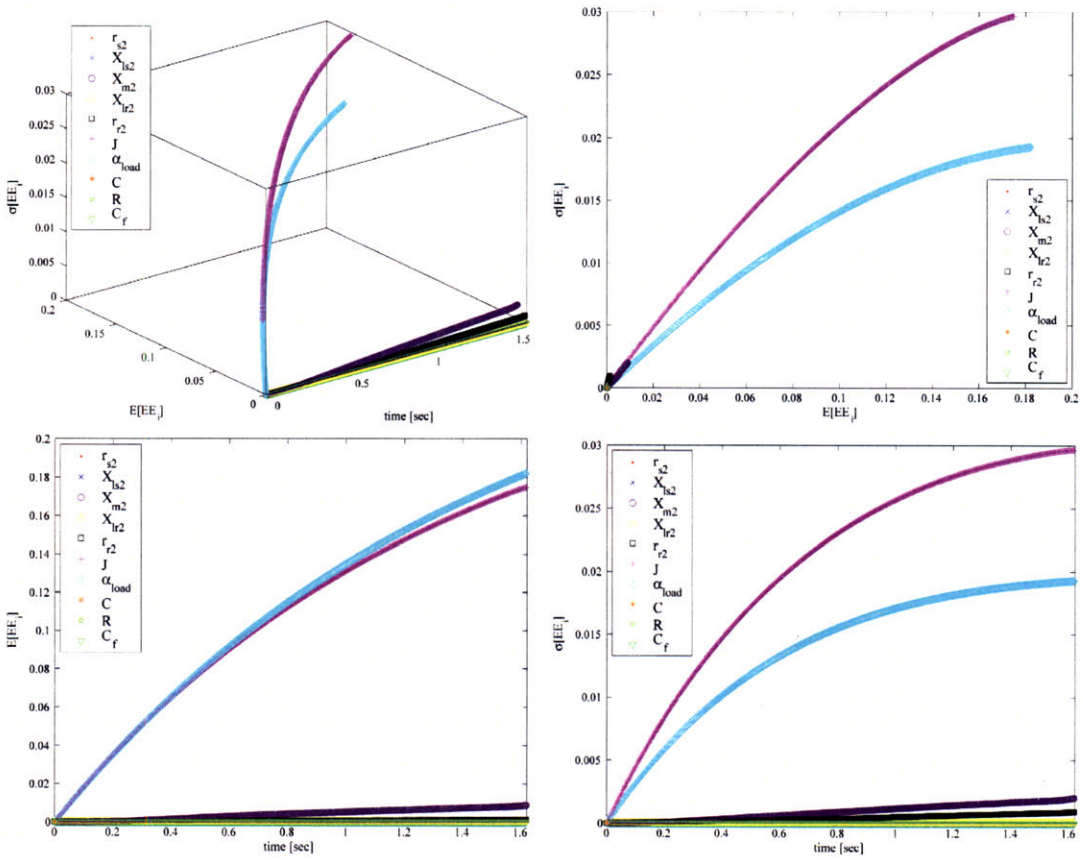

Figure 5-101: For a y_{25} variable or ω_r of the IM, the normalized $E[EE_i]$ and $\sigma[EE_i]$ trajectories of the 7 induction machine parameters and 3 bus parameters as a function of time, $t \in [0, 1.62]$ seconds, using the MC Sampling method with $NN = 3,000$ and $\sigma_{x_i} = 0.3$ in three dimension (Top-Left), the Side view (Top-Right) for emphasizing the first-order effect, the Top view (Bottom-Left) for emphasizing the inputs' interaction effect, and the Front view (Bottom-Right).

because the controller needs to compensate for a large torque error during the IM's acceleration. Only the state variables of the RC bus and the power converter are sensitive to the power converter's parameters, which implies that the controller can separate the interaction between the generator and the induction motor. In Figure 5-104, when the electrical time constant is dominated, most of the IM state variables are sensitive to its electrical and mechanical parameters, including X_m, r_r, J, and α_{load}. However, when the mechanical time constant dominates, the IM's states are sensitive only to two mechanical parameters, J and α_{load} with a large average gradient magnitude. Notice that the IM's parameters only affect its own states. This again implies that the controller is very active to compensate for any variation of the IM's parameters.

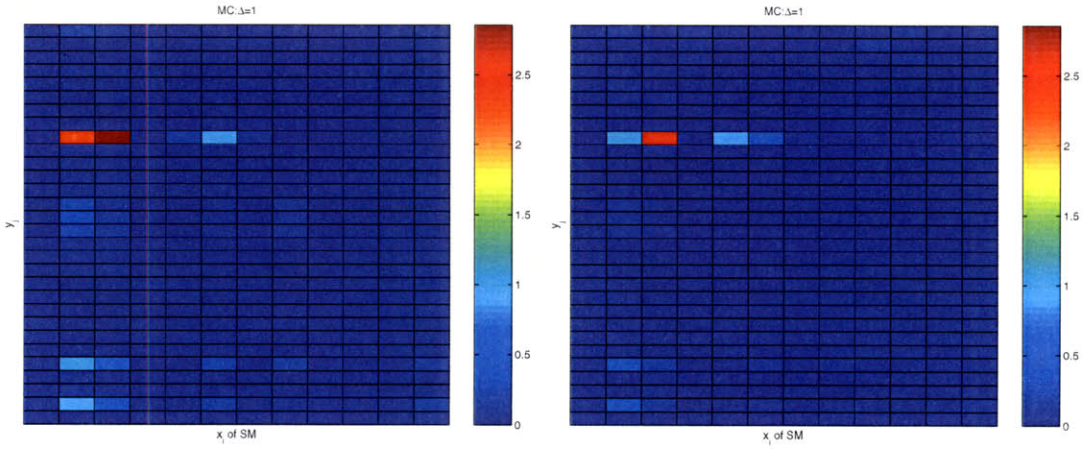

Figure 5-102: The $ES_{2,(j,i)}$ plots using the Monte Carlo Sampling method with $NN = 3000$ and $\sigma_{x_i} = 0.3$ for ranking the input sensitivity within $t \in [0, 0.2]$ (Left) and $t \in [0, 1.62]$ (Right). Note that the order of the **synchronous generator's parameters** (x_i) on the x-axis are [r_s, X_{ls}, X_{md}, X_{mq}, r_{fd}, X_{fd}, r_{kd}, X_{lkd},) r_{kq1}, X_{lkq1},r_{kq2}, X_{lkq2}] from left to right and the order of y_j outputs on the y-axis are [ψ^e_{qs}, ψ'^e_{kq1}, ψ'^e_{kq2}, ψ^e_{ds}, ψ'^e_{fd}, ψ'^e_{kd}, ψ^e_{0s}, θ, e'_{xfd}, VF, V_{an}, V_{bn}, V_{cn}, i_a, i_b, i_c, V_{c1}, V_{c2}, V_{c3},ψ^e_{qs}, ψ'^e_{qr}, ψ^e_{ds}, ψ'^e_{dr}, ψ^e_{0s}, ω_r] from top to bottom.

The sensitivity analysis of the AC power distribution with both open- and closed-loop control of the propulsion system shows us that this integrated power system without any controller reveals very strong parameter coupling between the synchronous generator and the induction machine. For this integrated power system with the constant-slip current control, the controller can isolate the interaction between the

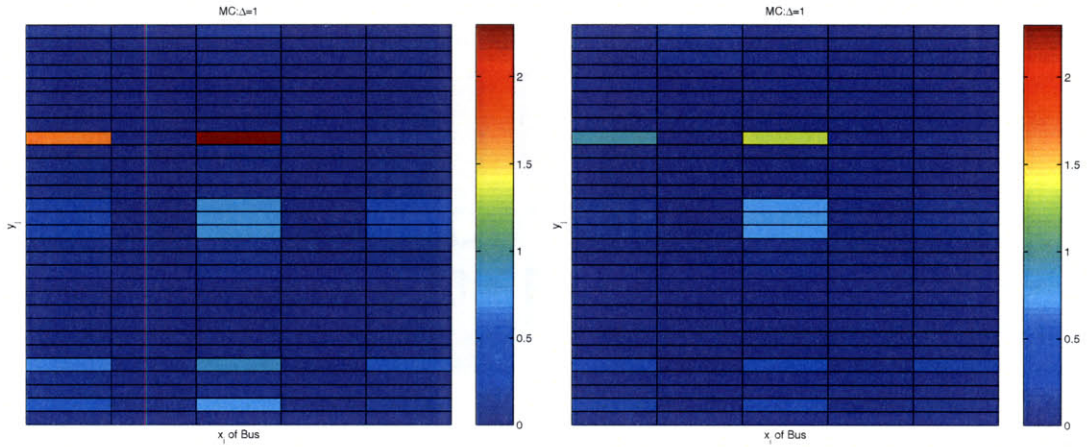

Figure 5-103: The $ES_{2,(j,i)}$ plots using the Monte Carlo Sampling method with $NN = 3000$ and $\sigma_{x_i} = 0.3$ for ranking the input sensitivity within $t \in [0, 0.2]$ (Left) and $t \in [0, 1.62]$ (Right). Note that the order of the **RC bus's parameters** (x_i) on the x-axis are $[C,\ R,\ C_f,\ r_f,\ L_f]$ from left to right and the order of y_j outputs on the y-axis are $[\psi^e_{qs},\ \psi'^e_{kq1},\ \psi'^e_{kq2},\ \psi^e_{ds},\ \psi'^e_{fd},\ \psi'^e_{kd},\ \psi^e_{0s},\ \theta,\ e'_{xfd},\ VF,\ V_{an},\ V_{bn},\ V_{cn},\ i_a,\ i_b,\ i_c,\ V_{c1},\ V_{c2},\ V_{c3}, \psi^e_{qs},\ \psi'^e_{qr},\ \psi^e_{ds},\ \psi'^e_{dr},\ \psi^e_{0s},\ \omega_r]$ from top to bottom.

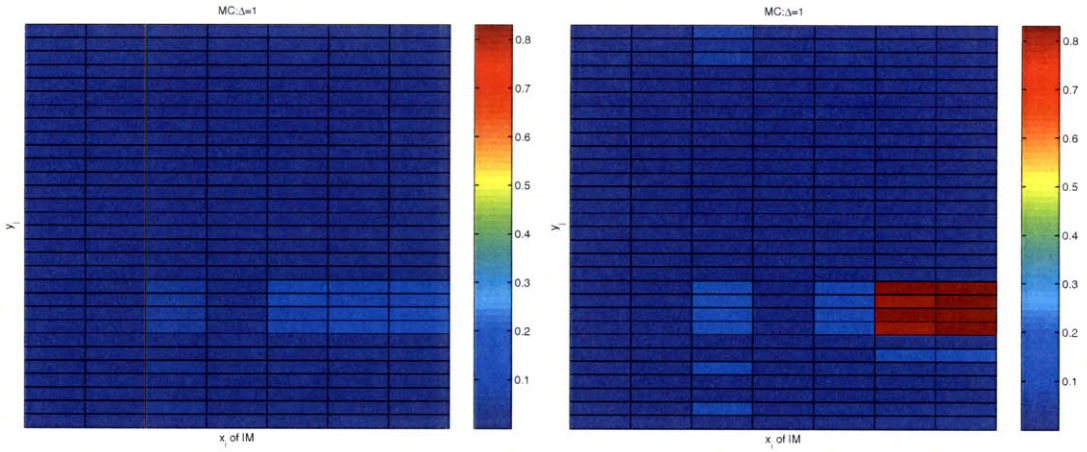

Figure 5-104: The $ES_{2,(j,i)}$ plots using the Monte Carlo Sampling method with $NN = 3000$ and $\sigma_{x_i} = 0.3$ for ranking the input sensitivity within $t \in [0, 0.2]$ (Left) and $t \in [0, 1.62]$ (Right). Note that the order of the **induction machine's parameters** (x_i) on the x-axis are $[r_{s2},\ X_{ls2},\ X_{m2},\ X_{lr2},\ r_{r2},\ J,\ \alpha_{load}]$ from left to right and the order of y_j outputs on the y-axis are $[\psi^e_{qs},\ \psi'^e_{kq1},\ \psi'^e_{kq2},\ \psi^e_{ds},\ \psi'^e_{fd},\ \psi'^e_{kd},\ \psi^e_{0s},\ \theta,\ e'_{xfd},\ VF,\ V_{an},\ V_{bn},\ V_{cn},\ i_a,\ i_b,\ i_c,\ V_{c1},\ V_{c2},\ V_{c3}, \psi^e_{qs},\ \psi'^e_{qr},\ \psi^e_{ds},\ \psi'^e_{dr},\ \psi^e_{0s},\ \omega_r]$ from top to bottom.

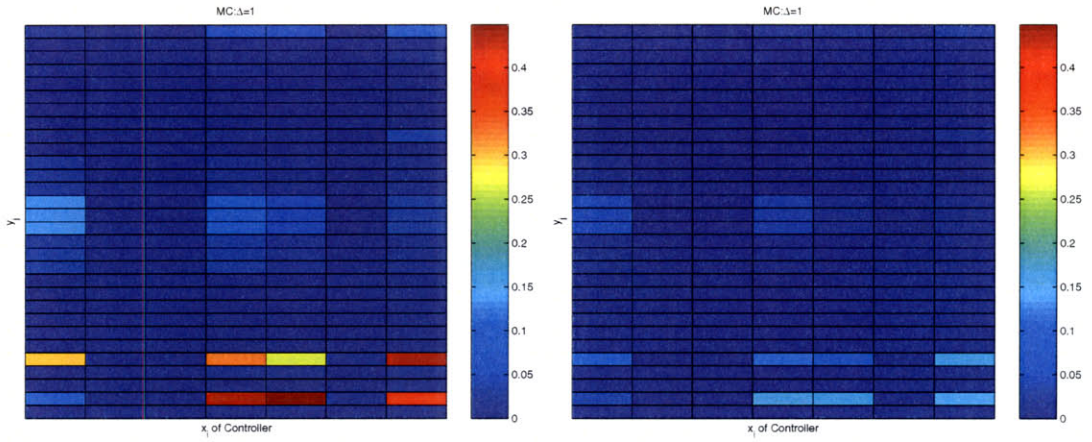

Figure 5-105: The $ES_{2,(j,i)}$ plots using the Monte Carlo Sampling method with $NN = 3000$ and $\sigma_{x_i} = 0.3$ for ranking the input sensitivity within $t \in [0, 0.2]$ (Left) and $t \in [0, 1.62]$ (Right). Note that the order of the **power converter's parameters** (x_i) on the x-axis are [L_c, r_{dc}, L_{dc}, C_{dc}, L_{filter}, r_{filter}, C_{filter}] from left to right and the order of y_j outputs on the y-axis are [ψ^e_{qs}, ψ'^e_{kq1}, ψ'^e_{kq2}, ψ^e_{ds}, ψ'^e_{fd}, ψ'^e_{kd}, ψ^e_{0s}, θ, e'_{xfd}, VF, V_{an}, V_{bn}, V_{cn}, i_a, i_b, i_c, V_{c1}, V_{c2}, V_{c3},ψ^e_{qs}, ψ'^e_{qr}, ψ^e_{ds}, ψ'^e_{dr}, ψ^e_{0s}, ω_r] from top to bottom.

synchronous generator and the induction machine. Moreover, as the percent variation of parameters increases, all parameters have a stronger impact on the system with the open-loop propulsion, while the system with the closed-loop propulsion becomes more sensitive only to the motor's and the controller's parameters. Therefore, these sensitivity techniques can be used to examine the robustness of the controller against the load and parametric uncertainties. In addition, when the magnitude of parameter fluctuation becomes larger, the characteristics of the system response can either increase the output magnitude or cause the phase shift in the output response.

Chapter 6

Conclusions and Future Work

In this last chapter, we would like to summarize all the key contributions of this thesis. In addition, some possible research directions continuing from this work will be discussed. In the first chapter, we introduced the concept of the All-Electric-Ship (AES) and its associated challenges, especially in the integrated power system, such as power sharing or load shedding and performance prediction under uncertain conditions. Moreover, the problems associated with the Galerkin and Collocation techniques in stochastic analysis as well as the sensitivity analysis were presented. Next, we described our primary contributions in the integration of multiple discipline areas (power system, numerical stochastic analysis, and sensitivity analysis), and the development of numerical techniques, as well as the demonstration of feasibility in extending these numerical techniques for the large-scale shipboard integrated power system. Chapter 2 presented the modeling of electric machines, the transmission line, the pulsed-power load, and their interconnection, which are bases for constructing the entire AES model. We identified possible sources of uncertainties in the AES system for further stochastic analysis.

In Chapter 3, various numerical stochastic algorithms - the Monte Carlo method, the Galerkin (gPC) and Collocation (PCM) approaches of the polynomial chaos - were introduced along with their underlying theories and implementation techniques. The representation of stochastic inputs as random variables or processes was briefly introduced. A new approach to combining the multi-element technique with the

collocation provides an improvement on accuracy and efficient convergence, when the long-time integration is required or the statistical solutions are discontinued. Also, the possibility of adaptive multi-element PCM was discussed. For the Galerkin approach, the ability of the gPC to deal with non-polynomial nonlinearity is extended by using the Hybrid gPC+PCM technique.

A thorough convergence study of all stochastic techniques was demonstrated in Chapter 4 on several simple systems with both continuous and discontinuous stochastic solutions, on electric machines, as well as on the AC power system section of the AES. For the system with the continuous stochastic solution, gPC, PCM, and Hybrid gPC+PCM yield the exponential convergence rate as a function of the polynomial order (p) or the number of collocation points (Nc) per random dimension (d). Their Multi-Element technique has the algebraic convergence rate as a function of the element number per d raised to the power $p+1$ or Nc, while the Monte Carlo approach exhibits only the algebraic convergence as a function of random realization (NN). When the stochastic solutions become discontinuous, the convergence rate of the Monte Carlo, gPC, PCM, Hybrid gPC+PCM, and their Multi-Element technique became algebraic as functions of NN, p/d, $(Nc-1)/d$, and N/d. For a small random dimension ($d < 10$), the full-grid PCM is the most efficient algorithm for the same accuracy with reduced computational cost. As the random dimension of inputs increases, particularly in the AES system, the sparse-grid PCM seems to be competitive against the Monte Carlo method, the convergence rate of which did not scale with the random dimension. The adaptive MEPCM has shown a promising result of faster convergence than MEPCM alone, when a system has the discontinuity in its solution. In the long-time integration problem, the full-grid PCM still yields the fastest convergence rate for systems with continuous solutions and the full-grid MEPCM is competitive against QMC for systems with discontinuous solutions. Moreover, when the integration is prolonged, the sparse-grid PCM loses its efficiency quickly and all the convergence curves of MEPCM with any Nc merge together and align with that of QMC.

Chapter 5 introduced four new techniques - Monte Carlo Sampling, Collocation,

Variance, and Inverse Variance - for analyzing the system sensitivity, both ranking the importance of inputs on the output variation and capturing the nonlinear and coupling effects of inputs. Then, the accuracy and efficiency of these sensitivity analysis techniques were compared with those of the Morris method. All four sensitivity analysis techniques ranked the input significance correctly for multiple input or static functions. Using the advantage of the full-grid PCM, the Collocation and Variance methods provided faster convergence of sensitivity indices compared to the Morris and Sampling methods. Both IEE and IIEE indices of the Variance and Inverse Variance Methods give more weight to the coupling effect than to the high-order nonlinearity, while $\sigma[EE]$ in the gradient methods weight both effects equally. Only three techniques - Sampling, Collocation, and Variance methods - are successfully extended to study sensitivity of the ODE systems with a small number of inputs, e.g., the Duffing's oscillator, and a large number of inputs, e.g., the induction machine and the AC power distribution and propulsion system. As a result, these techniques can identify when certain inputs become dominant as a function of the system response.

6.1 Future Work

We list below some possible directions for future research.

1) A thorough and systematic study of the shipboard AC and DC power systems, particularly with the pulse power load in the DC zone, requires a further investigation with stochastic disturbances and situations, since the future requirement on Navy warships will demand more electrical power to support more advanced high-power equipment. The power and thermal management are another significant topic in the AES system, and sensor diagnostics could be combined with stochastic prediction from the system model to validate system performance and increase the situation awareness.

2) An adaptive multi-element technique using a combination of full- and sparse-grid PCM can be further developed for better accuracy with smaller computational cost. Moreover, a stochastic technique with knowledge from the random process

might improve the convergence characteristics of the collocation technique due to the limitation in random dimension dependency.

Appendix A

Polynomial Chaos

In this section, we briefly include the properties of various types of orthogonal polynomials: Legendre, Jacobi, and Chebyshev.

Table A.1: The first few terms of the Legendre polynomials ($L(\xi)$) [1]

$L_i(\xi)$
$L_{-1}(\xi) = 0$
$L_0(\xi) = 1$
$L_1(\xi) = 2\xi$
$L_2(\xi) = \frac{1}{2}(3\xi^2 - 1)$
$L_3(\xi) = \frac{1}{2}(5\xi^3 - 3\xi)$
$L_4(\xi) = \frac{1}{8}(35\xi^4 - 30\xi^2 + 3)$
$L_5(\xi) = \frac{1}{8}(63\xi^5 - 70\xi^3 + 15\xi)$
$L_6(\xi) = \frac{1}{16}(231\xi^6 - 315\xi^4 + 105\xi^2 - 5)$

Table A.2: Summary of the properties of the Legendre polynomials [1]

Relation	**Legendre Chaos**
Weight function	$W(x) = 1$
Recurrence	$(j+1)L_{j+1}(x) = (2j+1)xL_j(x) - jL_{j-1}(x)$
Orthogonal	$\int_{-1}^{1} L_m(x)L_n(x)W(x)dx = \frac{2}{2n+1}\delta_{mn}$

Table A.3: The first few terms of the Jacobi polynomials ($J^{\alpha,\beta}(\xi)$) [1]

$J_i^{\alpha,\beta}(\xi)$
$J_{-1}^{\alpha,\beta}(\xi) = 0$
$J_0^{\alpha,\beta}(\xi) = 1$
$J_1^{\alpha,\beta}(\xi) = \frac{1}{2}[2(\alpha+1) + (\alpha+\beta+2)(\xi-1)]$
$J_2^{\alpha,\beta}(\xi) = \frac{1}{8}[4(\alpha+1)(\alpha+2) + 4(\alpha+\beta+3)(\alpha+2)(\xi-1) + (\alpha+\beta+3)(\alpha+\beta+4)(\xi-1)^2]$

Table A.4: Summary of the properties of the Jacobi polynomials [1]

Relation	**Jacobi Chaos**
Weight function	$W(x) = (1-x)^{\alpha}(1+x)^{\beta}$
Recurrence	$a_j^1 J_{j+1}^{\alpha,\beta}(x) = (a_j^2 + a_j^3 x)J_j^{\alpha,\beta}(x) - a_j^4 J_{j-1}^{\alpha,\beta}(x)$ $a_j^1 = 2(j+1)(j+\alpha+\beta+1)(2j+\alpha+\beta)$ $a_j^2 = (2j+\alpha+\beta+1)(\alpha^2-\beta^2)$ $a_j^3 = (2j+\alpha+\beta)(2n+\alpha+\beta+1)(2j+\alpha+\beta+2)$ $a_j^4 = 2(j+\alpha)(j+\beta)(2j+\alpha+\beta+2)$
Derivative	$b_j^1 \frac{d}{dx} J_{j+1}^{\alpha,\beta}(x) = b_j^2 J_n^{\alpha,\beta}(x) + b_j^3 J_{n-1}^{\alpha,\beta}(x)$ $b_j^1 = (2n+\alpha+\beta)(1-x^2)$ $b_j^2 = j[\alpha-\beta-(2n+\alpha+\beta)x]$ $b_j^3 = 2(n+\alpha)(n+\beta)$

Table A.5: The first few terms of the Chebyshev polynomials of the first kind ($T(\xi)$) [1]

$T_i(\xi)$
$T_{-1}(\xi) = 0$
$T_0(\xi) = 1$
$T_1(\xi) = \xi$
$T_2(\xi) = 2\xi^2 - 1$
$T_3(\xi) = 4\xi^3 - 3\xi$
$T_4(\xi) = 8\xi^4 - 8\xi^2 + 1$
$T_5(\xi) = 16\xi^5 - 20\xi^3 + 5\xi$
$T_6(\xi) = 32\xi^6 - 48\xi^4 + 18\xi^2 - 1$

Table A.6: Summary of the properties of the Chebyshev polynomials [1]

Relation	**Chebyshev Chaos**
Weight function	$W(x) = (1 - x^2)^{-1/2}$
Recurrence	$T_{j+1}(x) = 2xT_j(x) - T_{j-1}(x)$
Orthogonal	$\int_{-1}^{1} T_m(x)T_n(x)W(x)dx = \begin{cases} \frac{1}{2}m\delta_{ij} & \text{for } i \neq 0,\ j \neq 0 \\ m & \text{for i = j = 0} \end{cases}$

Appendix B

Machine Parameters

There are two set of machine parameters. The first set, which is from [38], expresses all parameters in per unit system, while the parameters of in the ONR challenge problem [27] in the second set are described in the volt-amperes unit.

Table B.1: Parameters of the induction machines [38] in per unit with $V_{base} = 450$ V

Hp	r_s	X_{ls}	X_m	X'_{lr}	r'_r	H
200	0.01	0.0655	3.225	0.0655	0.0261	0.922
150	0.0051	0.00553	2.678	0.0553	0.0165	1.524

Table B.2: Parameters of the 3.125 MW synchronous generator [38] in per unit with $V_{base} = 450$ V

$r_s = 0.00515$	$r'_{kq} = 0.0613$	$r'_{fd} = 0.00111$	$r'_{kd} = 0.02397$
$X_{ls} = 0.8$	$X'_{lkq} = 0.3298$	$X'_{lfd} = 0.13683$	$X'_{lkd} = 0.33383$
$X_{mq} = 1.0$	$X_{md} = 1.768$	$H = 2.137$	

Table B.3: Parameters of the IEEE type DC1A exciter/voltage regulator (Type 1) [38] in per unit

$T_R = 0$	$V_{REF} = 1$	$K_A = 400$	$T_A = 0.01$
$V_{RMAX} = 8.4$	$V_{RMIN} = 0$	$K_F = 0.01$	$T_{F1} = 0.15$
$T_{F2} = 0.06$	$K_E = 1$	$T_E = 0.1$	

Table B.4: Parameters of the simplified gas turbine with speed governor [38] in per unit

$K_c = 22.5$	$T_c = 0.55$	$T_{FV} = 0.01$	$T_{FT} = 0.05$
$W_{F10s} = 0.23$	$C_{2GT} = 0.251$	$C_{1GT} = 1.3523$	$C_{GNGT} = 0.5$

Table B.5: Parameters of the 50-hp induction machines [27] with $V_{base} = 570$ V

Hp	$r_s(\Omega)$	$X_{ls}(H/s)$	$X_m(H/s)$	$X'_{lr}(H/s)$	$r'_r(\Omega)$	$J(kg \cdot m^2)$
50	0.087	0.302	13.08	0.302	0.228	1.662

Table B.6: Parameters of the 59 KW synchronous generator [27] with $V_{base} = 570$ V

$r_s = 0.0286$	$r'_{kq1} = 0.0170$	$r'_{kq2} = 0.0802$	$r'_{fd} = 0.0089$	$r'_{kd} = 0.1272$
$X_{ls} = 1.8122$	$X'_{lkq1} = 7.7496$	$X'_{lkq2} = 0.8956$	$X'_{lfd} = 1.3487$	$X'_{lkd} = 0.7750$
$X_{mq} = 15.3562$	$X_{md} = 15.3562$	$J = 2.5$	$P = 4$	

Table B.7: Parameters of the full-brigde rectifier and DC-link filter [27]

$L_c = 0.001\ H$	$R_{dc} = 0.01\ \Omega$	$L_{dc} = 0\ H$	$C_{dc} = 500 \times 10^{-6}\ F$
$r_f = 0.056\ \Omega$	$L_f = 0.0114\ H$	$C_f = 1.988 \times 10^{-3}\ F$	

Table B.8: Parameters of the RC bus with the harmonic filter [27]

$$R = 500\ \Omega \qquad C = 4 \times 10^{-5}\ F$$
$$R_{filter} = 0.039\ \Omega \quad L_{filter} = 0.00561\ H \quad C_{filter} = 4.975 \times 10^{-5}\ F$$

Table B.9: Parameters of the constant-slip current control [27]

$$r'_{r,est} = 0.228\ \Omega \quad L'_{rr,est} = 3.5496 \times 10^{-2}\ H \quad L_M = 3.4695 \times 10^{-2}\ H \quad P = 4$$

Bibliography

[1] Abramowitz M., and Stegun I. A., Handbook of Mathematical Functions with Formulas, Graphs, and Mathematical Tables, 9th printing. New York: Dover, 1972.

[2] Allen E.H, Ilić M.D., Interaction of Transmission Network and Load Phasor Dynamics in Electric Power Systems, *IEEE Trans. on Circuits and Systems-1. Fundamental Theory and Applications*, Vol. 47, No. 11, pp. 1613-1620, 2000.

[3] Anderson P.M., and Fouad A.A., *Power System Control and Stability*, Second Edition, IEEE Press and Wiley-Interscience, NJ 2003.

[4] Baldwin T.L., Lewis S.A., Distribution Load Flow Methods for Shipboard Power Systems, *IEEE Trans. on Industry Applications*, Vol. 40, No. 5, pp. 1183-1190, 2004.

[5] Baran M.E., Wu F.F., Network reconfiguration in distribution systems for loss reduction and load balancing, *IEEE Trans. Power Delivery*, vol. 4, pp.1401-1407, 1989.

[6] Bose B.K., *Power Electronics And AC Drives*, Prentice-Hall, New Jersey, 1986.

[7] Box G.E.P., Hunter W.G., and Hunter J.S., *Statistics for Experimenters. An Introduction to Design, Data Analysis and Model Building*, Wiley, New York, 1978.

[8] Boyd R.R., *Tolerance Analysis of Electronic Circuits using Matlab*, CRC Press LLC., 1999.

[9] Butler K.L., Sarma N.D.R. Ragendra Prasad V., Network Reconfiguration for Service Restoration in Shipboard Power Distribution Systems, *IEEE Trans. on Power Systems*, Vol.16, No. 4, pp. 653-661, 2001.

[10] Cameron, R.H., and Martin, W.T., The orthogonal development of non-linear functionals in series of Fourier-Hermite functionals, *Annals of Mathematics*, **48**, pp. 385-392, 1947.

[11] Campolongo F., Screening methods in sensitivity analysis - The Morris method and its applications, *JRC-Ispra*, Nov. 2005.

[12] Campolongo F., Cariboni J., Saltelli A., and Schoutens W., Enhancing The Morris Method, *Los Alamos National Laboratory; http://library.lanl.gov*, 2005.

[13] Chaboki A., Thurmond L., Grater G., Bauer D., Beach F., and Clayton D., Integration of electromagnetic rail gun into future electric warship, *High Powered Weapons Systems for Electric Ship Conference*, Dec. 2004.

[14] Chapman J.W., Power system control for large-disturbance stability: Security, robustness and transient energy, Ph.D. thesis, MIT, Department of Electrical Engineering and Computer Science, 1996.

[15] Chapman J.W., Ilić M.D., King C.A., Eng L., Kaufman H., Stabilizing a Multimachine Power System via Decentralized Feedback Linearizing Excitation Control, *IEEE Trans. on Power Systems*, pp. 830-839, Vol. 8, No. 3, August 1993.

[16] Clayton D.H., Sudhoff S.D., Grater G.F. ,Electric Ship Drive and Power System, *Conf. Rec. 2000 24th Int. Power Modulation Symp.*, 2000, pp. 85-88.

[17] Cotter S.C., A screening design for factorial experiments with interactions, *Biometrika*, Vol. 66, pp. 317-320, 1979.

[18] Gerstner T., and Griebel M., Numerical Integration using Sparse Grids, *Numerical Algorithms*, Vol. 18, No. 3-4, pp. 209-232, 1998.

[19] Ghanem R., and Spanos P., *Stochastic Finite Elements: A Spectral Approach*, Springer-Verlag, New York, 1991.

[20] Helton J.C. and Iuzzolino H.J., Construction of complementary cumulative distribution functions for comparison with the EPA release limits for radioactive waste disposal, *Reliab. Engng. Syst. Safety*, Vol. 40, pp. 277-293, 1993.

[21] Hockenberry J.R., Evaluation of Uncertainty in Dynamic, Reduced-Order Power System Models, Ph.D. thesis, Massachusetts Institute of Technology, 2000.

[22] Hockenberry J.R. and Lesieutre B.C., Evaluation of Uncertainty in Dynamic Simulations of Power System Models: The Probabilistic Collocation Method, *IEEE Trans. on Power Systems*, Vol. 19, pp. 1483-1491, 2004.

[23] IEEE Committee Report, Computer Representation of Excitation Systems, *IEEE Trans. on Power Apparatus and Systems*, Vol. PAS-87, pp. 1460-1464, June 1968.

[24] IEEE Recommended Practice for Excitation System Models for Power System Stability Studies, IEEE Standard 421.5-1992.

[25] Ilić M., Zaborszky J., *Dynamics and Control of Large Electric Power Systems*, John Wiley & Sons, Inc., 2000.

[26] Iyengar R.N., Basak B., Investigation of a non-linear system under partially prescribed random excitation, *International Journal of Non-Linear Mechanics*, vol. 40, pp. 1102-1111, 2005.

[27] PC Krause and Associates, ONR Control Challenge Benchmark, November 2003.

[28] PC Krause and Associates, Power System Control Development, Final Report, Contract F33615-99-D-2974 for NSF/ONR Partnership in Electric Power Network Efficiency and Security (EPNES), March 2003.

[29] Krause P.C., Wasynczuk O., and Sudhoff S.D., *Analysis of Electric Machinery and Drive Systems*, Second Edition, IEEE Press and Wiley-Interscience, NY, 2002.

[30] Kuhn B., Sudhoff S.D., Pulsed Power System with Railgun Model, A deliverable for ONR contract N00014-02-1-0623, *Electric Ship Research and Development Consortium (ESRDC)*, Recent Papers, nerc.aticorp.org/esrdc_recent_papers.html.

[31] Kundur P., *Power System Stability and Control*, McGraw-Hill, Inc., 1994.

[32] Lee S. and Nam K., Dynamic Modelling and Passivity-Based Control of an Induction Motor Powered by Doubly Fed Induction Generator, *Industry Applications Conference*, Vol. 3, pp.1970-1975, Oct. 2003.

[33] Leon-Garcia A., *Probability and Random Processes for Electrical Engineering*, Second Edition, Addison Wesley, 1994.

[34] Logan K.P., Intelligent Diagnostic Requirements of Future All-Electric Ship Integrated Power System, *Petroleum and Chemical Industry Conference*, p. 151-163, 2005.

[35] Lucor D., Su C.H., and Karniadakis G.E., Generalized polynomial chaos and random oscillators, *Int. J. Numer. Meth. Engng*, Vol. 60, pp. 571-596, 2004.

[36] McKay M.D., Latin Hypercube Sampling As A Tool In Uncertainty Analysis of Computer Models, *Proceedings of the 1992 Winter Simulation Conference*, pp. 557-564, 1992.

[37] McNab J.R., Pulsed Power for Electric Guns, *IEEE Trans. on Magnetics*, Vol. 33, No. 1, Jan. 1997.

[38] Mayer J.S., Wasynczuk O., An efficient method of simulating stiffly connected power systems with stator and network transients included, *Transactions on Power Systems*, Vol. 6, No. 3, Aug 1991.

[39] Morris M.D., Factorial Sampling Plans for Preliminary Computational Experiments, *Technometrics*, Vol. 33, No. 2, May 1991.

[40] Niederreiter H., Hellekalek P., Larcher G., and Zinterhof P., *Monte Carlo and Quasi-Monte Carlo Methods*, Springer-Verlag, New York, 1998.

[41] Ngamroo I., Dechanupaprittha S., Robust decentralized design of power system stabilizers taking into consideration system uncertainties, *Optimal Control Applications and Methods*, Vol. 26, pp. 35-53, 2005.

[42] Ong C.M., *Dynamic Simulation of Electric Machinery*, Prentice-Hall PTR, Upper Saddle River, NJ, 1998

[43] Ortega R., Loria A., Nicklasson P.J., and Sira-Ramirez H., *Passivity-based Control of Euler-Lagrange Systems: Mechanical, Electrical and Electromechanical Applications*, Springer-Verlag, 1998.

[44] Orszag S.A., Bissonnette L.R., Dynamical properties of truncated Wiener-Hermite expansions, *Physics of Fluids*, Vol. 10, No. 12, pp. 2603-2613, 1967.

[45] Petras K., Smolyak cubature of given polynomial degree with few nodes for increasing dimension, *Numer. Math.*, 93, pp. 729-753, 2003.

[46] Press, W.H., Teukolsky, S.A., Vetterling, W.T., and Flannery, B.P., *Numerical Recipes in C*, second edition, Cambridge University Press, 1992.

[47] Prousalidis J.M., Hatziargyriou N.D., Papadias B.C., On Studying Ship Electric Propulsion Motor Driving Schemes, *IPST Conference*, June 2001.

[48] Rabitz H., Kramer M., and Dacol D., Sensitivitiy analysis in chemical kinetics, *Annu. Rev. Phys. Chem.*, Vol. 34, pp. 419-461, 1983.

[49] Rowen W.I., Simplified Mathematical Representations of Heavy-Duty Gas Turbines, *Journal of Engineering for Power*, vol. 105, pp. 865-869, Oct 1983.

[50] Saltelli A., Andres T.H., Homma T., Sensitivity analysis of model output. Performance of the iterated fractional factorial design method, *Computational statistics and data analysis*, Vol. 20, No. 4, pp.387-407, 1995

[51] Saltelli A., Chan K., Scott M., *Sensitivity Analysis*, John Wiley & Sons Ltd, 2000.

[52] Saltelli A., Tarantola S., Campolongo F., and Ratto M., *Sensitivity Analysis In Practice, A Guide to Assessing Scientific Models*, John Wiley & Sons Ltd, England, 2004.

[53] Sobol, I.M., Global sensitivity indices for nonlinear mathematical models and their Monte Carlo estimates, *Mathematics and Computers in Simulation*, Vol. 55, No. 1-3, pp. 271-280, 2001.

[54] Su Q. and Strunz K., Stochastic circuit modelling with Hermite polynomial chaos, *Electronics letters*, Vol. 41, No. 21, Oct. 2005.

[55] Sudhoff S.D., Corzine K.A., Glover S.F., Hegner H.J., and Robey H.N., DC Link Stabilized Field Oriented Control of Electric Propulsion Systems, *IEEE Transactions on Energy Conversion*, Vol. 13, No. 1, March 1998.

[56] Sudhoff S.D., Kuhn B.T., Zivi E., Delisle D.E., and Clayton D., Impact of Pulsed Power Loads on Naval Power and Propulsion Systems, *Electric Ship Research and Development Consortium (ESRDC)*, Recent Papers, nerc.aticorp.org/esrdc_recent_papers.html.

[57] Sudhoff S.D., Glover S., Pekarek S.D., Zivi E.J., Delisle D.E., and Clayton D., Stability Analysis Methodologies For DC Power Distribution Systems, *Electric Ship Research and Development Consortium (ESRDC)*, Recent Papers, nerc.aticorp.org/esrdc_recent_papers.html.

[58] Sudhoff S.D., Pekarek S., Kuhn B., Glover S., Sauer J., Delisle D., Naval Combat Survivability Testbeds for Investigation of Issues in Shipboard Power Electronics Based Power and Propulsion Systems, *Power Engineering Society Summer Meeting, IEEE*, Vol. 1, pp. 347 - 350, July 2002.

[59] Venkatesh B., Ranjan R., Gooi H.B., Optimal Reconfiguration of Radial Distribution Systems to Maximize Loadability, *IEEE Trans. on Power Systems*, Vol. 19, No. 1, pp. 1311-1319, 2004.

[60] Wan X. and Karniadakis G.E., An Adaptive Multi-Element Generalized Polynomial Chaos Method for Stochastic Differential Equations, *Journal of Computational Physics*, Vol. 209, pp.617-642, 2005.

[61] Webster M., Tatang M.A., and McRae G.J., Application of the probabilistic collocation method for an uncertainty analysis of a simple ocean model, Tech. Rep. 4, Joint Program on the Science and Policy of Global Change, MIT, Cambridge, MA, 1996.

[62] Xiu D., Karniadakis G.E., The Wiener-Askey polynomial chaos for stochastic differential equations, *SIAM Journal for Scientific Computation*, Vol. 24, No. 2, pp. 619-644, 2002.

[63] Xiu D., and Hesthaven J.S., High-order collocation methods for differential equations with random input, *SIAM J. SCI. COMPUT.*, Vol. 27, No. 3, pp. 1181-1139, 2005.

[64] Xiu, D., Lucor, D., Su, C.-H., and Karniadakis, G. Em, Stochastic modelling of flow-structure interactions using generalized polynomial chaos, *J. Fluids Engineering*, **124**, pp. 51-59, 2002.

[65] Cdr. Young S., RN, Cdr. Newell J., RN, Cdr. Little G., RN, Beyond Electric Ship, *Naval Engineers Journal*, April 2001.

[66] Zivi E.L., Integrated Shipboard Power and Automation Control Challenge Problem, *Power Engineering Society Summer Meeting, 2002 IEEE*, Vol.1, pp. 325 - 330, July 2002.

[67] Zivi E., McCoy T.J., Control of a Shipboard Integrated Power System, *Proceedings of the 33th Annual Conference on Information Sciences and Systems*, March 1999.